

Explorations of Magnetic Phases in $F = 1$ ^{87}Rb Spinor Condensates

by

Jennie Sara Guzman

A dissertation submitted in partial satisfaction of the

requirements for the degree of

Doctor of Philosophy

in

Physics

in the

Graduate Division

of the

University of California, Berkeley

Committee in charge:

Professor Dan M. Stamper-Kurn, Chair

Professor Holger Müller

Professor Phillip Geissler

Fall 2012

The dissertation of Jennie Sara Guzman, titled Explorations of Magnetic Phases in $F = 1$ ^{87}Rb Spinor Condensates, is approved:

Chair _____ Date _____

_____ Date _____

_____ Date _____

University of California, Berkeley

Explorations of Magnetic Phases in $F = 1$ ^{87}Rb Spinor Condensates

Copyright 2012

by

Jennie Sara Guzman

Abstract

Explorations of Magnetic Phases in $F = 1$ ^{87}Rb Spinor Condensates

by

Jennie Sara Guzman

Doctor of Philosophy in Physics

University of California, Berkeley

Professor Dan M. Stamper-Kurn, Chair

Spinor Bose Einstein condensates have widely been sought after as perfect emulators of condensed matter phenomena, providing widely tunable and highly controlled systems. Utilizing a novel spin sensitive phase contrast imaging technique, the vector magnetization is measured *in-situ* with high spatial and temporal resolution and applied to a number of experiments. Using optically trapped $F = 1$ ^{87}Rb spinor condensates, the equilibrium phase diagram of a spin-1 Bose gas is quantitatively explored by observing the evolution of unmagnetized spin textures and their thermal equilibrium properties. Spin domain coarsening and a strong dependence of the spin configuration on the quadratic Zeeman shift is observed, supporting the predicted mean-field equilibrium phase diagram for small values of the quadratic shift. Additionally, spinor Bose gases are demonstrated to be an effective tool in calibrating and characterizing experimental imaging systems. Sinusoidal test patterns of varying pitch are created and used to extract the modulation transfer function and quantify optical aberrations which are of immense importance in systems which claim to have high spatial resolution. Lastly we realize an optical kagome geometry in a two-dimensional optical superlattice with a scalar Bose gases. The optical superlattice can be tuned between various geometries, including kagome, one-dimensional stripe, and decorated triangular lattice. Using atom optics we characterize the various geometries and demonstrate the versatility of this optical superlattice. The kagome geometry presents a new experimental arena for studies of geometrically frustrated systems.

Contents

List of Figures	v
List of Tables	viii
1 Introduction	1
1.1 Bose-Einstein Condensation	1
1.1.1 Interactions	2
1.1.2 Spinor Condensates	3
1.2 Kagome Optical Lattice	4
1.2.1 Lattice Basics	5
1.3 History of the Experiment	6
1.4 Outline of this thesis	8
2 Experimental Apparatus	9
2.1 Vacuum Chamber	9
2.1.1 Oven Chamber	10
2.1.2 Rotary Feedthrough	11
2.1.3 MOT Chamber	12
2.1.4 Science Chamber	13
2.2 Oven	13
2.3 Optical System	15
2.3.1 Cooling lasers	15
2.3.2 Trapping laser	20
2.4 Zeeman Slower	23
2.4.1 Windings	24
2.4.2 Measuring the slower fields	24
2.5 Magneto-Optical Trap	27
2.6 Magnetic Transport Coils	27
2.7 Applied Fields	32
2.7.1 Microwave field: evaporation	32
2.7.2 RF fields	36
2.7.3 DC magnetic bias field	36
2.7.4 DC magnetic field gradients	40
2.7.5 Applying quadratic Zeeman shifts using microwave fields	41

2.8	Computer Control	45
2.9	Water-cooling	46
2.10	Making a BEC	49
3	Imaging Magnetization	51
3.1	Phase Sensitive Imaging	51
3.1.1	Basic Principle	51
3.2	Dielectric properties of an $F = 1$ spinor gas	52
3.2.1	Dielectric Constant	52
3.2.2	Spinor Order Parameter: Ferromagnetic vs Polar state	54
3.3	Phase shift	55
3.4	Variations on Phase Sensitive Imaging	56
3.4.1	Phase-Contrast Imaging (PCI): Phase dot and circularly polarized light	56
3.4.2	Polarization Contrast Imaging	57
3.5	Imaging the vector magnetization	59
3.5.1	Larmor Precession Imaging	59
3.5.2	Spin-Echo Imaging	59
4	Design of a High Resolution Imaging System	70
4.1	Design of a high resolution imaging system	70
4.1.1	Design Criteria	70
4.1.2	Imaging Objective	71
4.1.3	Imaging Resolution	72
4.2	Characterizing the lens on the bench	74
4.2.1	Test Pattern	74
4.2.2	Experimental MTF	75
4.2.3	Extracting the PSF	78
4.2.4	Astigmatism	79
4.3	<i>In-situ</i> Characterization	80
4.3.1	Imaging Test Pattern	81
4.3.2	Extracting the MTF	84
5	Equilibrium Properties of Spinor Condensates	90
5.1	Spinor Basics	90
5.1.1	Theoretical description of a spinor BEC	91
5.1.2	Mean-Field Phase Diagram	92
5.2	Why study the magnetic phases of an $F = 1$ spinor gas?	94
5.3	Experimental Tools	95
5.3.1	Magnetic Fields	95
5.3.2	Modulated magnetic fields	96
5.3.3	Spin Mixtures	96
5.4	Experiment 1	97
5.4.1	$\eta = 0$ spin mixture results	98
5.4.2	$\eta = 1/4$ spin mixture results	99
5.4.3	Characterizing the magnetic order	101

5.4.4	Equilibrium Properties?	103
5.5	Equilibrium Properties: Attempt 2	104
5.5.1	Apparatus Improvements	105
5.5.2	Experimental Sequence	105
5.5.3	Temporal Evolution	106
5.5.4	Comparing to the $F = 1$ Phase diagram as predicted by Mean-Field Theory	119
5.5.5	Remaining Questions	123
6	Exploration of long-range order in $F = 1$ ^{87}Rb spin textures	125
6.1	Why explore long-range order in a magnetic spin texture?	125
6.2	Experimental Sequence	126
6.2.1	Measurement of the coherence length	127
6.3	Analysis and Results	129
6.3.1	Scalar BEC	129
6.3.2	Spinor BEC	129
6.3.3	Coherence Length	130
7	Realization of an optical kagome lattice	136
7.1	Changes to the experimental apparatus	137
7.1.1	Coordinate system	137
7.2	Kagome Lattice Geometry	138
7.2.1	Triangular lattice	138
7.2.2	Bi-chromatic optical lattice	140
7.2.3	Unit Cell	141
7.3	Tuning the lattice geometry	142
7.4	Other lattice geometries	144
7.5	Calibrating the lattice potential	145
7.6	Measurement Techniques	146
7.6.1	Kaptiza-Dirac	147
7.6.2	Momentum-space analysis	149
7.7	Lattice Optics	152
7.7.1	Lattice optics layout	152
7.7.2	Lattice Alignment	153
7.7.3	Laser table optics	154
7.7.4	New optical trap	154
	Bibliography	159
A	Operation of the Ti-sub pump	172
A.1	Operating Procedure	172
A.2	Pumping Area	172
B	Initial installment of an ODT	174
C	Generating the rf-pulse sequence	175

D Alignment of an imaging system	178
E Phase contrast imaging 101	181
E.1 Phase contrast signal with no phase dot	181
F Lattice Alignment	183
F.1 Alignment Procedure	183

List of Figures

2.1	Entire Vacuum Chamber	10
2.2	Illustration of the oven chamber	11
2.3	Illustration of the MOT chamber	12
2.4	Oven nozzle used to hold multichannel array	14
2.5	Photograph of the various types of nozzles made in the group	16
2.6	Cooling laser frequencies used in this experiment	17
2.7	Illustration of cooling optics layout	19
2.8	Zeeman slower coil winding pattern	25
2.9	Measured magnetic fields from Zeeman slower	26
2.10	Number of trapped atoms in glass cell versus MOT power	28
2.11	Illustration of magnetic transport system	29
2.12	Magnetic transportation sequence	30
2.13	Aspect ratio of atom cloud along transportation axis	31
2.14	Measured magnetic fields from the coils used in the magnetic transport system	32
2.15	Microwave evaporation setup	33
2.16	Population in $ F = 2, m_F = 0\rangle$ state as function of time when irradiated with microwaves.	34
2.17	Microwave Rabi frequency as a function of rf sideband power	35
2.18	The condensate axes as compared to the geographical coordinate system	37
2.19	Mount for shim coils	38
2.20	Calibration of bias magnetic fields	39
2.21	Illustration of microwave setup used to generate ac Zeeman energy shifts	42
2.22	Breit-Rabi Diagram for ^{87}Rb	43
2.23	Rabi frequency calibration for quadratic Zeeman shift	45
2.24	Illustrated of water-cooling system	47
2.25	Illustration of interlock logic circuit	48
2.26	Phase-space density measurement of cooling sequence as of April 30 2009	50
3.1	Measurement of magnetic field in the lab over the weekend	61
3.2	Population within the Zeeman sublevels after a Ramsey $\pi/2$ rf pulse sequence	63
3.3	Spin-echo sequence to extract the transverse magnetization	65
3.4	Spin-echo sequence to measure the longitudinal magnetization	66
3.5	Raw data of vector magnetization profile	68

3.6	TOF images showing the population within the Zeeman sublevels after 4 consecutive π rf pulses	69
4.1	Imaging objective and mount	72
4.2	1951 USAF resolution test chart	75
4.3	Measured test pattern and extracted MTF curves	77
4.4	STM images of the pinhole and image taken with the aspheric lens	78
4.5	Image of the new pinhole taken with objective lens system	79
4.6	Measure of astigmatic aberrations from imaging system	80
4.7	Schematic of spin texture preparation	82
4.8	Unprocessed polarization contrast images of helical test patterns	83
4.9	Measured MTF curve from helical test pattern	85
4.10	Spatial Fourier transforms of helical spin texture for different wave vector orientations	87
4.11	MTF from out-of-focus imaging system of helical spin texture	88
4.12	Power spectrum of helical spin texture after 100 ms evolution time	89
5.1	Ground state phase diagram for $F = 1$ spinor condensate	93
5.2	Dissolution of helical spin textures	94
5.3	Condensate fraction as a function of the final temperature for an $\eta = 1/4$ spin mixture	99
5.4	TOF density profile and <i>in-situ</i> transverse magnetization profile of spin textures at various temperatures for an initial thermal spin mixture with $\eta = 0$	100
5.5	Instantaneous measure of the transverse magnetization profile for $\eta = 1/4$ spin mixture	101
5.6	Power spectra for $\eta = 0$ and $\eta = 1/4$ spin mixtures	102
5.7	Images of the transverse magnetization profile for an initial $\eta = 1$ spin mixture	104
5.8	Sample TOF images for an $\eta = 0$ spin mixture	107
5.9	Temporal evolution of condensate fractions for $\eta = 0$ and $\eta = 1/4$ spin mixtures	108
5.10	Temporal evolution of condensate fraction for and $\eta = 1/4$ thermal spin mixture at high quadratic Zeeman shift	109
5.11	Temporal evolution of vector magnetization profile for $\eta = 0$ spin mixture .	110
5.12	Temporal evolution of magnetization variance for $\eta = 0$ spin mixture at variable quadratic shift	112
5.13	Phase contrast amplitudes for a fully polarized gas	114
5.14	Temporal evolution of the spin domain	116
5.15	Temporal evolution of domain sizes at $q = -5$ Hz and $q = 0$ Hz	118
5.16	Temporal evolution of the power spectrum at $q/h = 0$ Hz	120
5.17	Temporal evolution of the power spectrum at $q/h = 5$ Hz	121
5.18	Temporal evolution of the power spectrum at $q/h = -5$ Hz	122
5.19	Instantaneous snapshot of the vector magnetization profile at 2 s evolution time for an $\eta = 0$ spin thermal spin mixture at different quadratic Zeeman shifts	124

6.1	Experimental setup of two pulse Ramsey-like method	128
6.2	Image of interference pattern for a scalar condensate	132
6.3	Measurement of first-order correlation function for a scalar condensate . . .	133
6.4	First order correlation function for $\eta = 0$ and $\eta = 1/4$ spin mixtures	134
6.5	Spatial interference pattern for $\eta = 0$ and $\eta = 1/4$ initial spin mixtures . .	135
7.1	Picture of Japanese kagome basket	137
7.2	Illustration of intensity nodes for the SW and LW triangular lattice	138
7.3	Contour map of triangular lattice intensity profile	140
7.4	Contour map of the kagome lattice potential	141
7.5	The unit cell of the kagome lattice	142
7.6	Illustration of two-color Mach-Zehnder interferometer	143
7.7	Tuning the relative displacement of 532 nm intensity nodes with respect to the 1064 nm intensity nodes	144
7.8	Illustration of other accessible lattice geometries in this bi-chromatic lattice	145
7.9	Calibration curve for SW lattice depth for Beam 1 and Beam 2	147
7.10	Kapitza-Dirac scattering from a one-dimensional bi-chromatic lattice	148
7.11	TOF calculations of the momentum population ratio as a function of the LW lattice position	150
7.12	TOF calculations for misaligned lattices	155
7.13	Layout of lattice optics on science table	156
7.14	Position of Beam 2 of the SW lattice with respect to the in-trap location of the condensate.	156
7.15	Layout of 1064 nm optics on laser table.	157
7.16	Schematic of dimple optics	158
C.1	Schematic of pulse generators used to create rf-pulse sequence for spin-echo imaging.	177
D.1	Image of Andre Wenz while trying to align final lens with respect to the imaging camera. For this image, a 300 mm lens was being aligned. In order to place the lens a position f away from the camera, the objects needs to be located distance away that is $\gg f$. Here that distance was between 3-4 m. .	180

List of Tables

2.1	ODT Parameters	22
2.2	Coil Parameters	29
2.3	Dedicated power supplies for magnetic transport coils	29
2.4	Atom number and temperature	50
7.1	Summary of momentum distribution and corresponding unit cell populations for the different lattice geometries.	152

Chapter 1

Introduction

Since the first observation of Bose-Einstein condensation (BEC) in dilute atomic gases in 1995 [1, 2], the field of ultracold atoms has seen a tremendous growth, both theoretically and experimentally. Since then, ultracold atom experiments can be classified into two categories. The first category consists of experiments which study the fundamental properties of ultracold atomic gases, much like the initial pioneering experiments in the field, many of which include studies of supersolidity, dipolar quantum gasses and ultracold molecules. The second category encompasses the other class of experiments that instead seek to use ultracold atomic gas as a tool, such as for technological applications, including magnetometers and gyroscopes [3, 4, 5, 6, 7], or as an experimental test bed for exploring new physics [8, 9].

The work described in this thesis falls within both categories. While the first few chapters are concerned with the design and construction of the experimental apparatus, the last few chapters fit within the two classes of ultracold atomic physics experiments with one chapter dedicated to exploring magnetic phases in a spinor gas, and the other chapter dedicated to the construction of an optical kagome lattice.

Given the extraordinary amount of experimental and theoretical work that proceeds this thesis, only a brief introduction to BEC's, spinor condensates and optical lattices will be presented here and in Chapter 5. For a more detailed introduction to Bose-Einstein condensation and laser cooling and trapping see the following theses [10, 11, 12, 13, 14], review articles [15, 16, 17, 18, 19, 20, 21, 22, 23, 8] and books [24, 25, 26] on the subject.

1.1 Bose-Einstein Condensation

In this section, a brief overview of the salient features of BEC's will be presented. The BEC phase transition occurs when there is a macroscopic occupation of a single quantum state. The condition for condensation can be expressed in terms of the spatial extent of each atom, described by the thermal deBroglie wavelength,

$$\lambda_{dB} = \frac{h}{\sqrt{2\pi m k_B T}}, \quad (1.1)$$

where h is Planck's constant, m is the atomic mass, k_B is the Boltzmann constant, and T is the temperature. At fairly high temperatures, for instance room temperature, the de-Broglie wavelength is much smaller than the inter-particle spacing of atoms. However, upon decreasing the temperature of a sample of atoms, the spatial extent of each atom increases, and when they begin to overlap, the system undergoes a phase transition to a Bose-Einstein condensate. At this point, we can no longer think of the atoms as distinguishable particles, but instead as a giant matter wave. Thus, we can describe the condition for condensation in terms of the phase space density of the gas, $\rho = n\lambda_{dB}^3$, where condensation occurs when $\rho \sim 1$.

Assuming that a gas of N noninteracting bosons occupy the same spatial wave function, $\phi(\mathbf{r})$, the Hamiltonian describing such a system is

$$H = \sum_{i=1}^N \left[\frac{\mathbf{p}_i^2}{2m} + V_{ext}(\mathbf{r}_i) \right], \quad (1.2)$$

where V_{ext} describes the external trapping potential. As is the case with most ultracold atom experiments, our BEC is formed in a harmonic trapping potential,

$$V_{ext} = \frac{1}{2}m(\omega_x^2 x^2 + \omega_y^2 y^2 + \omega_z^2 z^2) \quad (1.3)$$

where ω_i is the trapping frequency in the i^{th} direction. While in the ground state, the macroscopic wavefunction is given by the product of single particle states, $\Phi(\mathbf{r}_i) = \prod_i \phi(\mathbf{r}_i)$.

The transition temperature for Bose condensation can be computed from the total number of particles using the Bose-Einstein distribution function,

$$N = \sum_i \frac{1}{e^{(\epsilon_i - \mu)/k_B T}}, \quad (1.4)$$

where ϵ_i is the energy of the i^{th} state, and μ is the chemical potential. In the limit of large N and a harmonic trapping potential the BEC transition temperature is

$$T_c = \hbar\bar{\omega} \left(\frac{N}{\zeta(3)} \right)^{1/3} \quad (1.5)$$

where $\bar{\omega}$ is the geometric mean of the trapping harmonic trapping frequencies, and $\zeta(3) \approx 1.202$ is the Riemann zeta function. The fraction of atoms in the condensate at a specific temperature is

$$\frac{N_0}{N} = 1 - \left(\frac{T}{T_c} \right)^3 \quad (1.6)$$

where N_0 is the number of atoms in the condensed state, and N is the total number of atoms.

1.1.1 Interactions

The theory presented above is formulated for an ideal-gas and neglects the effect of interactions. In experiments using alkali atoms, however, atom-atom interactions must

often be taken into account. At large interatomic distances, the interaction is described by van der Waals forces. These interactions would eventually bind the atoms together. However, the rate at which this happens is very slow since binding can only take place in a three-body collision in which one atom pair forms a bound state while the excess kinetic energy is carried off by the third atom. Given the typically low densities of BEC's, $n \sim (10^{11} - 10^{14}) \text{ cm}^{-3}$, the probability of three particles colliding simultaneously is low [11]. Thus, the collisions between atoms is almost entirely two-body in nature. We can make a further approximation if we only consider interactions at low temperatures, commonly referred to as s-wave scattering for bosons. Here the interaction can be approximated by a Dirac delta-function

$$V(\mathbf{r}_1 - \mathbf{r}_1) \approx g\delta(\mathbf{r}_1 - \mathbf{r}_2), \quad (1.7)$$

where the constant $g = 4\pi a_s \hbar^2/m$ characterizes the strength of the two-body interaction and a_s is the s-wave scattering length. In general, two-body interactions do not greatly affect the BEC transition temperature or condensate fraction, but they do affect the density distribution of the condensate.

Taking into account atom-atom interactions, a nonlinear term is added to the Hamiltonian. The Hamiltonian for a system of N interacting bosons is

$$H = \sum_{i=1}^N \left[\frac{\mathbf{p}_i^2}{2m} + V_{ext}(\mathbf{r}_i) \right] + \frac{4\pi a_s \hbar^2}{m} \sum_{i < j} \delta(\mathbf{r}_i - \mathbf{r}_j). \quad (1.8)$$

Defining the condensate wavefunction as $\psi(\mathbf{r}) = \sqrt{N}\phi(\mathbf{r})$, where $\phi(\mathbf{r})$ is the single particle wavefunction, the energy of the system, in the context of mean-field theory, is given by

$$E = \int d^3\mathbf{r} \left[\frac{\hbar^2}{2m} |\nabla\psi(\mathbf{r})|^2 + V_{ext}(\mathbf{r})|\psi(\mathbf{r})|^2 + \frac{4\pi a_s \hbar^2}{m} |\psi(\mathbf{r})|^4 \right]. \quad (1.9)$$

1.1.2 Spinor Condensates

The vast majority of research involving BEC's typically deals with a single-component systems, often involving a single Zeeman sublevel. A particularly intriguing variant of BEC's, however, is the extension to multi-component systems, where the internal spin of the BEC is a new degree of freedom. For instance, the three Zeeman sublevels in $F = 1$ ^{87}Rb BECs. These multi-component systems are referred to as spinor condensates.

Like the scalar BEC interaction described above, the low energy dynamics of a spinor condensate are described by a pairwise interaction. This contact interaction is rotationally invariant and preserves the hyperfine spin of the individual atoms. The general form of this interaction is

$$V(\mathbf{r}_1 - \mathbf{r}_1) = \delta(\mathbf{r}_1 - \mathbf{r}_2) \sum_{F=0}^{2f} g_F P_F, \quad (1.10)$$

where $g_F = 4\pi a_F \hbar^2/m$ is the strength of the interaction, a_F is the s-wave scattering length in the total spin F channel, and P_F is the projection operator which projects pair 1 and 2 into a total hyperfine spin F [27]. For the experimental studies pursued here, $F = 1$ ^{87}Rb is

used. In such a system, cold s-wave collisions between two $F = 1$ atoms are characterized by total angular momentum 0 or 2 due to symmetry requirements. The resulting contact interaction potential is

$$V(\mathbf{r}_1 - \mathbf{r}_2) = c_0 + c_2 \mathbf{F}_1 \cdot \mathbf{F}_2, \quad (1.11)$$

where we have used the relation $\mathbf{F}_1 \cdot \mathbf{F}_2 = \sum_{F=0}^{2f} P_F$ to simplify the functional form of the interaction potential, and $c_{0(2)}$ characterize the strength of the spin independent (dependent) contact interaction. They are defined as $c_0 = (g_0 + 2g_2)/3$ and $c_2 = (g_2 - g_0)/3$.

For a spin-1 spinor condensate, the condensate is either ferromagnetic or anti-ferromagnetic [27]. In the case of rubidium, $c_2 < 0$ since $a_2 < a_0$, resulting in a ferromagnetic ground state. This is in contrast to sodium spinor condensates, where $a_2 > a_0$, yielding an anti-ferromagnetic ground state. We can gain a slightly more intuitive understanding of the ferromagnetic nature of rubidium by considering the effective scattering lengths for total angular momentum, F . The effective scattering length for collisions of total angular momentum $F = 0$ is $a_0 \approx 5.39$ nm (where the spin of the atoms are roughly anti-aligned) in ^{87}Rb . This is a slightly larger than the scattering length for collisions of total angular momentum $F = 2$, $a_2 \approx 5.31$ nm (where the spins are roughly anti-aligned). This tends to favor the spin of the atoms to line up, which is what is meant by a ferromagnetic state. In fact, the experimental work described in the later chapters of this thesis is primarily due to these spin-dependent contact interactions and their effect on the ground state magnetic phase for $F = 1$ spinor condensates.

1.2 Kagome Optical Lattice

In 1968, Vladilen Letokhov first suggested that atoms could be confined to the wavelength-sized regions of a standing wave of light by means of the dipole force [28]. However, it would be approximately 20 years later before the first experimental demonstration of atoms trapped in a one-dimensional standing wave [29]. Since this first successful trapping, the field of optical lattices using ultracold quantum gases has rapidly flourished, with current lattices occupying multiple dimensions and various geometries, including square, triangular, honeycomb, double-well, and kagome [30, 31, 32, 33, 34, 35, 36, 37, 38, 39, 40].

With the confinement and control that accompany these engineered optical crystals, they have become a tool for cleanly simulating particular Hamiltonians, thereby serving as a probe for studying fundamental condensed-matter phenomena. Such studies include pioneering work by Immanuel Bloch [30] and Markus Greiner [31], who have lead the field of optical lattices with impressive work using a two-dimensional square lattice with single-site imaging, studying quantum magnetism, and the Mott insulator to superfluid physics, to name a few [41, 42, 43, 30].

Much of the work in optical lattices so far has involved primitive Bravais lattices, the square lattice for instance, with a single lattice site per unit cell [32, 41, 30]. Recently, however, lattice geometries with multiple-site bases such as the honeycomb, checkerboard, and double-well superlattice have attracted much interest [37, 38, 39, 40]. Such lattices have a low-energy orbital degree of freedom which can lead to non-trivial ordering or a new quantum phase. This is where the lattice adventures of this experiment begin (often referred to as E5). Given that we are entering the game quite late, attempting to compete

with the forerunners of the field who have more than ten years of experience, one may ask what can we contribute to the field that no one else is able to do? Our answer is the kagome lattice, which had not been experimentally realized until our work in [38]. The kagome geometry, consisting of a planar lattice with corner sharing triangles, presents one of the most intriguing and highly studied crystal geometries in condensed-matter physics. This lattice geometry contains three s-orbital bands, one of which is non-dispersing, which serves to accentuate the role of atom-atom interactions. In fact, what happens to a BEC, which has a very narrow momentum distribution, when in this non-dispersing band? Furthermore, this lattice has a large degree of geometric frustration. For example, competing exchange interactions between spin 1/2 particles with antiferromagnetic interactions can not be simultaneously satisfied, leading to a macroscopic ground-state degeneracy. It is this ground-state degeneracy that make it a promising candidate for realizing unconventional quantum phases [44, 45, 46]. These are just a small sample of the many unanswered questions unique to the kagome geometry, thus making it a promising avenue for experimental pursuits.

1.2.1 Lattice Basics

Presented below is a very brief and basic overview of optical lattices. An optical lattice is formed by the interference of laser beams, resulting in a spatially periodic, “egg-crate” potential. This is accomplished by overlapping laser beams with different wave vectors, where the spatial periodicity of the lattice is $\lambda_L/[2 \sin(\theta/2)]$ and θ is the mutually enclosed angle of the light beams. The simplest optical lattice to consider is a one-dimensional pair of counter-propagating laser beams of the same polarization, which creates a standing wave interference pattern. The periodic potential has the form

$$V_{lat}(x) = V_0 \sin^2(k_L x) \quad (1.12)$$

where $k_L = 2\pi/\lambda_L$ is the wave vector of the laser light used to form the optical standing wave and V_0 is the depth of the lattice potential. However, the Gaussian beam profile of the laser beams superimposes a nearly harmonic trapping potential over the periodic potential. It is this weak harmonic confinement that adds an extra degree of complexity to studies of condensed matter physics, such as the superfluid-to-Mott insulator phase diagram [47]. Typically, the depth of the lattice potential is described in units of the recoil energy,

$$E_R = \frac{\hbar^2 k_L^2}{2m} \quad (1.13)$$

where m is the mass of a single atom. The recoil energy is a natural energy scale for atoms in optical lattices.

One of the easiest ways to gather information from these systems is to use time-of-flight (TOF) analysis. This technique is the same technique used to image BEC’s, which entails the sudden turn off of the optical traps followed by a duration of free expansion and then the use of resonant laser light to obtain an absorption image of the cloud. The density distribution after some expansion time t has the following form (see [48, 49]),

$$n_{TOF}(\mathbf{r}) = \left(\frac{m}{\hbar t}\right) |\tilde{w}_0(\mathbf{k})|^2 S(\mathbf{k}) \quad (1.14)$$

where $\mathbf{k} = m\mathbf{r}/\hbar t$, the envelope function \tilde{w}_0 is the Fourier transform of the Wannier wave function, which constitute a set of wave functions that are maximally localized to individual lattice sites [50], and the grating-like interference term is

$$S(\mathbf{k}) = \sum_{r_\mu, r_\nu} e^{i\mathbf{k}\cdot(\mathbf{r}_\mu, \mathbf{r}_\nu)} \langle a_\mu^\dagger \hat{a}_\nu \rangle. \quad (1.15)$$

Here a_μ^\dagger is the creation operator, creating an atom at site \mathbf{r}_μ and \hat{a}_ν is the annihilation operator. The resulting pattern after TOF is an interference pattern, closely resembling the Fourier transform of the real-space lattice geometry. Much like the double-split experiment which can be thought of as consisting of many wave packet of light that interfere, the origin of the interference pattern can be thought of as being assembled from many single-particle wave packets at each lattice site that expand and interfere after the sudden release from the optical trap. It is this method by which we extract information from our kagome lattice geometry. Currently, steps are being taken to use other means for data extraction, such as obtaining information about the quasi-momentum in the lattice using band-mapping techniques, or using direct spectroscopy in the lattice [36, 8].

1.3 History of the Experiment

I joined the Stamper-Kurn group in the spring of 2006 and began working on the first spinor experiment, referred to as “E1.” Already working on the experiment at that time were Lorraine Sadler, Sabrina Leslie, and Dr. Mukund Vengalattore. Having had no experience with a BEC machine, Mukund welcomed me to the project with easy tasks such as turning on the machine, lab notebook documentation, and fiber alignment optimization. One of my first independent tasks was to build a new laser dedicated for phase contrast imaging. The laser at the time offered too little power, ~ 1 mW at the fiber output, and the laser frequency would come out of lock when the turn-off of the Ioffe-Pritchard magnetic trap was initiated. This was primarily due to the proximity of the laser with respect to the power supplies. After a lot of trial and error of testing and killing many high-power diodes at 795 nm (~ 50 mW), we finally found a diode from Power Technology that worked reliably well. The final design was located on a work bench since there was no available room on the topics table.

After building the D1 diode laser, I began to work primarily on E1. The first major project that I was able to work on was the magnetometry project [3]. It was at this time that I truly learned the complicated nature of a BEC machine. E1, however, was not typical machine, as I think back comparing it now to E5. Everyday was a constant battle. The MOT needed to be tweaked everyday for hours on end, and at the time, it seemed that the only person who had the magic touch was Mukund. Fortunately, for us, Mukund never left the lab, often working 30-48 hours straight. Between learning how to run E1, and fixing the occasional laser (usually the repump laser) and electronic device, I along with Mukund and the guys from E2 would enjoy the occasional coffee break at Strada and the occasional late-night run to Kingpin Doughnuts. It would be during these next few years that I would learn how to independently run a BEC machine.

In early 2008 we were given news that Birge would shut down for an entire month, starting in mid-December of 2008. Believing that E1 would not recover from such a long period of being inoperative, we decided to move ahead with plans to build a replacement chamber for E1, referred to as “E5.” Because the construction of E5 had been planned to occur when Mukund arrived at Berkeley in the summer of 2005, most of the parts of the apparatus for E5 had been ordered by both Mukund and Sabrina. However, with the new science coming out of E1, E5 was put on hold and the ordered parts were left to gather dust in 75 LeConte. Now fast forward to 2008, Mukund and Sabrina are running E1, and at this point I was in charge of making and carrying out the plan necessary to get E5 up and running by the end of the year. Fortunately, at this same time, we gained Friedhelm Serwane, a fantastic researcher. Friedhelm came with a tremendous amount of experience in building a cold-atom machine, having done it in his previous group. The plan was that Friedhelm would work on the project for one year before going back to complete his doctoral program in Heidelberg. Together with Friedhelm, we designed and constructed a magnetic transportation system, used to transport atoms to a glass cell. This required many hours in the student machine shop, where Joseph kept a watchful eye on our use of Stycast around his ancient equipment. However, much thanks also needs to be given to the staff in the Physics Machine Shop. Our countless revisions to technical drawings for the water-cooling mount for the magnetic coils, and their unending patience helped us quickly move forward with the construction of the magnetic transportation system. Soon after, I began the construction of the Zeeman slower while Friedhelm designed a high numerical aperture objective, with a design resolution of $\sim 1 \mu\text{m}$. His knowledge and expertise in the optics design software, OSLO, not only helped in designing the objective we are currently using today, but also greatly benefited the lab. Together, we characterized the objective under a variety of conditions, verifying that it was performing as expected.

In the fall of 2008, we were fortunate to have Dr. Kater Murch join our project. In his blindingly fast manner, he built the necessary interlock box for the water-cooled coils and began winding the Helmholtz coils necessary for the compensation fields in the magneto-optical trap. Then comes the dreaded shut down in December. All electrical and water to the building are turned off for necessary renovations. We are told of a predicted date when electricity, water, and air conditioning will be restored to the building, but we are skeptical. Then in early January, Friedhelm leaves for the better life in Germany, Mukund leaves for his professorship at Cornell University, and Birge is fully operational once again. At this point, we put Kater up to the task of telling Dan of our plans to dismantle E1. With his okay we move forward with E5. At Kater’s staggering pace, we dismantle E1 within a few hours. We separate the two optics table and with the help of the entire group, we move the E5 vacuum chamber from B175 to B173/B171. Within two weeks of dismantling E1, we have atoms in the magneto-optical trap (MOT) of the new chamber. At this pace, we continue to proceed forward, by first magnetically trapping a cloud of rubidium atoms and then transporting them 200 mm to the glass cell. All within a few days of first observing atom in the magneto-optical trap. Then on March 30, 2009, much to the surprise of the group and ourselves, we achieved our first BEC in E5.

A few months after achieving our first BEC, we were joined by a visiting student, Andrew Wenz, who was also from the same group as Friedhelm. Thus, he was nicknamed

“the new Friedhelm.” With Andre and Kater on the project we listened to a lot of music, drank a lot of coffee from Nefelis Cafe, and made a tremendous amount of progress during our early explorations of the magnetic phases of a spinor condensate. However, in the fall of 2009 Kater ceased being a postdoc on our project and moved to the world of quantum nano-electronics in Professor Irfan Siddiqi’s research group. Shortly after Kater’s departure, we were joined by an equally fantastic postdoc, Gyu-Boong Jo. With Gyu-Boong’s help, we were able to wrap up the spinor equilibrium project and move on to the field of optical lattices, despite the departure of Andre in the summer of 2010. Midway through wrapping up spinors and starting lattices, we joined by graduate student Claire Thomas, whose enthusiasm and optimistic attitude provided a nice change to the atmosphere in the lab, which had been drenched with the pessimistic attitudes of senior graduate students. In the spring of 2011, at an impressive pace, we successfully trapped atom in our first two-dimensional optical lattice. However, much thanks needs to be given to Michael Solarz. His countless hours of help in designing and machining parts for the lattice experiment were essential to its success. Shortly after trapping atoms in the triangular lattice, we obtained our first experimental signal of atoms in an optical kagome lattice. We have only begun to scratch the surface of science to be explored in this system. Thus, I’m sure that with the current crew and the addition of graduate student Thomas Barter, that there will be unending slew of results coming out of the lab.

1.4 Outline of this thesis

The following chapters outline the efforts of my graduate student career. The construction and operation of the experimental apparatus is presented in Chapter 2. In chapter 3, a new vector magnetization imaging technique, referred to as spin-echo imaging, is discussed. The design and implementation of a high numerical aperture imaging system is presented in Chapter 4. This includes a characterization of the objective which uses the spinor condensate as a potential *in-situ* test pattern. Chapter 5 is the first chapter with published experimental results. Here the equilibrium phase diagram of an $F = 1$ spinor condensate is experimentally verified. Chapter 6 presents an attempt to measure the long-range order in spinor gases. Finally, in Chapter 7, we cease to study spinor condensates and instead dive into the world of optical lattices, a little late in the game none the less. Here a description of the optical kagome lattice is presented. Helpful procedures for obtaining a phase contrast signal and for aligning an optical lattice are included in the Appendices.

Chapter 2

Experimental Apparatus

This chapter gives a brief overview of the experimental apparatus used for our studies of spinor condensate. Changes to the apparatus specific to the implementation of optical lattices are discussed in Chapter 7.

Necessary in making a Bose-Einstein condensate are a few critical elements. These elements include:

- **Ultra-high vacuum (UHV) chamber** - A versatile machine, able to achieve pressures ranging from $\simeq 10^{-9}$ Torr where the atom source is located to $\lesssim 10^{-11}$ Torr where the data and measurements take place, with the latter pressure is typically determined by the type of experiment.
- **Atom source** The atom source must provide a sufficiently high flux to be subsequently laser cooled and trapped. For this particular experiment, the source is a recirculating rubidium oven.
- **Laser system** A laser system with adequate tunability of the laser frequency and power for laser cooling and manipulation of the atomic sample.
- **Atom Traps** This can be a magnetic trap or an optical trap. It is in these traps that the probing and manipulation of the atomic sample will take place.
- **Computer and Electronic control** Also important in the production of ultracold gases is a precisely timed sequence of events. This includes control over many electronic components such as power supplies, acousto-optic modulators (AOMs), optical beam shutters, mirror flippers, etc.

The bulk of this chapter is dedicated to describing each of these systems in some detail.

2.1 Vacuum Chamber

The UHV system is divided into three sections referred to as the ‘‘Oven chamber,’’ the ‘‘MOT chamber,’’ and the ‘‘Science chamber.’’ An illustration of the entire experimental apparatus is shown in Figure 2.1.

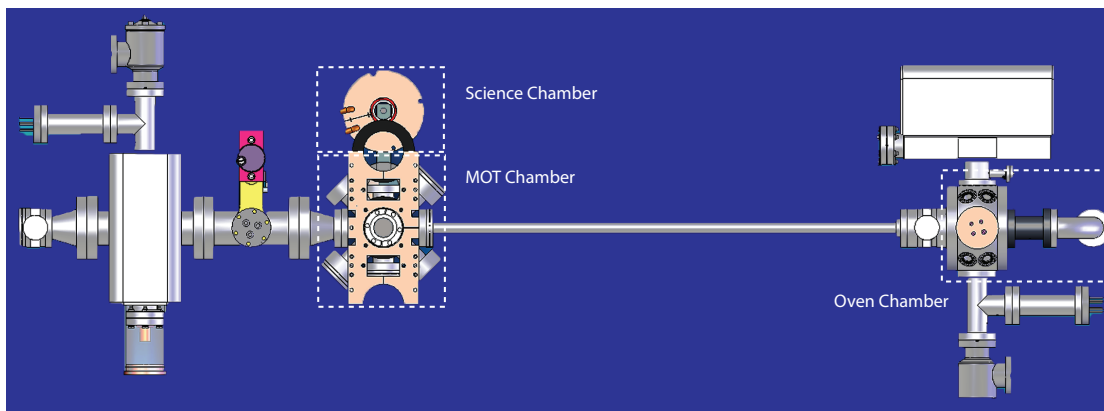


Figure 2.1: Entire Vacuum Chamber.

2.1.1 Oven Chamber

The goal of the oven chamber is to create a high-flux shuttered atomic beam while simultaneously maintaining the integrity of the remaining vacuum chamber (MOT and Science chamber). It is designed to be compact in size, allowing for quick and relatively easy bake-outs, while still permitting the easy replacement of the rubidium reservoir. An illustration is shown in Figure 2.2. Briefly discussed below are the relevant components to the oven chamber.

The rubidium reservoir lies in a stainless-steel elbow, and is attached to a nozzle consisting of a multichannel array of stainless shell tubes. Connected to this is a spherical square from Kimball Physics (Part MCF600-SS200408). Within the Kimball sphere is a custom built u-shaped thermoelectrically cooled copper plate (referred to as the “oven cold catcher”) used to trap the bulk of the rubidium emitted from the oven that does not travel through to the slower. Between the two copper plates of the oven cold catcher is a rotary shutter from MDC (Part 54032-GE02-0002) and rigidly attached to this is a thin copper plate, which is used to block the atomic beam.

Between the oven chamber and the Zeeman slower is a differential pumping tube. The tube is 70 mm long with an inner diameter of ~ 7 mm, yielding an approximate conductance of ~ 0.5 liters/sec for rubidium atoms at room temperature. Typical operating pressures in the oven are $\sim 10^{-9}$ Torr (last measured in Summer 2009). Lastly, the oven chamber is isolated from the remaining UHV apparatus via a Viton O-ring-sealed gate valve from MDC.

Cold Catcher

The oven cold catcher is cooled using a thermo-electric cooler (TEC). The TEC is attached to a vacuum copper feedthrough which allows for good thermal conduction between the copper plate in vacuum and the TEC located out of vacuum. A typical problem with this setup, however, is related to condensation forming on the cold side of the TEC, typically operated at -13° C. As condensation forms, the performance of the TEC deteriorates until

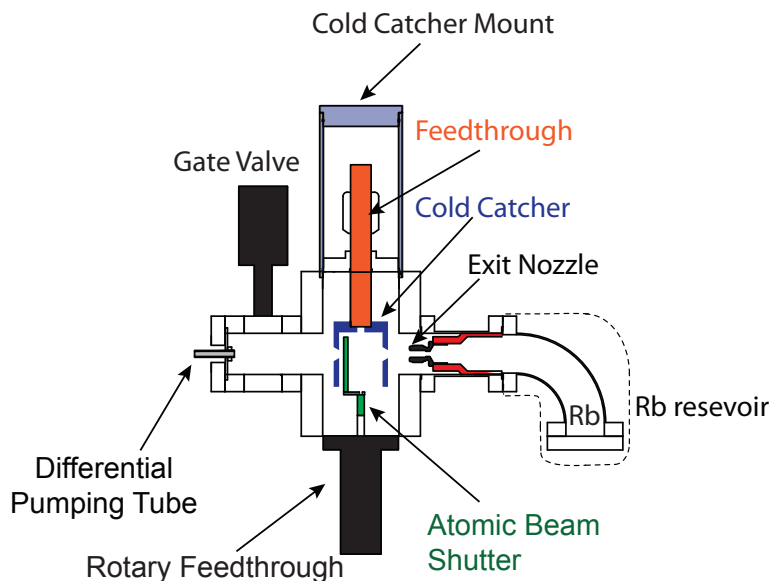


Figure 2.2: Illustration of the oven chamber.

it has to be replaced, presumably due to corrosion or electrical shorting as water seeps into the interior of the TEC. To reduce the amount of condensation, we have attached a cap over the TEC and feedthrough, secured to the spherical square using a highly moldable clay. This separates the TEC from the moisture ridden environment. Furthermore, we have filled the cap with desiccant and secured a rough vacuum within the cap using the house vacuum provided by the building. The TEC is water-cooled using city tap water which is fed into the cap via brazed copper pipe feedthroughs. The TEC is also powered using electrical feedthroughs.

To give a little perspective, in the previous experiment, E1, the TECs on the oven and main chamber cold catcher were replaced every 6-8 months, approximately. The TEC in this new system have never been replaced, operating continuously since January 2009.

2.1.2 Rotary Feedthrough

The rotary feedthrough from MDC (Part Number 670002) allows for external control of the atomic beam shutter. Unfortunately, the lifetime of these rotary feedthroughs are limited. The ball bearings of the feedthrough need to be lubricated, which is accomplished by rotating the feedthrough by 360 degrees. However, normal operation only rotates the feedthrough by 45-60 degrees. Thus over time, it becomes more challenging to rotate. We estimate that the feedthrough worked flawlessly for approximately 400,000-500,000 rotations (30 s duty cycle, 8-10 hours/ day, 5 days/week, 45 weeks/year, 3 years), after which it can no longer be used. An MDC representative suggests that by rotating the feedthrough by 360 degrees more frequently, perhaps as often as once a day, one could possibly circumvent

or postpone this problem. We have yet to come up with a viable solution to this problem that does not involve breaking vacuum. Currently, we do not operate with a shuttered atomic beam, but instead leave the shutter open while operating the experiment.

2.1.3 MOT Chamber

The magneto-optical trap (MOT) is formed in the MOT chamber, consisting of a custom 10-way cross. This is illustrated in Figure 2.3. Specifically, the chamber has ten $2\frac{3}{4}$ inch flanges with two oriented along gravity (up/down in Figure 2.3) and 8 in the orthogonal plane (the perspective of the drawing in Figure 2.3 only permits 4 flanges to be easily seen). Four flanges are located three inches from the chamber center, while the remaining six are four inches from the center. Connected to the shorter flanges are the Zeeman slower, two glass cells and a four-way cross. By minimizing the distance between the chamber center and the end of the Zeeman slower, we aimed to reduce the amount of transverse heating from the slowed atomic beam. The six remaining viewports are allocated for the MOT laser beams, which do not necessitate short distances to the chamber center.

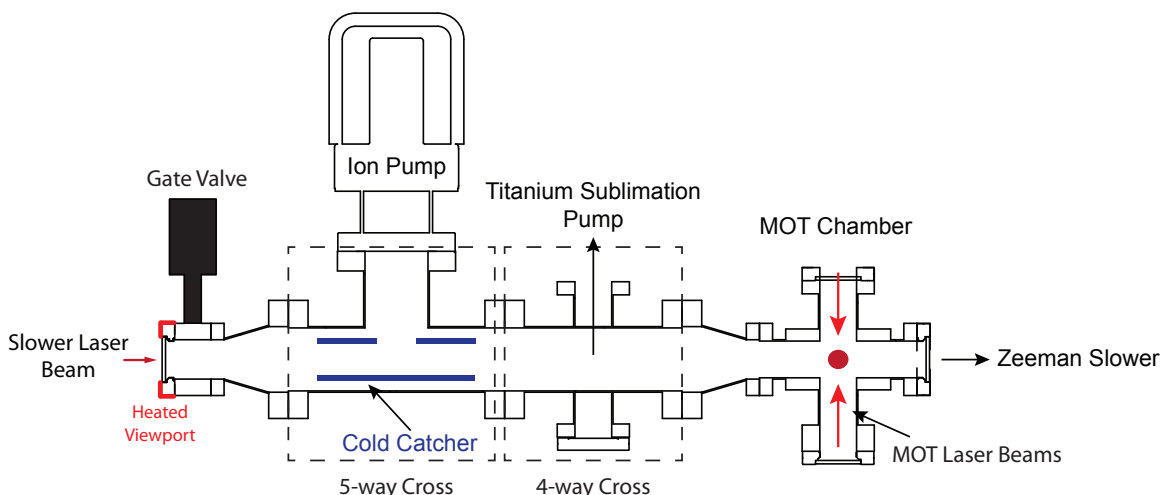


Figure 2.3: Illustration of the MOT chamber. The glass cell are not shown in this perspective of the drawing. If shown, they would be oriented along the axis perpendicular to the page.

One major flaw in this chamber pertains to the flanges which are only three inches from the chamber center. Careful inspection of this design would have foreseen the lack of space for bolts and plate-nuts, which are necessary secure any vacuum component to these flanges. To ameliorate this situation, the bolts and plate-nuts were filed down using a mechanical grinder in the graduate student machine shop. Several millimeters were taken off in order to secure vacuum components to these flanges.

The main pumping elements for the chamber are located on a 4-way cross and a 5-way cross. This houses the titanium sublimation pump (Ti-sub). The Ti-sub is connected to a retractable vacuum piece (Thermionics Z-275 Series Translator), which permits the deposition of titanium along the entire interior of the main MOT chamber and slower tube

without blocking the slower laser beam which propagates along this axis (see Figure 2.3). For operation procedures for the Ti-sub see Appendix A

Connected to the 5-way cross is an additional cold catcher, a 110 l/s ion pump (Varian Vacion Plus), and a viewport, via an additional gate valve. The main chamber cold catcher is cylindrical in shape, where the shape geometry was determined by trying to maximize its surface area while considering the spatial constraints due to the vacuum chamber. It is situated next to a heated viewport allocated for the slower laser beam, as shown in Figure 2.3. Like the oven cold catcher, the main chamber cold catcher collects the atoms that are not captured by the MOT and those which bounce off of the heated slower vacuum viewport. When initially installed (January 2009), the temperature of the main chamber cold catcher was -15°C , but today it is at -10°C while at the same operating current (2.45 A). This temperature decrease is most likely attributed to moisture buildup on the interior of the TEC.

2.1.4 Science Chamber

The science chamber consists of a single glass cell (for now), connected to the shortened flange of the 10-way cross (MOT chamber). The motivation for the having a science chamber separate from the main chamber and the use of a glass cell as opposed to a stainless steel chamber is the potential for more optical access. In the previous experiment, E1, optics used for steering the laser beams for the MOT reduced the available space for other laser beams, including light used for optical trapping and imaging of the atomic sample. Thus, by transporting the atoms a short distance from the MOT chamber, we move to an area uncluttered with optics. However, once all of the magnetic traps, optics for the optical traps, and bias field coils were positioned, there was very little space left.

Glass Cell

The glass cell is made of Hellma Borosilicate with a thickness of $\simeq 2.5\text{ mm}$ and a refractive index of $n = 1.46$. The size of the cell is approximately $1 \times 1 \times 3\text{ inches}^3$, with the glass-to-metal seal not included in these measurements. The cells were purchased without the glass-to-metal seal and were later sent to a different company where the seals were made. However, careful inspection of these glass cells show the front face of the cell to be littered with scratches. By comparing these glass cells to those without the glass-to-metal seals, we have determined that these scratches were made by the company which attached the metal seal. However unfortunate this may be, the scratches on this front face have not greatly influenced the experiments so far.

2.2 Oven

The oven consists of a rubidium reservoir and a small aperture from which the rubidium can escape, referred to as the nozzle. The general concept of this oven design has been described in other references and won't be elaborated in too much detail here [51, 52]. The main focus here will be on the elements unique to this oven design.

The rubidium reservoir is contained in a stainless-steel elbow. A rubidium ampoule, with approximately 5 g, is situated within the elbow and acts as the source to the reservoir. The vapor pressure, and hence the flux of atoms, has a strong dependence on temperature, and can thus be well controlled by tuning the temperature of the reservoir. This is accomplished by a band heater surrounding the bottom flange of the elbow. Roughly, the vapor pressure increases by an order of magnitude every 20°C, with a pressure of 10^{-4} Torr at 100°C and 10^{-3} Torr at 120°C.

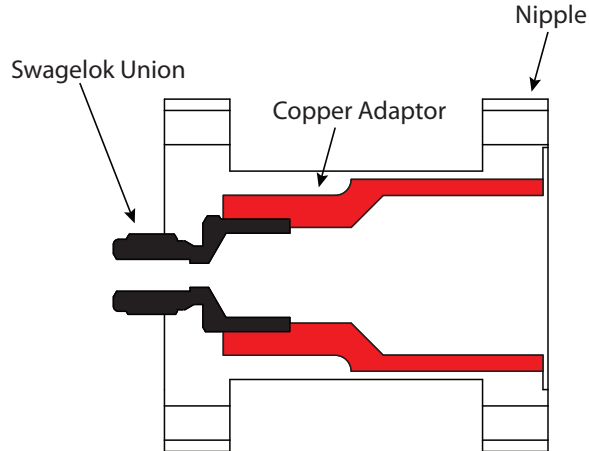


Figure 2.4: Oven nozzle used to hold multichannel array.

The flux of atoms leaving the rubidium reservoir is controlled by a nozzle (see Figure 2.4). The nozzle is comprised of a multichannel array of stainless steel tubes (see Figure 2.5) [53, 54]. Each tube consists of a 17 AWG stainless steel needle with an inner diameter of 1.295 mm and a length of 25 mm, resulting in a fairly large aspect ratio of ~ 20 . The seven tubes are held in a Swagelok union and a custom machined vacuum nipple using a sintering method. To do this, the tubes were placed in liquid nitrogen, where they thermally contracted in size, then placed into a 4.8 mm tube and held using the Swagelok union. The Swagelok union is attached to a custom-machined Conflat nipple via a copper adaptor. The Conflat nipple is machined such that a cylindrically symmetric copper adaptor is able to be press fit into the nipple. The union is then press fit into the copper mount (see Figure 2.4). The reason for the copper mount is ensure good thermal contact between the heated stainless steel nipple and the Swagelok union which holds the multichannel array.

This multichannel array is ideal for providing a large flux of highly collimated atoms [4, 53, 54, 55]. The large aspect ratio of the tubes prevents atoms with large transverse velocities from traversing through the array. Simply, an atom that approaches a tube either goes through the tube or collides with the tube wall and is reflected back into the reservoir. The atoms that make it through the tubes must have a ratio of its longitudinal to transverse velocity that is similar to the aspect ratio of the tubes. The effect of this is to provide a well collimated atomic beam.

The criteria for determining the aspect ratio of the stainless steel tubes is based on the solid angle subtended by the MOT and the collimation due to the Zeeman slower tube.

We define the degree of collimation as the largest acceptable angle, $\theta = \arctan(r_{id}/l)$, where r_{id} is the radius of the inner diameter and l is the length. We aimed for the collimation of the nozzle, θ_n , to be comparable to the collimation of the slower tube, θ_s . For instance, $\theta_n \gg \theta_s$ would result in a larger percentage of atoms failing to reach the end of the slower tube. However, we decided not to have $\theta_n \ll \theta_s$, as we were unsure of whether the alignment of the nozzle would be a problem. The collimation angle of a single stainless steel tube is $\arctan(1.295/25/2) \approx 1.3^\circ$, while the collimation angle of the slower tube is $\arctan(.76/80) \approx 0.5^\circ$. Thus, it seems that we are close to our desired criteria, but if we decide to redesign the nozzle, a multichannel array with a larger aspect ratio can be used.

Furthermore, the rejection of atoms with large transverse velocities into the atomic beam allows for the recirculation of rubidium. Neglecting collisions occurring at the edge of the tubes, only atoms with sufficiently low transverse velocities compared to their longitudinal velocity are admitted into the atomic beam. To get a sense of the extent that the oven is recirculating, we can compute the time necessary to deplete the entire reservoir, assuming no recirculation. The number of atoms traversing through an aperture of area A per unit time is $r = nA\bar{v}/4$, where $\bar{v} = \sqrt{8k_B T/m\pi}$ is the mean velocity of the Maxwell-Boltzmann distribution. Assuming typical experimental parameters of 115°C for the reservoir temperature, a density of $1.5 \times 10^{13} \text{ cm}^{-3}$, and an open area of $A = 0.1415 \text{ cm}^2$, the rate of atoms leaving the oven is $1.6 \times 10^{16} \text{ s}^{-1}$. A 5 g ampoule of rubidium has approximately 3.5×10^{22} atoms, which translates to a time of $\sim 10^6 \text{ s}$, or equivalently 30 days of nonstop operation.

In practice, the reservoir is run at a temperature of 115°C and the nozzle is continuously run at 200°C . The reason for this is to prevent the oven chamber from undergoing many temperature cycles of cooling and heating. We assumed that this would maintain the integrity of the system. The higher operating temperature of the nozzle prevents rubidium from depositing onto the nozzle and clogging the tubes. However, its proximity to the reservoir prevents the reservoir temperature from dropping below 69°C when it is not externally heated, resulting in a continuous flux of atoms leaving the oven. Under these operating conditions, the oven has been fully operational since January of 2009, running for approximately 50-60 hours per week, for a total run time of over 8000 hours with a 5 g rubidium ampoule. Based on the calculation above and the estimated run time on this reservoir, the oven appears to be recirculating. As of yet, there is no indication that the oven needs to be changed in the immediate future.

2.3 Optical System

The optical system necessary to achieve ultra-low temperatures in these cold-atom systems is quite extensive. For the sake of simplicity, the optical system is divided into two systems, the cooling system and the trapping system. Each system is discussed in some detail below, along with the finicky nature of certain elements.

2.3.1 Cooling lasers

One of the major selling points of cooling rubidium is the easily accessible laser light, conveniently derived from external cavity diode lasers (ECDL). To cool rubidium,



Figure 2.5: Photograph of the various types of nozzles made in the group. The nozzles consists of 17 gauge tubes made of 304 stainless steel. The tubes have a diameter of roughly 1 mm and are 25 mm long. The tubes were mounted into a Swagelok housing sintering 7-12 tubes. For our particular experiment, we are using the right-most nozzle pictured.

essentially two colors of light are necessary; light near the cycling transition $F = 2$ to $F' = 3$ transition, referred to as the “cooling” light, and light near the $F = 1$ to $F' = 2$, referred to as the “repumper” light. However, for each stage in the cooling process, slightly different frequencies are needed, which make these laser systems for ultracold atomic physics experiments fairly complex. This is illustrated in Figure 2.6. For simplicity, we’ll focus on the cooling light first. Light near the cycling transition is derived from a commercial ECDL laser from Toptica (DL Pro), dubbed the “master” laser, with an output power of ≈ 60 mW at $\lambda = 780.242$ nm (measured after an optical isolator). However, prior to 2011, the master laser light was derived from a home-built laser that preceded my start in the group. The master laser light is split into two paths, approximately 5 mW is sent down one path to stabilize its frequency and 55 mW is sent along the other path which is used for cooling and imaging. The cooling path is then split into three parallel paths (see Figure 2.7): one path for the slower cooling light, one for the imaging laser light, and the third is for the MOT cooling light.

For optimal performance, the laser light necessary for the Zeeman slower needs to be detuned from the $F = 2 \rightarrow F' = 3$ cycling transition by ≈ 700 MHz and requires 16 – 24 mW of laser power (empirically determined). To accomplish this, light derived from the master laser is downshifted in frequency by 265 MHz, via a double-pass AOM, and sent to a free-running diode laser to establish a master-slave injection lock. The output of the slave

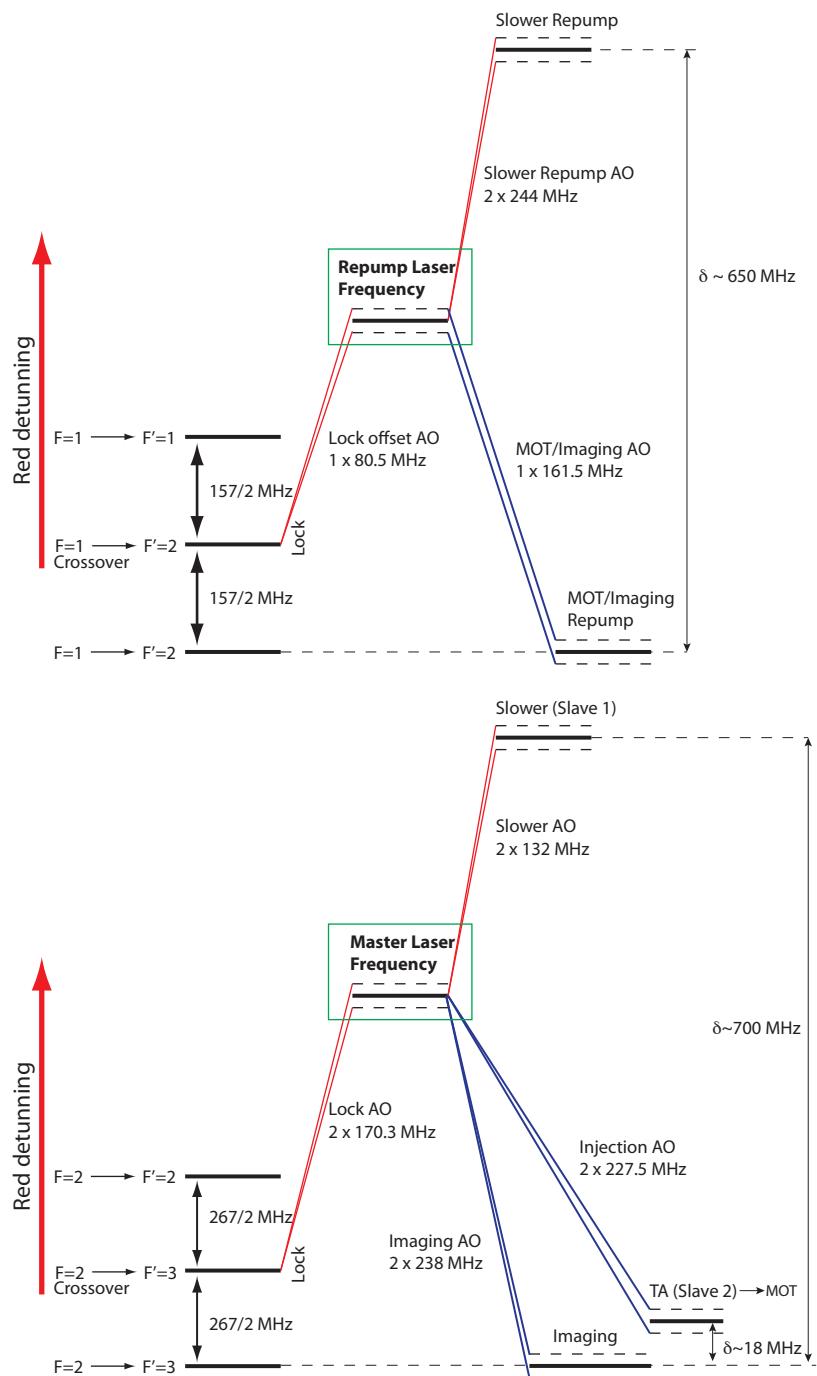


Figure 2.6: D2 laser frequencies used for cooling ^{87}Rb D2. (top) The detunings used for the D2 ($5s_{1/2}$ to $5p_{3/2}$) $F = 1 \rightarrow F' = 2$ transition, referred to as the repumper light. (bottom) Cooling frequencies derived from the “master” laser, referenced with respect to the cycling transition ($F = 2 \rightarrow F' = 3$).

laser is then combined with the slower repump light (see below) before being fiber coupled using fiber couplers from Schäfter Kirchhoff (60FC-4-M12-10) and fibers from OZ optics, then delivered to the science table (optics table with the vacuum chamber). Measuring the power before and after the fiber, we have a $\lesssim 50\%$ coupling efficiency, with ≈ 50 mW before the fiber and ≈ 20 mW immediately after the fiber.

To obtain a MOTs with $\sim 10^{10}$ atoms, we require at least 150 mW with a detuning to the red of the $F = 2 \rightarrow F' = 3$ cycling transition of -18 MHz. This was accomplished by first sending the master laser light to a free-running diode laser for a master-slave injection lock and then upshifting the frequency of the injection laser, which provides the necessary power of ~ 20 mW for seeding a tapered amplifier (TA). The output of the injection laser is then amplified using a tapered amplifier (1 W chip from Eagleyard). The output of the tapered amplifier, however, is 500 mW (before the optical isolator). This is primarily due to running the TA current below the standard operating settings. For more power, the TA current could be increased from its current setting of 1.4 A to 2-2.5 A (3 A max). The output of the TA is then combined with the MOT repump laser light (see below) before being fiber coupled. The typical power at the fiber output is currently 130 mW (33% coupling efficiency), but was as high as 210 mW (50 % coupling efficiency) when it was initially installed in 2009.

The repump light is derived from a separate homebuilt ECDL. The output of this laser is split into three paths, one of which is used to stabilize the laser frequency (see below), while the other two paths are designated for the MOT repump and slower repump cooling laser beams. The MOT repump light requires light resonant with the $F = 1 \rightarrow 2'$ transition, accomplished by upshifting the frequency of the repump laser by 161.5 MHz. From here, a small fraction of the light is picked off and fiber coupled, used during imaging ($\sim 0.3 - 1$ mW at the fiber output), while the remaining light is combined with the MOT cooling light and fiber coupled. In contrast to the frequency of the MOT repump light, the slower repump laser frequency needs to be down shifted in frequency by 488 MHz, after which it is combined with the slower cooling light and fiber coupled. Typically, the power at the fiber output for the slower repump is 8 mW and the MOT repump is 2.5 mW.

The laser frequency of the repump and master laser is stabilized by frequency modulating the probe beam in the saturation-absorption spectroscopy of a rubidium vapor cell. The probe beam is focused onto a New Focus fast photodiode (1.5 GHz bandwidth) where the output is then mixed down at the modulation frequency. From this we obtain a Doppler-free error signal, where we lock to the $F = 2 \rightarrow 3'$ crossover for the master laser and the $F = 1 \rightarrow 2'$ crossover for the repump laser.

The use of a Toptica laser for the master laser has many benefits, some of which include a stable laser frequency with \sim GHz regions that are free of mode-hops and the “turn-key” operation. However, a major drawback of using this system is the piezoelectric transducer (PZT). On two occasions, the PZT was mysteriously destroyed, either due to poor manufacturing, or due to a voltage spike originating from the locking electronics. Replacing a PZT is not difficult and in fact, takes no more than an hour of time. But, because Toptica has a custom PZT, they can only be replaced by PZTs from Toptica. Thus, to prevent the further destruction of PZTs, as a fix, we stopped using the Toptica PZT electronic box and added a low pass filter between the PZT and the electronic control

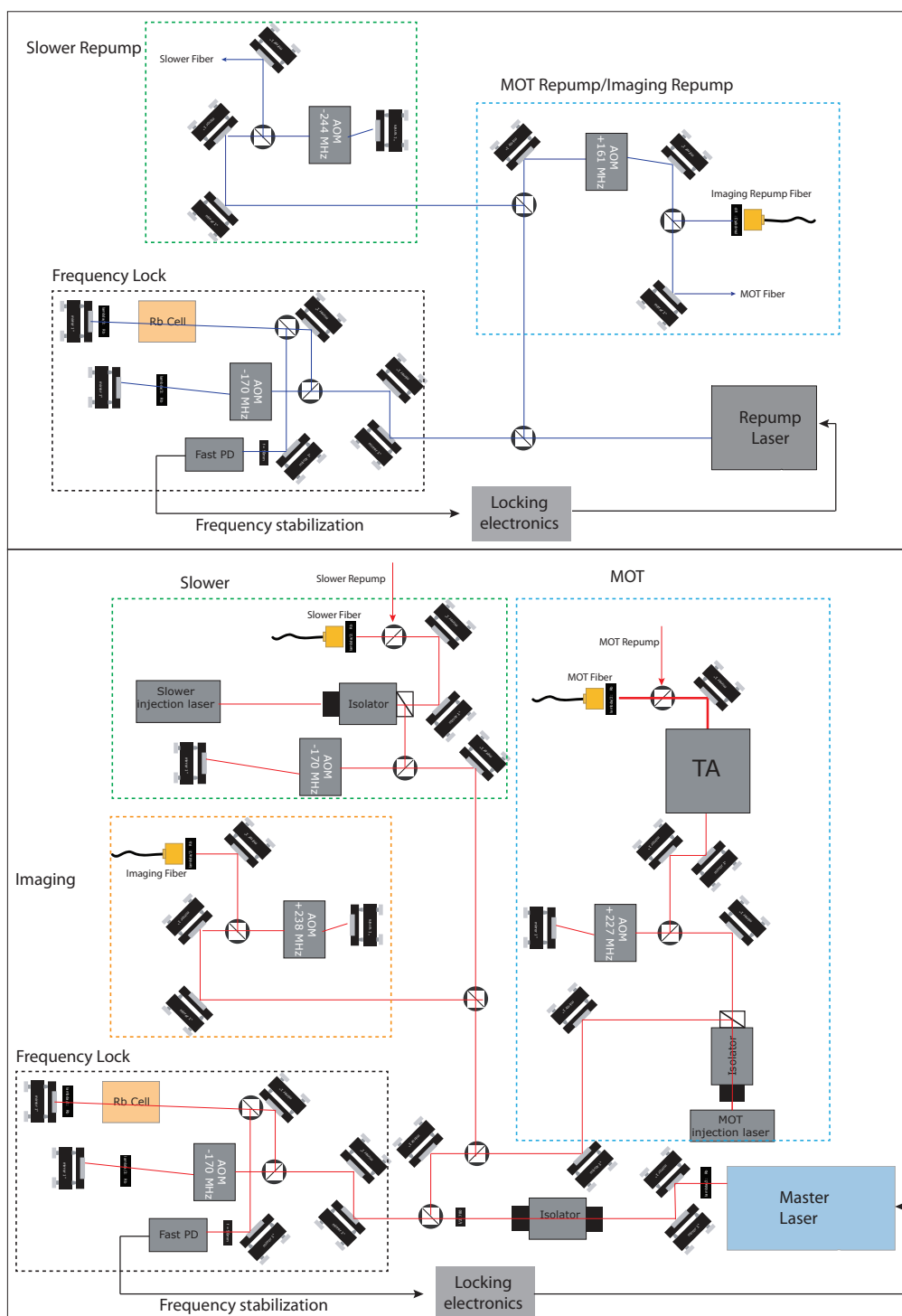


Figure 2.7: Illustration of cooling optics layout.

signal from our homebuilt lock boxes. We have yet to encounter any problems since replacing the PZT over a year ago.

2.3.2 Trapping laser

The impact of optical traps is so broad that merely searching for “optical trap” in any internet search engine will immediately bring up numerous review articles, some of which are listed here [56, 28, 26, 57, 58, 59, 60, 61]. However, for the sake of completeness, the basic theory of optical trapping is presented below, with some emphasis on its characterization.

The working principle of the optical dipole trap (ODT) is contained in the following equation,

$$H_1 = -\mathbf{d} \cdot \mathbf{E}, \quad (2.1)$$

where \mathbf{E} is the electric field of the laser light and \mathbf{d} is the atomic dipole moment. However, for neutral atoms, since there is no permanent electric dipole moment, the energy shift of the ground state using first order perturbation theory is zero. To compute the energy shift, we go to second-order (non-degenerate) perturbation theory, which leads to an energy shift of the following form

$$\Delta E_i = \sum_{j \neq i} \frac{|\langle j | H_1 | i \rangle|^2}{E_i - E_j}, \quad (2.2)$$

where E_i is the energy of the unperturbed state. The ground-state energies can be estimated assuming a two-level system and using the dressed-state picture, where the field energy is $n\hbar\omega$ and the total energy for the unperturbed state is $E_i = n\hbar\omega$. The excited state energy is $E_j = (n-1)\hbar\omega$, where by putting the atom into the excited state one photon was removed from the laser field. Assuming a we have a two-level system, we can rewrite the energy shift of the ground state as:

$$\Delta E_i = U_{dip} = |\langle e | H_1 | g \rangle|^2 \left(\frac{1}{\omega_0 - \omega_L} + \frac{1}{\omega_0 + \omega_L} \right) \quad (2.3)$$

$$U_{dip} = -\frac{3\pi c^2}{2\omega_0^3} \left(\frac{\gamma}{\omega_0 - \omega_L} + \frac{\gamma}{\omega_0 + \omega_L} \right) I(x, y, z) \quad (2.4)$$

where, U_{dip} is the ac Stark shift of the ground state, ω_0 is the atomic transition frequency, ω_L is the laser frequency, and γ is the linewidth of the upper state. We have also used the following relations for the intensity and linewidth of the upper state,

$$\gamma = \frac{\omega_0^3}{3\pi\epsilon_0\hbar c^3} |\langle e | d | g \rangle|^2, \quad (2.5)$$

and the intensity

$$I = 2\epsilon_0 c |\mathbf{E}|^2, \quad (2.6)$$

to further simplify the expression. The first term in the parentheses of Equation 2.4 represents the Stark shift due to atomic resonances, while the second term, known as the Bloch-Siegert shift, is interpreted as the Stark shift due to resonances at the corresponding

negative frequencies. In some situations, the laser frequency of the trapping beam is close to atomic resonance, which means that the equation for U_{dip} can be simplified by ignoring the Bloch-Siegert term. However, when the trapping laser frequency is sufficiently detuned from atomic resonance, both the terms in the dipole potential are of nearly the same magnitude, and no overall simplification can be made. This is true for the experiment discussed here where the wavelength of the light used to create the ODT is $\lambda = 1064$ nm, which is sufficiently detuned from the D1 and D2 transitions in ^{87}Rb , 780 and 795 nm.

In order to apply this to the multi-level atom that we have here, we need to sum over the dipole-matrix elements between the ground and excited states and their respective detunings,

$$U_{dip}(x, y, z) = -\frac{3\pi c^2 \gamma}{2\omega_0^3} \times I(x, y, z) \sum_j \left(\frac{c_{i,j}^2}{\omega_j - \omega_L} + \frac{c_{i,j}^2}{\omega_j + \omega_L} \right), \quad (2.7)$$

where $c_{i,j}$ is the Clebsch-Gordan coefficient between the ground and excited state. In our experiment, the optical potential is derived from a fiber laser at 1064 nm. At this detuning, the energy splittings due to the hyperfine structure are not relevant, and only the fine structure needs to be considered: $J = 1/2 \rightarrow J' = 1/2$ and $J = 1/2 \rightarrow J' = 3/2$. Substituting the appropriate Clebsch-Gordan coefficients into Equation 2.7 yields:

$$U_{dip}(x, y, z) = -\frac{3\pi c^2 \gamma}{2\omega_0^3} \left[\frac{1}{3} \left(\frac{1}{\omega_{D1} - \omega_{1064}} + \frac{1}{\omega_{D1} + \omega_{1064}} \right) + \frac{2}{3} \left(\frac{1}{\omega_{D2} - \omega_{1064}} + \frac{1}{\omega_{D2} + \omega_{1064}} \right) \right] \times I(x, y, z). \quad (2.8)$$

Beam-shaping

From the functional form of U_{dip} , it is clear that by shaping the intensity profile, we can tune the shape of the optical potential. In general, to gain some perspective about the overall shape of the trapping potential, we typically site the harmonic trapping frequencies or the shape of the intensity profile. In general, trapping frequencies are the more intuitive parameters that we use to describe the trapping potential. The trapping frequencies can be extracted directly from U_{dip} by a Taylor series expansion about the potential minimum. This leads to the following form for the trapping frequencies:

$$\omega_x = \sqrt{\frac{4U_{dip}}{mw_x^2}} \quad (2.9)$$

$$\omega_y = \sqrt{\frac{4U_{dip}}{mw_y^2}} \quad (2.10)$$

$$\omega_z = \sqrt{\frac{2U_{dip}}{mz_R^2}}. \quad (2.11)$$

Note here that w_x is the beam waist, which should not be confused with ω_x , which is the trapping frequency. To arrive at these trapping frequencies, we assumed an intensity profile

of the following form,

$$I(x, y, z) = \frac{2P}{\pi w_x(z)w_y(z)} \exp \left[- \left(2 \frac{x^2}{w_x(z)^2} + 2 \frac{y^2}{w_y(z)^2} \right) \right], \quad (2.12)$$

where $w_{x(y)}(z)$ is the $1/e^2$ waist defined as

$$w_{x(y)}(z) = w_{x(y)}^2 \sqrt{1 + (z/z_R)^2}, \quad (2.13)$$

$z_R = \pi w_x w_y / \lambda_L$ is the Rayleigh range, and $w_{x(y)}$ is the transverse beam waist in the \hat{x} - and \hat{y} -direction

In our particular trap geometry, the profile of the beam located at the atoms resembles that of a surfboard potential, with the tightest confinement along gravity, w_y , and the weakest confinement, w_x , along the propagation direction. To create such a potential, we take the output of the fiber laser and shape the profile using cylindrical lenses. For instance, in the current experiment, the beam waist along gravity, w_y , is approximately ten times larger than w_x .

In practice, the trapping laser beam passes through many optics before reaching the atoms. The output of the fiber laser is sent through an acousto-optic modulator to stabilize the beam intensity. Following this, the beam is sent through a single-mode optical fiber which delivers the beam to the science table and spatially filters the beam profile. From here the beam is sent through two pairs of cylindrical telescopes, which shape the two transverse waists, w_y and w_x . The resulting profile is a collimated elliptical beam profile, with a beam waist of $w_x \approx 2 - 3$ mm and $w_y \approx 30$ mm. In addition, one lens from each telescope pair is on a translation stage. This is to ensure that the two transverse foci occur at the same position. Before reaching the atoms, the trapping beam passes through one final spherical lens, positioned such that the focus of the trapping potential coincides with the location of the atoms. The typical optical trap parameters in this experiment are shown in Table 2.1.

Table 2.1: ODT Parameters

Beam waist: w_x at atoms	100 μm
Beam waist: w_y at atoms	8-10 μm
Initial Power	$\sim 4\text{-}5$ W (~ 0.3 mK)
Final Power	~ 30 mW (~ 1 μK)

Characterizing the laser profile

Before attempting to trap atoms in an optical trap, it is necessary to characterize the beam profile after it has traversed through all of the optical shaping elements using a profiling camera. To do this, we direct the laser beam, onto a beam profiling camera, mounted to a translation stage. Then as a function of the camera position, the two transverse waists are measured. Once this is done, the two waists are plotted as a function of the camera position and fit to a function of the form described in Equation 2.13. From here,

adjustments can be made to ensure that the two waists occur at the same location on the beam profiler and that the minimum value of $w(z)$ matches what is expected theoretically. Although this procedure does not ensure that the final lens is in the correct location with respect to the atoms, it does reduce potential errors associated with an astigmatic beam.

2.4 Zeeman Slower

A complete description on the functionality of a Zeeman slower is given in [62, 63, 64] and will not be discussed in detail here. Briefly, an inhomogeneous magnetic field is shaped such that an atomic beam is kept in resonance with a fixed frequency laser slowing beam. As atoms scatter photons from the slowing laser beam they are decelerated and Doppler cooled. Thus, in order to compensate the reducing Doppler shift, a spatially varying magnetic field shifts the atomic resonance via the Zeeman effect in order to maintain resonance,

$$\omega_0 \approx \omega_L + kv + \Delta\mu B/\hbar, \quad (2.14)$$

where $\Delta\mu$ is the difference in magnetic moments between the excited and ground states, ω_0 is the zero-field resonance, and ω_L is the frequency of the slower laser light. Using this, atoms exiting the oven at velocities near 300 m/s are slowed to MOT capture velocities near $v \lesssim 30$ m/s.

The Zeeman slower used in this experiment was originally designed to produce slowed atomic beams of rubidium and lithium. To accomplish this, a three-stage Zeeman slower was designed. The details of this can be found in [4] and (hopefully soon) the theses of Ryan Olf and Ed Marti. However, for the sake of completeness, the basic design concept will be briefly discussed here.

The dual species Zeeman slower consists of three sections: Section I, Section II, and Section III, where Section II (Section I and Section III) is aimed primarily at slowing rubidium (lithium). The key concept of this design stems from the detrimental effects of transverse heating, which leads to a divergence of the atomic beam, characterized by $\theta = v_\perp/v_\parallel$, where $v_\perp \sim \sqrt{v_r v_\parallel}$ is the transverse velocity, v_r is the recoil velocity, and v_\parallel is the longitudinal velocity. This is of particular importance for the lighter lithium beam (larger v_r), where its larger initial velocity can lead to a larger divergence of the atomic beam, thus requiring that its slowing take place in close proximity to the location of the MOT [64]. In Section II, a moderate magnetic field profile is used to slow rubidium to a final velocity well within the capture velocity of the MOT. This is followed by a high-gradient stage, Section III, where the magnetic field abruptly increases in magnitude over a very short distance (\sim cm). The increase in the magnetic field is large enough that the heavier rubidium atoms can not adiabatically follow the field and are then no longer slowed, whereas the lighter lithium can now be slowed. Section I also serves to slow lithium as well. For our setup here, we did not operate the slower with current running through the coils of Section III and Section I.

2.4.1 Windings

For uniform deceleration, the necessary magnetic field profile is of the following form,

$$B_{slower}(z) = B_v \sqrt{1 - z/L_{slower}} + B_0, \quad (2.15)$$

where $B_v = \hbar k \bar{v} / \Delta \mu$, $L_{slower} = \bar{v}^2 / 2a_{max} f$ defines the length of the Zeeman slower in terms of atomic parameters, $f = a/a_{max}$ is the dimensionless slower parameter, and B_0 is the offset magnetic field (used to achieve a large separation of the rubidium hyperfine levels). The slower parameter, f , defines the desired acceleration in terms of the maximum acceleration given by dissipative cooling, $a_{max} = \hbar k \gamma / 2m = 0.11 \times 10^6$ m/s, and is used to determine the aggressiveness of the Zeeman slower, with $f \approx 1$ being very aggressive. For the Zeeman slower used here $f = 0.66$, which is fairly typical for the Zeeman slowers used in this group.

The desired magnetic field profile is obtained by stacks of coils along the length of a tube, which can be used to approximate the desired profile. The theoretical magnetic field profile and the coil arrangement used to approximate the field for Sections I, II, and III is shown in Figure 2.8.

To achieve this desired coil winding pattern, the lathe was used. A brass tube of similar dimensions to the vacuum slower tube, was positioned on the lathe and a thin layer of thermally conductive Stycast was spread over the tube. A lathe tool, pictured in Figure 2.8(c), was used to carefully position and hold the wire. With the aide of the lathe in mind, the spacing between turns was designed to equal one of the threading options. Thus, with the lathe configured in “threading mode” the wire was wrapped onto the brass tube at the desired spatial frequency with fairly good accuracy. However, during the wrapping process, careful attention must be made as the wire is wrapped onto the slower tube in order to prevent the wire from rotating such that it is no longer flush with the tube surface. This will ensure that subsequent layers are able to be accurately positioned.

Section II of the slower consists of two different types of square wire; insulated 1/8 inch square hollow wire used for providing water-cooling to slower and solid 1/16 inch enamel coated square wire. The first two layers of Section II consist of the insulated 1/8 inch square wire wrapped at a threading pitch of 7 turns per inch. The remaining layers are wrapped using the solid 1/16 inch wire at 14, 7, and 3.5 turns per inch. The first five layers of the coil winding pattern are shown in Figure 2.8(b).

2.4.2 Measuring the slower fields

The magnetic field of the Zeeman slower was measured using a Hall probe that was translated along the length of the slower. The field profile was measured using a single current supply. A current of 1 A was applied to the coils. The resulting field measurement is shown in Figure 2.9, which has been rescaled. The field agrees quite well with the expected profile from Section II assuming a scaling factor of 6.5 or a current of ≈ 6.5 A. In practice, the current used is 5.74 A, which was empirically determined.

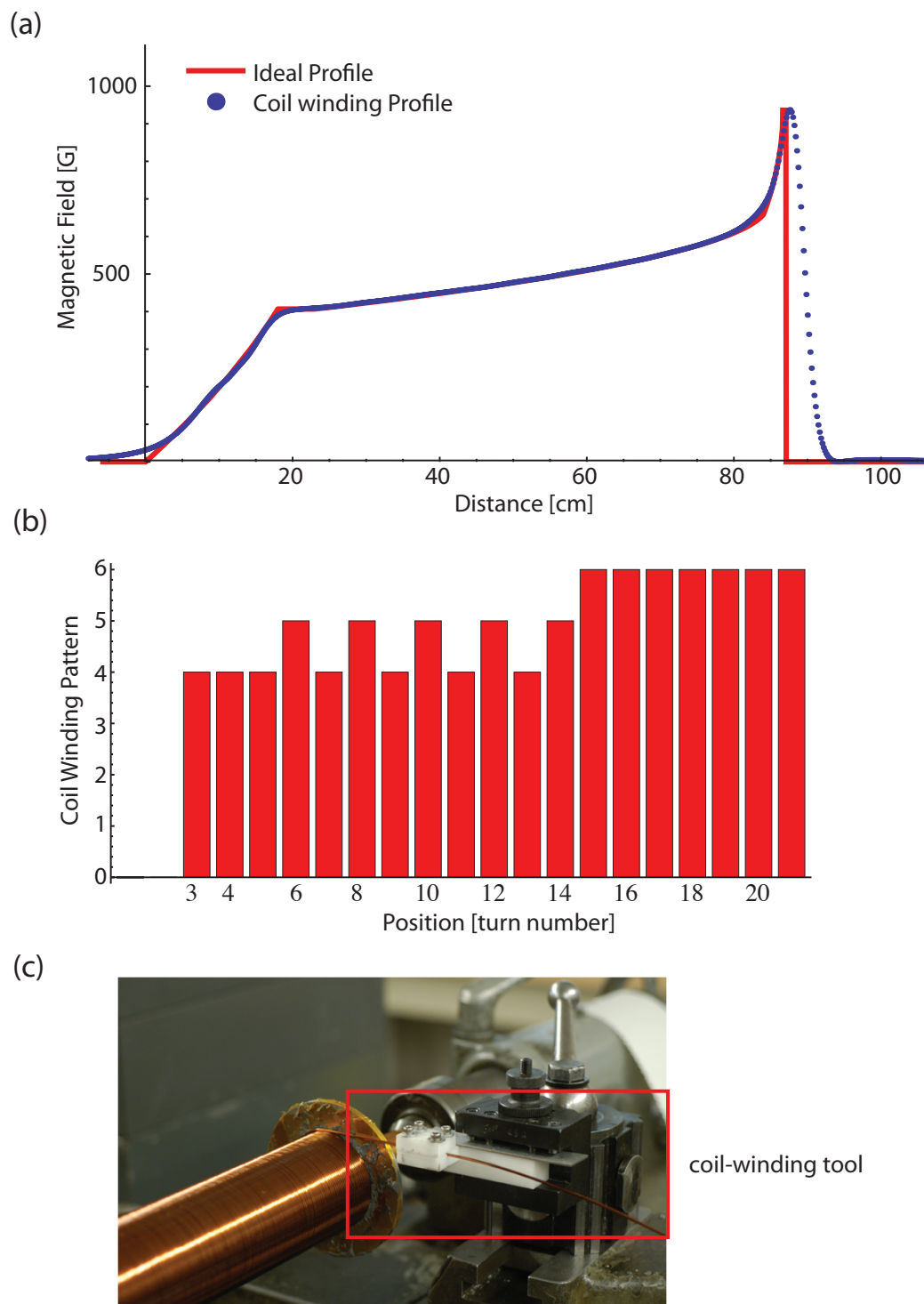


Figure 2.8: (a) Magnetic field profile from Zeeman slower. The solid red line is the desired magnetic field profile and the filled circles is the profile generated from stacks of coils. (b) The coil winding pattern used to approximate the desired magnetic field profile. (c) Photograph of the coil winding tool used to position the wire on the brass slower tube.

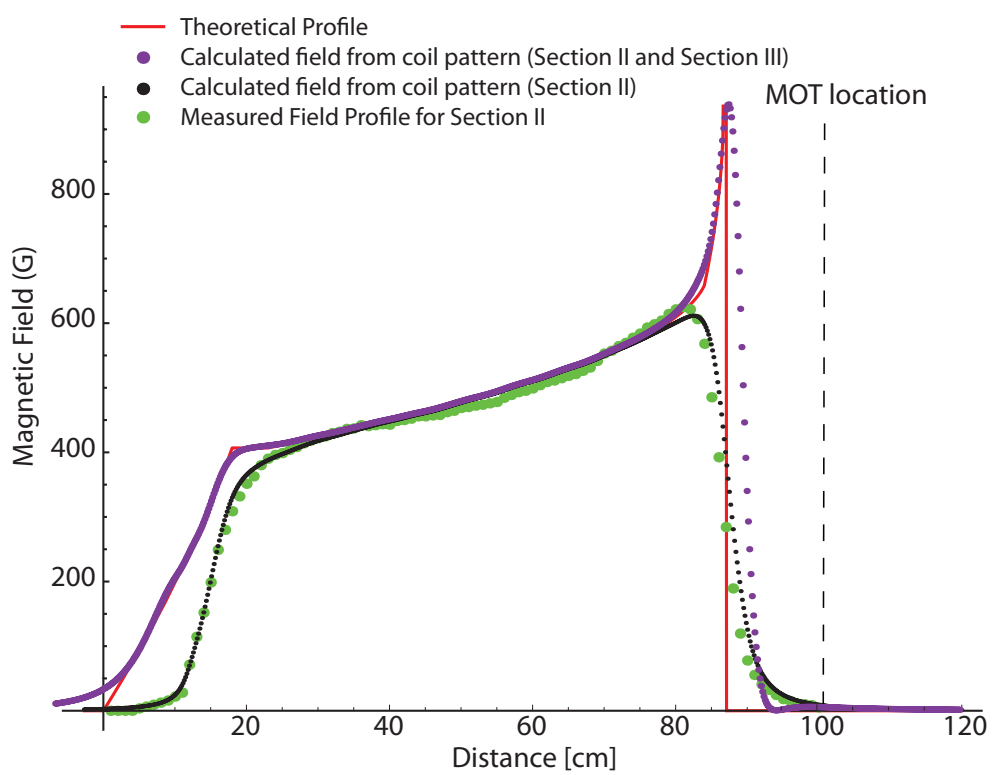


Figure 2.9: Measured slower fields compared to ideal magnetic field profile.

2.5 Magneto-Optical Trap

The MOT used in this work is the fairly standard configuration used in many cold-atom experiments, consisting of six independent laser beams and a magnetic quadrupole coil, positioned to be concentric on the vacuum flanges. References pertaining to the theory and functionality of a MOT can be found here [26, 65, 58, 66, 67, 68, 69, 70, 71]. The laser beams are approximately 1.5" in diameter and comprised of cooling and repumper light. The cooling light consists of light detuned by 18 MHz to the red of the $F = 2 \rightarrow 3'$ cycling transition, with approximately 25 mW per beam (130-150 mW in total). The repump light consists of light resonant with the $F = 1 \rightarrow 2'$ transition, with approximately 0.42 mW of repump power per beam (2.5 mW in total). The spherical quadruple trap is obtained by running 15 A through the coil, which is also the first transport coil, TP0 (see below), resulting in a magnetic field gradient of approximately 15 G/cm.

In order to guide such large beams, we ordered custom elliptical mirrors from Lambda Optics (Part Number BBHR 600-900-0-EW-3806U). The minor and major axes of the elliptical mirrors are 1.5" and 2.2" which allows us to use beams with diameters of 1.5", where the standard 2" mirrors would slightly aperture the profile of the MOT laser beams.

In this MOT about 10×10^9 atoms are loaded in about 4 s, using 150 mW of cooling light and 2.5 mW of repump light. Increasing the amount of cooling and repump light did not show a significant increase in the number of atoms loaded in the MOT. To better illustrate this saturation, we extracted the number of atoms that are transported to the glass cell as a function of the MOT power. This is shown in Figure 2.10. Since this plot was taken, the number of atoms in the glass cell is a approximately of 3-4 times larger.

2.6 Magnetic Transport Coils

To transfer the atoms from the MOT Chamber to the glass cell, we make use of a magnetic transport system consisting of partially overlapping magnetic quadrupole coils [72, 73]. This method relies on the interaction of magnetic dipole moment of an atom with the magnetic trapping potential. When placed in an inhomogeneous magnetic field, the atom is subject to an external force, which is directed either towards the magnetic field minimum or maximum, depending on the sign of the magnetic moment. Atoms that are attracted to a magnetic field minimum are known as weak-field seekers. The simplest magnetic trap is the spherical quadrupole trap, consisting of two coaxial coils that carry opposite currents such that the magnetic field at their center cancels. To lowest order, the magnetic field profile has the form

$$\mathbf{B}(\mathbf{r}) = B'(\mathbf{x}, \mathbf{y}, -2z). \quad (2.16)$$

This is achieved using two coils of the same radius, each carrying opposite flowing currents.

We magnetically transport the trapped atoms using a series of partially overlapping magnetic quadrupole coils, from the MOT, over a distance of 20 cm, to the glass cell. To accomplish this, the cylindrical symmetry of a single quadrupole trap must be broken. This is done with the addition of a second pair of quadrupole coils, with its symmetry axis parallel to the first coil pair. In our experiment this axis is parallel to gravity. Suppose for

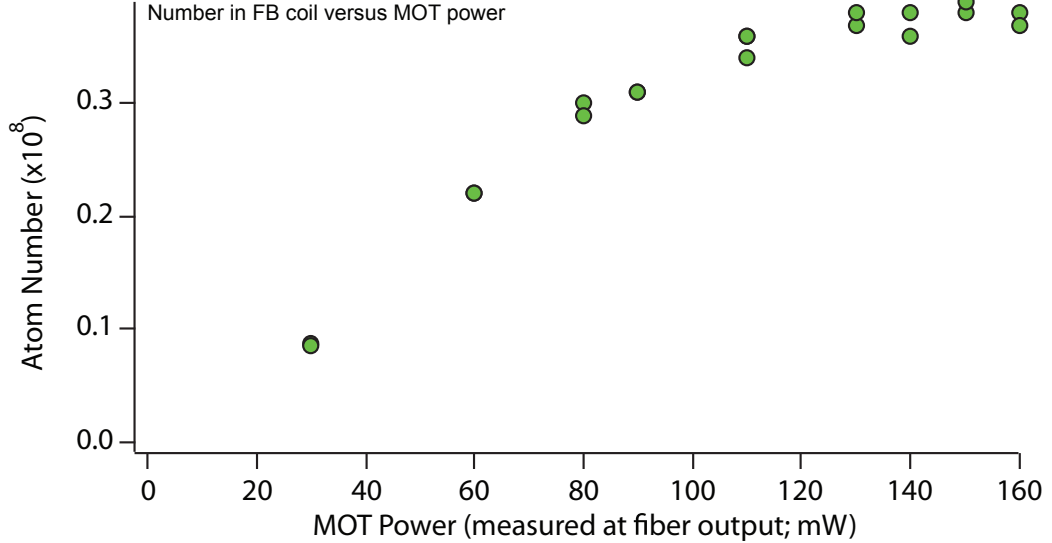


Figure 2.10: Number of trapped atoms in glass cell versus MOT power. For powers greater than 130 mW, the number of atoms reaching the glass cell is saturated. However, decreasing the power below 130 mW results in a decreased number in the glass cell. For safe operation, the MOT power should be kept above or near 130 mW. These measurements were conducted at a MOT repump power of 2.5 mW (total).

instance the first coil pair with radius R_1 is at $(0, 0, 0)$ and the second with radius R_2 is at $(x_0, 0, 0)$. Running currents I_1 and I_2 through the respective coils leads to a superposition of the two fields. By varying the ratio of I_1 and I_2 , the location the magnetic field zero can be made to smoothly move from $x = 0$ to $x = x_0$. This is the principle behind magnetic transport.

The magnetic transport systems consists of four quadrupole coils. A diagram of the coils is shown in Figure 2.11. The size of each coil and the relative overlap between coils was determined by the physical dimensions of the vacuum chamber and potential heating of the atomic sample that could be accrued during the transportation sequence. The coils were made using $0.280 \times .025$ inch flat wire, as oppose to the square hollow wire, which allowed us to reduce the overall size of each coil. The transport coils were dubbed the “MOT coils” (Transport 0), “Transport 1”, “Transport 2”, and “Feshbach Coils” (Transport 3). The last pair of coils, “Feshbach coils” are not configured to provide a a bias field as their name seems to imply. It is currently setup to provide a quadrupole field. However, if configured in a “Helmholtz” configuration with the current in each coil flowing in the same direction, the Feshbach coils are capable of producing a field of ≈ 1100 G, intended for exploration of the ^{87}Rb Feshbach resonance [74]. The relevant parameters for each coil are listed in Table 2.2 and Table 2.3.

In order to ensure proper overlap of the transport coils, we opted to use a common mount for all coils except the Feshbach coils. This was also motivated by the overall simplicity of a single cooling mount. In following this route, we have reduced the number of cooling connections necessary and reduced the possibility of a potential water leak, which

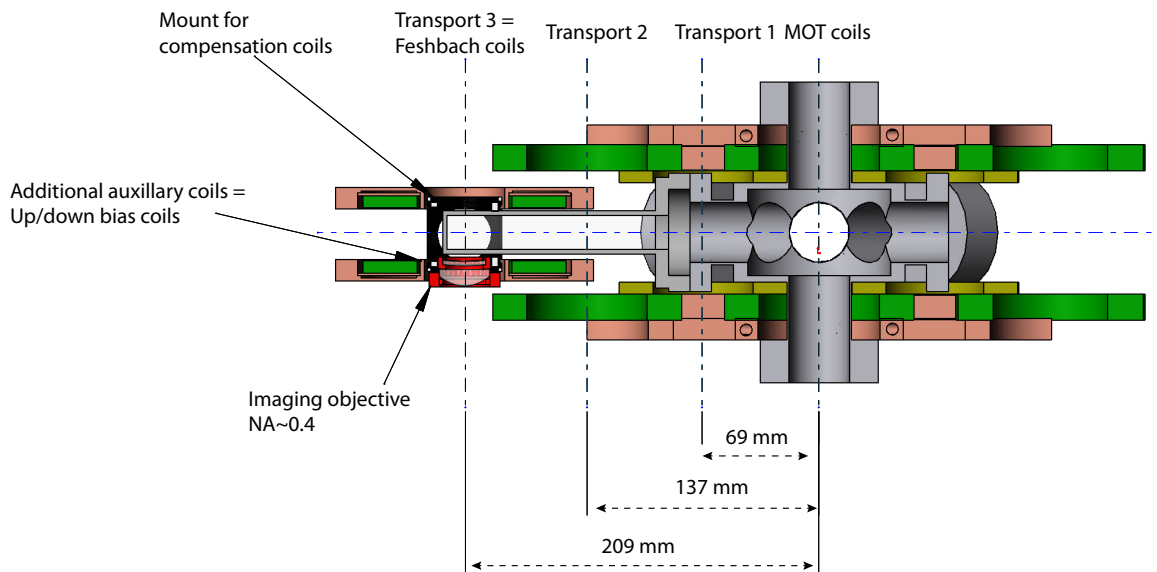


Figure 2.11: Illustration of magnetic transport system. Four overlapping quadrupole coils are used to transport the atoms from the MOT chamber to the glass cell. The illustration accurately depicts the relative size and overlap of the coils used.

Table 2.2: Coil Parameters

	MOT/TP0	TP1	TP2	Feshbach/TP3	Up/Down Bias
Position	0 mm	69 mm	137 mm	209 mm	209 mm
# Turns	32	33	32	50	13
# Layers	2	1	2	1	1
B'/Amp [G/cm/A]	1	0.8	1	1.8	1.6
Max Current	50	100	100	100	10
Inductance [μH]	< 300	< 100	< 300	< 500	< 5

Table 2.3: Dedicated power supplies for magnetic transport coils

Coil	Power Supply
MOT	2 Kepco 50 A, 6 V; wired in series
TP1	2 Kepco 100 A, 10 V; wired in parallel
TP2	1 Lambda 20 V, 400 A
Feshbach	same supply as MOT
Up/Down Bias	1 Kepco 6V 10 A

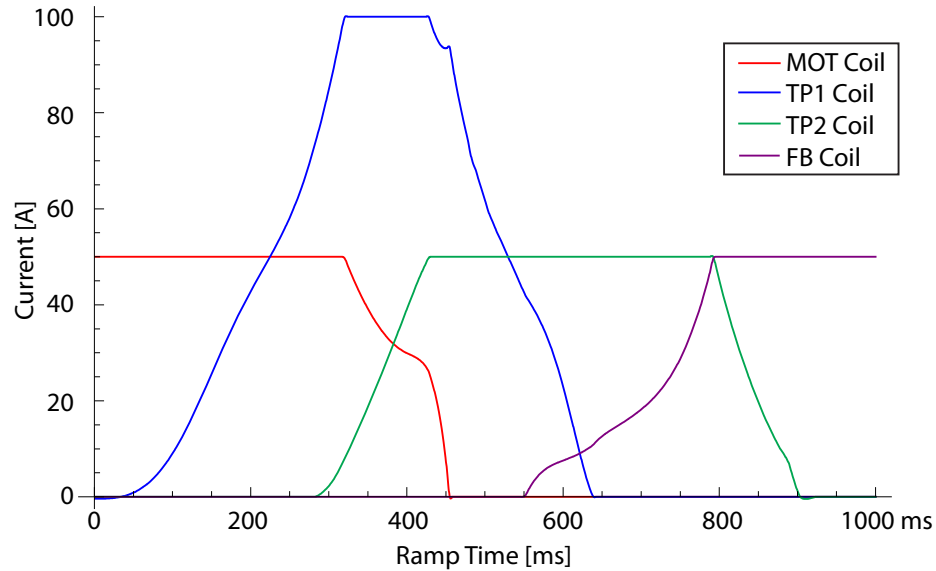


Figure 2.12: Magnetic transportation sequence. Plotted is the current as a function of transport time for each pair of coils in the magnetic transport sequence.

becomes more likely with multiple connections. The mount consists of two hollow copper plates, top and bottom, each shaped to the geometry of the overlapping coils. The coils are secured to the mount using thermally conductive Stycast and the top and bottom mounts are connected by several rods that go between the two. Thus, the relative overlap of each coil and the separation between each coil pair is well constrained.

Because the Feshbach coils were intended to go to currents as high as 100 A, a dedicated cooling mount for these coils was needed. The cooling mount is shown in Figure 2.11. The coils are secured to the mount using thermally conductive Stycast, thus providing heat dissipation through the top and sides of the coils which are in contact through the mount. However, after testing each coil by running 100 A through the coil pair, one coil was found to have a significant temperature increase. This sets an upper limit of a ~ 3 s duty cycle for the coil assuming a current of 100 A. The temperature increase is most likely attributed to the production process; the copper mount was not heated uniformly during the gluing process, preventing the Stycast from being uniformly distributed between the coil and mount.

The magnetic transport sequence is shown in Figure 2.12. This sequence was obtained by first picking a trial overlap between coils and then optimizing the current through each coil while trying to maximize the aspect ratio of the gas, where the aspect ratio is defined to be less than or equal to one. The best trial overlap was then selected. The current ramps for that sequence are shown in Figure 2.12.

An unfortunate consequence of this scheme is that the aspect ratio of the sample along the transportation axis changes significantly during the transfer process. The aspect ratio at each stage in the transfer process is shown in Figure 2.13. We can understand this by considering the case when the same current is flowing through two quadrupole coils.

In the overlap region of the coil pairs, the net magnetic field tends to cancel due to the opposite flowing current directions, resulting in a strongly deformed trap geometry. This in turn will lead to a modulation of the aspect ratio which could result in heating of the atom cloud. However, by using a third quadrupole coil pair, it is possible to maintain a constant trap geometry during the transport process [72]. Unfortunately, we were unable to accomplish this with the coil configuration used here. This is evident in the calculated aspect ratio (see Figure 2.13) which fluctuates at each stage in the transfer process.

The original planned transportation time was to be one second long. However, transporting the atoms in this short time not only resulted in a severe temperature increase from $120 \mu\text{K}$ at the start of the transport sequence to over 1 mK by the end, but also significant atom loss. Increasing this time to 6 s reduced the observed heating, with a final temperature of $\sim 800 \mu\text{K}$ in the glass cell. In addition, there was no observed atom loss. We observed no significant benefits by further increasing the transportation time.

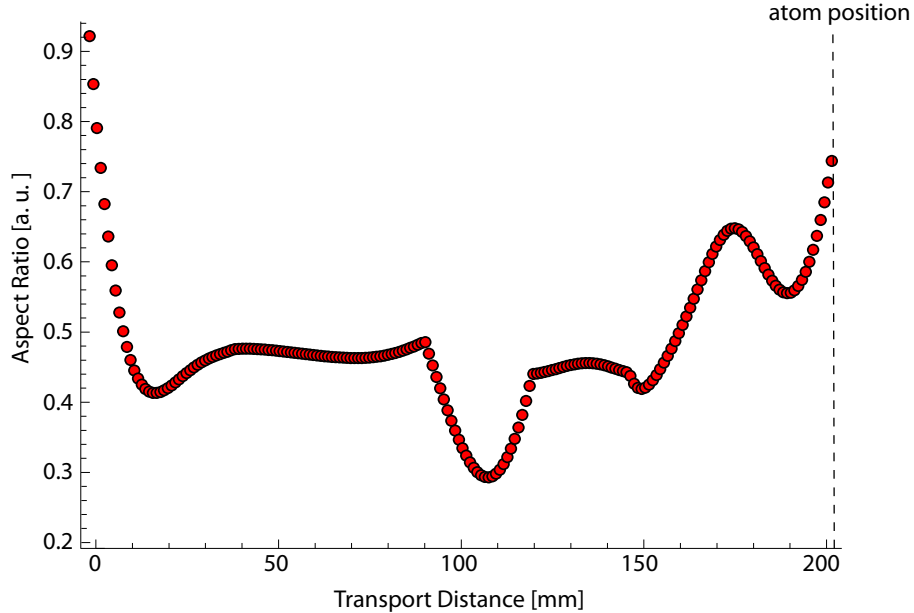


Figure 2.13: Calculated aspect ratio of the atomic sample as a function of the transport distance. In order to reduce the effects of heating from the changing aspect ratio, the ramp sequence can be slowed. The original planned time was a 1 s transportation sequence, but due to severe heating, this is now 6 s .

We confirm that the field from each coils agrees well with theory. After positioning the coils in the mount, we made measurements of the magnetic fields along the transportation axis for each coil. This is shown in Figure 2.14. Our measurements are in agreement with theory.

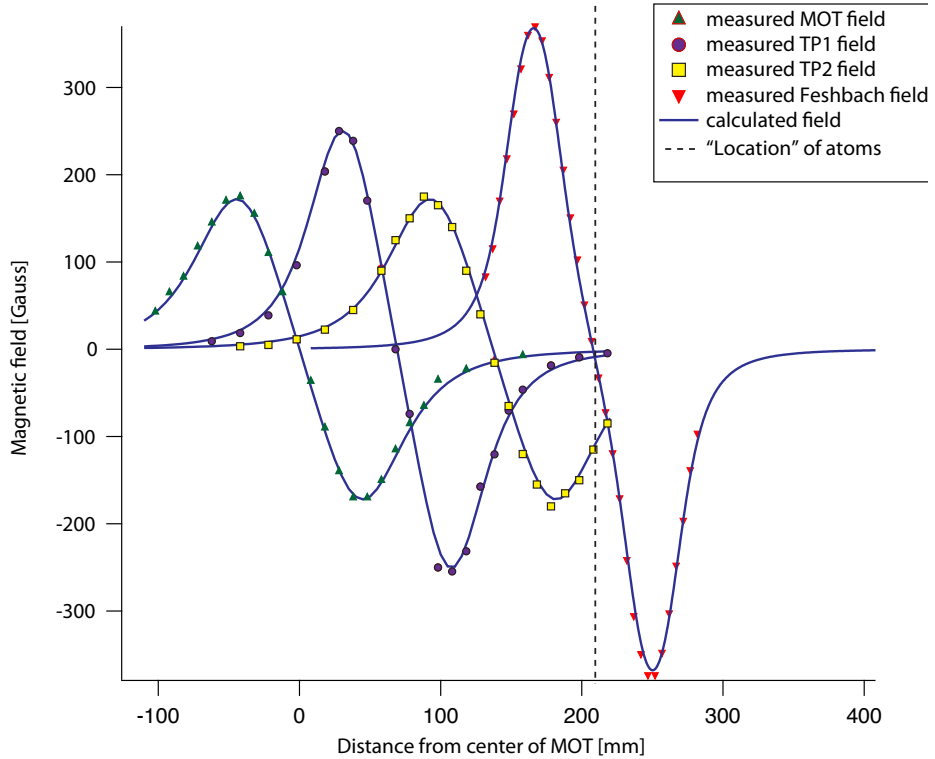


Figure 2.14: Magnetic fields for the coils used in the magnetic transport system. The solid lines are derived from calculations and the data points are measurements using a Hall probe. The magnetic field measurements agree well with theory.

2.7 Applied Fields

For the experiments on spinor condensates, we require precise control over the magnitude and orientation of the background magnetic field. To do so requires the use of pairs of coils to produce dc and ac magnetic fields.

2.7.1 Microwave field: evaporation

En route to making a BEC there are a few stages of cooling. Above we discussed the Zeeman slower, and the MOT, but these do not yield the necessary phase-space densities to achieve quantum degeneracy. Forced evaporation, using radio-frequencies or microwaves is a widely used technique in ultracold atom experiments to make quantum degenerate atomic samples [75, 76, 77, 78]. For our experiment, we make use of microwaves to evaporate the sample, thus, below we will only discuss microwave evaporation.

In principle, a microwave field of well defined frequency is resonant with a particular transition, for instance the $|F = 1, m_F = -1\rangle \rightarrow |F = 2, m_F = -2\rangle$. As a result, the spin of the atom is flipped, and expelled from the magnetic trap, since $|F = 2, m_F = -2\rangle$ is not a magnetically trappable state. This technique can be used to selectively choose atoms with energies that are larger than the average energy of the sample, and in doing so, cool

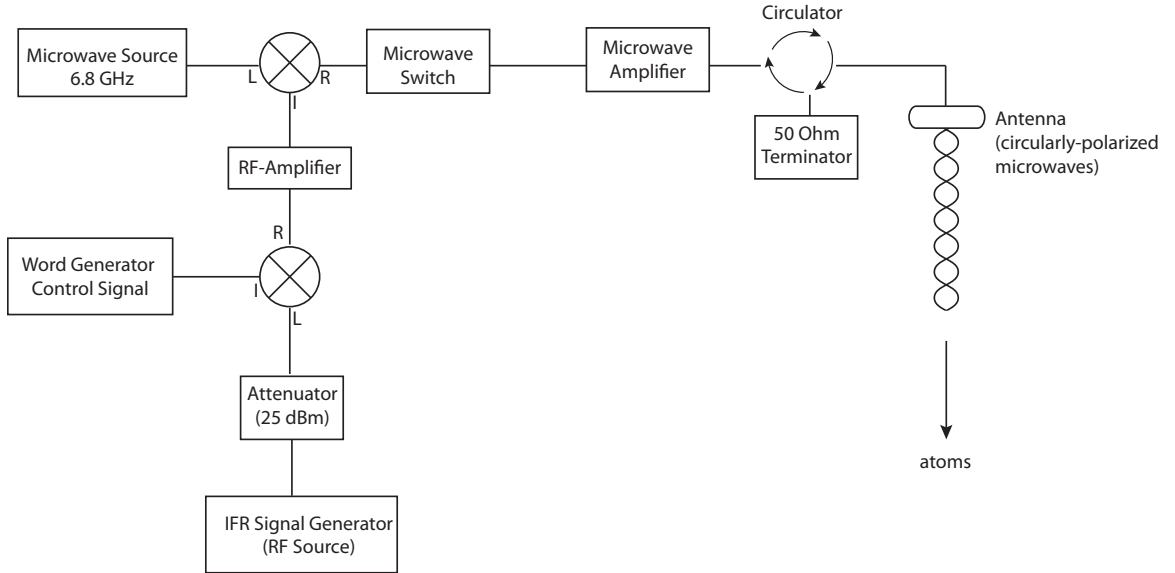


Figure 2.15: Microwave evaporation setup.

the sample as it thermalizes.

In our experiment, we applied circularly polarized microwave fields detuned from the $|F = 1, m_F = -1\rangle \rightarrow |F = 2, m_F = -2\rangle$ hyperfine ground states. The microwaves were derived from a 6.8 GHz source from Microwave Dynamics (Part Number PLO-4000-06.80, S/N: 6214-1021-001). This source was not easily tuned, so to reliably control the amplitude and frequency of the microwaves, we added radio frequency (rf) sidebands from a radio-frequency source, IFR 2023A. The resulting signal consisted of power at the microwave frequency, $f_\mu = 6.7$ GHz, which is purposefully detuned from resonance, and power at harmonics of the rf frequency sidebands, $\pm n \times f_{rf}$, where $f_{rf} \sim 100$ MHz. Only the first harmonic had substantial rf power, $n = 1$. After passing through a microwave switch (Part Number HMC-CO11) and amplifier (Microwave Dynamics Part Number: AM53-6.85-4040), the microwave signal was sent to a microwave circulator (Ditom Part Number D3C4080; S/N 2110), which was used as an isolator to protect the amplifier from back-reflections of the microwave field. The output of the circulator was then sent to a 6.8 GHz impedance-matched spiral antenna.

An additional mixer was added to the setup described above. The purpose of this component was to add a fast amplitude modulation control of the microwaves. The turn-on time of the microwave switch (\sim ms) was too slow for our purposes here. There are faster microwave switches, but none were available at the time we installed the evaporation setup. This mixer combined a dc signal from the computer control program (Word Generator) to the IFR signal, essentially multiplying the two signals, allowing for fast turn-on of the microwave signal on $\sim 10 \mu\text{s}$ timescale. To do this, the rf signal, with a maximum output of 10 dBm, was sent to a Mini Circuits attenuator, -24 dBm, before passing through a Mini Circuits phase detector. Because there was $\simeq 5$ dBm attenuation from the phase detector, we added a 30 dBm Mini Circuits amplifier (Part Number ZHL-1-2W-S). This signal was

then sent to the mixer, as discussed above. An illustration of the microwave components is shown in Figure 2.15. It was this capability that enables the Rabi frequency measurements discussed below.

Calibration

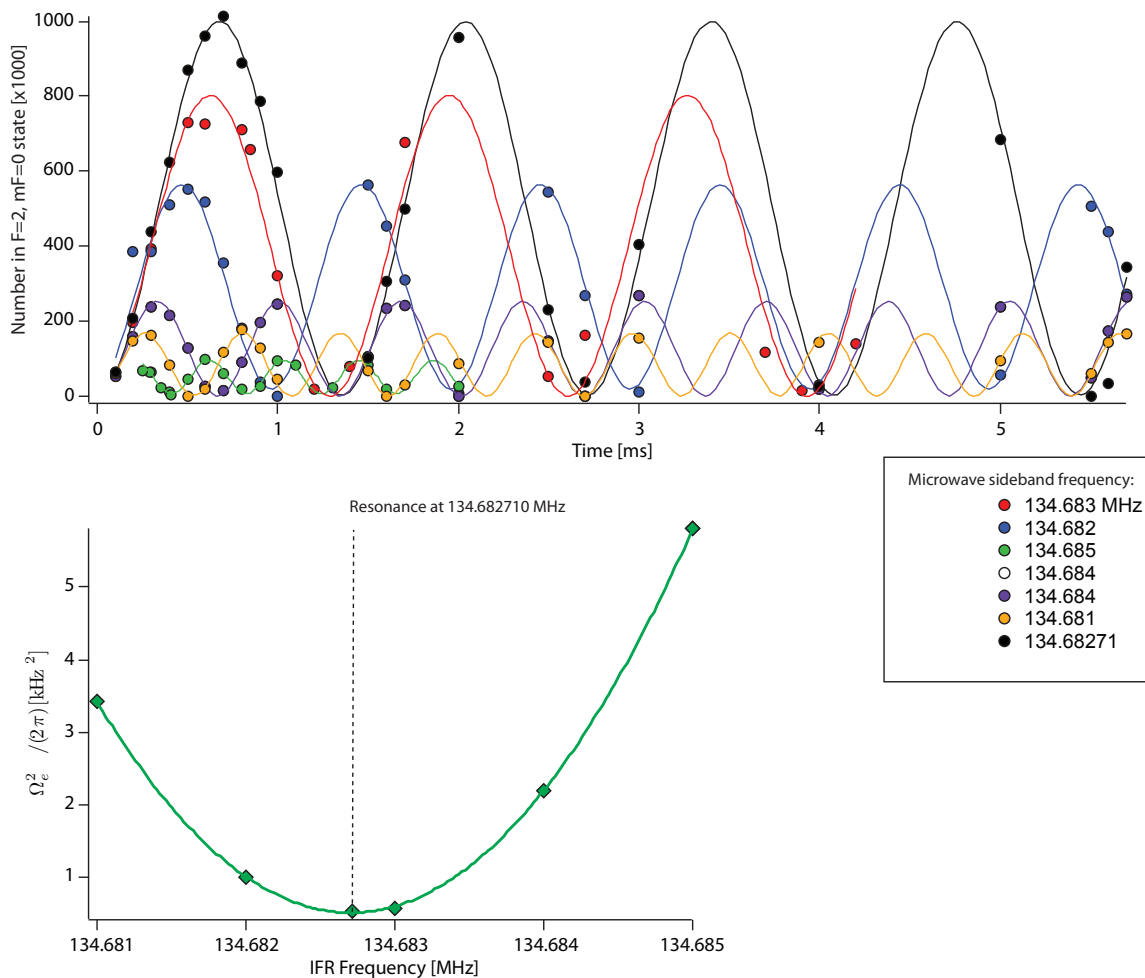


Figure 2.16: Rabi oscillation between $|F = 1, m_F = 0\rangle$ and $|F = 2, m_F = 0\rangle$ states when irradiated with microwaves. As a function of time, the atoms periodically oscillate between the two levels. This oscillation is the Rabi frequency. To determine the on-resonance (bare) Rabi frequency, we repeated this measurement for different detunings of the microwave frequency, ranging from 134.683 MHz to 134.681 MHz. The oscillation frequency as a function of the microwave detuning is shown below. This is fitted to a parabola, where the minimum is the bare Rabi frequency, Ω_R . For these studies, $\Omega_R = 134.682710 \pm 2.6$ MHz

We calibrated the strength of the applied microwaves by measuring the microwave Rabi frequency, Ω_R . This was done by measuring the fraction of atoms transferred from

$|F = 1, m_F = 0\rangle$ to the $|F = 2, m_F = 0\rangle$ hyperfine level as a function of time and at a constant microwave amplitude. This was then repeated for different microwave detunings. Assuming the system is well approximated by a two-level system, the population in the excited state scales as

$$N_{ex} \propto \sin^2\left(\frac{\Omega_{eff} \times t}{2}\right) \quad (2.17)$$

$$= \sin(\Omega_{eff}t), \quad (2.18)$$

where t is the time duration of the applied microwave field and the effective Rabi frequency is defined as $\Omega_{eff} = \sqrt{\Omega_R^2 + \delta^2}$, with the detuning from resonance defined as δ . Using this model, we fit the data to a sinusoid and extracted the effective Rabi frequency from the temporal evolution of the population in the $|F = 2, m_F = 0\rangle$ hyperfine level. A specific instance of one of these runs is shown in Figure 2.16. By maintaining a constant microwave power while varying the frequency, we were able to measure the effective Rabi frequency, Ω_{eff} . Plotting the Ω_{eff} as a function of the IFR sideband frequency, we were able to accurately determine the bare Rabi frequency, Ω_R . The bare Rabi frequency, Ω_R , occurs at the minimum of the Ω_{eff} versus detuning. To determine this minimum, we fit the data to a parabola and measured resonance to be at an IFR frequency of 134.682710 ± 2.6 MHz.

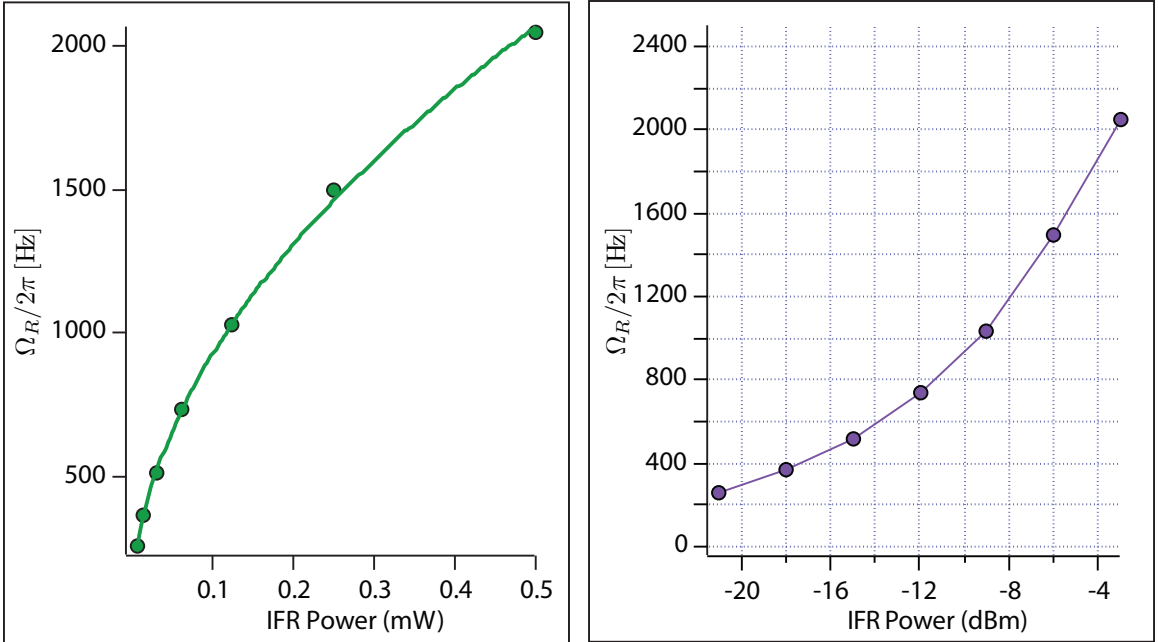


Figure 2.17: Microwave Rabi frequency calibration curves. The Rabi frequency as a function of the rf sideband power is measured (filled circles) and fit to an exponential (line).

Next we calibrated the bare Rabi frequency as a function of the sideband amplitude. To do this, like above, we measured the population in the $|F = 2, m_F = 0\rangle$ hyperfine level as a function of time, while maintaining a constant detuning. This was repeated for

different sideband amplitudes. For different sideband powers, we expected the bare Rabi frequency to scale as an exponential, where the argument is a function of the IFR power, due to the nonlinear nature of the mixer. A plot of the bare Rabi frequency for different IFR powers is shown in Figure 2.17. Fitting the data to an exponential we found that the Rabi frequency scales as

$$\Omega_R = 2920 \times 10^{P/20}, \quad (2.19)$$

where P is the IFR sideband power entered into the Word Generator, in units of dBm.

2.7.2 RF fields

The condensate was typically prepared in the $|F = 1, m_F = -1\rangle$ hyperfine level. To explore the other Zeeman sublevels within the $F = 1$ hyperfine manifold, we used resonant radio frequency (rf) fields. The rf fields were derived from a function generator (SRS 345 30 MHz Function Generator) which was sent to an rf switch before being amplified. The rf was then capacitively coupled to a 25 mm diameter coil located directly above the glass cell, approximately 30 mm from the in-trap location of the atoms. The typical rf parameters are described in later chapters.

2.7.3 DC magnetic bias field

We compensated and controlled the external magnetic field through the use of external magnetic field coils. This was accomplished by means of three pairs of coils situated outside the glass cell. The coils were dubbed “up-down,” “east-west,” and “north-south,” where their names were labelled according to their geographical orientation. The coils, however, were not oriented along the condensate axes as shown in Figure 2.18. These coils were held in a custom-built mount made of Delrin. The choice of Delrin was to prevent possible electrical shorts with the mount and the other coils. A sketch of the mount and the respective coils is shown in Figure 2.19.

The coils were assembled after the design and construction of the magnetic transportation system. Thus, in order to prevent the coils from obstructing valuable optical access and to maintain a compact design, a coil mount that fits within the Feshbach coils was determined an optimal solution. In order to comply with the spatial dimensions dictated by the Feshbach coils, the bias coils could not be larger than 40 mm in diameter. Thus we settled on coils that were 40 mm in diameter and roughly 30 mm apart. Realizing that these coils were not a true Helmholtz pair, we took precautionary steps to provide extra coils in the mount that could be used to compensate curvature magnetic fields. These are labeled at the “curvature coils” in Figure 2.19.

Despite these precautionary steps, an electric short was found between the east-west coils and the experimental table. Thus, in the fashion of the experiments in B171/B173, coils were wound around the glass cell well after the experimental apparatus had been assembled. This coil pair was instead oriented along the \hat{z} axis of the condensate. The reason for this was that there was already a magnetic field gradient coil along this axis and adding a second coil to this axis was fairly easy.

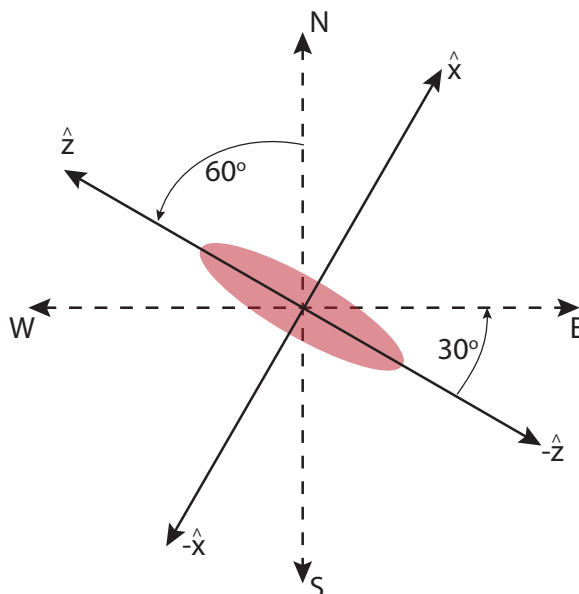


Figure 2.18: The condensate axes as compared to the geographical coordinate system. The coils in the lab are often named based on their geographical orientation. This plot is meant to clarify the orientation of the condensate axes with respect to the applied magnetic fields.

Magnetic Field Calibration

To calibrate the external bias coils, we used the linear Zeeman shift of the atoms as a measure of the magnetic field at the condensate. To do this, we applied a relatively weak rf field to the atoms and measured the populations within the magnetic sublevels using Stern-Gerlach analysis [79, 52, 80]. When the rf frequency matched the energy difference between the Zeeman sublevels, the atoms were transferred from the $|F = 1, m_F = -1\rangle$ to the $|F = 1, m_F = 0, 1\rangle$ sublevel. By recording the rf frequency that resulted in the largest transfer, we could determine the magnitude of the magnetic field. By using this approach for each applied magnetic bias field, we were able to isolate the rf resonance to within 5 kHz. Using this somewhat laborious procedure, the total magnetic field (measured in kHz) versus control voltage (Word Generator) was obtained for each bias field coil. An example of such a curve is shown in Figure 2.20.

The expected functional form for these curves is a hyperbolic shape, linear at large currents, but with a minimum that was determined by the transverse magnetic field. By fitting these curves to determine the center control voltage and the slope at large voltages, we were able to obtain a measure the calibration, relating the magnetic field dependence on the applied computer control voltage. Using these coils, the typical field we operated at was 187 kHz or equivalently 267 mG along the \hat{x} -direction.

Once calibrated, we were able to apply a magnetic field of a specific magnitude and orientation. For instance, the necessary currents for each coil can be determined from

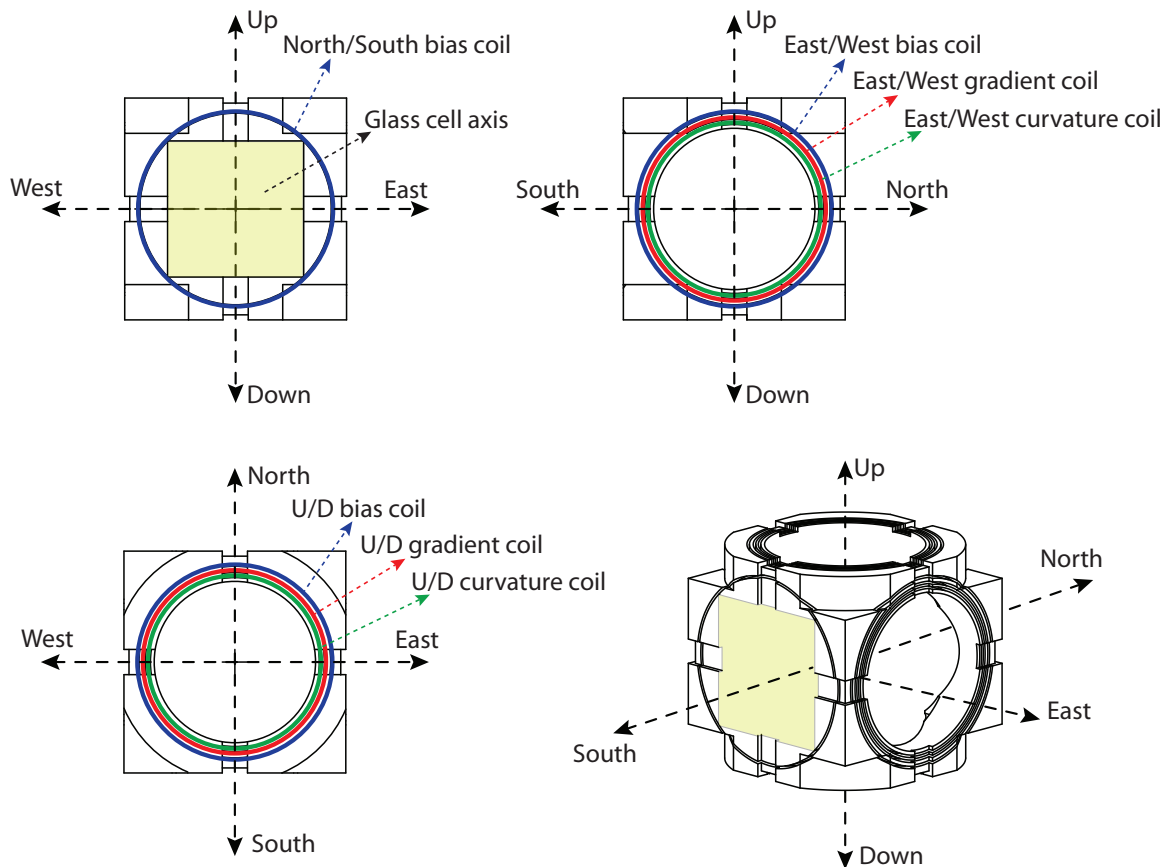


Figure 2.19: Mount for shim coils using an electrical insulating material (Delrin). The coils are wrapped directly onto the mount and secured in place using Stycast. Once in place, the mount is placed between the Feshbach coils, making for a very compact design for field compensation.

the coupled equations below,

$$\begin{pmatrix} B \cos(\theta) \\ B \sin(\theta) \end{pmatrix} = \begin{pmatrix} \alpha_z \cos \theta_1 & \alpha_n \cos \theta_2 \\ 0 & \alpha_n \sin \theta_2 \end{pmatrix} \begin{pmatrix} I_1 \\ I_2 \end{pmatrix}. \quad (2.20)$$

Here B is the magnitude of the magnetic field, θ is the orientation, $B_z = B \cos(\theta)$, $B_x = B \sin(\theta)$, α_z and α_n are the calibrations in units of Volts/Gauss for the “z” coils and the “north-south” coils, derived from the slope at large currents from the calibration curves above, and $\theta_{1,2}$ are the angles listed in Figure 2.18. Not listed here is the up/down field, since magnetization sensitive imaging technique requires in-plane magnetic fields. Furthermore, to make changing the magnetic field simpler, we made a graphical user interface (GUI) in the data analysis software, IGOR Pro. Using this GUI, we simply typed in the desired field and the necessary control voltages were returned. An even better improvement would have enabled communication between Igor and the Word Generator, then by simply typing in the desired fields, the Word Generator would be automatically updated.

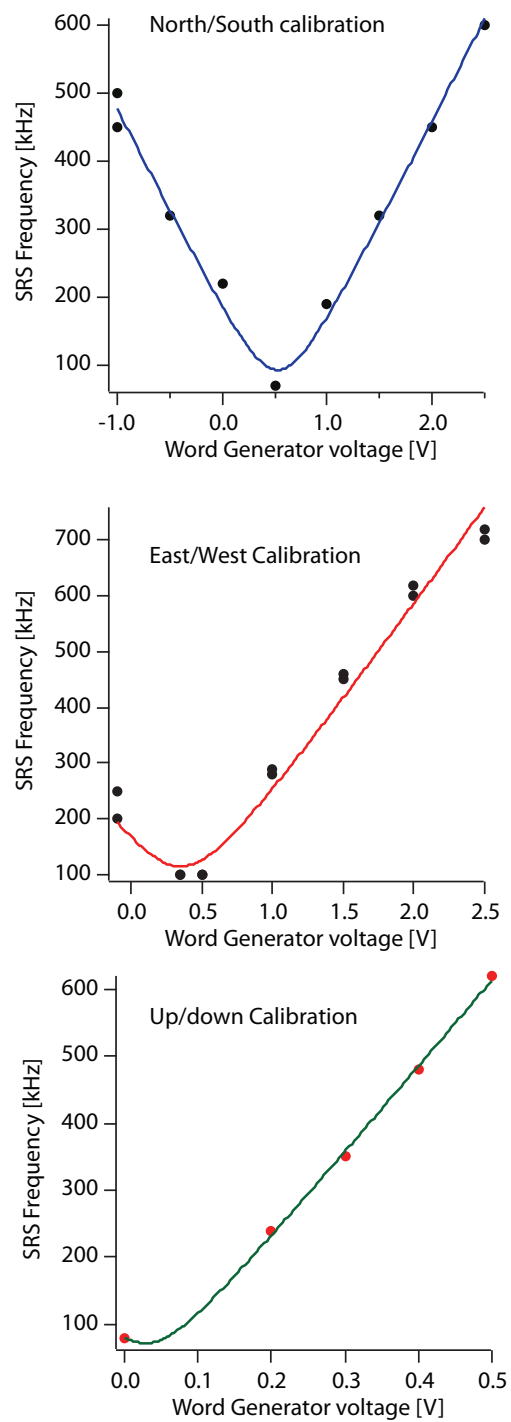


Figure 2.20: Calibration of bias magnetic fields. By applying a current to a specified coil, we could measure the magnetic field by measuring the resonant rf frequency. This was determined by looking recording the rf frequency where the maximum transfer occurred.

2.7.4 DC magnetic field gradients

In addition to the bias fields described above, it was also necessary to control the spatial inhomogeneity of the bias magnetic field. This was done by the addition of magnetic field gradient coils, with opposite flowing currents causing a cancellation of the magnetic field at their center. From the Maxwells equations ($\nabla \cdot B = 0$, $\nabla \times B = 0$), we know that there are potentially five magnetic field gradients that need to be compensated. However, based on the geometry of our spinor condensate, we could ignore gradients with spatial variations along the \hat{y} -axis, $dB_x/dy (= dB_y/dx)$ and $dB_z/dy (= dB_y/dz)$. This is because our condensate is essentially two-dimensional with respect to spin, with the Thomas-Fermi radius along the \hat{y} -axis being much smaller than the spin healing length, making any spatial variation of the spin along this axis energetically unfavorable [81, 51]. Thus, only cancellation of the following gradients was necessary: dB_z/dz , dB_z/dx , and dB_x/dx .

We used three pairs of coils configured in an anti-Helmholtz configuration to cancel the residual magnetic field gradients. They were referred to as: “up-down” gradient coil, the “z” gradient coil, and the “north-shim” gradient coil, named according to their geographical orientation or their orientation with respect to the condensate axes.

In order to cancel the residual magnetic field gradients we needed to spatially resolve the magnetic field. This was done by imaging the Larmor precession of the condensate magnetization (see Chapter 3), where accrued phase, $\delta\phi(r)$, after a given evolution time is proportional to the local magnetic field. Then by constructing a spatial map of the relative phases, we could determine the spatial variation of the background magnetic field, $\delta B(r) \propto \delta\phi(r)/t$ [79, 3, 80]. For example, following a given evolution time, the contribution to the background field from a magnetic field gradient oriented in the \hat{z} -direction was determined from,

$$\frac{dB_z}{dz} = \frac{\hbar}{g_F \mu_B t} \frac{d\phi_z}{dz}, \quad (2.21)$$

where the phase gradient $d\phi_z/dz$ ($\mathbf{B} = B_0 \hat{z}$) was determined from a polynomial fit to $\phi(\mathbf{r})$, averaged in the \hat{x} -direction over a central region of the condensate. We compensated this by applying current to the “z” gradient coil. Then by gradually increasing the evolution time, a more sensitive measurement the magnetic field gradient could be made. A similar method was used to compensate the magnetic field gradient along the \hat{x} -direction, dB_x/dx . However, due to the narrow width of the \hat{x} -dimension of the condensate, this measurement was more challenging. In this particular system, the uncompensated gradients were $dB_z/dz \simeq 40$ kHz/cm, $dB_x/dx \simeq 20$ kHz/cm, and $dB_x/dz \simeq 28$ kHz/cm.

In practice, this routine was complicated by the fact that a single coil can be tuned to cancel a magnetic field gradient along one axis, but only at the expense of introducing magnetic field gradients along other axes. By using three coils, however, we were able to cancel the following gradients: dB_z/dz , dB_x/dz , and dB_x/dx . This resulted in a series of

coupled equations described below,

$$\begin{pmatrix} I_z \\ I_{shim} \\ I_{u/d} \end{pmatrix} = \begin{pmatrix} -\frac{2}{3\alpha_z} & -\frac{2(\tan\theta - \cot\theta)}{3\alpha_z} & -\frac{2}{3\alpha_z} \\ 0 & \frac{2\csc\theta\sec\theta}{3\alpha_{shim}} & 0 \\ \frac{4}{3\alpha_{u/d}} & -\frac{2\cot\theta}{3\alpha_{u/d}} & \frac{2}{3\alpha_{u/d}} \end{pmatrix} \begin{pmatrix} \frac{dB_x}{dx} \\ \frac{dB_z}{dx} \\ \frac{dB_z}{dz} \end{pmatrix}, \quad (2.22)$$

where the magnitude of α_n for each n was determined from calibration measurements, the sign of α_n was determined by the coil orientation, and $\theta = 30^\circ$ was the orientation of the "shim" gradient coil with respect to the condensate axes. From our calibration measurements the values we determined for α_z , α_{shim} , and $\alpha_{u/d}$ were 25, 150, and -200, in units of kHz/cm/Volt. Using these coils, we were able to reduce the spatial variation of the magnetic field to $< 1 \mu\text{G}$ across the long axis of the condensate. In fact, we were able to observe Larmor precession for times up to 3 s of free evolution, where at 3 s, we had yet to observe any spatial variation of the magnetic field as indicated by the spatial profile of the condensate magnetization. Presumably, our ability to resolve Larmor precession at longer times is limited by the lifetime of the condensate in the optical trap.

2.7.5 Applying quadratic Zeeman shifts using microwave fields

In addition to properly compensated dc magnetic fields, necessary measures were taken to provide a magnetic field environment free from ac magnetic fields. This was difficult as the noise sources in the magnetic field environment of the room were characterized by rf frequencies up to 100 kHz, with intermittent noise between 100 kHz and 130 kHz, greatly limiting the study of spinor condensates at variable magnetic fields. Thus, to prevent their influence on our studies of spin-mixing dynamics in spinor condensates (see Chapter 5), we operated at a magnetic field where the noise in the magnetic field environment had no frequency component resonant with the energy scales in our system and introduced the use of modulated magnetic fields.

In optically trapped gases of $F = 1$ atoms, spin-mixing dynamics are governed by two spin-dependent interactions: the quadratic Zeeman shift, q , and the s-wave contact interaction [27, 82, 52, 79, 83, 80]. For the case of $F = 1$ ^{87}Rb , the quadratic Zeeman shift prefers an unmagnetized gas, with preferential population in the $|F = 1, m_F = 0\rangle$, while the contact interaction prefers a state which is magnetized (see Chapter 5 for more details). Essentially, the net effect of these interactions can be seen to promote an atom pair initially in the $|F = 1, m_F = 0\rangle$ state to a final state with one atom in the $|F = 1, m_F = -1\rangle$ state and the other in the $|F = 1, m_F = +1\rangle$ state. These dynamics can be controlled by tuning the energy difference between the initial and final states of the colliding pair,

$$q_B = \frac{E_{m_F=+1} + E_{m_F=-1} - 2E_{m_F=0}}{2} \propto B^2 \quad (2.23)$$

where E_{m_F} is the energy corresponding the $|F = 1, m_F\rangle$ state, and q_B is the quadratic shift due to the static magnetic field. Thus, when $q_B > 0$, the $|F = 1, m_F = 0\rangle$ state is lowest in energy, and when $q_B < 0$, the opposite is true. Typically, q_B is tuned using dc magnetic fields, which means that q_B is always positive. This can be seen in the Breit-Rabi diagram

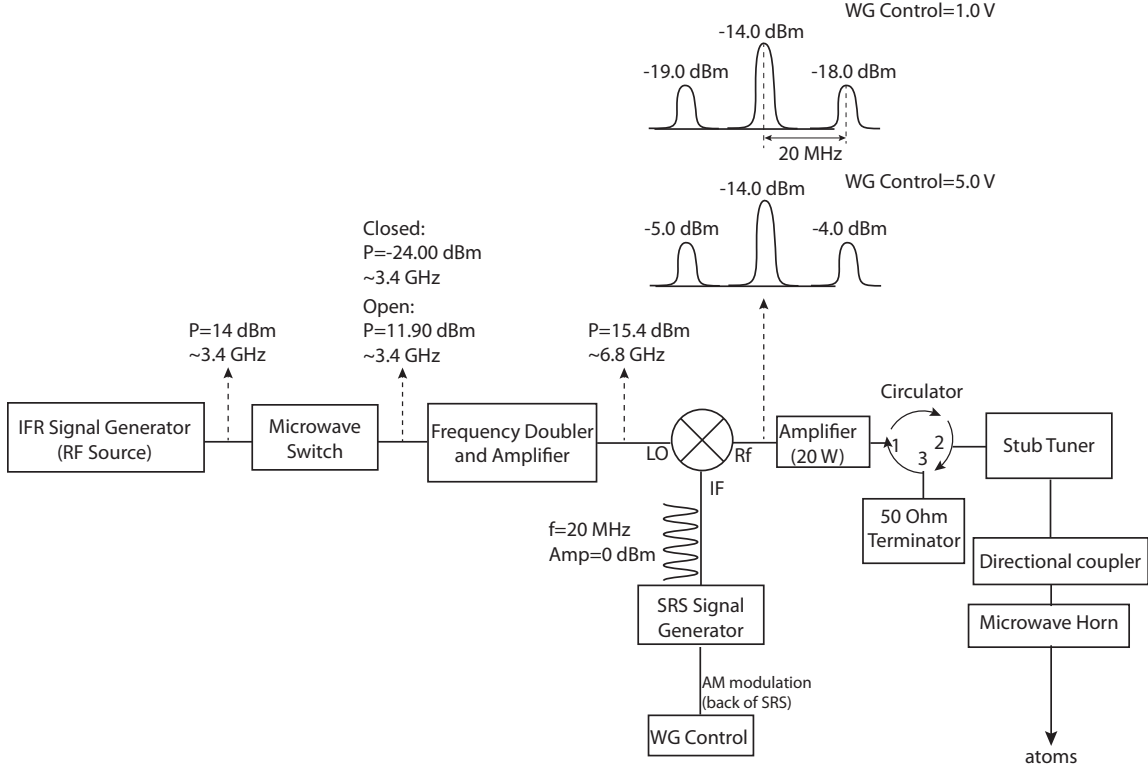


Figure 2.21: Shown here is an illustration of the microwave components used to generate the ac Zeeman shifts. Also shown is the power after each component, which we used as a reference in order to determine if any component needed to be replaced or adjusted.

for ^{87}Rb (see Figure 2.22). However, with the use of modulated magnetic fields, we can introduce an additional term, q_μ , which is the contribution to the quadratic Zeeman shift from a modulated field. As will be shown below, using this field, we can tune the total quadratic Zeeman shift, $q = q_B + q_\mu$, such that it can take on values that are negative or positive, greatly increasing the tunability of spin-mixing dynamics.

ac Zeeman shift

To implement such a scheme, we applied a linearly polarized microwave field, $\mathbf{B}^\mu(t) = B^\mu \sin(\omega_\mu t) \hat{\mathbf{x}}$, detuned from the $|F = 1, m_F = 0\rangle$ to $|F' = 2, m'_F = 0\rangle$ hyperfine levels. This induces an ac Zeeman shift, where the Hamiltonian describing the interaction is

$$H = \mu \cdot \mathbf{B}^\mu, \quad (2.24)$$

where μ is the magnetic moment. We can write this in terms of the Pauli matrices,

$$\mu = -g_F \mu_B m_F \left[\begin{pmatrix} 0 & 1 \\ 1 & 0 \end{pmatrix} \hat{\mathbf{x}} + \begin{pmatrix} 0 & -i \\ i & 0 \end{pmatrix} \hat{\mathbf{y}} + \begin{pmatrix} 1 & 0 \\ 0 & 1 \end{pmatrix} \hat{\mathbf{z}} \right], \quad (2.25)$$

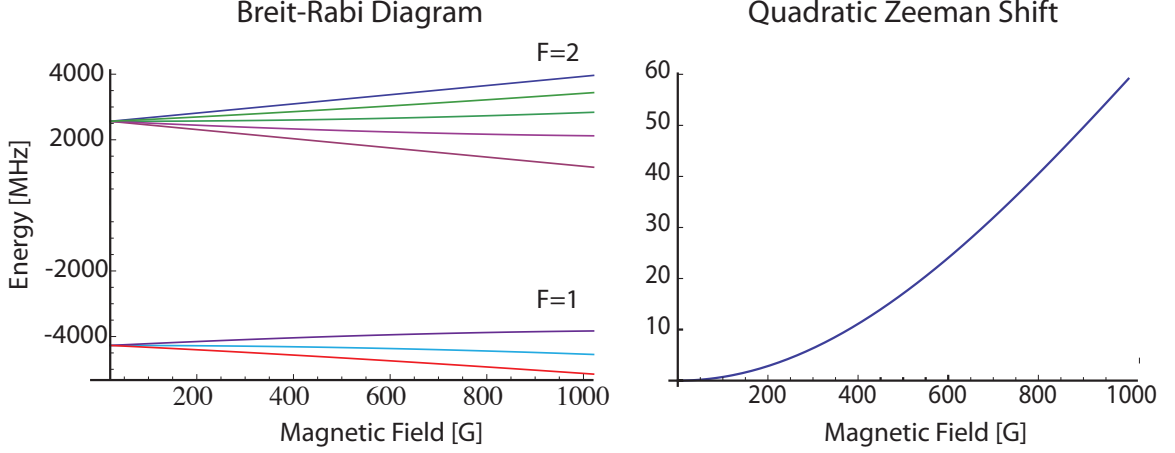


Figure 2.22: Breit-Rabi Diagram for ^{87}Rb (left) and quadratic Zeeman shift (right).

where we have assumed just a two-level system, in which the upper and lower states are described by

$$|2\rangle = \begin{pmatrix} 1 \\ 0 \end{pmatrix} \quad (2.26)$$

$$|1\rangle = \begin{pmatrix} 0 \\ 1 \end{pmatrix}. \quad (2.27)$$

The two-level approximation is valid when we are far from any hyperfine resonance, which is the case here (see below). After a bit of algebra we have

$$H_{Dressed-State} \approx \begin{pmatrix} \hbar\delta/2 & -i\hbar\Omega_R/2 \\ i\hbar\Omega_R/2 & -\hbar\delta/2 \end{pmatrix} \quad (2.28)$$

where $\delta = \omega_0 - \omega_\mu$ is the detuning from resonance and $\hbar\Omega_R = g\mu_B|B^\mu|$ is the Rabi frequency. Here the Hamiltonian is rewritten in the dressed-state picture. This is done by going into a frame rotating at ω_μ and applying the rotating-wave approximation, where the counter-rotating terms are far from resonance and can be ignored. Solving for the energy shift we have

$$\Delta E_1 = -\frac{\Omega_R^2}{4\delta} \quad (2.29)$$

where we have made use of the fact that $\Omega_R \ll \delta$, which allowed us to achieve the simplified expression shown above. In practice, we apply linearly polarized microwaves detuned from the $|F = 1, m_F = 0\rangle$ to $|F = 2, m_F = 0\rangle$ hyperfine levels, which represent the two levels discussed above, with $|1\rangle = |F = 1, m_F = 0\rangle$. Thus, under these approximations, the resulting quadratic Zeeman shift is

$$q_\mu = -\frac{\hbar\Omega_R^2}{4\delta}. \quad (2.30)$$

The detuning was chosen to be far from resonance to avoid populating the $F = 2$ hyperfine manifold, but close enough to achieve a large quadratic Zeeman shift. The detuning used in the experiment was $\delta = 2\pi \times 40$ kHz. The typical value for the magnetic fields was 267 mG, resulting in a linear Zeeman shift of 187 kHz. Thus, to a fairly good approximation, only the $|F = 1, m_F = 0\rangle$ level is shifted, since the coupling to the other sublevels is suppressed by $\sim 1/(\delta - \omega_{LP})$, where $\omega_{LP} \simeq 190$ kHz is the Larmor precession frequency.

Microwave Setup

The microwaves were applied using the setup as shown in Figure 2.21. Here, microwaves are derived from a microwave frequency source, IFR, referenced to a Rb atomic clock. The output of the IFR, which provides a signal at ≈ 3.4 GHz at an amplitude of 14 dBm, passes through a microwave switch, controlled using a TTL, before being sent to a frequency doubler and amplifier (Marki microwave DA-0210K). To control the frequency and amplitude of the applied microwaves, we add rf sidebands using a function generator (Stanford Research System DS340). This is accomplished by using a mixer, where the microwave source provides the input for the local oscillator (LO) and the rf function generator provides the input for the intermediate frequency (IF). The resulting signal has a carrier, f_μ and sidebands at $f_\mu \pm f_{rf}$, where the amplitude of the sidebands are computer controlled using the amplitude modulation port of the function generator. The signal is then amplified using a 40 dB amplifier with a maximum total output power of 20 Watts. The output of the amplifier then connects to a microwave circulator (Ditom Part Number D3C4080; S/N 2110) followed by a stub tuner (Maury Microwave Model 1819D). This is then attached to a microwave waveguide (ATM Advanced Technical Material WG P/N 137-201B-2), rated for frequencies ranging from 5-8 GHz. The waveguide is then secured to a 1/2" stainless steel optical post and rigidly attached to the optics breadboard, located approximately 125 mm from the atoms.

Calibration

We calibrated the applied quadratic shift by monitoring the temporal evolution of atoms in the $|F = 2, m_F = 0\rangle$ state. This was done by first preparing a sample of atoms in the $|F = 1, m_F = 0\rangle$ sublevel. Next, the sample was irradiated with microwaves resonant with the $|F = 1, m_F = 0\rangle \rightarrow |F = 2, m_F = 0\rangle$ transition and the total number of atoms in the $|F = 2, m_F = 0\rangle$ state was recorded. This was repeated for different time durations of the applied microwaves field. An example of such a scan is shown in Figure 2.23 (top), where the population in the $|F = 2, m_F = 0\rangle$ oscillates in time at the Rabi frequency, Ω_R .

In the experiment, we vary the magnitude of the quadratic shift by tuning the magnitude of the microwave Rabi frequency using the amplitude modulation port of the SRS frequency generator. We determine the calibration of the Rabi frequency versus the computer control voltage by repeating this same time-resolved scans described above, but while varying the amplitude of the rf sidebands between iterations of the experiment. Such a curve is shown in the bottom plot of Figure 2.23. The curve is fit to a line where the offset is constrained to zero and from this we extract dependence of the Rabi frequency on

the sideband power.

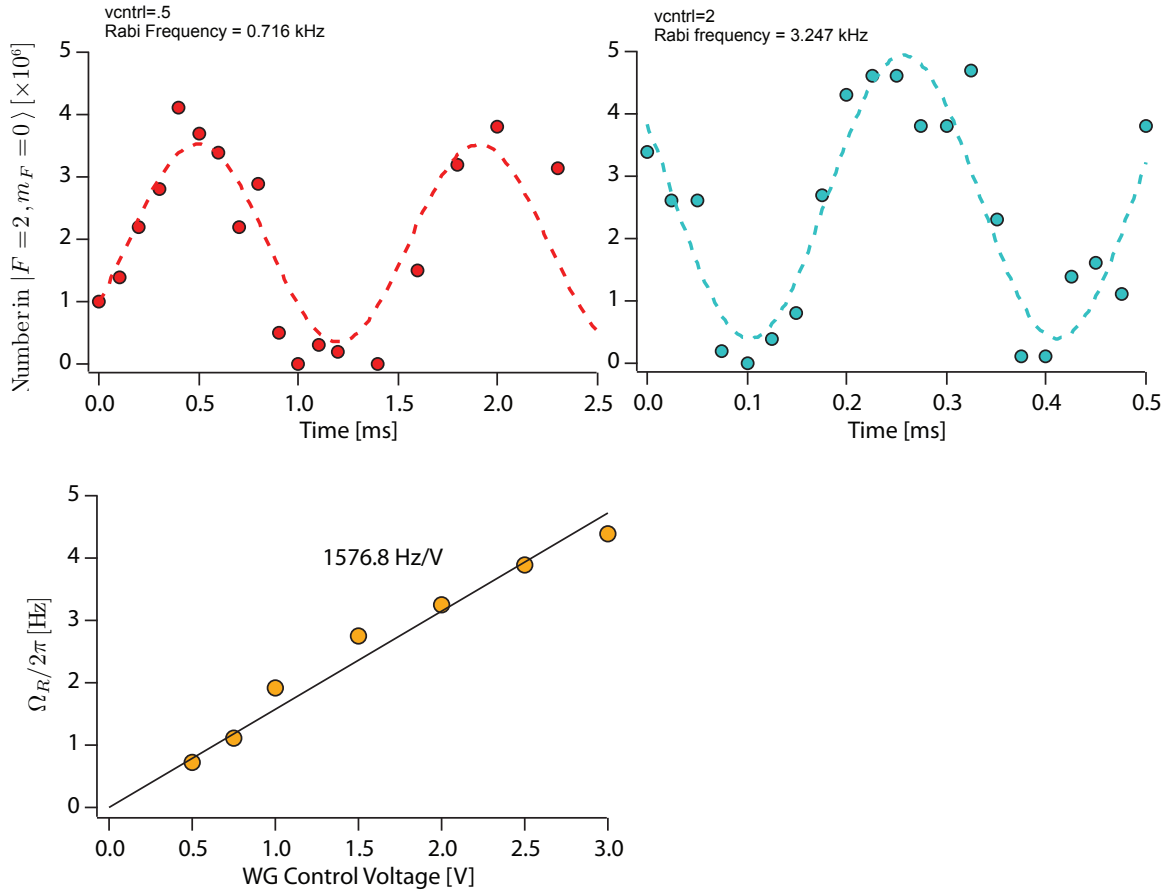


Figure 2.23: Rabi oscillation between two lower hyperfine states, $F = 1$ and $F = 2$. The Rabi frequency is measured by fitting the oscillation to a sinusoid. The dependence on the sideband power is obtained by measuring the Rabi frequencies for different sideband powers and fit to a line. For the experiments here, the maximum Rabi frequency was roughly 5 kHz, where the dependence on the computer control voltages was 1.5 kHz/V. The resulting quadratic Zeeman shift is dependent on the detuning from resonance, but at $\delta = 40$ kHz, quadratic shifts as high as $\simeq 500$ Hz could be achieved.

2.8 Computer Control

Creating an ultracold sample of atoms requires precise timing and control of many elements of the experimental apparatus, such as optical laser beams, optical beam shutters, power supply currents, to name a few. To implement such control, we have chosen to use a graphical-user-interface (GUI) called Cicero Word Generator (WG), developed in the Ketterle group at MIT, programmed by Aviv Keshet. Presented below is a very brief description of the hardware used and how it pertains to our experiment. An in-depth

review about the source code can be found at Ketterle’s physics webpage and in the recent publication [84].

Briefly, the WG provides a GUI that is useful for running National Instruments digital and analog output cards. The cards are controlled using a client-server architecture where the client, Cicero, is the interface for controlling, editing, and saving time-resolved sequences, while the server, Atticus, handles the hardware configuration. Using the WG, we are able to create time-resolved sequences using National Instruments digital and analog cards, with user specified times as short as $50 \mu\text{s}$. On a day-to-day basis, we typically work with Cicero and rarely make any changes the Atticus panel.

In our experiment, the WG controls the experiment using National Instrument analog and digital output cards. Currently installed, we have four analog output cards (PCI NI 6713), 3 digital cards (PCI NI 6533 and PCI NI 6534) and one gpib card, used to control the IFR during the evaporation sequence. Each analog card supplies us with 8 output channels, where each channel can output a 12-bit signal between -10 and 10 V and each digital card supplies us with 32 TTL channels. Typically, most computers today have at most two to three PCI slots. To accommodate the 8+ PCI cards, we used a PCI expander slot (Magma PE6R4) in addition to our main computer, giving us an additional six PCI slots.

Unfortunately, user-specified times shorter than $50 \mu\text{s}$ are needed to run the experiment. For instance, when imaging using absorption imaging, pulse durations as short as $30 \mu\text{s}$ are needed, and for phase-contrast imaging, probe pulse durations near 200 ns are needed. This time is limited by the sample clock of the PCI card. New generation experiments can achieve much shorter times due to higher onboard clock frequencies, but the cards inherited from the older generation E1 experiment, prevented us from accessing these shorter word times. The onboard clock frequency is 50 kHz, which should enable a pulse duration as short as $20 \mu\text{s}$. However, from my experience, times shorter than $50 \mu\text{s}$ are unreliable.

To circumvent this problem, we use an 4-channel pulse generator (Digital Delay/Pulse Generator DG535). The pulse generator is able to achieve pulses as short as 50 ps and as long as 1000 s. Rather than rely on the WG, we instead use the WG to trigger the pulse generator, which can be subject to 5 ps delays, and use this to dictate the pulse durations for our probe beams or any other signal that is sensitive to time delays as short as $\sim 10 \mu\text{s}$.

2.9 Water-cooling

To cool the coils used in the experiment, we employ the use of a Neslab recirculating chiller. Cold water exits the recirculating chiller at a temperature of 18°C and a pressure of 30 pounds per square inch (PSI). This water is fed into $3/8$ inch flame resistant rubber tubing from Goodyear (because you just never know) rated up to pressures of 300 PSI before being split into six parallel channels, where each channel is directed into a valve then to the coil. Currently only three channels are being used to cool three coils: slower, Feshbach, and magnetic transport coils. However, the remaining three channels are stopped using a high pressure valve from Swagelok. These extra lines allow for more coils to be easily

incorporated into the system. Water exiting each coil is then directed to flowmeters (Lake Monitor Style R) which then transmit analog readings, indicative of the flow through each coil, to an interlock box, described below. After the flowmeters, the parallel paths are recombined and returned to the recirculating chiller where the water is cooled using a heat exchanger which is cooled by the building chilled water supply.

Birge Chilled Water

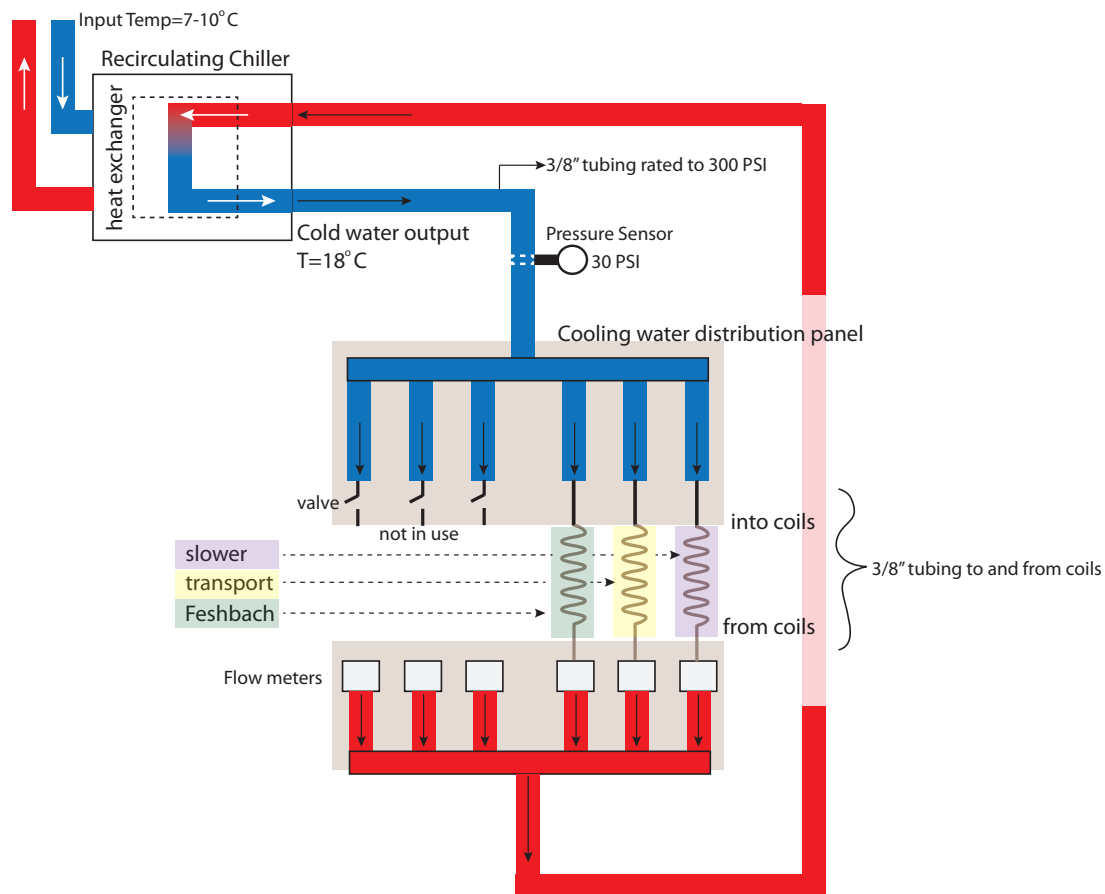


Figure 2.24: Illustrated here is the water cooling system for three coils. To cool the coils for the slower, magnetic transport system, and Feshbach coils, we use water from a recirculator. Water leaving the recirculator is at a temperature of $\approx 18^\circ\text{C}$ and has a pressure of ≈ 30 PSI. It is split into several paths, where each path specifies a specific system to cool. Extra water cooling lines are available for additional coils.

To ensure that cooling water is running through the coils before current is allowed to flow through the coils, an interlock logic box is used. The analog output of each flowmeter is directed to home-built interlock, where the flowmeter signal is compared to a threshold value set by a potentiometer, which can be adjusted using the front panel of the box. The comparison is made using a simple comparator circuit consisting of a single op amp. The three outputs (Slower coil, Feshbach coil, and Magnetic transport mount) are then

ANDed together and fed into a flip-flop circuit consisting of two NAND gates. The output is normally low but can be pulled up by means of a reset button on the front panel of the interlock box, where the LED on the front panel is indicative of the output state. The ac wall power dedicated to the high-current power supplies is also controlled in a similar manner. The ac wall power passes through a set of relays, whose output state is determined by the output state of the two NAND gates.

Interlock Design

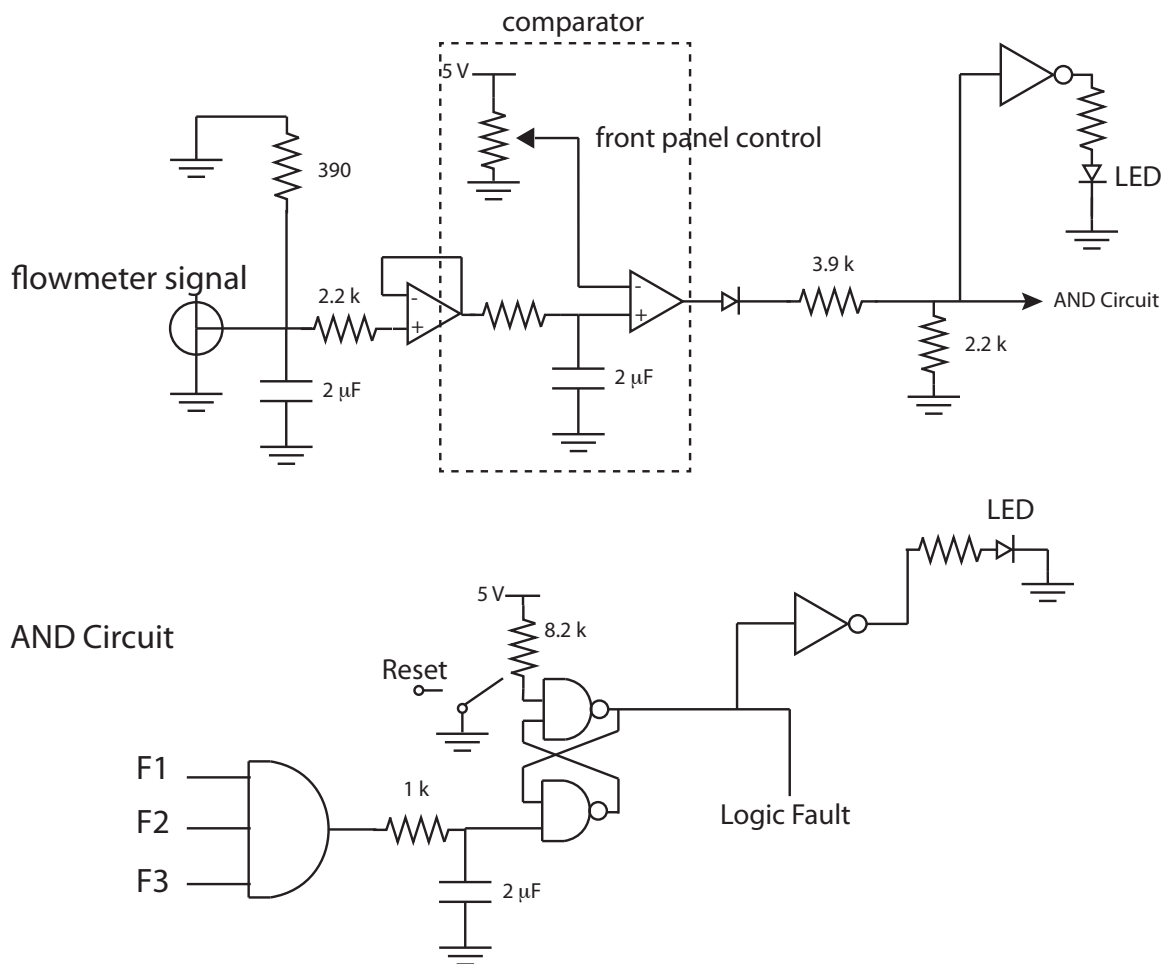


Figure 2.25: Illustration of interlock logic circuit used to ensure water is flowing through the magnetic coils and coil mounts before current is run.

The logic for the interlock is as follows. When the reset is not being pressed and no logic fault has occurred (i.e. no cooling water), the output will remember what was the previous state. Pushing the rest button forces the output to be high. It will remain in this state until a fault has occurred. Once a fault is registered, the output is forced low,

shutting off ac power to the high-current supplies, and will remain so even if the logic fault was momentary. This design is deliberate and used to force a conscious decision on part of the experimentalist to either proceed forward with the experiment or to understand the origin of the logic fault. In order to restore ac power to the supplies, the manual reset button must be pressed again. In the present experiment, two manual reset buttons can be found on the flowmeter interlock box, located above the power supplies, and on the ac power interlock box located on wall near the ac power lines.

2.10 Making a BEC

On March 30, 2009, just a mere three to four months after replacing older generation apparatus, E1, we achieved our first BEC of 1×10^6 atoms in the new experimental apparatus. Forewarned by the problems that plagued E1, we sought to make a more stable BEC-making machine; one that would make large-numbered condensates at a fairly high duty cycle. The result of our efforts are summarized in Figure 2.26. After some improvements, the BEC number was increased, and the machine was able to produce condensates containing $\approx 2.5 \times 10^6$ atoms in the $|F = 1, m_F = -1\rangle$ hyperfine state every 26 s.

A breakdown of the cooling process is reviewed here and the relevant parameters are listed in Table 2.4. The sequence begins with loading atoms into a MOT for 4 s from a Zeeman slower, after which, the atoms are compressed by nearly extinguishing the repump laser light in the MOT and increasing the magnetic quadrupole gradient and decreasing the MOT cooling light detuning. This process is commonly referred to as the compressed MOT (cMOT) [11, 51, 52]. Following the complete turnoff of the MOT (laser beam power and quadrupole field), the atoms evolve in a nearly gradient free field for 1.5-2 ms before the magnetic trap is rapidly turned on. This short evolution period where the atoms are not trapped was found to be very critical for efficient transfer into the magnetic trap. Decreasing or increasing this time substantially resulted in lower numbers in the magnetic trap. The magnetic trap is rapidly turned on within $10\mu\text{s}$ of this free evolution time using a resonant circuit. Next, the atoms are magnetically transported to the glass cell, where the optimal transport time was found to be 6 s. Decreasing this to as short as 5 s had a detrimental effect on the atom number and temperature. Once in the glass cell the atoms undergo forced microwave evaporation for 10 s, where the IFR sideband frequency is scanned from 80 MHz to 129 MHz. This produces cold thermal gases containing $100 - 120 \times 10^6$ atoms at a temperature of $30 - 40 \mu\text{K}$. Midway through the evaporation sequence, the power for the ODT is ramped to full power. Approximately $12 - 15 \times 10^6$ atoms are transferred to the optical trap, where the atoms are evaporated using an exponential ramp of the optical trap power over 2.4 s with a time constant of $\tau = 0.6$ s. This results in nearly pure condensates of $2.4 - 2.6 \times 10^6$.

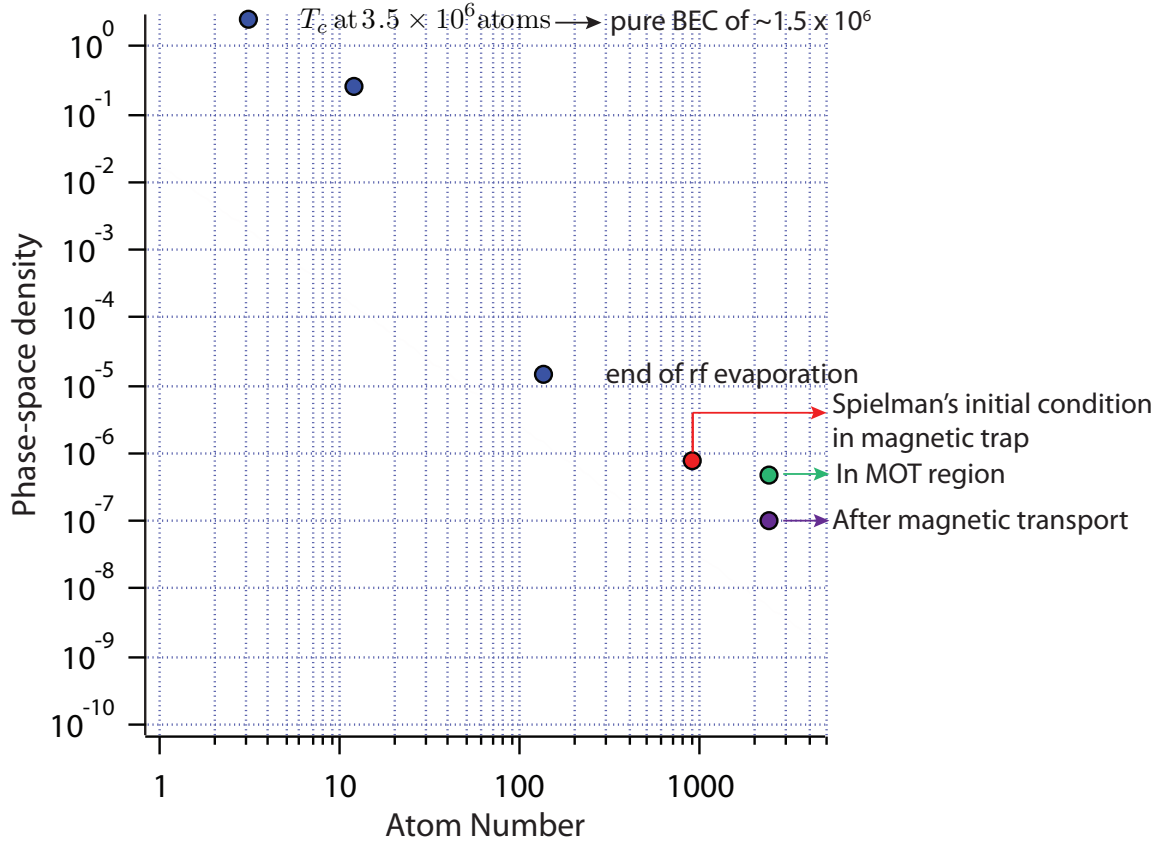


Figure 2.26: Initial phase-space density measurement of cooling sequence on April 30 2009. We compare our phase-space density to another experiment with a similar combined magnetic and optical trapping potential for making quantum degenerate samples of ^{87}Rb in the $|F = 1, m_F = -1\rangle$ hyperfine state [85].

Table 2.4: Atom number and temperature

Stage	Temperature	Number	Phase-space Density
Oven	475 K (~ 300 m/s)		
Zeeman Slower	4 K (~ 20 m/s)		
MOT	$\sim 150 - 200 \mu\text{K}$	8×10^9 ($2 \times 10^9 \text{ s}^{-1}$)	$\sim 10^{-6}$ (4 s loading)
Magnetic Trap (TP0)	$\sim 150 - 200 \mu\text{K}$	2×10^9	$\sim 10^{-6}$
Glass Cell, no evap.	$\sim 600 - 900 \mu\text{K}$	2×10^9	$\sim 10^{-7}$
End of μ -Evaporation	$\sim 30 \mu\text{K}$	100×10^6	$\sim 5 \times 10^{-4}$
End of Optical Trap Evap.	~ 100 nK	2.5×10^6	~ 1

Chapter 3

Imaging Magnetization

In order to observe the rich array of physics associated with a $F = 1$ spinor Bose condensate, we must obtain as much information as possible from such a system, such as the separate spin populations as well as the coherences among them. To do this we use a combination of absorption imaging and magnetization sensitive imaging to extract the populations as well as coherences among them (diagonal and off-diagonal components of the one-body density matrix). Our imaging technique enables us to image in-situ the vector magnetization profile of the gas with high spatial resolution and enables the possibility of temporally resolving magnetization dynamics. Presented in this chapter is a brief summary of the phase contrast imaging technique and a new method to image the vector magnetization which is called polarization contrast imaging.

3.1 Phase Sensitive Imaging

In many experiments on spinor gases, imaging is performed by first spatially separating spin components via a magnetic field gradient (Stern-Gerlach) then imaged using standard optical absorption. Although this method allows enables us to count the populations within each spin component, it is destructive and unable to probe the coherences between differing spin components. An alternative technique is to utilize the dielectric properties of the spinor Bose condensate, where the measured signal depends upon the internal spin state. Thus by analyzing the intensity, phase, and polarization of light propagating through an atomic cloud, information about the spinor order parameter, specifically the density and spin density can be retrieved.

3.1.1 Basic Principle

The phase contrast technique is a fairly standard interferometric measurement technique, which exploits the differing refractive indices within a sample, yielding a measure of the structures that might otherwise be transparent. First developed by Frederick Zernike in 1942 [86, 87], for which he was later awarded the Nobel prize, the use of this technique has flourished, becoming a standard tool for non evasive imaging, with applications extending across many disciplines within the sciences [1, 88, 51, 89, 90].

In this method, light from a single source is split into a local oscillator and a probe. The probe passes through an atomic gas and acquires a phase shift relative to the local oscillator. The resulting interference pattern yields information about the local properties of the sample. A simple model for this can be found in other theses [79, 52, 80], but for clarity it will be presented here. The electric field of light propagating in the \hat{x} -direction can be described by a plane wave, $\mathbf{E} = \mathbf{E}_0 e^{ikx}$, where k is the wave vector. Upon passing through a medium, a few things occur; the phase velocity is varied and light is absorbed, resulting in overall attenuation and phase shift of the electric field. For now, we will assume that any absorption is negligible, and can be ignored. Thus, the electric field is said to have acquired a phase shift upon exiting the medium, $\mathbf{E}_{out} = \mathbf{E}_{in} e^{i\phi}$, where $\mathbf{E}_{in} = \mathbf{E}_0 e^{ikx}$.

In this technique, we measure the phase shift acquired by the outgoing light, ϕ , and in measuring this phase shift we are able to characterize the spinor order parameter (density, spin). However, the exact relation between ϕ and the properties of a spinor condensate is not completely obvious and it is this relation that will be addressed in the following sections.

3.2 Dielectric properties of an $F = 1$ spinor gas

In order to understand how we are able to gather information about the spinor order parameter, we must first review the dielectric properties of an $F = 1$ spinor gas. This has been reviewed quite thoroughly in other theses [80, 79, 52, 91] and in the literature [92], thus it will only be presented briefly here.

All materials have a refractive index that tells that us how light or any other form of radiation propagates through the medium. The most common appearance of the refractive index is in Snell's law, which describes how light is bent as it crosses an interface between two materials. In general a material can be described not only by its refractive index, n , but also by its dielectric constant, ϵ ,

$$\epsilon = 1 + \chi \tag{3.1}$$

or, χ , the dielectric susceptibility, where both are related to the refractive index by,

$$n^2 = 1 + \chi = \epsilon. \tag{3.2}$$

Any one of these is sufficient describe the propagation of light in a medium, but for now we will focus primarily on the dielectric susceptibility χ . (This choice will become more clear in the following sections.) Thus, by characterizing the dielectric susceptibility, we can obtain a complete description of the three-component spinor order parameter ψ .

3.2.1 Dielectric Constant

In the case of spin-1 atoms, the one-body density matrix, m_{ij} , is a useful representation which encases the properties of a spin-1 object, consisting of a tensor product of two spin-1 objects, ψ and its conjugate ψ^\dagger . As has been done with photons, we can then represent this as a sum of irreducible tensor components with angular momenta 0, 1 and 2,

with ρ , S , and N representing the density, spin vector, and nematicity. Their general form is shown below:

$$\rho(\mathbf{x}) = \sum_j m_{jj} = \psi^\dagger(\mathbf{x}) \cdot \psi(\mathbf{x}) \quad (3.3)$$

$$S_j(\mathbf{x}) = -i\varepsilon_{jkl}m_{kl}(\mathbf{x}) \quad (3.4)$$

$$N_{ij}(\mathbf{x}) = \frac{1}{2}(m_{ij}(\mathbf{x}) + m_{ji}(\mathbf{x}) - \frac{\rho(\mathbf{x})}{3}\delta_{ij}). \quad (3.5)$$

Next we need to understand the relation between the elements of the one-body density matrix and the dielectric susceptibility, and in this case this is a tensor. Now starting with the Hamiltonian of an electromagnetic field in a homogeneous medium and taking a few giant leaps, or following the formalism presented in [92], we can write the dielectric susceptibility in terms of the irreducible tensor components of the one-body matrix with appropriate scaling coefficients as:

$$\chi_{jk} = c_0\langle\rho\rangle\delta_{jk} - ic_1\varepsilon_{jkl}\langle S_l\rangle + c_2\langle N_{jk}\rangle \quad (3.6)$$

where the coefficients c_0, c_1, c_2 , correspond to the polarizability, optical activity, and the birefringence of the medium, respectively. These coefficients are dependent on the internal structure of the atom as well as the final excited state, F' . Assuming we start in the ground state with total angular momentum $F = 1$, the coefficients for $F' = 1$ are: $c_0 = 2a_1/3$, $c_1 = -a_1/2$, and $c_2 = -a_1$, where $a_1 = -2|d_{11}|^2/\epsilon_0\hbar\delta$, d_{11} is the dipole matrix element between the $F = 1 \rightarrow F' = 1$ state, and δ is the detuning from atomic resonance. These can also be written for the excited state $F' = 2$ as follows: $c_0 = 5a_2/9$, $c_1 = 5a_2/12$, and $c_2 = a_2/6$, where $a_2 = -2|d_{12}|^2/\epsilon_0\hbar\delta$, and d_{12} is the dipole matrix element between the $F = 1 \rightarrow F' = 2$ state.

For our specific experimental setup, which will be discussed in more detail below, we are detuned from the $F = 1 \rightarrow F' = 2$ state of the D1 transition lines in ^{87}Rb . Given that there is not a single excited state within the $5p_{1/2}$ manifold, the dielectric susceptibility has contributions from each state, $\chi_{F'=1,2}$, each weighted by their respective detunings, $1/\delta$. The differing numerical pre-factors for each $\chi_{F'=1,2}$ can be related using appropriate Clebsch-Gordan coefficients and the reduced dipole matrix element,

$$a_1 = \eta\frac{1}{12}\langle J = 1/2 || e\mathbf{r} || J' = 1/2 \rangle \quad (3.7)$$

$$a_2 = \eta\frac{1}{2}\langle J = 1/2 || e\mathbf{r} || J' = 1/2 \rangle \quad (3.8)$$

where the reduced matrix elements are related to the dipole matrix elements d_{mn} via Wigner 3(6)-j symbol and the proportionality constant η above can be rewritten in terms of more convenient parameters. Putting these all together we can now write the dielectric suscepti-

bility in terms of experimental parameters and the irreducible tensor components as,

$$\chi_{F'=1} = \frac{2}{3}\rho \begin{pmatrix} 1 & 0 \\ 0 & 1 \end{pmatrix} + \frac{1}{2} \begin{pmatrix} S_{11} & S_{12} \\ S_{21} & S_{22} \end{pmatrix} - \begin{pmatrix} N_{11} & N_{12} \\ N_{21} & N_{22} \end{pmatrix} \quad (3.9)$$

$$\chi_{F'=2} = \frac{5}{9}\rho \begin{pmatrix} 1 & 0 \\ 0 & 1 \end{pmatrix} - \frac{5}{12} \begin{pmatrix} S_{11} & S_{12} \\ S_{21} & S_{22} \end{pmatrix} + \frac{1}{6} \begin{pmatrix} N_{11} & N_{12} \\ N_{21} & N_{22} \end{pmatrix} \quad (3.10)$$

$$\chi_{jk} = \frac{\sigma_0 n \Gamma \lambda}{4\pi} \left(\frac{1}{2} \frac{\chi_{F'=2}}{\delta} + \frac{1}{12} \frac{\chi_{F'=1}}{\delta + 800} \right) \quad (3.11)$$

where η is now expressed in terms of experimental parameters, δ is the detuning of the probe field from the $F = 1 \rightarrow F' = 2$ transition (measured in MHz), 800 is the energy separation between the hyperfine levels in the $5p_{1/2}$ state, $\sigma_0 = 3\lambda^2/2\pi$ is the resonant cross-section, n is the condensate density, $\Gamma = 6$ MHz is the natural linewidth of the excited state, and λ is the wavelength of the probe field. In writing the dielectric tensor in this form, we have glossed over a few important details. One is that the dielectric susceptibility is now represented by a 2×2 rather than a 3×3 matrix. This is because information is gathered via the polarization of the probe field, which is perpendicular to the propagation direction, thus only sensitive to the components of the dielectric susceptibility which are also transverse to the direction propagation.

3.2.2 Spinor Order Parameter: Ferromagnetic vs Polar state

Now that we have presented the dielectric susceptibility in terms of the spin vector, density, and nematicity, we can then fill in the elements of each matrix using the spinor order parameter, ψ , using the relations discussed in Equations 3.3-3.5.

Opening an advanced quantum mechanics book, or referring to Professor Robert Littlejohn's quantum mechanics lecture notes (Notes 10: Rotations in quantum mechanics), one will see that a spin-1/2 object pointing in the \hat{n} direction can be arbitrarily represented using a series of rotations, $U_0 = U(\alpha)U(\beta)U(\gamma)$, where α, β, γ are Euler rotation angles. This can easily be extended to a spin-1 system.

In our experiments, there are two classes of spinors that we use to explore various phenomena, those which are characterized by a macroscopic magnetization,

$$\psi_{FS} = U(\alpha, \beta, \gamma) \begin{pmatrix} 1 \\ 0 \\ 0 \end{pmatrix}, \quad (3.12)$$

also referred to as a ferromagnetic state, and those which are unmagnetized

$$\psi_{PS} = U(\alpha, \beta, \gamma) \begin{pmatrix} 0 \\ 1 \\ 0 \end{pmatrix}, \quad (3.13)$$

otherwise referred to as a polar state [27]. Using these representations (shown in the spher-

ical basis), S_{ij} and N_{ij} for the ferromagnetic and polar states are,

$$S_{FS} = \begin{pmatrix} \cos \beta & 0 \\ 0 & -\cos \beta \end{pmatrix} \quad (3.14)$$

$$N_{FS} = \begin{pmatrix} \frac{1}{24}(1 + 3 \cos 2\beta) & -\frac{1}{4} \sin^2 \beta (\cos 2\alpha + i \sin 2\alpha) \\ -\frac{1}{4} \sin^2 \beta (\cos 2\alpha + i \sin 2\alpha) & \frac{1}{24}(1 + 3 \cos 2\beta) \end{pmatrix} \quad (3.15)$$

$$S_{PS} = \vec{0} \quad (3.16)$$

$$N_{PS} = -2N_{FS}. \quad (3.17)$$

Here, β defines the angle with respect to the imaging axis and α is the angle in the plane transverse to the imaging axis.

Prior to making any measurements, it is typically a good idea to have a general understanding of what parameters your measurement is sensitive to. From the matrices above, some insight can be gained about each class of states. For instance, we can easily see that for a ferromagnetic state, a measurement of the spin vector is dependent on the angle β , and for a maximum signal, it is best for the spins to be aligned along the imaging axis. In addition, information of the polar state can only be gained through measurements of the nematic order, since its spin vector is zero. Thus, it is our job as clever experimentalists to devise methods by which we are able extract this information.

3.3 Phase shift

Now comes the more interesting task of relating the phase shift to the dielectric susceptibility. As an electric field traverses through a medium, two things occur, the electric field is attenuated and undergoes a phase shift. Neglecting any attenuation in the electric field (since we are far detuned from any atomic transition), we turn our attention to the origin of the phase shift, $e^{i\phi}$.

An electric field traversing through a medium along the \hat{y} -axis with refractive index n can be written as:

$$\mathbf{E}_{out} = \mathbf{E}_{in} e^{ik_0 \int n_{jk} dy}, \quad (3.18)$$

where n_{jk} is the refractive index tensor. In order to further simplify this expression, we make an approximation that the medium is very thin (thin-lens approximation) and that that $n_{jk} = \sqrt{\delta_{jk} + \chi_{jk}}$ is close to unity,

$$\mathbf{E}_{out} = \mathbf{E}_{in} e^{ik_0 \int n_{jk} dy} \quad (3.19)$$

$$= \mathbf{E}_{in} e^{ik_0 (2r_y) n_{jk}} \quad (3.20)$$

$$\approx \mathbf{E}_{in} e^{ik_0 (2r_y) (\delta_{jk} + \chi_{jk}/2)}, \quad (3.21)$$

where r_y is the Thomas-Fermi radius of the condensate along the direction of integration [93, 94]. We can now write the phase shift as:

$$\phi_{jk} = \phi_0 \delta_{jk} + \phi_0 \chi_{jk}/2, \quad (3.22)$$

where $\phi_0 = 2k_0 r_y$ is an overall phase shift acquired by the probe and χ_{jk} is the spin dependent phase shift.

3.4 Variations on Phase Sensitive Imaging

We've just seen how the phase shift is related to the spinor order parameter via the susceptibility. There are a few different techniques to extract this information and the primary focus of this section will be to review those which have been used in the lab: phase-contrast imaging and polarization-contrast imaging. For a more extensive review on the different variations of dispersive imaging, I refer the reader to James Higbie's thesis [79].

3.4.1 Phase-Contrast Imaging (PCI): Phase dot and circularly polarized light

In the early years of imaging spinor gases in the lab (E1), phase sensitive imaging was conducted by interfering light that has traversed through the condensate with light that has passed through a known dielectric medium, known as phase-contrast imaging [51, 3]. Specifically, circularly polarized light detuned by 500 MHz from the D1 transition lines travels along the \hat{y} -axis (parallel to gravity) and passes through the condensate. The probe beam used is approximately 2-3 mm in diameter and the spatial extent of the long axis of the condensate is approximately 300 μm . Due to the radically different sizes between the condensate the probe beam, the probe beam can be thought of as consisting of two parts, the scattered and un-scattered parts, or the probe and the local oscillator. Having passed through the condensate, the scattered part of the probe beam comes to a focus at a different position compared to the un-scattered part. This is due to the spatially varying index of refraction of the condensate which acts like a convex lens (see Equation 3.22 and 3.5). Now having spatially separated the foci of the two beams, a thin circular dielectric (phase dot, \varnothing 250 μm) is placed at the focus of the un-scattered beam (local oscillator), advancing its phase by $\approx \pi/2$. The scattered beam also passes through the phase dot (its focus occurred well before the location of the phase dot), but due to its fairly large angular extent at the phase dot, this effect can be ignored. The two beams are then re-imaged at the imaging plane (CCD camera) such that:

$$\mathbf{E}_{unscatt} = \mathbf{E}_{in} e^{i\phi_{pd}} \quad (3.23)$$

$$\mathbf{E}_{scatt} = \mathbf{E}_{in} (e^{i\phi_{atom}} - 1) \quad (3.24)$$

$$\mathbf{E}_{out} = \mathbf{E}_{unscatt} + \mathbf{E}_{scatt} \quad (3.25)$$

$$= \mathbf{E}_{in} (e^{i\phi_{pd}} + e^{i\phi_{atom}} - 1) \quad (3.26)$$

where \mathbf{E}_{in} is the incoming probe field. The signal measured at the camera is the normalized intensity $= |\mathbf{E}_{out}|^2 / |E_{in}|^2$:

$$|\mathbf{E}_{out}|^2 / |E_{in}|^2 = 3 + 2 [\cos(\phi_{pd} - \phi_{atom}) - \cos(\phi_{pd}) - \cos(\phi_{atom})]. \quad (3.27)$$

We can further simplify the expression by assuming that the phase shift acquired by the atoms is small and substituting the $\pi/2$ phase advance introduced by the phase dot:

$$|\mathbf{E}_{out}|^2 / |E_{in}|^2 \approx 1 + 2\phi_{atom}. \quad (3.28)$$

By introducing the phase dot, the signal now has a linear dependence on the phase shift, which is ideal for the small phase shifts introduced by the spinor gas.

Magnetization Sensitivity

So far, we have not considered the polarization of the incoming probe field, and recall that the light polarization is a vital element in determining what component of the dielectric susceptibility we are able to measure. Using the spherical basis, where σ^+ light has the form (10)[†], we can rewrite the outgoing electric field, \mathbf{E}_{out} , in matrix form as

$$\frac{\mathbf{E}_{out}}{E_{in}} = e^{i\phi_{pd}} \begin{pmatrix} 1 \\ 0 \end{pmatrix} + e^{i\phi_0\chi_{jk}/2} \begin{pmatrix} 1 \\ 0 \end{pmatrix} - \begin{pmatrix} 1 \\ 0 \end{pmatrix} \quad (3.29)$$

where χ_{jk} is the spin-dependent phase shift acquired by the light, E_{in} is the amplitude of the incoming probe field, ϕ_0 is the overall phase shift acquired by the probe beam, and ϕ_{pd} is the phase shift imposed by the phase dot. This expression can be further simplified by substituting the value of the ϕ_{pd} and approximating $e^{i\phi_0\chi_{jk}/2} \approx 1 + i(\phi_0\chi_{jk}/2)$ (valid when the spin-dependent phase shift is much smaller than unity), yielding

$$\frac{\mathbf{E}_{out}}{E_{in}} \approx i(\delta_{jk} + \phi_0\chi_{jk}/2) \begin{pmatrix} 1 \\ 0 \end{pmatrix}. \quad (3.30)$$

This, however, is not the signal we measure in the lab, and to get that we need the normalized intensity distribution at the camera:

$$|\mathbf{E}_{out}|^2/|E_{in}|^2 \approx 1 + \phi_0\langle\chi_{11}\rangle + \mathcal{O}(2), \quad (3.31)$$

where we have only kept terms up to first order in ϕ_0 . This can also be written as

$$\begin{aligned} |\mathbf{E}_{out}|^2/|E_{in}|^2 \approx & \quad (3.32) \\ & 1 + \sigma_0\tilde{n}\gamma \left[\frac{5}{18} \frac{1}{\delta} + \frac{1}{18} \frac{1}{\delta + 800} + \left(\frac{1}{24} \frac{1}{\delta + 800} - \frac{5}{24} \frac{1}{\delta} \right) \langle F_y \rangle \right. \\ & \left. + \frac{1}{72} \left(\frac{1}{\delta} - \frac{1}{\delta + 800} \right) \langle F_y^2 \rangle \right] \end{aligned}$$

where we have made use of the relations specified in Equation 3.11. Thus, we see that by using both the phase dot and circularly polarized light, we have a signal which is sensitive to the density and spin of the condensate. The sensitivity to a spin-independent component is very useful when extracting a measure of the condensate density which is independent of the magnetization. The typical experimental parameters used for phase contrast imaging are: $\delta = -400$ MHz (blue-detuned), $n \approx 2 \times 10^{14}$, $r_y \approx 1.8 \mu\text{m}^2$, and $\gamma = 2\pi \times 6$ MHz.

3.4.2 Polarization Contrast Imaging

In the early developmental stages of E5 (the next generation of E1), a reasonable phase-contrast signal was not easy to come by. There are many reasons for this, so I refer the reader to Appendix E. Thus we sought out an alternative method, which forgoes the use of a phase dot and instead uses the polarization of the probe field to obtain a measurement of the magnetization, which we refer to as polarization contrast imaging. This is by no means the first instance of this type of imaging nor is it a recently developed idea. This

method is used across many disciplines with applications extending to geology, physics, and biology, to name a few [90, 95, 96].

In this technique a measurement of the magnetizations comes about from the rotation of probe polarization. Specifically, we illuminate the condensate with linearly polarized light, detuned from the D1 transition lines. As it passes through the condensate, the two circular components of the light field experience different phase shifts, due to the circular birefringent properties of the sample. For instance σ^+ having the larger Clebsch-Gordan coefficients (larger refractive index), has the larger phase shift compared to σ^- , resulting in a rotation of the probe field polarization. The rotation angle is measured using a linear polarizer with its axis oriented at 45° with respect to the initial probe polarization, and subsequently imaged. This rotation of the light field polarization as it propagates through a medium is analogous to the Faraday effect [97, 98, 99].

We can further understand how this rotation angle (phase shift) relates to the spinor order parameter by computing the polarization contrast signal. By making a few adjustments to the equations in the previous section, the outgoing electric field in matrix form can be written as:

$$\frac{\mathbf{E}_{out}}{E_{in}} = \frac{1}{2} \begin{pmatrix} 1 & i \\ -i & 1 \end{pmatrix} \left(\begin{pmatrix} 1 \\ 0 \end{pmatrix} + e^{i\phi_0\chi_{jk}/2} \begin{pmatrix} 1 \\ 0 \end{pmatrix} - \begin{pmatrix} 1 \\ 0 \end{pmatrix} \right) \quad (3.33)$$

where $\phi_{pd} = 0$, and in the spherical basis notation, horizontally polarized light is written as $\sigma_H = (1 - 1)^\dagger/\sqrt{2}$, and the linear polarizer oriented at 45° with respect to the probe polarization is

$$\frac{1}{2} \begin{pmatrix} 1 & i \\ -i & 1 \end{pmatrix}. \quad (3.34)$$

Using the relations in Equation 3.11, the intensity distribution is

$$|\mathbf{E}_{out}|^2/|E_{in}|^2 \approx \frac{1}{2} + \frac{\phi_0}{4} (\langle\chi_{22}\rangle - \langle\chi_{11}\rangle + \langle\chi_{12}\rangle - \langle\chi_{21}\rangle) + \mathcal{O}(2), \quad (3.35)$$

keeping only the terms which are linear in ϕ_0 and χ_{jk} . Rewriting this in terms of experimental parameters, the signal measured by the camera is

$$|\mathbf{E}_{out}|^2/|E_{in}|^2 \approx \frac{1}{2} + \frac{\sigma_0\tilde{n}\gamma}{2} \left(\frac{1}{24} \frac{1}{\delta + 800} - \frac{5}{24} \frac{1}{\delta} \right) \langle F_y \rangle \quad (3.36)$$

where

$$\begin{aligned} \chi_{11} = \sigma_0\tilde{n}\gamma & \left[\frac{5}{18} \frac{1}{\delta} + \frac{1}{18} \frac{1}{\delta + 800} + \left(\frac{1}{24} \frac{1}{\delta + 800} - \frac{5}{24} \frac{1}{\delta} \right) \langle F_y \rangle \right. \\ & \left. + \frac{1}{72} \left(\frac{1}{\delta} - \frac{1}{\delta + 800} \right) \langle F_y^2 \rangle \right] \end{aligned} \quad (3.37)$$

$$\begin{aligned} \chi_{22} = \sigma_0\tilde{n}\gamma & \left[\frac{5}{18} \frac{1}{\delta} + \frac{1}{18} \frac{1}{\delta + 800} - \left(\frac{1}{24} \frac{1}{\delta + 800} - \frac{5}{24} \frac{1}{\delta} \right) \langle F_y \rangle \right. \\ & \left. + \frac{1}{72} \left(\frac{1}{\delta} - \frac{1}{\delta + 800} \right) \langle F_y^2 \rangle \right] \end{aligned} \quad (3.38)$$

$$\chi_{12} = 0 \quad (3.39)$$

$$\chi_{21} = \chi_{12}. \quad (3.40)$$

The signal is only dependent on the spin, $\langle F_y \rangle$, lacking the spin-independent contribution that occurs in the situation with a phase dot and circularly polarized light, as well as any contamination from the nematic order, $\langle F_y^2 \rangle$. The drawback of this feature, however, is the reduced signal. By using a linear polarizer, only half of the signal is being utilized. In our particular setup, we used a half-waveplate in combination with a polarizing beam splitter, which has the potential to allow us to use all of the imaging light. The difficulty comes when attempting to combine both signals at the camera. To do this both beams must come to a focus at the camera and have separation that can be easily tuned, especially if the kinetics mode of the camera is to be used [79, 52].

3.5 Imaging the vector magnetization

The technique discussed in the previous section is a method to image one component of the magnetization, but not the full vector magnetization. To do this, we need to devise a way to project each magnetization component along the imaging axis. This is done by utilizing the Larmor precession of the gas, where the precession of the magnetization periodically aligns each transverse component of the magnetization along the imaging axis. By taking a series of phase contrast images in rapid succession, we can obtain a complete description of the vector magnetization within a single experimental cycle.

3.5.1 Larmor Precession Imaging

In Larmor precession imaging, the magnetization transverse to the magnetic field precesses about the field, causing the projection of the transverse magnetization along the probe axis to vary sinusoidally in time. This results in a phase contrast signal which oscillates with an amplitude proportional to the magnitude of the magnetization. Additionally, by knowing the frequency of the oscillation, we can obtain a measure of the phase variation across the gas, where the phase is a measure of the orientation of the magnetization. Specifically, we expect the functional form of the sinusoidally varying phase contrast signal to be $A \sin(\omega_s + \phi)$, and the transverse magnetization to be described by $F_{\perp} = Ae^{i\phi}$. Imaging the longitudinal magnetization can be accomplished by applying a $\pi/2$ radio frequency (rf) pulse midway through the sequence, causing the projection of the longitudinal magnetization with respect to the imaging axis to oscillate in time, thus yielding a measure of the vector magnetization [51, 79, 3, 80].

3.5.2 Spin-Echo Imaging

The principle of Larmor precession (LP) imaging relies on the ability to image the temporal oscillation of the magnetization. The typical precession periods are $\sim \mu s$, much faster than the frame transfer time of the camera ($1 \mu s/\text{row} \times 100 \text{ rows} \approx 100 \mu s$), and must therefore be imaged at an aliased frequency, where this frequency is the difference between the sampling rate of the camera ($\approx 20 \text{ kHz}$) and the Larmor precession frequency. In fact, by accurately measuring the aliased oscillation frequency, one has an instantaneous measure of the ambient magnetic field [51].

One of the drawbacks of this method, however, is its susceptibility to shot-to-shot fluctuations in the ambient magnetic field. As the field fluctuates between experimental repetitions, the sampling frequency necessary to ensure a few temporal oscillations of the magnetization must also change. Altering the sampling frequency is very easy, but the ease of determining when this must occur is dependent on whether there is a substantial magnetization signal present to help determine if the LP frequency has drifted away from optimal settings.

To alleviate the complications associated with the field fluctuations, we have developed a novel scheme which obtains a direct snapshot of the vector magnetization within just three images by applying spin-echo rf pulses between images [100]. Specifically, we apply the first imaging pulse which sends linearly along the \hat{y} axis. As the light propagates throughout the atoms, the circular birefringence of the sample causes a rotation of the probe polarization. Measuring the rotation angle of the light polarization resolves one transverse component of the column-integrated magnetization, $\tilde{\mathbf{M}}(\rho)$. Following a precisely timed delay, t_0 , a π rf pulse is applied to the sample, reversing the direction of Larmor precession. A time delay of t_0 following the π rf pulse results in the already transverse component of the magnetization to be aligned along the imaging axis. A second imaging probe pulse is applied to the sample after an additional delay of $t = t_0 + 1/4t_{LP}$, where t_{LP} is the Larmor precession period. This then records the second component of the transverse magnetization. The longitudinal magnetization is measured by applying a third imaging pulse after a properly timed $\pi - \pi/2 - \pi$ rf pulse sequence. The appeal of this technique is that it is insensitive to shot-to-shot fluctuations in the magnetic field and is able to function reliably in the presence of > 10 kHz variations in the Larmor precession rate between experimental runs.

Magnetic Field Fluctuations

The magnitude of the background magnetic field at the location of the atoms fluctuates by ≈ 10 kHz throughout the peak work hours of the day. The lab is located across from the hall from the primary source of the fluctuations, the elevator. The elevator with its iron counterweight is capable of altering the DC magnetic field in the room, as seen in Figure 3.1. To get a more quantifiable measure of these fluctuations, we used a three-axis magnetometer from Honeywell (Part Number HMC2003), specifically aimed at measuring small magnetic fields, with a dynamic range of $40 \mu\text{G}$ - 2G . Using this magnetometer, we monitored the DC magnetic field in our lab over the weekend. Dominating the measurement are $5 - 10$ mG fluctuations that occur during the peak working hours of Birge, mainly between 8 am to 9 pm. Given the sporadic behavior of the magnetic field over the weekend and in the late evenings, we were able to rule out other possible sources such as BART (local subway system).

In order to apply accurate rf pulses, and accommodate the fluctuating magnetic field, we decided to use rf pulses with a large Rabi frequency, Ω_R , such that the ambient magnetic field appears constant during the application of an rf pulse. This is accomplished by an rf pulse with a short pulse duration and large amplitude. Our typical experimental parameters include working at a magnetic field of 265 mG (187 kHz). The rf pulses are generated using an Stanford Research System function generator (SRS DS345). To create

π rf pulses, we operate the SRS in “Burst Mode” at the following settings: function, sine; amplitude, -6.5 dBm; counts, 4. These settings yield an rf Rabi frequency of $\Omega_R \approx 25$ kHz, larger than the shot-shot magnetic field fluctuations we observe.

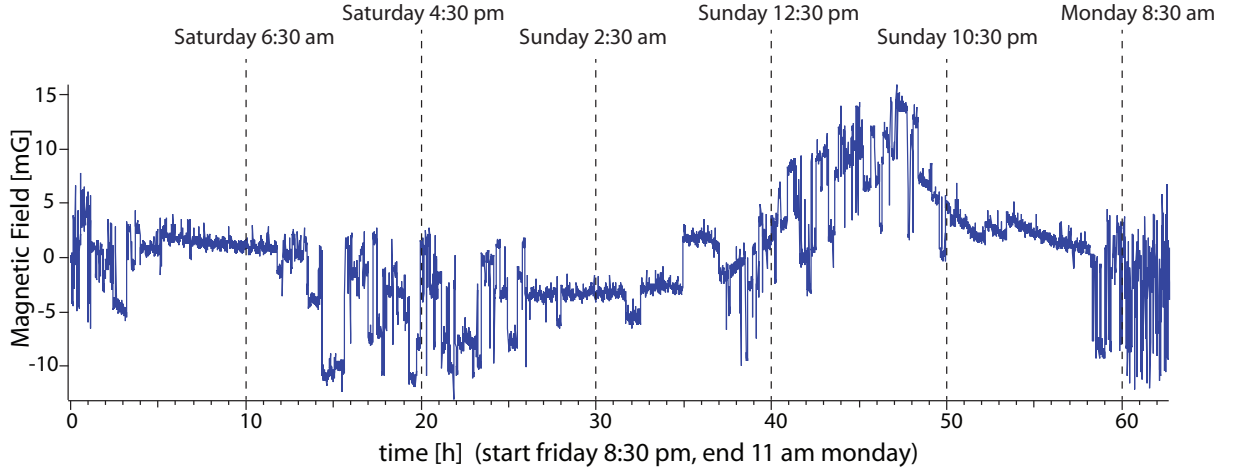


Figure 3.1: Measurement of magnetic field over the weekend. The sensor used is a three-axis magnetometer. Dominating the measurement are $\sim 5 - 10$ mG fluctuations that occur during the peak working hours of Birge, mainly between 8 am to 9 pm. We attribute the cause of these fluctuations to the elevator, located ≈ 7 m from the atoms/sensor.

Ramsey Sequence in Time-of-Flight

To test the validity of the spin-echo technique, we first performed a Ramsey $\pi/2 - \pi/2$ rf pulse sequence to characterize the influence of external magnetic fields on the evolution of spinor condensates imaged in time-of-flight [101, 102, 103]. We begin with spin polarized condensates in the $\psi_{mf} = (\psi_+, \psi_0, \psi_-) = (0, 0, 1)$ state. Next, we apply a resonant $\pi/2$ rf pulse, creating a superposition state, $(\psi_+, \psi_0, \psi_-) = (-1/2, i/\sqrt{2}, 1/2)$ which can then undergo Larmor precession about the background magnetic field. The immediate application of another $\pi/2$ pulse will transfer all of the population to the $(\psi_+, \psi_0, \psi_-) = (1, 0, 0)$ state. The addition of a delay time between the two pulses results in the spin-1 analog of the Ramsey experiment for spin-1/2 particles (Figure 3.2(a)), which is sensitive to the phase evolution of the system [103]. The last $\pi/2$ pulse transforms the phase information into population information, which is then accessible for detection. We measure the population within the magnetic sublevels by releasing the atoms from the optical trap, applying a magnetic field gradient to spatially separate the atoms and then image them using resonant light. The typical TOF time is 25 ms.

Following the initial $\pi/2$ pulse, the populations are allowed to evolve for times up to 100 μ s. This is shown in Figure 3.2(b-top). The resulting population in the $|F = 1, m_F = -1\rangle$ state is random, showing no oscillatory dependence on the time between $\pi/2$ rf pulses. We attribute this random dependence on the evolution time to fluctuations in the background magnetic field between experimental runs. The magnitude of these fluctuations,

~ 10 kHz, is approximately 5% of the Larmor precession frequency. To understand the impact of these fluctuations on the Ramsey sequence, we can make a few simple estimates. For instance, in one iteration of the experiment, during the time between rf pulses, the atoms may undergo as many as 18.73 revolutions in $100 \mu\text{s}$, assuming an ambient magnetic field of 267 mG. However, if the ambient magnetic field changes by 1-2%, increasing to 270 mG, the number of revolutions becomes 18.90 for the same time delay between rf pulses. Since only the fractional part of the number of revolutions is relevant in determining the populations with the Zeeman sublevels, in this particular example a 1% field uncertainty in the magnetic field leads to a 25% error in the accrued phase. In general, small magnetic field uncertainties can lead to random accrued phases, and hence random populations in the Zeeman sublevels.

Here, the addition of a π rf pulse between the $\pi/2$ rf pulses is used as echo technique [100]. Similar to above, the first $\pi/2$ rf pulse rotates the magnetization into the transverse plane, which then undergoes Larmor precession. After a time τ_0 , a π rf pulse is applied, reversing the direction of precession of the magnetization. The final $\pi/2$ rf pulse is subsequently applied τ_1 after the π rf pulse, where the time between the $\pi/2$ rf pulses is kept constant, $\tau_0 + \tau_1 = 150 \mu\text{s}$. This allows for exact cancellation of the accrued phase up to the difference in τ_1 and τ_0 . The phase evolution of the system is now sensitive to $\tau_0 - \tau_1$ which is $\sim 5 \mu\text{s}$, comparable to $2\pi/\Omega_L$. The effect of this is shown in Figure 3.2 (b-bottom), where coherent oscillation in the population of the $|F = 1, m_F = -1\rangle$ state is observed.

Transverse Magnetization

Given the success of the rf pulse sequence measured in TOF, we would next like to determine whether this technique can accurately and reliably extract each component of the transverse magnetization. To do this we use the polarization contrast technique to extract the transverse magnetization. In order to differentiate between the two transverse components, we test this technique using a helical spin texture described by $\mathbf{F} = \cos(\kappa z + \omega_L t)\hat{x} + \sin(\kappa z + \omega_L t)\hat{y}$ where $\kappa = (g_F \mu_B / \hbar)(dBz/dz)\tau\hat{z}$ is the wave vector. Compared to a homogeneously magnetized gas, the helical spin texture has the advantage that the two transverse magnetization components, F_x and F_y can be easily distinguished, as they are $\pi/2$ out of phase.

To make the helical spin texture, we use a combination of rf pulses and a transitory linear magnetic field gradient. Following the creation of a spin-polarized ^{87}Rb condensate of $|F = 1, m_F = -1\rangle$ state [104], we prepare transversely magnetized condensates by the application of a resonant $\pi/2$ rf pulse in a static magnetic field of $B = 267$ mG oriented along the \hat{z} axis. The magnetization undergoes Larmor precession in the $\hat{y} - \hat{x}$ plane at the Larmor frequency $\Omega_L = 2\pi \times 187$ kHz. Next a transitory magnetic field gradient, dBz/dz is applied for 20 ms causing the magnitude of the magnetic field to vary spatially along the long axis of the condensate. This causes atoms at different axial positions to precess at different rates, resulting in a magnetization pattern that varies sinusoidally along the condensate length.

We image the spin helix using a similar procedure to the spin-1 analog of the Ramsey sequence discussed above. To do this, we replace each $\pi/2$ rf pulse with an imaging probe pulse. The application of the first imaging pulse makes an instantaneous mea-

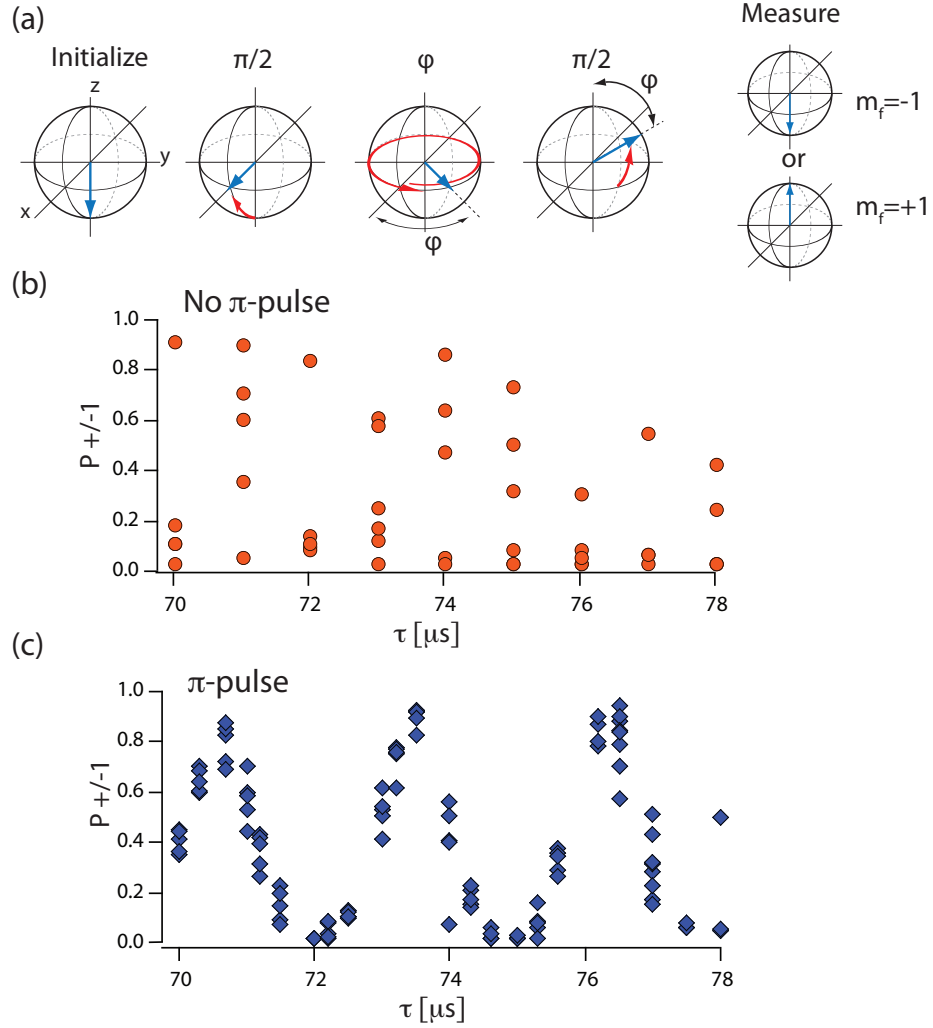


Figure 3.2: (a) Time-of-flight Ramsey sequence to measure the coherent oscillation of the Zeeman sublevel population as a function of the elapsed time. A resonant rf $\pi/2$ pulse is applied to a spin polarized BEC, creating a superposition of the Zeeman sublevels at $\tau = 0$. Following a variable evolution time, during which the populations evolve freely, a second resonant rf $\pi/2$ pulse is applied, projecting the evolution of the populations into a population difference of the spin components from the initial spin composition. (b) Time-of-flight Ramsey sequence with an additional resonant rf π pulse inserted between the two rf $\pi/2$ pulses.

sure of one transverse magnetization density component, which we label as \tilde{M}_x , where $\tilde{M}_{x,y} = g_F \mu_B \tilde{n} F_{x,y}$, and \tilde{n} is the column-integrated density. Following a time τ_0 , a π rf pulse is applied, reversing the direction of Larmor precession. Waiting an additional time $\tau_1 = \tau_0$ after the π rf pulse returns the system to its original state where an image of the magnetization would return an image identical to the first. However, by allowing for

$\tau_1 = \tau_0 + \tau_{LP}/4$, the second transverse component, \tilde{M}_y will be imaged. Thus, by tuning $\tau_1 - \tau_0 = n \times \tau_{LP}/4$, we are able to accurately determine which transverse magnetization component we image, \tilde{M}_x for n even and \tilde{M}_y for n odd. This is shown in Figure 3.3.

Longitudinal Magnetization

To image the longitudinal magnetization (\tilde{M}_z), we follow a slightly different procedure. Here we create a longitudinally magnetized gas, by omitting the first resonant $\pi/2$ pulse, thus leaving the gas in the $|F = 1, m_F = -1\rangle$ state. Next, the gas is imaged using a $\pi - \pi$ rf pulse sequence as described above, but with an additional $\pi/2$ rf pulse, occurring during the third probe pulse. To lessen the extent of losses due to scattering with the probe field, the probe light is off during this third pulse (see Figure 3.4).

The application of the $\pi/2$ rf pulse during the imaging sequence corresponds to a rotation of the spin ensemble, with the longitudinal and a component of the (former) transverse magnetization now precessing about the magnetic field. Specifically,

$$\mathbf{F}_\perp = \cos(\omega_L t) F_x + i \sin(\omega_L t) F_y, \quad (3.41)$$

where as now the transverse magnetization is described by

$$\mathbf{F}'_\perp = \cos(\omega_L t) F_{x,y} + i \sin(\omega_L t) F_z, \quad (3.42)$$

where the prime is used to distinguish the transverse magnetization before and after the $\pi/2$ rf pulse, $F_{x,y} = aF_x + bF_y$ is a component of the transverse magnetization before the $\pi/2$ rf pulse, and F_z is the longitudinal component. Thus, by adjusting the timing of the rf pulse, we can determine in which imaging frame we are sensitive to F_z . In Figure 3.4 we measure the amplitude of the phase contrast signal as a function of the τ_3 , which determines the start of the $\pi/2$ rf pulse. The signal follows the expected sinusoidal oscillation between $F_{x,y}$, where the signal is at a minimum, having no initial transverse magnetization, and F_z where the magnitude of the signal is at a maximum, with a frequency consistent with $\tau_{LP}/2 \approx 2.5 \mu\text{s}$. We fit this oscillation and extract the appropriate timing for the $\pi/2$ pulse. In this specific case, the time we chose for the pulse occurred at $290.9 \mu\text{s}$.

Drawbacks

Although spin-echo imaging has many attractive features, it also has a few drawbacks. In particular, this method is susceptible to interference fringes. These fringes are due to the coherence of the laser beams used to image the atoms and mechanical vibrations of the optical elements. For instance, each image is computed from

$$\text{Signal}(x, z) = \frac{I(x, z)_a - I(x, z)_d}{I(x, z)_b - I(x, z)_d} \quad (3.43)$$

where $I(x, z)_a$ is the intensity of the probe field having passed through the atoms, $I(x, z)_d$ is the background signal with no light on the detector, and $I(x, z)_b$ is the intensity of the probe field with no atoms. If there were no mechanical vibrations, then the fringes from $I(x, z)_a$ and $I(x, z)_b$ would be identical and there would be no interference fringes in the signal

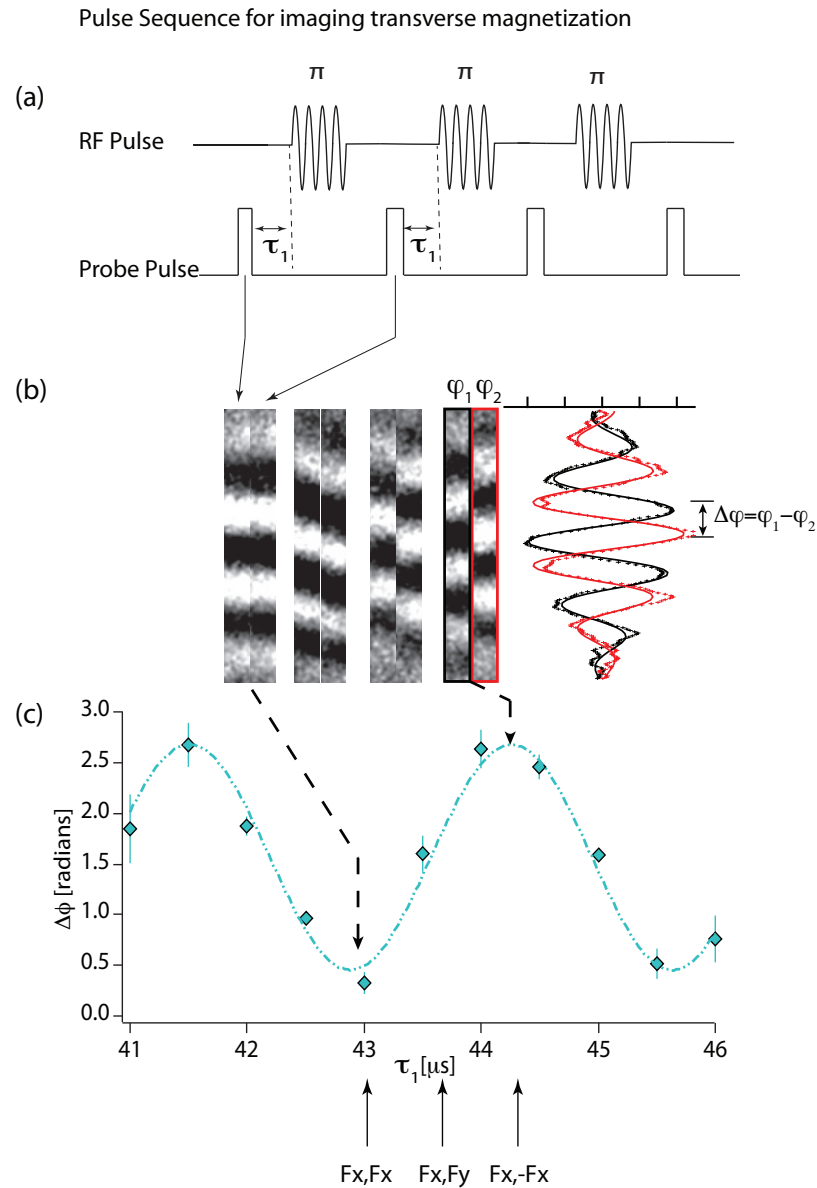


Figure 3.3: a) Spin-echo sequence to measure the transverse magnetization profile. (b) Sequential images of spin textures for different times between τ_1 times. As τ_1 is changed, the phase difference between consecutive images for a single experimental run varies from imaging F_x, F_x to F_x, F_y or $F_x, -F_x$. A one dimensional profile is shown to better illustrate the π phase shift between image on the right. The solid lines are the fit and the dots are the raw data. (c) Plotted phase difference between consecutive images for each τ_1 . The signal oscillates between $0 - \pi$ at a period that is consistent with $\tau_{LP}/2 = 2.5 \mu\text{s}$. The data is the average of 5 consecutive images with one experimental run and error bars are statistical.

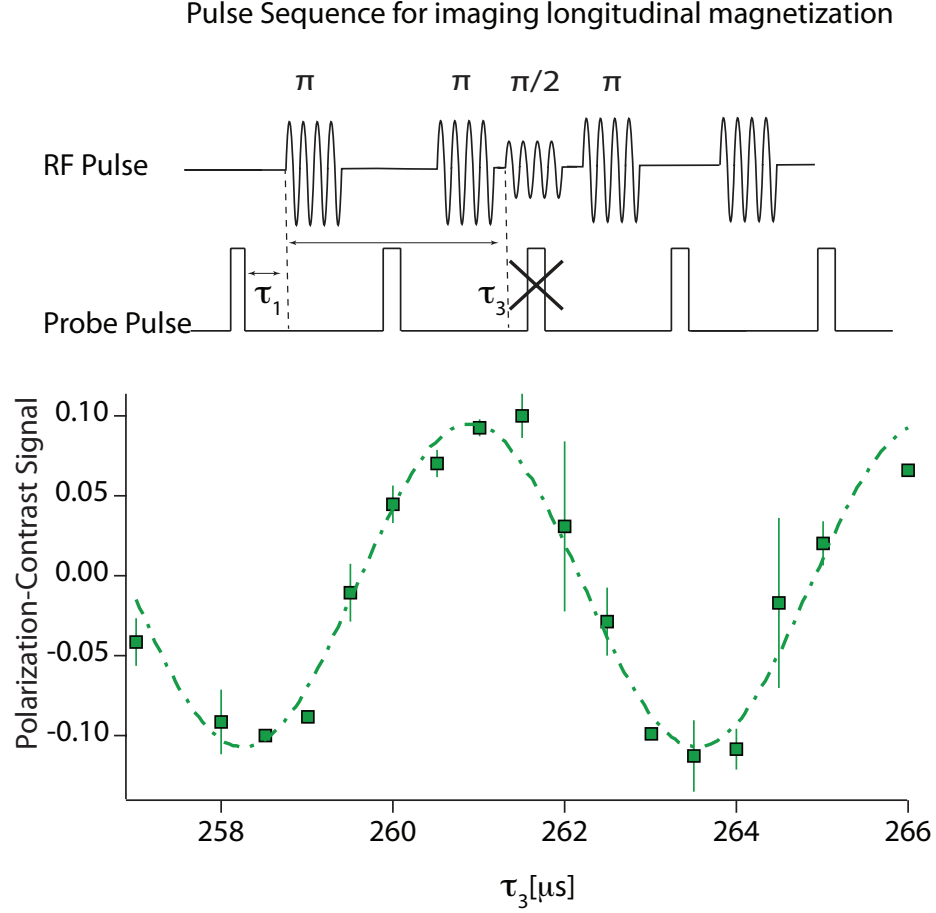


Figure 3.4: Spin-echo sequence to measure longitudinal magnetization and the phase shift as a function of the delay time between the $\pi/2$ and π rf pulse sequence. The signal oscillates between $0 - \pi$ at a period that is consistent with $\tau_{LP}/2 = 2.5 \mu s$.

(*Signal*). However, mechanical vibrations of the optical elements cause slight differences in the interference fringes for $I(x, z)_a$ and $I(x, z)_b$ resulting in a signal contaminated with interference fringes.

To reduce the effect of interference fringes in the signal, we have developed a procedure for isolating and removing the fringe pattern from each image. We do this by comparing nearly identical copies of M_z and $M_{x,y}$, where the distinguishing feature between the copies is an overall reduction in the signal (due to light scattering). The repeated copies of the magnetization is a fortunate consequence of spin-echo imaging. Simply, we create an image copy with no fringe, I_{NF} , modeling it as

$$I_{NF} = M_z - M_{z,2}, \quad (3.44)$$

where $M_{z,2}$ is the second occurrence of M_z . We then create a rescaled version of M_z that we define as

$$M'_z = a \times I_{NF}, \quad (3.45)$$

and a fringe image as

$$I_F = F_z - M'_z. \quad (3.46)$$

We use the difference between I_F and M_z as a figure of merit (FOM) that we subsequently minimize, the result of which should give the appropriate value of a . This is done by taking the spatial Fourier transform of each and minimizing the spectral power at the spatial frequency of the interference fringe pattern. The result of this subtraction routine is shown in Figure 3.5. There, M_x , M_y , and M_z have significant interference fringes mostly likely due to dust on an optic which has two different positions during the bright field and atom field, but by subtracting the appropriate fringe pattern from each image, we are able to achieve nearly fringe-free images. There is an overall reduction of M_z after we have removed the fringes, partly due to improper scaling of the images. We are able to reduce this by using the duplicate copies of $M_{x,y}$ to determine a fringe image and combining this with the result from M_z .

RF π Pulses The successful implementation of spin-echo imaging requires fine control over the time sequence of the rf pulses as well as a well a carefully tuned π rf pulse. This is necessary to ensure that we extract the vector magnetization profile, as opposed to a single component of the magnetization.

We are able to determine the optimal parameters of the rf pulses by applying several π rf pulses to the atoms and imaging the population decomposition within the magnetic sublevels. The populations within the sublevels are resolved using Stern-Gerlach analysis where an inhomogeneous magnetic field spatially separates the components within the $F = 1$ manifold [79, 52]. An optimized image is shown in Figure 3.6 (right). After the application of four π rf pulses, essentially all the population remains in the $m_F = -1$ state. The careful tuning of the rf pulses is accomplished by adjusting the amplitude of the rf pulse. However, if the amplitude is not optimized, a small amount of population will be observed in the $m_F = 0, 1$ state, as seen in the Figure 3.6 (left). When applying many π rf pulses in a row, the population within the Zeeman sublevels becomes very sensitive to the amplitude of the rf pulse. The difference in amplitude between the two images in Figure 3.6 is 0.3 dBm.

Future Prospects

The proof-of-principle demonstration of spin echo imaging as a technique to image the vector magnetization has not been fully utilized. By extracting the vector magnetization in just three imaging frames, we have the capability to implement dual-pulse imaging, where we can image the vector magnetization as a function of time while using the same atomic sample (within a single experimental cycle). This would give us the ability to trace the dynamics of a single vortex, domain, or domain wall. Such a scheme would be sensitive to atom loss during the imaging sequence, and steps would need to be taken to reduce this effect.

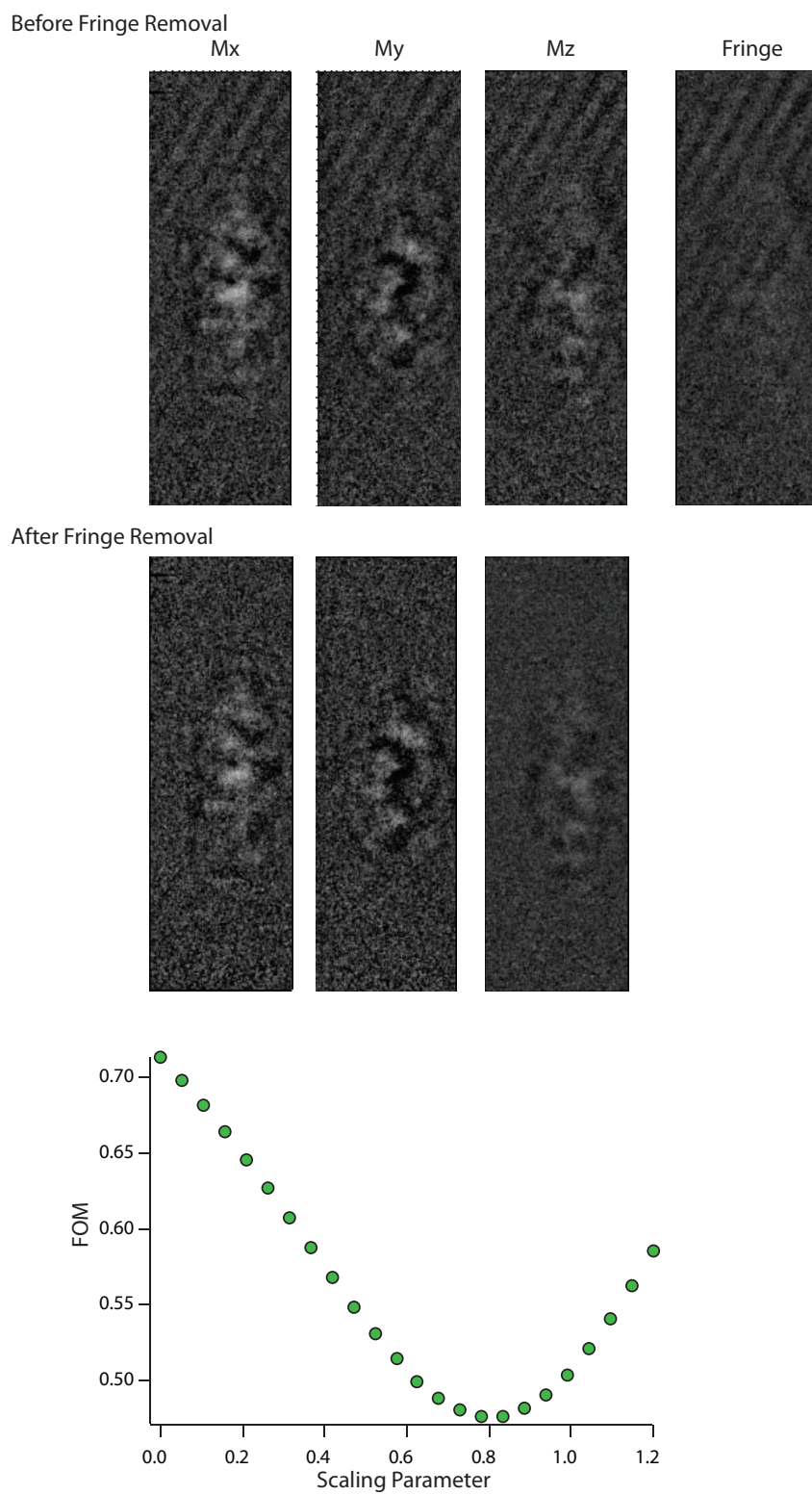


Figure 3.5: Magnetization images before and after removing interference contamination.

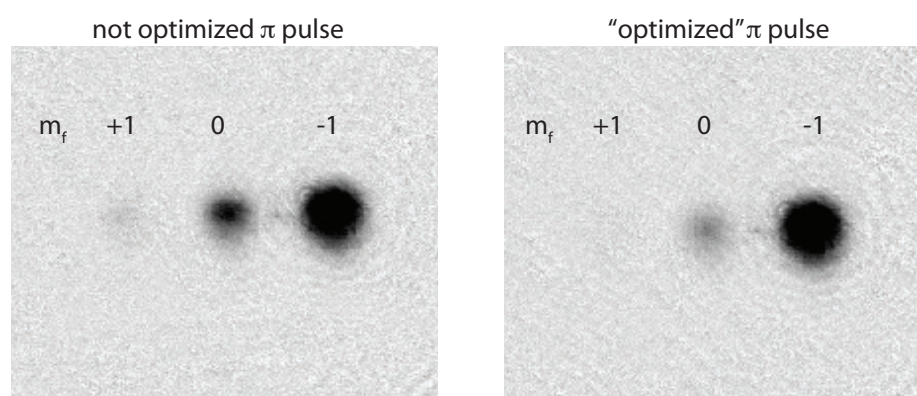


Figure 3.6: Time-of-flight image of Zeeman sub level population after the application of 4 consecutive π rf pulses.

Chapter 4

Design of a High Resolution Imaging System

Presented in this chapter is the design, implementation and characterization of a 1 μm resolution imaging system.

4.1 Design of a high resolution imaging system

Since the observation of the first quantum degenerate gas, the field of ultracold atomic gases has expanded rapidly, with their primary use as a tool for mimicking condensed-matter phenomena [8, 9]. Necessary in these studies is a highly versatile toolbox for observing these degenerate gases. The most popular technique for imaging ultracold atomic gases has been time-of-flight (TOF) absorption imaging. While this method has the advantage of its inherent simplicity, providing quantitative information about the momentum distribution of the sample, it is insensitive to the spatial profile of the sample. Recently, however, *in-situ* imaging (“in position” imaging) with high spatial resolution has become the imaging technique of choice in ultracold atomic physics, allowing for space- and time-resolved measurements [41, 105, 43]. Presented in the following sections is the design and characterization of a 1 μm imaging system, followed by the use of spinor condensates as an *in-situ* test pattern.

4.1.1 Design Criteria

The design criteria for this imaging system takes into account the future experimental pursuits as well as spatial constraints due to the experimental apparatus. The design criteria for the high resolution imaging system are listed below:

- Working distance of 13 mm, constrained by the 25 mm-sized glass cell.
- Additional optics to compensate for the optical properties of the glass cell.
- Large field of view capable of imaging the entire spinor gas ($\sim 200 \mu\text{m}$) with few aberrations.

- Resolution comparable to the spin healing length ($\sim 1.5 \mu\text{m}$) in order to distinguish individual spin domains.
- Flexible imaging system. For instance, the ability to image the atoms in the trap as well as after some free fall.
- Reproducibility when displacing the objective.
- Small optical chromatic shift. The experimental apparatus is also designed to make ultracold samples of lithium. Thus, to be compatible with imaging lithium, which has resonant absorption lines at 670 nm, a small chromatic shift is desirable.

Attempting to satisfy these criteria, a two element objective was designed with a theoretical resolution of $1 \mu\text{m}$, consisting of an aspheric and meniscus lens.

4.1.2 Imaging Objective

Design Procedure

The design of the imaging system simplifies significantly when starting with a high quality lens. Ideally, the lens should be free of spherical aberrations up to a fairly high numerical aperture (i.e. $\text{NA} \sim 0.5$), where NA is a measure of the light-gathering ability of the lens, and a working distance which enables sufficient room for adjustment. As a starting point, we began with the simplest setup, a commercially available aspheric lens from Thorlabs and modeled it using OSLO, an optics design software program. According to OSLO, the aspheric lens (see below) is diffraction limited over its entire diameter up to a numerical aperture $\text{NA} = 0.52$.

Upon inserting the glass cell (Hellma Borosilicate) with a thickness of 2.5 mm and a refractive index of $n = 1.46$ at 780 nm into OSLO, the aspheric lens is only diffraction limited to $\text{NA} \approx 0.2$, approximately half the resolution without the glass cell. This is attributed to aberrations introduced by the glass cell. To compensate these aberrations, a general second lens is introduced into OSLO, parameterized by (Figure 4.1):

- two radii, $r1$ and $r2$
- thickness, $t1$
- two distances, $d1$ (asphere to lens) and $d2$ (lens to glass cell)
- lens material.

Since the exact specifications of the lens are unknown, an optimization routine in OSLO can be used to determine these parameters. As a first overall simplification, the lens material was set to BK7, in order to ensure a high probability of finding a likely candidate. Next, due to the finite working distance of the asphere, a small value for $d1$ was necessary, thus $d1 = 2$ mm was fixed. Finally, $t1 = 3$ mm was set as an initial trial thickness. Once a satisfactory solution is found by manually adjusting the lens parameters, OSLO can optimize the other free parameters by minimizing the certain aberration coefficients. This is conveniently

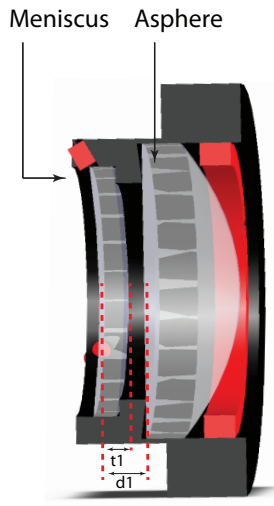


Figure 4.1: Imaging objective and mount. The aspheric lens is held in place with a retaining ring. The meniscus is held with three set screws (not easily seen here). In this configuration, the angle of the combination can be adjusted with respect to the glass cell and imaging axis (defined by the propagation axis of the imaging light) and in addition, the set screws allow for the angle between the meniscus and asphere to be tuned.

done using OSLO Premium edition and running the spot size/ wavefront error function. A solution can always be found if one allows enough parameters to be varied. In principle, this can be difficult given the constraints of the apparatus and aspheric lens. Fortunately, the optimization routine returned reasonable suggestions for r_2 , with $r_1 \approx r_2$ and a focal length $f = 1000$ mm. Next, the task at hand was to filter the huge database of commercially available lenses in search of a lens with similar specifications. A reasonably good match was quickly found at JML optical.

Asphere

The aspheric lens used is a large-diameter asphere from Thorlabs (Part# AL3026-B). It is made using S-LAH54 glass, has an effective focal length of 26.0 mm, a NA= 0.52, and a working distance of ≈ 20 mm.

Meniscus

The purpose of the meniscus lens is to compensate the distortion due to the glass cell (Hellma Borosilicate). The meniscus used is from JML optical, part # CMN11258. It is made using BK7 and has a focal length of $f \approx 1000$ mm.

4.1.3 Imaging Resolution

Resolution is often defined as the separation at which two discrete objects can be easily discerned or the frequency at which the modulation transfer function (see below)

falls below some threshold [93, 94]. Using either definition, resolution is a single-number performance specification, and as such, is more convenient but less precise than defining it via a function, such as the modulation transfer function (see below).

Before we can discuss the performance of the imaging system used here, we briefly review some terminology that will be used in the next few sections. For a more comprehensive review of the concepts discussed below, I refer the reader to the following articles and references [106, 94, 93, 107, 108, 109, 110].

Numerical Aperture The NA of an objective is defined as $n \sin \alpha$, where α is the half angle of the maximal cone of light (with its tip on the image plane) that can enter or exit the lens, and n is the refractive index of the medium between the objective front and the object, which in most cases is typically air with $n = 1.0$.

The resolution of an objective is defined as the smallest distance between two points on a specimen that can still be distinguished as two separate objects, also known as the Rayleigh criterion. The relation between the imaging resolution, d_{res} and NA is

$$d_{res} = \frac{0.61\lambda}{n \sin \alpha}, \quad (4.1)$$

where λ is the wavelength of light used. From this equation it is easy enough to see that a small imaging resolution can be achieved by increasing the angle α (by increasing the diameter of the lens while keeping the focal length fixed), decreasing λ , or increasing the refractive index of the medium between the objective front and the object. In practice, commercially available objectives that are reasonably priced are limited to $NA \lesssim 0.6$ and the wavelength of light is limited by the atomic species used. However, increasing the refractive index is an alternative route to a larger imaging resolution.

F-number F-number, like numerical aperture, is another term which describes the light-gathering power of a lens system. It is defined as the ratio of the lens focal length to the diameter of the entrance pupil and is related to the numerical aperture as follows,

$$NA = n \sin \alpha = n \sin \left[\arctan \left(\frac{D}{2f} \right) \right] \quad (4.2)$$

$$\approx n \frac{D}{2f} \quad (4.3)$$

$$f/\# = \frac{f}{D} \quad (4.4)$$

$$\approx \frac{1}{2NA}, \quad (4.5)$$

where D is the diameter of the entrance pupil (lens diameter commonly), f is the focal length of the lens, and the refractive index is approximated as one.

Modulation Transfer Function The modulation transfer function (MTF) is a useful measure for objectively characterizing the performance of optical systems. It is a measure of an imaging systems' frequency response, determining how faithfully a lens reproduces

the detail of an object [107, 108, 109, 110]. Whereas NA and $f/\#$ are often used to specify the performance of an imaging system, the MTF provides more complete performance information, specifying not only resolution, but also the response to an entire spectrum of length scales. As we will see below, knowledge of the performance at intermediate spatial frequencies as well as the limiting resolution are imperative to our studies of spinor condensates.

The MTF is defined as the magnitude of the response of an optical system to sinusoids of different spatial frequencies, with values ranging between zero and one, and is typically plotted versus spatial frequency. In practice, higher values of the MTF at a specific spatial frequency equate to the ease at which that spatial frequency will be imaged by the lens. It can be computed theoretically (assuming diffraction limited optics) by calculating the autocorrelation function of the exit pupil, which in most situations is a circle the size of the objective. For a circular aperture, the diffraction limited MTF is

$$\text{MTF} = \frac{2}{\pi} \left(\arccos(x) - x\sqrt{1-x^2} \right), \quad (4.6)$$

where x is the normalized spatial frequency defined as

$$x = d/d_{res} \quad (4.7)$$

where d is the absolute spatial frequency and d_{res} is the incoherent diffraction limited spatial frequency defined in Eq. 4.1. This curve defines the upper limit to the performance of an imaging system.

Point Spread Function The point spread function, like the MTF, is a measure of the response of an imaging system, but to a point object. In other words, it is the Fourier transform of the MTF, existing in the real space domain, as opposed to the frequency domain. It parameterizes the blurring of the object in the image plane; the image is the convolution of the PSF with the object. The narrower the PSF, the smaller the extent of blurring or spreading of the object.

4.2 Characterizing the lens on the bench

Although numerous simulations can be conducted to test the response of an imaging system, it is often good practice to also reproduce these results on a test bench, prior to its insertion into the experimental apparatus.

Proper alignment is critical in high NA imaging systems. The order in which optics are aligned is determined by their relative position to the camera, beginning with the lens nearest to the camera and ending with the objective. A step-by-step procedure for alignment of this imaging system is described in Appendix D.

4.2.1 Test Pattern

A 1951 USAF resolution test chart was used to characterize the performance of the objective. The chart consists of square black bars of precisely defined width and spacing.

The pattern is organized into groups, numbering between -2 to 9, where groups 8 and 9 are available only on the high resolution test pattern. Within each group, there are between 3 to 6 elements, where within a single group increasing element number indicates increasing spatial frequency. The spatial frequencies range from from 645 lp/mm to 0.25 lp/mm, where lp (line-pairs) denotes the distance between adjacent black bars. An image of the test pattern is shown in Figure 4.2.

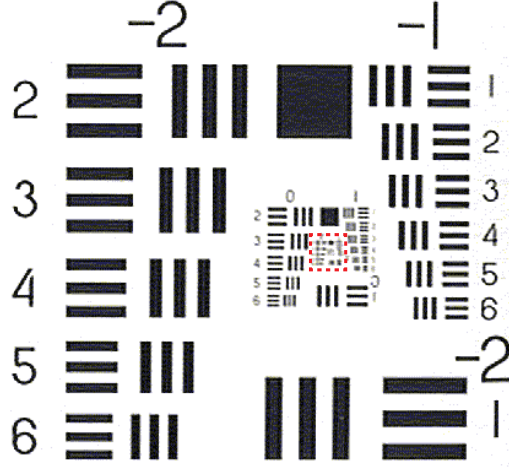


Figure 4.2: 1951 USAF resolution test chart. The inner red box highlights the bars that are used to test the asphere-meniscus imaging system.

4.2.2 Experimental MTF

Using the 1951 test pattern, light at 780 nm (generally an incoherent source is ideal) was used to illuminate the test pattern and imaged using an AVT Guppy Firewire camera (Edmund Optics Part #NT59-242). The MTF curve was obtained by measuring the contrast for a range of spatial frequencies. The contrast is defined as

$$C(f) = \frac{V_{max} - V_{min}}{V_{max} + V_{min}} \quad (4.8)$$

where V_{max} is the maximum of the spatially varying signal and V_{min} is the minimum value. $C(f)$ is extracted by fitting test pattern image to a model. Specifically, each pattern of bars is fit to a two-dimensional sine wave,

$$f(x, y) = a + b \sin(c \cdot x + d \cdot y + e). \quad (4.9)$$

This form of the model allows for possible spatial tilts of the test pattern to be taken into account, as well as allowing the information for each set of bars to contribute to the contrast measurement as opposed to a single row or column of pixels. From this, the contrast is redefined in terms of the fit function parameters,

$$C(f) = \frac{V_{max} - V_{min}}{V_{max} + V_{min}} = b/a. \quad (4.10)$$

The MTF, however is defined as the response to a sinusoidally varying signal, thus, we need to convert the spatially varying square pattern into a sinusoid. The Fourier series for a square wave function of length L is

$$f(x) = \frac{\pi}{4} \sum_n \frac{1}{n} \sin\left(\frac{n\pi x}{L}\right). \quad (4.11)$$

Thus, by fitting the test pattern to a sine wave, the contrast is overestimated by a small factor, so $C(f)$ must be scaled by $\pi/4$ to compensate for this overestimate.

An MTF curve was extracted for three different configurations:

1. Aspheric lens in a commercial lens mount, with no glass cell, and no meniscus lens. Doing this allowed us to eliminate possible sources of error from the glass cell and meniscus. The commercial mount is less obstructive than the custom-built mount, which limits the $NA \approx 0.43$ due to the 1" retaining ring. In this mount the full aperture of the lens is available, and the $NA \approx 0.52$.
2. Aspheric lens in the custom-built mount, no glass cell, and no meniscus. The purpose of this was to experimentally verify the reduced aperture of the lens due to the retaining ring.
3. Aspheric lens, meniscus lens and glass cell. This duplicates our experimental setup.

In order to extract an MTF curve that could be compared with theory, the entire spectrum of spatial frequencies needs to be imaged. The lowest spatial frequency provides a reference for unity. As can be seen in Figure 4.3, imperfections in the image due to etaloning, dust, or a noisy beam profile can reduce the overall contrast measured. Furthermore, the position of the focus is most sensitive to the smallest test pattern markers, thus necessitating the need to image both high and low spatial frequencies.

Here, a relatively high magnification ($M \sim 25$) is needed in order to resolve the markers with the highest spatial frequency (elements within group 9). Given a CCD pixel size of $\approx 18 \mu\text{m}$ and a spatial frequency of 645 cycles/mm ($\approx 1.5 \mu\text{m}$), at a magnification of 10, a single pixel would correspond to $1.8 \mu\text{m}$ in the imaging plane. This means that a test pattern cycle (black bar+no bar) would be mapped to one pixel, resulting in an inability to measure contrast at these frequencies, due to pixelation. For the measurements made here, each pixel corresponded to half of the theoretical imaging resolution, $\frac{1}{2}d_{res} \simeq 0.5 \mu\text{m}$.

Lens Performance and Resolution

The MTF values for the aspheric lens in the un-obstructive commercial lens mount are generally higher than the values where the aspheric lens is in the custom objective mount. We attribute this degradation in the performance of the objective to the retaining ring in the custom mount which slightly reduces the full aperture. Extrapolating the curve to an MTF which is 10% of its initial value, yields a spatial frequency of $\approx 1 \mu\text{m}$, in agreement with the Rayleigh criterion. The MTF of the asphere in the custom mount is comparable to the objective and glass cell combination (asphere and meniscus), confirming that the meniscus is compensating the presence of the glass cell. Extrapolating these curves to 10%

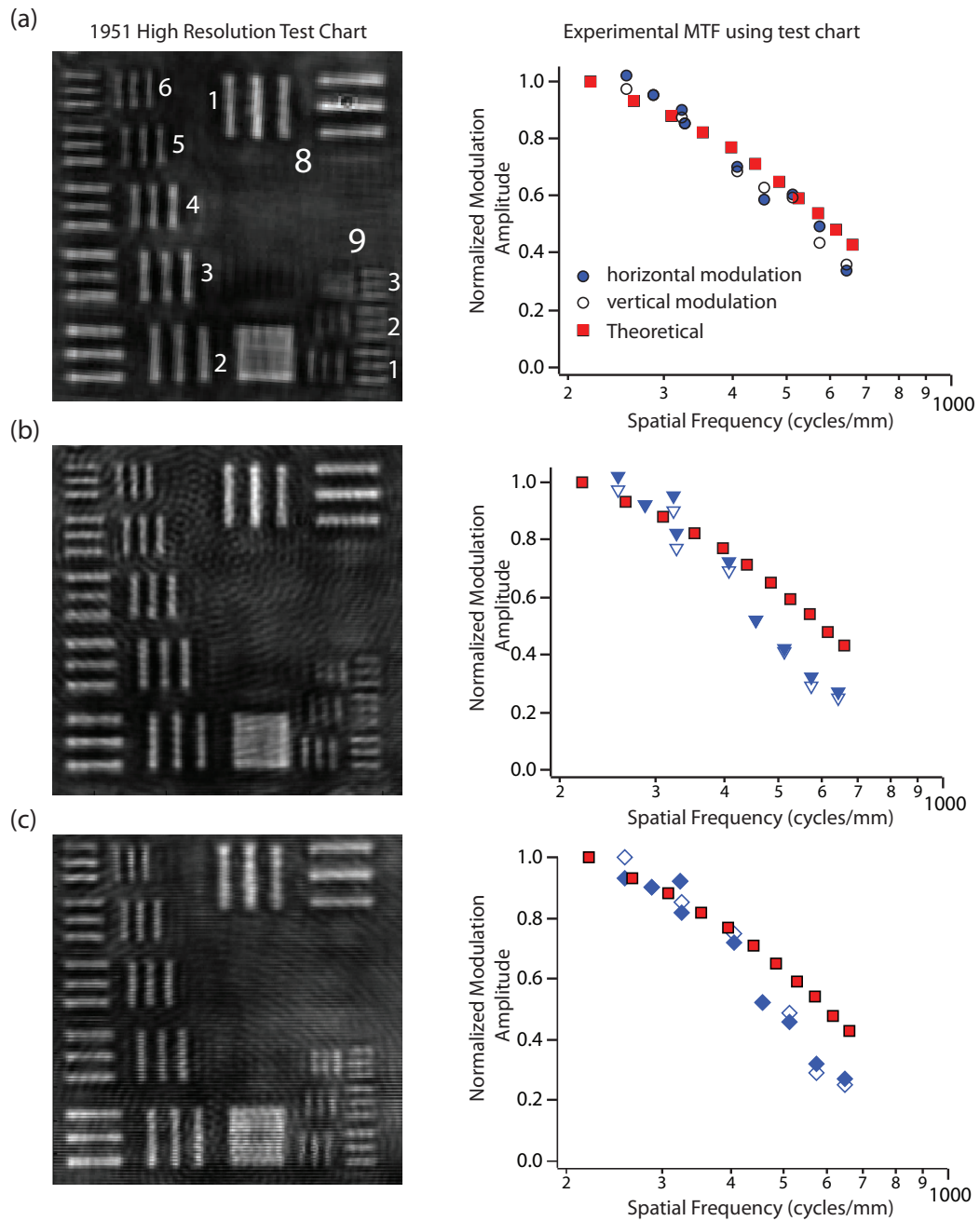


Figure 4.3: Test pattern and extracted MTF curves for three configurations: (a) aspheric lens in unobstructed mount, with $NA \approx 0.5$, (b) aspheric lens in custom-built mount with $NA \approx 0.43$, and (c) aspheric-meniscus combination with glass cell with $NA \approx 0.43$. The bars range from 250 cycles/mm (group 8 element 1) to 645 cycles/mm (group 9 element 3). Due to the high magnification and relatively small sensor on the CCD, only groups 8 and 9 are able to be seen. A area of the test pattern can be imaged by using a smaller magnification.

of the initial MTF value results in a resolution of $\approx 1.2 \mu\text{m}$. This yields an $\text{NA} \simeq 0.4$. Furthermore, there appears to be little to no astigmatism. The vertically and horizontally oriented rectangular bars yield similar contrast values.

4.2.3 Extracting the PSF

Due to the limited number of spatial frequencies on the test pattern, we were not able to fully characterize the objective at spatial frequencies higher than 645 lp/mm. Because of this, the resolution was “measured” by extrapolating the MTF curve to higher spatial frequencies, thus leaving room for error due to possible misalignments in the focal position. To obtain a more quantitative measure of the resolution, an aperture smaller than the resolution of the objective can be measured. This would yield a measure of the PSF, which takes the form of an Airy pattern, consisting of a uniformly illuminated circular region, surrounded with concentric bright rings. The resolution can be extracted by fitting the PSF to a two-dimensional Airy pattern. Measuring the distance between the first maximum and the first minimum of the Airy pattern would result in a measurement of the diffraction limited resolution.

As a first attempt, we measured the PSF using a pinhole from Data Optics, with a specified diameter of $d_{\text{pinhole}} = 0.5 \pm 0.3 \mu\text{m}$. The resulting images showed highly asymmetric profiles, with an aspect ratio of 2:3. This unexpected measure led us to believe that there may be a problem with the objective. Upon measuring the same aspect ratio using only the aspheric lens, we speculated that the asymmetry may be related to the pinhole.

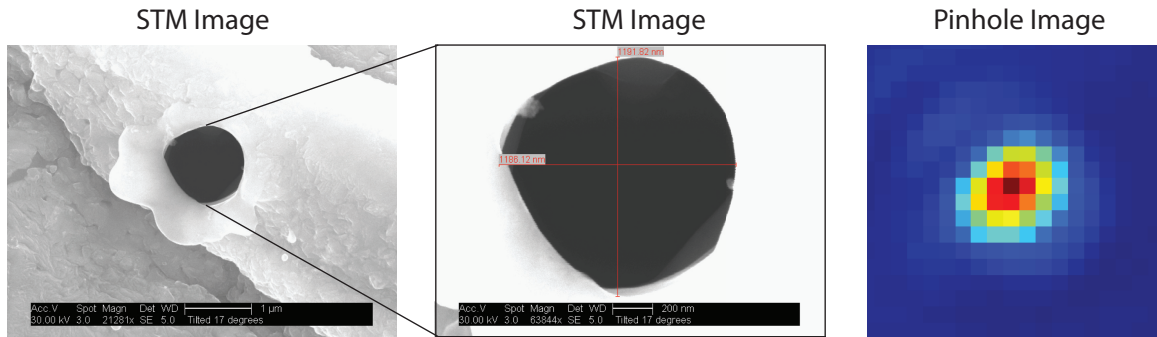


Figure 4.4: STM images of the pinhole and image taken with the aspheric lens. With $d_{\text{pinhole}} \approx 1 \mu\text{m}$, the pinhole is twice as large as ordered and provides only an upper bound for the resolution. The deformation and tilt can be seen in the image which was taken without meniscus lens and glass cell. The magnification was 25. One pixel in the image has dimensions $w_x = 0.34 \mu\text{m}$ and $w_y = 0.39 \mu\text{m}$.

Shown in Figure 4.4 is an image of the pinhole using an scanning tunneling microscope (STM). The pinhole has a diameter of $d_{\text{pinhole}} \gtrsim 1 \mu\text{m}$, twice the specification criteria, and a tilt from the normal of $\approx 17^\circ$.

Imaging a new pinhole proved to be more successful. The new pinhole was both smaller in diameter and more symmetric. An image of the pinhole using the objective is shown in Figure 4.5. Fitting the image to an Airy pattern proved difficult due to the

limited signal to noise. As a way to circumvent this issue, we instead modeled the image as two-dimensional Gaussian. This is only an approximation, so in order to relate this to the actual resolution, the extracted $1/e^2$ radius of the fit must be scaled accordingly. The scaling factor between the first maximum to minimum of the Airy pattern and $1/e^2$ radius is $2.44/1.83 \approx 1.33$ [106]. Fitting the new pinhole using this model we obtained the following resolutions:

$$d_x = 2.95 \text{ pixels} \times 8.4 \frac{\mu\text{m}}{\text{pixel}} \frac{1}{25} \times \frac{2.44}{1.83} = 1.32 \mu\text{m} \quad (4.12)$$

$$d_y = 2.6 \text{ pixels} \times 9.8 \frac{\mu\text{m}}{\text{pixel}} \frac{1}{25} \times \frac{2.44}{1.83} = 1.35 \mu\text{m}. \quad (4.13)$$

These values are consistent with the diffraction limited value of $1.33 \mu\text{m}$, assuming an NA of approximately 0.37, which is slightly less than the 0.4 value extracted from the MTF curves.

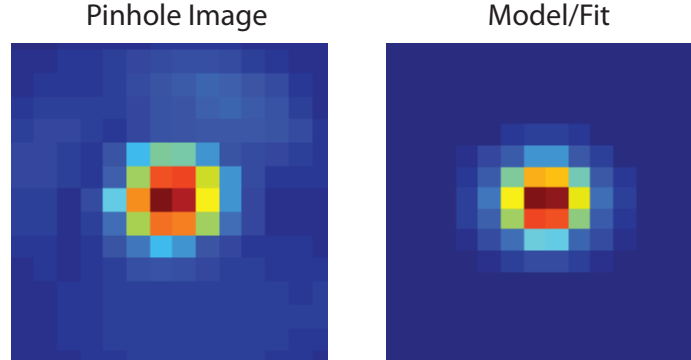


Figure 4.5: Image of the new pinhole taken with objective lens system in combination with the glass cell and the corresponding fit to a two-dimensional Gaussian. The new pinhole has a diameter of $d_{pinhole} \simeq 0.5 \mu\text{m}$. One pixel in the image has dimensions $w_x = 0.34 \mu\text{m}$ and $w_y = 0.39 \mu\text{m}$.

However, one may ask whether an image of the pinhole is a faithful representation of the PSF, given that it is roughly half the imaging resolution. To get at rough understanding of this system, we modeled this in one dimension, approximating the pinhole as a top-hat function and the PSF as a Gaussian with a FWHM that is twice that width of the top-hat. Comparing the computed image, which is the convolution of the pinhole and the PSF, to the PSF, we found that there is a $\sim 5\%$ overestimate of the resolution using an object of finite size as opposed to a delta function. Thus, the finite-sized pinhole is a fair test image for extracting a measure of the imaging resolution.

4.2.4 Astigmatism

The astigmatism of this objective was characterized by placing the pinhole at the same location with respect to the optical axis as the condensate is presumed to be. Then the size of the pinhole as a function of the objective focal position was measured. An

astigmatism would result in an asymmetry between the measured vertical and horizontal widths of the pinhole as a function of this position. Figure 4.6 shows the measured pinhole widths as a function of the objective position. The data are fit to a parabola, where the minimum of the fit indicates the location of the objective focus. The horizontal and vertical widths are nearly identical (when taking into account the rectangular nature of the pixels), and the focal minima occur at essentially the same position, indicating that any astigmatism present in the imaging system is beyond our measurement capabilities and most likely insignificant.

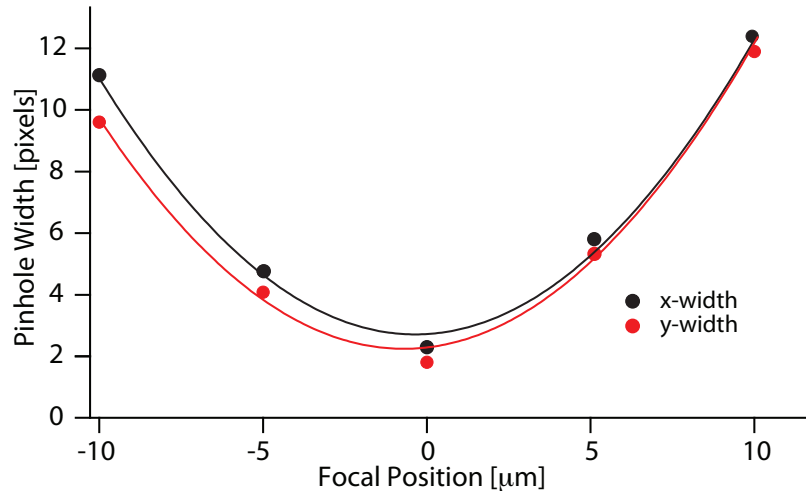


Figure 4.6: Measured horizontal and vertical widths of the pinhole as a function of the objective focal position. Using a linear translation stage, the objective position was scanned through the focus and for each position the horizontal and vertical widths of the pinhole were measured. The solid lines are fits to the data assuming a model which is parabolic. The similar minima of the fits and lack of asymmetry between the widths is an indication that the objective is stigmatic.

4.3 *In-situ* Characterization

In this section, we show how we use *in-situ* measurements of spinor condensates to characterize an imaging system via the modulation transfer function, determining how faithfully the imaging system is able to reproduce the spatial detail within the profile of our spinor condensate. There have been other approaches to measure the MTF, typically based on the imaging of individual atoms or non-interacting thermal gases [111, 112]. While both approaches use density fluctuations inherent in ultracold atomic gases to characterize their respective imaging system, neither has controllably simulated a test pattern using a spin texture to directly measure the MTF.

4.3.1 Imaging Test Pattern

For our experiments here, we produce optically trapped, spin-polarized ^{87}Rb condensates of 3×10^6 atoms in the $|F = 1, m_F = -1\rangle$ state in a manner similar to Ref. [113], at a temperature 70 nK and trap frequencies of $(\omega_x, \omega_y, \omega_z) = 2\pi \times (25, 480, 7.3)$ Hz in a focused, linearly polarized light beam with a wavelength of 1064 nm. We next prepare transversely magnetized condensates by applying a resonant $\pi/2$ radio frequency (rf) pulse in the presence of a static magnetic field of $B = 267$ mG, applied along the \hat{x} axis. The applied magnetic field causes the magnetization in the $\hat{y} - \hat{z}$ plane to precess with respect to the \hat{x} axis at the Larmor frequency of $\Omega_L = 2\pi \times 187$ kHz. The magnetic field inhomogeneity is reduced to below $1 \mu\text{G}$ across the extent of the gas, resulting in a negligible spatial variation of less than 1 Hz in the Larmor precession frequency

A sinusoidal spin texture was then created by rotating the orientation of the bias field to be pointed along \hat{z} and applying a transient magnetic field gradient dB_z/dz for times ranging between $\tau = 0 - 30$ ms. Larmor precession of the atomic spins in this field resulted in a gradient spin pattern with spin $\mathbf{F} = \cos(\kappa z + \omega_L t)\hat{x} + \sin(\kappa z + \omega_L t)\hat{y}$, where $\vec{\kappa} = (g_F \mu_B / \hbar)(dB_z/dz)\tau\hat{z}$ is the wave vector. Similar to the experiment in [113], we ignore the time evolution of the spin due to the rapid Larmor precession, as we are probing the gas at a particular instant in time. By varying the time of the applied magnetic field gradient, the pitch of the sinusoidal spin texture ranged between 4-50 μm .

Following a given evolution time, the magnetization profile was imaged using a sequence of polarization contrast images (see Chapter 3). In particular, the magnetization was imaged using 200-ns-long imaging pulses of linearly polarized light propagating along the \hat{y} -direction. After traversing through the condensate, the resulting optical rotation of the probe polarization was measured, yielding a spatially resolved signal of the transverse magnetization, $\mathbf{M}_\perp = (g_F \mu_B)\tilde{n}\mathbf{F}_\perp$, where \tilde{n} is the two-dimensional column-integrated condensate density.

Tuning κ

Necessary to the measurement of the MTF is a test pattern with a wide range of frequency components. In optical test patterns such as the 1951 USAF test chart, a grid of rectangular bars, ranging in sizes from 0.25 to 645 line pairs/mm, is used to measure the MTF. Here, we are able to create a sinusoidal test pattern using our spinor Bose gas by applying an inhomogeneous magnetic field, using a pair of quadrupole coils, with their symmetry axis oriented along the long axis of the condensate (\hat{z} -axis). The effect of this is to cause a local change in the magnetic field, whereby each spin in the condensate will then precess at a rate that proportional to the magnetic field in that region. Thus, atoms at opposite ends of the condensate will precess at different rates. These differing rates result in an accrued phase shift across the extent of the gas, resulting in a spatial oscillation of the magnetization along the “direction” of the field gradient, where “direction” here specifies the axis over which the magnitude of the magnetic field varies.

In order to vary the magnitude of the wave vector, κ , we use two control knobs: the pulse duration, τ , and the strength of the magnetic field gradient, B' , where the quantity which determines the pitch is $\propto B' \times \tau$. By scanning these two knobs, we are able to create

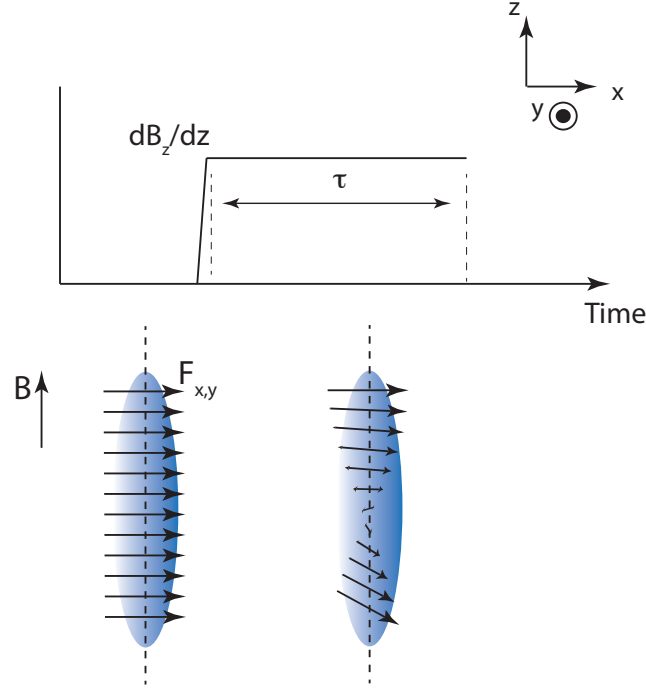


Figure 4.7: Schematic of texture preparation. The system is initialized with a transversely magnetized condensate, where the magnetic field is oriented along the \hat{x} -axis and the spins are in the $\hat{y} - \hat{z}$ plane. Next, the orientation of the magnetic field is rotated such that it is aligned along \hat{z} -axis and a magnetic field gradient, dB_z/dz , causing the magnitude of the magnetic field to vary as a function of the position along the long axis of the condensate (\hat{z} -axis), resulting a helical spin pattern.

a spin texture of a well defined wave vector, which scales linearly with τ and $B' = dB_z/dz$. Shown in Figure 4.8 are a series of polarization contrast images of sinusoidal spin textures. The application of a magnetic field gradient, dB_z/dz , causes a spatial variation of the magnetization along the \hat{z} -axis. Repeating this for increasing pulse durations results in a helical spin pattern with a larger spatial frequency.

We verify that $\kappa/2\pi$ scales linearly with the pulse duration. To do this, we take the spatial Fourier transform of the magnetization spatial profile, \mathbf{M}_\perp . Then using the Fourier spectra, we extract the magnitude of $\kappa/2\pi$ and plot this as a function of the pulse duration. At a magnetic field gradient of $dB_z/dz \approx 140$ mG/cm, the resulting wave vectors range from $\approx 0.01 - .2$ pixels $^{-1}$. In order to convert this to more experimentally friendly units, we convert the pitch, in units of 1/pixels, to microns, where $\lambda = 2\pi/\kappa \times 0.62 \mu\text{m}/\text{pixel}$, and $0.62 \mu\text{m}/\text{pixel}$ is the effective pixel size in the imaging plane. This yields length scales which range from $50 - 4 \mu\text{m}$. The dependence of λ and pulse duration is shown in the bottom right plot of Figure 4.8.

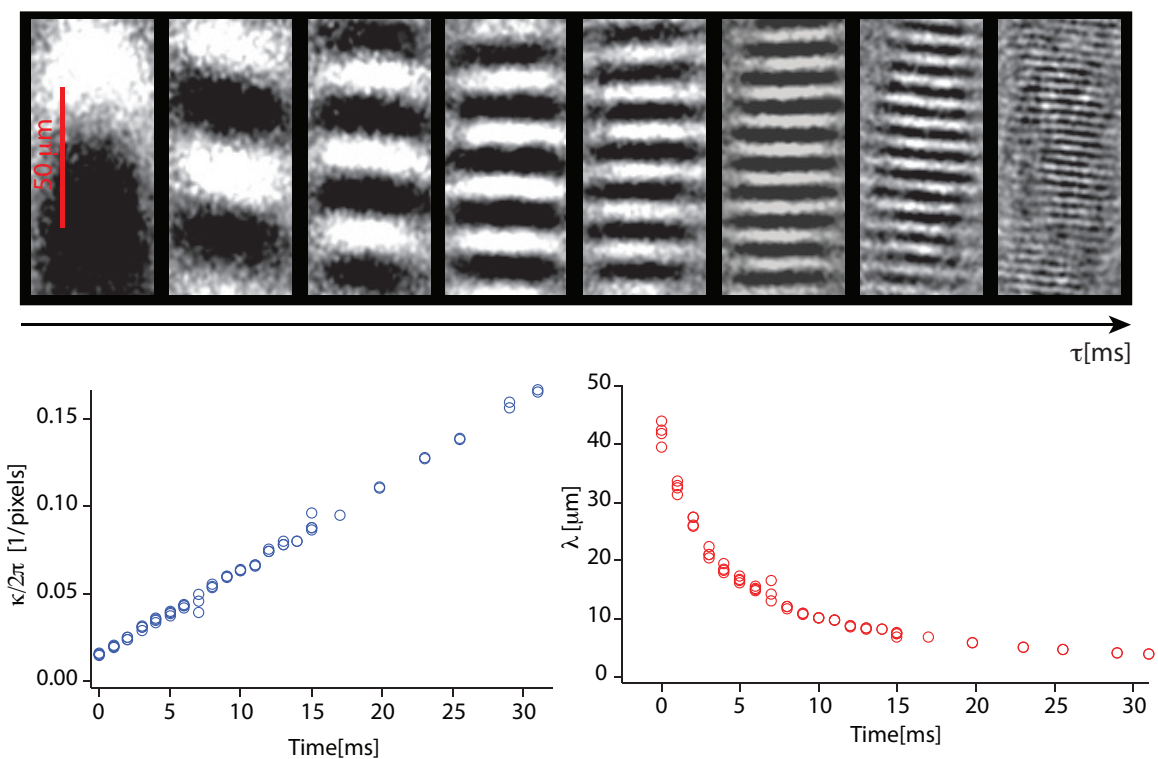


Figure 4.8: Unprocessed polarization contrast images of helical test patterns. As a function of the applied magnetic field gradient, the pitch of the test pattern increases. Here the pulse duration, τ , ranges from 1 ms to 30 ms, yielding a pitch that ranges from 50 μm (left) to 4 μm (right). The reproducibility and control is shown in the plots of the frequency and wavelength versus time. The spatial frequency of the texture is related to the wavelength by the pixel size in the imaging plane, which is $\simeq 0.6$ pixels/ μm .

Limitations on κ

The range over which we are able to vary the pitch appears to be limited. The condensate size determines the largest values of λ , while the smallest length scales appear to be $\sim 4 \mu\text{m}$. Despite using longer pulse durations or larger magnetic field gradients, the largest wave vector measured saturates at $4 \mu\text{m}$. The reason for this is unclear. There are a few possible explanations, one of which is related to the previous experimental work in this group investigating the temporal evolution of helical spin textures [113]. In that work, a helical spin texture with pitch $\lambda = 60 \mu\text{m}$ was created. After just ~ 50 ms of free evolution, the spin texture spontaneously dissolved into a highly corrugated spin pattern. The formation of the modulated spin structure was ascribed to magnetic dipolar interactions, which energetically favor short-wavelength domains over the long-wavelength helix. Furthermore, this dissolution was found to occur so long as $\lambda < 2r_z$, where $r_z = 80 \mu\text{m}$ is the Thomas-Fermi radius along the long axis of the condensate. For the helical spin patterns studied here, $\lambda \simeq r_z$ for $\tau < 3$ ms. In order to prevent the condensate from forming this modulated magnetic phase, the pulse durations were kept shorter than the free evolution times used in the previous work. The pulse durations used here were < 30 ms and the field gradient was ~ 100 kHz/cm.

Another potential culprit is the alignment of the imaging system. The smallest features depend more critically on the position of the objective focus and small misalignments in this position would yield an overall reduced contrast of the sinusoid. For a well aligned imaging system, the contrast at the smallest pitches is expected to be much smaller than unity, and a misalignment in the focal position of the objective could make it impossible to image. Thus, despite exploring a wide range of pulse durations and field gradients, λ was still limited to $4 \mu\text{m}$, possibly limited by misalignments in the imaging system or the dissolution of the spin texture.

4.3.2 Extracting the MTF

We extract the MTF of our imaging system by measuring the contrast of the modulation pattern from the helical spin texture and repeat this measurement for different wave vectors. As described above, we imprint a helical spin texture by applying an inhomogeneous magnetic field. By applying the field gradient for various times, we are able to carefully control the pitch of the helix (see Figure 4.8). Shown in Figure 4.9 is data from several experimental runs, where we vary the time of the applied magnetic field gradient. We create helices where $2\pi/\kappa$ are comparable to the length of the condensate ($\simeq 50 \mu\text{m}$) down to a few microns, where the smallest observable helix pitch is on the order of the spin healing length of our condensate, $\xi_s = (8\pi\Delta an)^{-1/2} \sim 2 \mu\text{m}$.

We measure the contrast of the helix by integrating along the direction which is orthogonal to the modulation direction, creating a one-dimensional profile. The resulting profile has a Thomas-Fermi envelope, and within the envelope a sinusoidal modulation. For simplicity, we approximate the Thomas-Fermi profile as a Gaussian, and fit the profile to a sinusoid times a Gaussian. We model the profile as:

$$f(x) = A \times e^{((x-x_0)/x_w)^2} \times \sin(\kappa x + \phi) + offset, \quad (4.14)$$

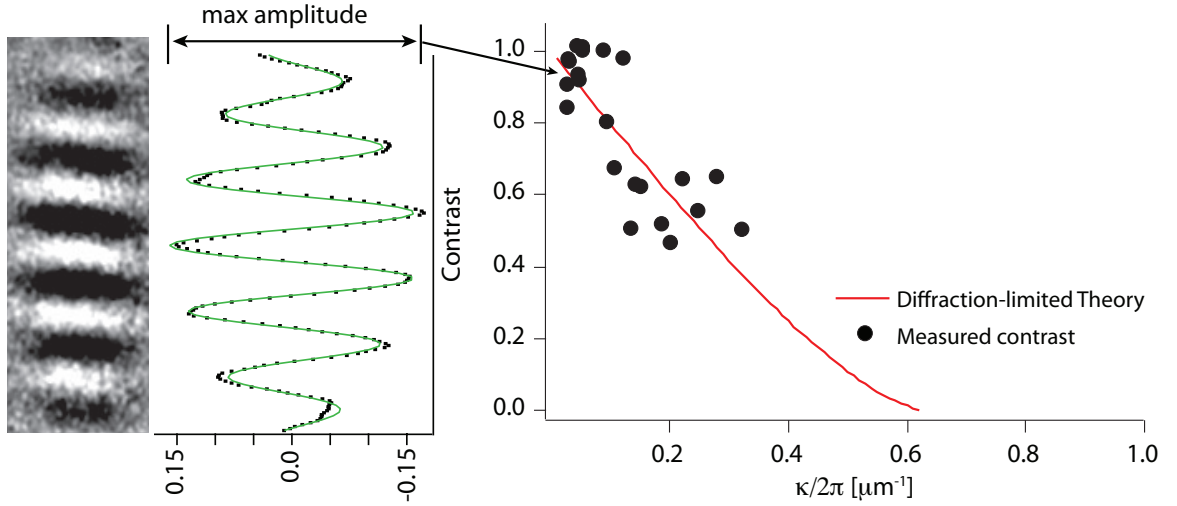


Figure 4.9: Polarization contrast images of a helical test pattern with a $20 \mu\text{m}$ wavelength. To the right of the test pattern is the corresponding one-dimensional profile (black dots). The contrast is extracted by fitting the one-dimensional profile to a modified sine curve (green solid curve). The measured contrast versus pitch is plotted and compared to a theory curve assuming an $\text{NA} \sim 0.31$.

where κ is the pitch of the texture, ϕ is an overall phase offset, A is the amplitude, x_0 is the offset from zero, and x_w is the width of the gas. Using the fit parameters of the model, we extract a measurement of the maximum contrast,

$$C(f) = (A_{max} - A_{min}) / (A_{max} + A_{min}), \quad (4.15)$$

where $A_{max} = A/2 + offset$ and $A_{min} = A/2 - offset$. Thus the contrast measurement reduces to $C(f) = A$. We next normalize this measurement to the phase contrast signal of a fully transversally magnetized gas. The result is shown in Figure 4.9. Initially at low κ , the data are near unity and with increasing κ , the contrast decreases smoothly, reaching a minimum contrast of ≈ 0.5 at $\lambda^{-1} \approx 0.25 \mu\text{m}^{-1}$.

Resolution

As discussed in the previous section, test patterns with $\lambda < 4 \mu\text{m}$ are difficult to produce, reducing the number of contrast measurements at the higher spatial frequencies. Thus, to circumvent this we compare the contrast measurement to a diffraction limited theory curve with one free parameter. Fitting the data while allowing the NA to vary, we extract a value of the $\text{NA} \approx 0.31$, approximately 30% lower than the expected value in the custom mount, $\text{NA}_{ideal} \approx 0.43$, but close to the value obtained from the PSF measurement, $\text{NA} \sim 0.37$ (see Figure 4.9).

We ascribe the lower NA to a slight tilt in the glass cell with respect to the objective mount. The glass cell is attached to the vacuum chamber on a non rotatable Conflat flange, with a tilt of $\approx 10^\circ$ with respect to gravity. To reduce this angle, the objective mount was

also tilted such that the remaining angle was reduced to $\approx 1-3^\circ$. Compensating this further is hindered by the objective mount, the mount holding the bias coils, and the water-cooling mount of the transportation coils.

Pitch vs angle

In addition to the test pattern discussed above, which had a modulation purely along \hat{z} , we were also able to create a modulation along any direction in the $\hat{x} - \hat{z}$ plane. This was accomplished by rotating the orientation of the applied bias field, using two pairs of Helmholtz coils, with their axes oriented along the \hat{x} and \hat{z} directions. Thus by changing the orientation of the bias field, we are able to easily tune the axis of the modulation.

Using this capability, our first goal was to determine the severity of any astigmatism in our imaging system. Ideally, this would involve the tedious process of measuring the contrast for a range of wave vectors and bias field orientations. Instead, as a quick check, we scanned the orientation of the bias field for a specific modulation wave vector, $\kappa/2\pi \approx 0.12 \mu\text{m}^{-1}$ (Figure 4.10). Magnetization maps for each orientation of the magnetic field were recorded, where the orientation of the bias field was scanned starting along $\mathbf{B} = B_0 \hat{z} (0^\circ)$ to $\mathbf{B} = B_0(-\hat{z}) (-180^\circ)$, with 15° increments. For each bias field orientation, the axis of the modulation rotates and the contrast appears to remain fairly constant.

To quantify this behavior, we considered the spatial Fourier transform of the magnetization shown in Figure 4.10. The spectrum contained a concentration at $\pm\kappa/2\pi$, representing the applied modulation. We integrated the spectral power at the frequency corresponding to the spatial frequency of the helix and defined this as the Fourier transform intensity (FT Intensity), indicated in Figure 4.10. For each orientation of the magnetic field, the spectral weight at $\kappa/2\pi \approx 0.12 \mu\text{m}^{-1}$ remains relatively constant, indicating that the effect of any astigmatism is either negligible or smaller than the noise in the images between experimental iterations.

Objective misalignments

A potential error that can come about with regards to an imaging system are misalignments with the objective focus which can lead to detrimental imaging aberrations. Below we investigate such effects by purposely misaligning the position of the objective focus and characterize the resulting aberrations using helical spin textures of varying pitch. Following this, we also study the effect of an out-of-focus imaging system on the modulated magnetic phases emanating from the breakup of helical spin textures (see Chapter 5).

To systematically study an out-of-focus imaging system, we displaced the position of the objective along the imaging axis (\hat{y} -axis) by $\simeq 0.3$ mm and characterized the imaging system using a helical spin texture. When the objective is positioned at a distance equivalent to its focal length away from the atoms, referred to as “in-focus,” the MTF curve smoothly decreases to zero. However, when “out-of-focus,” the objective is no longer able to image certain spatial frequencies and the exhibits an oscillation in the contrast measurements versus spatial frequency (see Figure 4.11). In particular, the contrast decreases from its value near unity at $\kappa \leq 0.2$, to zero at $\kappa \simeq 0.3$, and increases again at $\kappa \simeq 0.4$. Other oscillations are visible in the contrast measurements. This is due to the larger PSF for an

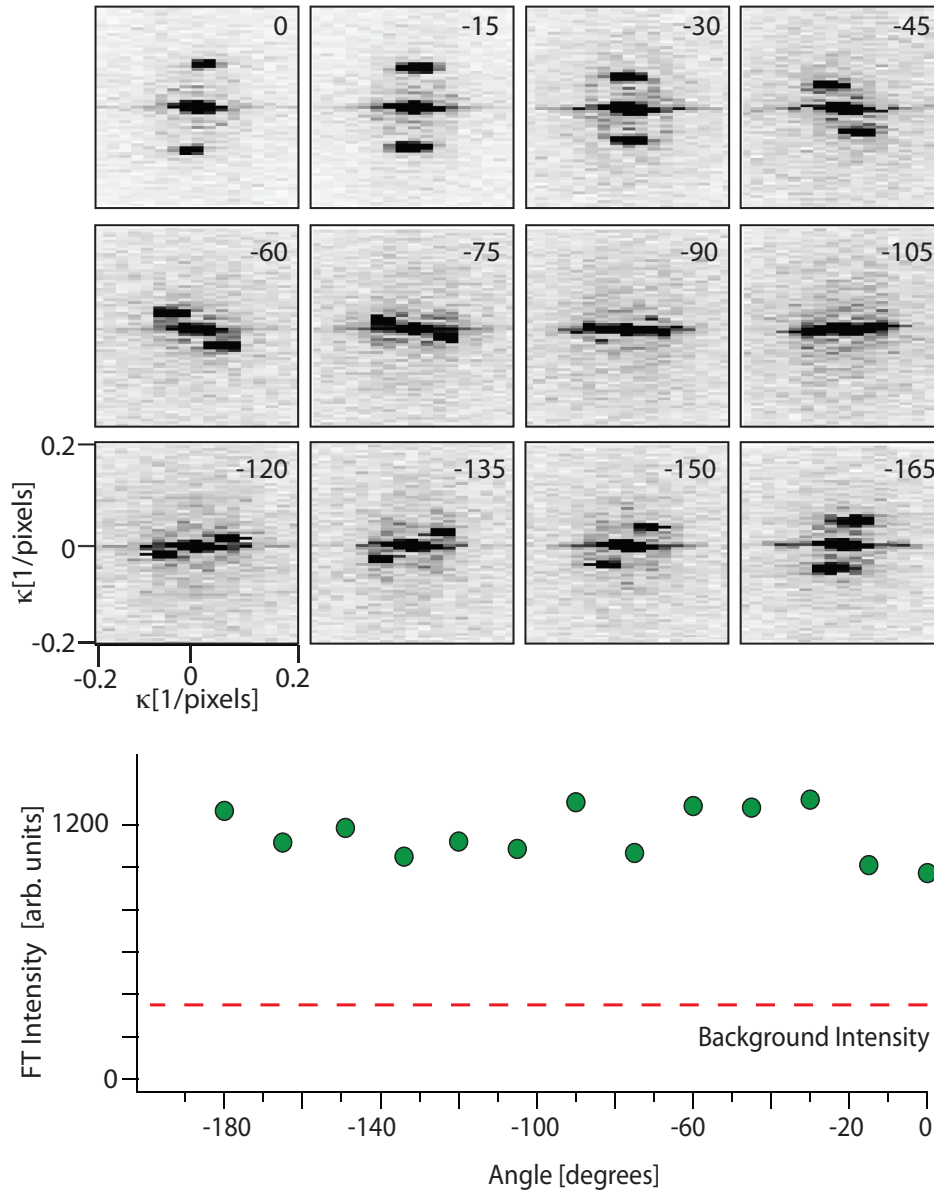


Figure 4.10: Spatial Fourier transforms of magnetization maps. The sinusoidal texture results in a spectrum with a signal concentration at the modulation wave vector, $\pm\kappa/2\pi \approx 0.12$. A magnetization map for each orientation of the bias field is recorded, starting with the field aligned along \hat{z} (0°) and increasing in 15° increments to $-\hat{z}$ (180°). The integrated spectral power of each Fourier transform is recorded and plotted for each bias field orientation. The absence of any dependence between the intensity and orientation angle indicates a stigmatic imaging system.

out-of-focus imaging system. For instance, when the center of the PSF coincides with a dark region of the helical test pattern, it also acquires information from adjacent regions

that may be brighter. This results in a slightly brighter signal. The opposite is also true when the PSF is located over a bright region of the test pattern. This net effect of the enlarged PSF due to an out-of-focus imaging system results in the oscillating contrast seen in the MTF and the overall reduction of the MTF at higher spatial frequencies.

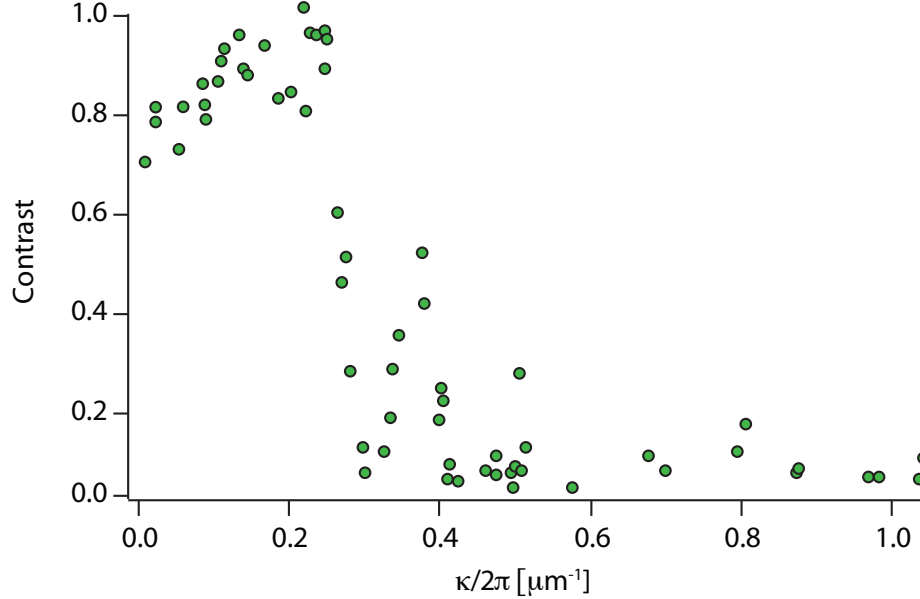


Figure 4.11: MTF for objective when displaced from the “in-focus” position by ~ 0.3 mm.

We also examined the effect of an out-of-focus imaging system and its ability to adequately image the breakup of helical spin textures as studied in previous experiments [113]. To do this created a helical spin texture with a $30 \mu\text{m}$ pitch and imaged it after 100 ms of free evolution, the details of which are described in reference [113]. The resulting magnetization profile from what we believed to be an “in-focus” imaging system showed a magnetization pattern described by a two-wave vector spatial modulation, with a length scale of $10 \mu\text{m}$ (Figure 4.12 (2.59)). However, upon changing the position of the objective with respect to the in-trap location of the atoms, a different spatial pattern was observed. The magnetization pattern at each position of the objective focus was consistent between experimental iterations, thus any differences are not due to random fluctuations. As a function of the objective position, the observed magnetization pattern varied from an annulus at roughly $10 \mu\text{m}$ at an objective position of 2.57 mm, to a two-wave vector modulation, then to a single wave vector at an objective position of 2.61 mm. Thus it seems that we can enhance certain spatial features by adjusting the position of the objective focus. Furthermore, the orientation of the modulation axis varies with the position of the objective focus. Previous observations found that the axis of the two-wave vector modulation remained unchanged between experimental iterations and under different experimental conditions. These observation leads us to doubt previous interpretations that a helical spin texture dissolves into a two-wave vector modulation pattern in the magnetization profile.

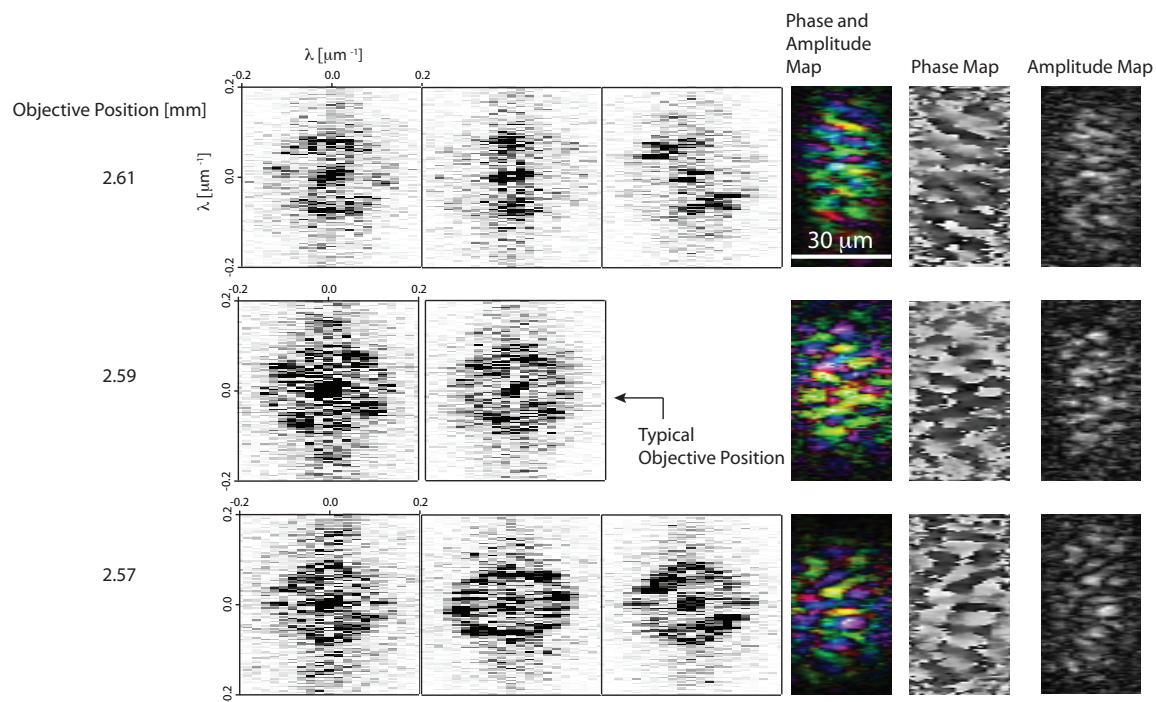


Figure 4.12: Two-dimensional spatial Fourier transform of the transverse magnetization profile for different positions of the objective focus. Following the application of a 100 kHz/cm magnetic field gradient and an evolution time of 100 ms, the transverse magnetization was imaged using phase contrast imaging. Each image is derived from a single experimental iteration. Multiple images taken at each focus is meant to show the fluctuations in the spatial Fourier transforms between experimental iterations. Also included are the spatial phase and amplitude profiles of the condensate magnetization. The “phase and amplitude” map incorporates the data from the two spatial profiles (phase and amplitude), where the brightness is indicative of the strength of the magnetization and the color determines the orientation of the magnetization.

Chapter 5

Equilibrium Properties of Spinor Condensates

This chapter presents work related to the equilibrium properties of spinor gases. This work was presented in the following publications:

- *M. Vengalattore, J. Guzman, S. R. Leslie, F. Serwane, and D. M. Stamper-Kurn. "Periodic spin textures in a degenerate $F = 1$ ^{87}Rb spinor Bose gas" *Physical Review A* **81**, 053612 (2010).*
- *J. Guzman, G. -B. Jo, A. N. Wenz, K. W. Murch, C. K. Thomas, and D. M. Stamper-Kurn. "Long-time-scale dynamics of spin textures in a degenerate $F = 1$ ^{87}Rb spinor Bose gas" *Physical Review A* **84**, 063625 (2010).*

The general understanding of non-equilibrium dynamics and their approach to equilibrium has remained an elusive topic in ultracold and condensed-matter systems. The strong interactions in solid state systems make observing quantum dynamics nearly impossible, as most systems reside at or near the thermal equilibrium state. In contrast, the relatively slow evolution of weak interactions associated with ultracold atomic systems enables the study of quantum dynamics on experimentally accessible timescales. While many research groups have extensively studied the dynamics of spin-mixing collisions in spinor condensates [83, 51, 52, 114, 115, 116, 117, 118, 119], less work has been dedicated to the experimental pursuit of equilibrium in these systems. In fact, given the limited lifetime of the samples, the question of whether ultracold atomic systems are able to reach equilibrium has remained unanswered.

In the next few sections, we discuss a few experiments where we systematically study the evolution of spin textures in a spin-1 Bose gas and address the question of whether a cold atom system is able to reach equilibrium by experimentally verifying the equilibrium phase diagram for an $F = 1$ spinor gas.

5.1 Spinor Basics

Spinor condensates are distinguished from their scalar counterparts by the introduction of a vector order parameter, well described within mean-field theory. This sec-

tion will present a short introduction to the theoretical treatment of spinor condensates. A more detailed treatment can be found in the following review article [82] and theses [27, 120, 79, 52, 80]. In particular, this section will focus on the spin dependent mean-field interaction and the quadratic Zeeman effect which contribute to the rich landscape of competing magnetic phases that are studied here. For more information regarding this topic, I refer the reader to the following theoretical [121, 122, 123, 124, 125, 126, 127, 128, 129] and experimental [115, 114, 81, 83] publications.

5.1.1 Theoretical description of a spinor BEC

The $F = 1$ spinor Bose gas can be represented by a three-component order parameter

$$\Psi(\mathbf{x}) = \sqrt{n(\mathbf{x})}\psi(\mathbf{x}) \quad (5.1)$$

$$= \sqrt{n(\mathbf{x})} \begin{pmatrix} \psi_{+1}(\mathbf{x}) \\ \psi_0(\mathbf{x}) \\ \psi_{-1}(\mathbf{x}) \end{pmatrix} \quad (5.2)$$

where the spinor $\psi(\mathbf{x})$ is normalized as $\psi(\mathbf{x})^\dagger\psi(\mathbf{x}) = 1$ and the subscripts reflect the three magnetic Zeeman sublevels, $m_F = 0, -1, +1$. For simplicity, we first determine the ground magnetic phase while ignoring effects from a magnetic field. The energy functional at zero magnetic field is described by

$$E = \int d^3x \left(\frac{\hbar^2}{2m} |\nabla\Psi|^2 + n(x)(U(x) - \mu) + \frac{n^2}{2} (c_0 + c_2\langle F^2 \rangle) \right) \quad (5.3)$$

where $F = \psi^\dagger(\mathbf{x})\mathbf{J}\psi(\mathbf{x})$ is the dimensionless magnetization, m is the mass, and J_i are the standard spin-1 matrices. The first term in the energy functional describes the kinetic energy and the second term describes the externally applied trapping potential. The last term describes the spin independent and dependent contact interaction. These interaction terms are characterized by the coefficients c_0 and c_2 , which are determined by the s-wave scattering lengths with total angular momentum 0 or 2,

$$c_0 = \frac{4\pi\hbar^2}{3m}(2a_2 + a_0) \quad (5.4)$$

$$c_2 = \frac{4\pi\hbar^2}{3m}(a_2 - a_0). \quad (5.5)$$

For ^{87}Rb , the scattering lengths are $a_0 = 101.8a_B$ and $a_2 = 100.4a_B$, where a_B is the Bohr radius [130]. Note c_2 is negative since $a_2 < a_0$, in contrast to $F = 1$ ^{23}Na spinor condensates, where $c_2 > 0$ [27].

The ground state structure of the spinor can be determined by minimizing the spin-dependent part of the energy functional, $n^2c_2\langle F^2 \rangle/2$ [27]. In doing so, considering only the spin-dependent contact interaction, we see that the energy is minimized when $\langle \mathbf{F} \rangle^2 = 1$. Thus, the spin-dependent contact interaction prefers the condensate to be in a magnetized state (ferromagnetic state).

Zeeman shift

The addition of an external homogeneous magnetic field, $\mathbf{B} = B_0 \hat{z}$, results in an additional term to the spin-dependent part of the energy functional described by

$$E_B = E_{LZ} + E_{QZ} \quad (5.6)$$

$$= \int d^3x n (g_F \mu_B B_0 \langle F_z \rangle + q \langle F_z^2 \rangle) \quad (5.7)$$

which includes contributions from both the linear and quadratic Zeeman shift. We discuss the influence of each shift below. The net effect of the linear Zeeman shift is just to induce Larmor precession of the transverse magnetization. We can compensate this by choosing a rotating frame of reference at the Larmor precession frequency, where there the shift due to the linear Zeeman effect is zero. The reasoning behind this lies in the conservation of magnetization, derived from the rotational symmetry of the spin interactions. However, spatial magnetic field inhomogeneities could have a substantial influence on the spinor ground state [131]. In the experiments discussed here, great care is taken to ensure that the magnitude of these inhomogeneities are far smaller than the spin-dependent contact interaction and the quadratic Zeeman shift.

The quadratic Zeeman shift, however, does have a strong influence on the spinor ground state properties. For an $F = 1$ gas of ^{87}Rb atoms, the applied magnetic field induces a shift proportional to $\propto m_F^2 B^2$, characterized by

$$q = \frac{E_{+1} + E_{-1} - 2E_0}{2}, \quad (5.8)$$

where E_{m_F} is the shift of the magnetic sublevel in the presence of a magnetic field. This corresponds to a shift of $q/h = 70.6 \times B^2 \text{ Hz/G}^2$, computed from the Breit-Rabi formula. We can see that for large magnetic fields, the effect of the quadratic Zeeman shift is to increase the energy of the $m_F = \pm 1$ levels with respect to the $m_F = 0$ level, resulting in a preference for a state which is unmagnetized, often referred to as a polar state. We note that the phase transition from a polar to ferromagnetic state is $q = 2|c_2|n$ [81]. However, for $q < 0$, the $m_F = \pm 1$ are now lower in energy, and once again a magnetized state is preferred. The energy functional in this scenario is minimized when the magnetization is oriented parallel or antiparallel to the magnetic field.

5.1.2 Mean-Field Phase Diagram

Summarizing the contributing factors to the spin-dependent energy functional, we have

$$E_{spin} = \int d^3x n \left(\frac{nc_2}{2} \langle F^2 \rangle + q \langle F_z^2 \rangle \right), \quad (5.9)$$

where we see that we have a set of competing interactions, each favoring a different magnetic ground state. The effect of these competing interactions has yielded a versatile playground for studies of magnetism, resulting in many experimental [81, 83, 132, 119] and theoretical [125, 126, 133, 134, 122] pursuits.

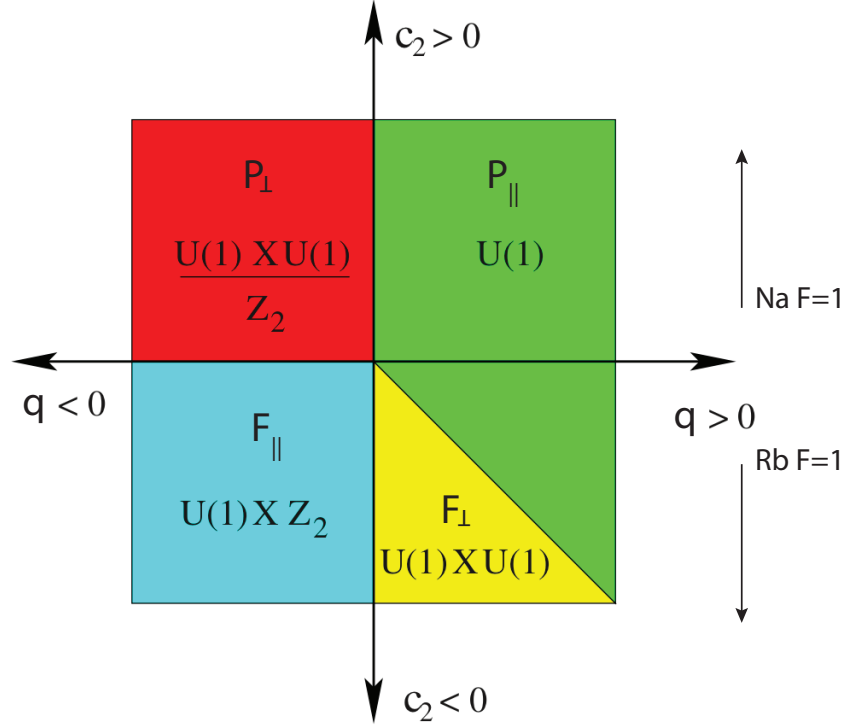


Figure 5.1: Ground state phase diagram for $F = 1$ spinor condensate as predicted by mean-field theory in presence of magnetic field from Mukerjee et al [134].

The resulting magnetic phases of the ground state structure as predicted by a mean field theory for a uniform condensate are summarized in Figure 5.1. The lower part of the phase diagram corresponds to the ferromagnetic case where $c_2 < 0$; such is the case for ^{87}Rb . The lower left quadrant corresponds to large negative quadratic shift, where a uniformly magnetized state is energetically favorable, F_{\parallel} , and the magnetization is likened to an easy-axis (Ising) magnet [134, 125]. Physically, this means that the condensate magnetization prefers to be aligned or anti-aligned with respect to the magnetic field. The lower right quadrant is divided into two parts by a straight line described by $q = -2|c_2|$. To the right of this line, it is energetically favorable for the system to be in an unmagnetized (polar) state, P_{\parallel} . To the left of this line, at intermediate values of the quadratic shift ($0 < q < 2|c_2|n$) the energetically preferred state is one which is a linear combination of a polar phase, P_{\parallel} , and a ferromagnetic phase F_{\perp} , where this ferromagnetic phase is one which prefers in-plane magnetization, likened to an easy-plane (XY) model.

5.2 Why study the magnetic phases of an $F = 1$ spinor gas?

During the course of fairly routine experimental procedures, we observed the magnetization of our $F = 1$ spinor gas to behave unexpectedly. After reducing the spatial inhomogeneities in the magnetic field, where there was roughly a $\Delta B \approx 15 \mu\text{G}$ difference across the spatial extent of the condensate, we observed the magnetization profile dissolve into a pattern of modulated spin domains. Believing this to be a one-time occurrence and noting this puzzling observation, we naively attributed this phenomena to improper gradient cancellation. However, our incomplete understanding of why spatial inhomogeneities in the magnetic field would lead to such unusual behavior motivated us to pursue a new experiment; one that would systematically study the temporal evolution of the spinor magnetization profile in the presence of a spatially inhomogeneous magnetic field [113].

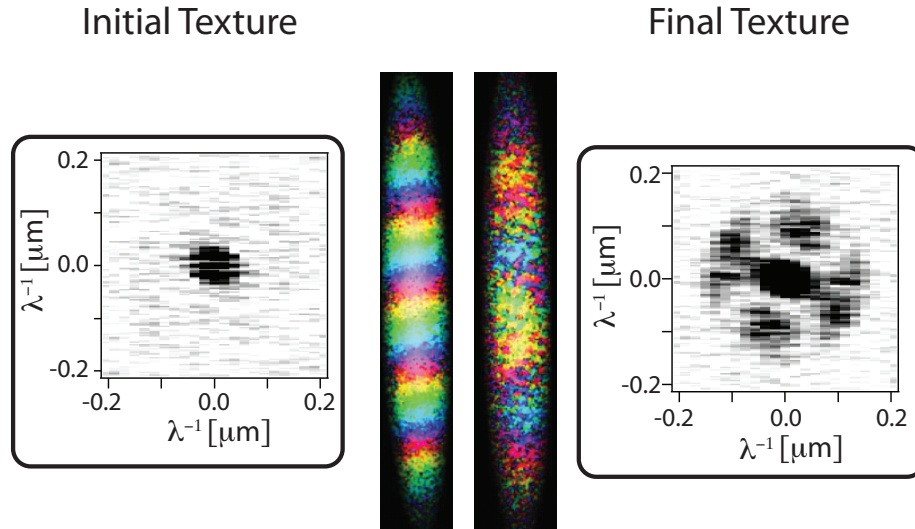


Figure 5.2: Dissolution of helical spin textures. On the left is the transverse magnetization of an initially prepared helical spin texture and the corresponding spatial Fourier transform. On the right is the temporal evolution of the texture after a couple ~ 100 ms evolution time. As can be seen in the Fourier transform and the *in-situ* magnetization map, the spin texture consists of corrugated pattern of spin domains, characterized by $\approx 10 \mu\text{m}$ modulation.

In that study we performed a time-resolved study of the spinor magnetization after imprinting a helical spin pattern with a $\sim 30 \mu\text{m}$ pitch. Following evolution times as short as 50 ms, we observed the transverse magnetization break up into a regularly occurring pattern of spin domains (Figure 5.2), not unlike a checkerboard lattice, persisting for times up to ~ 300 ms, where this evolution time was limited by the lifetime of the gas in the optical trap.

The persistence of the “crystalline” phase led us to question whether this was indeed the equilibrium ground state, or a long-lived non-equilibrium magnetic phase. A careful look at the magnetic phases predicted for an $F = 1$ spinor gas indicated that a homogeneous transversely magnetized condensate minimized the local contact interaction.

Thus, having prepared a helical spin texture, the evolution towards a spatially modulated pattern was highly unexpected, leading us to question whether there are effects beyond the local contact interaction that must be included to obtain a complete description of a spinor condensate, such as magnetic dipole-dipole interactions.

Thus, to resolve whether interactions not included in the spin-dependent energy functional play a significant role in the behavior of spinor gases, we investigated whether the equilibrium phase of $F = 1$ spinor condensates included additional magnetic phases not included in the phase diagram described above.

Discussed in the following sections are two separate experiments. Each using two different experimental apparatuses to probe the equilibrium properties of an $F = 1$ spinor condensate. First, we will discuss our initial results reported in [135], which explored the evolution of unmagnetized spin mixtures at different final temperatures. Such studies observed the emergence of a modulated magnetic phase, but were unsuccessful in determining whether this was an equilibrium property of the system. This was due to finite evolution times of up to 300 ms, limited by the lifetime of the atoms in the optical trap. Following this we will discuss the results reported in [104], where a new experimental apparatus enabled longer evolution times, upward of 3 – 4 s. There we observed the equilibrium properties of the $F = 1$ spinor gas within a small range of quadratic Zeeman shifts.

5.3 Experimental Tools

To explore the equilibrium properties of spinor condensates, a few experimental elements are necessary: precise control of the spatial profile of the magnetic field, control of the quadratic Zeeman shift, as well as a fine tune control of the initial spin composition. By having these tools available, a thorough exploration of the magnetic phases of a $F = 1$ spinor gas can be achieved.

5.3.1 Magnetic Fields

Our study of the magnetic phases of a spinor condensate required precise control of the magnetic field, specifically the orientation, spatial variation, and its magnitude. This was done by using three orthogonal pairs of coils, arranged in a Helmholtz configuration outside the glass cell (see Chapter 2). Using such coils, we were able to achieve reproducible magnetic fields on the order of ~ 1 mG, limited by the dc field fluctuations from the elevator which caused the background bias field to fluctuate by approximately 5 – 10 mG. Using these coils, the typical field we operated at was 110 kHz or equivalently 167 mG along \hat{z} -direction for the experiment in [135], referred to as Experiment 1, and 187 kHz or equivalently 267 mG along \hat{x} -direction for the experiment reported in [104], referred to as Experiment 2.

Magnetic Field Gradients

Additional coils, however, were required due to spatial inhomogeneities in the magnetic field at the location of the condensate, presumably due to imperfections in the coils as well as contributions from various components of the experimental apparatus, such

as translation stages or ball-drivers. The magnetic field gradients along the \hat{x} - and \hat{z} -directions were controlled using three pairs of coils arranged in an anti-Helmholtz configuration, located outside the glass cell. The coils were arranged such that we were able to control the magnetic field gradients along dB_x/dz , dB_z/dz , and dB_x/dx . Using these coils, the magnetic field gradients were compensated such that the spatial variation in the magnetic field was $< 0.1 \mu\text{G}/\text{cm}$ at the condensate, resulting in a $\lesssim 1 \mu\text{G}$ difference across the extent of the gas.

5.3.2 Modulated magnetic fields

The noise sources in the magnetic field environment were characterized by rf frequencies up to 100 kHz, with intermittent sources between 100 kHz and 130 kHz, which greatly limiting the study of spin dynamics at low magnetic fields. Thus, to prevent their influence on our studies of spin-mixing dynamics, we first operated at a magnetic field where the noise in the magnetic field environment had no frequency component resonant with the energy scales in our system, and second, introduced the use of modulated magnetic fields.

Quadratic Zeeman shift

Modulated magnetic fields were introduced into our system through a linearly polarized microwave field, detuned from the $|F = 1, m_F = 0\rangle$ to $|F = 2, m_F = 0\rangle$ hyperfine transition. The applied microwave field induces an ac quadratic Zeeman shift, which is either positive or negative, depending on the sign of the detuning from resonance. The resulting ac field-induced quadratic Zeeman shift is

$$q_\mu = -\hbar\Omega_R^2/4\delta, \quad (5.10)$$

where Ω_R is the Rabi frequency and δ is the detuning from the $|F = 1, m_F = 0\rangle$ to $|F = 2, m_F = 0\rangle$ hyperfine transition. Using the microwaves, the quadratic shift of q_μ was used to tune the total quadratic shift

$$q = q_B + q_\mu \quad (5.11)$$

$$= q_B - \hbar\Omega_R^2/4\delta, \quad (5.12)$$

by varying the Rabi frequency Ω_R and by choosing the sign of δ , enabling the necessary control to explore the $F = 1$ spinor phase diagram (Figure 5.1). In practice, the typical detuning was $\delta = \pm 2\pi \times 40$ kHz from the $|F = 1, m_F = 0\rangle$ to $|F = 2, m_F = 0\rangle$ hyperfine transition and the maximum Rabi frequency was $\Omega_{R_{max}} = 2\pi \times 5$ kHz. At this detuning, we expected an insignificant admixture of atoms from the $F = 2$ hyperfine state ($< 3\%$).

5.3.3 Spin Mixtures

To probe the equilibrium magnetic phases of an $F = 1$ spinor gas, we examined the magnetic order of gases produced by gradually cooling unmagnetized thermal spin mixtures into the regime of quantum degeneracy. These unmagnetized gases, characterized by zero vector spin, were prepared with zero longitudinal magnetization ($\zeta_1 = \zeta_{-1}$) and zero transverse magnetization (no coherences among the Zeeman sublevels). Under these constraints,

we studied the equilibrium magnetic phases of our spinor gas using three different initial spin compositions: $\eta = 0$, $\eta = 1/4$, $\eta = 1$, where η is defined as $\eta = \zeta_0 - \zeta_1$ and $(\zeta_1, \zeta_0, \zeta_{-1})$ denote the fractional populations within the three Zeeman sublevels (eigenstates of F_z). By performing the experiment under different initial conditions, we were able to determine whether the magnetic phases observed are independent of the initial condition.

The $\eta = 0$ thermal spin mixture requires equal population within the Zeeman sublevels, $\zeta_{m_F}^{th} = (1/3, 1/3, 1/3)$. To obtain this spin composition which is both thermal and has zero transverse magnetization, we started with a thermal gas ($T > T_c$) and applied a sequence of approximately 10 $\pi/2$ rf pulses while in the presence of a magnetic field gradient (≈ 50 mG/cm). The combination of an inhomogeneous magnetic field, the rapid Larmor precession about the magnetic field, and the rf pulse sequence, served to decohere the sample from diffusion [51], but also caused a random sampling of the Bloch sphere, resulting in an equal distribution of atoms within the Zeeman sublevels. To determine the population within the sublevels, we used Stern-Gerlach analysis, where a magnetic field gradient was applied to the atoms and was used to spatially separate the Zeeman sublevels before being illuminated with resonant imaging light. We also verified the absence of longitudinal and transverse magnetization by using phase contrast imaging [51].

To create the $\eta = 1/4$ thermal spin mixture, a single resonant $\pi/2$ rf pulse was applied, rotating the magnetization in a plane perpendicular to the magnetic field. Following the $\pi/2$ rf pulse, a transient magnetic field gradient of 50 mG/cm was applied to the atoms for times up to 400 ms to decohere the gas. This resulted in an incoherent thermal spin mixture with fractional populations within the Zeeman sublevels, characterized by $\zeta_{m_F}^{th} = (1/4, 1/2, 1/4)$. The initial populations and magnetization of the gas were characterized using Stern-Gerlach time-of-flight (TOF) analysis and phase contrast imaging.

To create the $\eta = 0$ thermal spin mixture, we applied a single $\pi/2$ rf pulse, followed by a large transient magnetic field gradient (≈ 30 G/cm), expelling atoms in the $m_F = \pm 1$ Zeeman sublevels. Using this technique was less efficient than a series of microwaves sweeps, but ultimately more reproducible. To verify the spin composition, we used Stern-Gerlach analysis at high quadratic shift. This was to avoid any confusion due to population within the $m_F = \pm 1$ states that occur via spin-mixing collisions.

5.4 Experiment 1

In this experiment, we began with 4×10^7 magnetically trapped ^{87}Rb atoms in the $|F = 1, m_F = -1\rangle$ state at a temperature of $1.5 \mu\text{K}$. The sample was then transferred to an optical dipole trap, characterized by initial trap frequencies of $(\omega_x, \omega_y, \omega_z) = 2\pi \times (80, 800, 9)$ Hz, using linearly polarized light, derived from a free-running diode laser at 825 nm. By applying resonant rf pulses as described above, unmagnetized thermal spin mixtures were created. Following this procedure, the spin mixtures were evaporatively cooled by decreasing the intensity of the optical trap over a time scale of 200 ms. Upon reaching the desired trap depth, the samples were then allowed to equilibrate for an additional 200 ms.

Throughout the equilibration and evaporation periods, a static magnetic field of $B = 167$ mG was applied along the \hat{z} axis, where the coordinate system is defined with respect to the optical trap, with the long axis of the trap defined as the \hat{z} axis, and the

most tightly confined direction, (parallel to gravity) the \hat{y} axis. The magnetic field caused the magnetization in the $\hat{y} - \hat{x}$ plane to precess about the \hat{z} axis at a Larmor precession frequency of $\Omega_L = 2\pi \times 110$ kHz. In addition to the rapid precession, this magnetic field also induced a quadratic Zeeman shift of $q_B/h \simeq 2$ Hz, which reduced the relative energy of the $|m_F = 0\rangle$ to the $|m_F = \pm 1\rangle$ states.

To quantify the evolution of these spin mixtures, we imaged them using two methods: TOF absorption imaging and phase contrast imaging. The first method is used to extract the bulk properties of the spin mixtures, mainly the atom number, condensate fraction, and temperature within each Zeeman sublevel. Phase contrast imaging is used to obtain a detailed image of the spatial vector magnetization profile. This was done by taking a sequence of phase-contrast images using $1.5 \mu\text{s}$ -long imaging pulses with circularly polarized light propagating along the \hat{y} direction. As described in Chapter 3, a temporally evolving precession signal was then recorded, where the amplitude and phase of this signal was used to extract the transverse magnetization density $\tilde{\mathbf{M}}_{\perp} = (g_F \mu_B) \tilde{n} \mathbf{F}_{\perp}$, where \tilde{n} is the integrated column density [51, 3]. The results of these analyses are discussed in detail in [135], but will be briefly reviewed here for clarity.

5.4.1 $\eta = 0$ spin mixture results

From measurements made in TOF, we observed a few classic hallmarks of a three-dimensional Bose gas. At the highest temperatures, well above the condensation temperature, the density profile imaged in TOF most closely resembled a Gaussian profile. Upon cooling the gas below the condensation temperature, a bimodal profile was observed. To quantify these observations, we TOF density profiles were fitted to the sum of a Gaussian and parabolic distribution, with the fitted number within the Gaussian and parabolic profiles associated with the thermal (N_{th}) and condensate number (N_c). From these measurements, we were able to extract the condensation temperature, T_{c,N_0} , where the density profile first becomes bimodal. This is consistent with the theoretical prediction for a scalar Bose gas, where T_{c,N_0} is defined as

$$T_{c,N_0} = \hbar\bar{\omega}(N_0/1.21)^{1/3} \quad (5.13)$$

and N_0 is defined as the number in the $|m_F = 0\rangle$ state. We also obtained a measure of the condensate fraction, derived from the following equation

$$\frac{N_c}{N_{th} + N_c} = 1 - \left(\frac{T}{T_c}\right)^3, \quad (5.14)$$

and observed fairly good agreement with this theoretical prediction (see Figure 5.3). We also note that the populations within each Zeeman sublevel remained roughly equal for each iteration of the experiment, independent of the final temperature.

Given the striking similarities of the features observed in TOF between those of the spin mixtures and those of a scalar Bose condensates, we expected no new features when imaging the vector magnetization profiles. Above the condensation temperature, the magnetization remained roughly zero, evident by the lack of Larmor precession in the images. This expected observation is due to the reduced cross-section for the spin-mixing

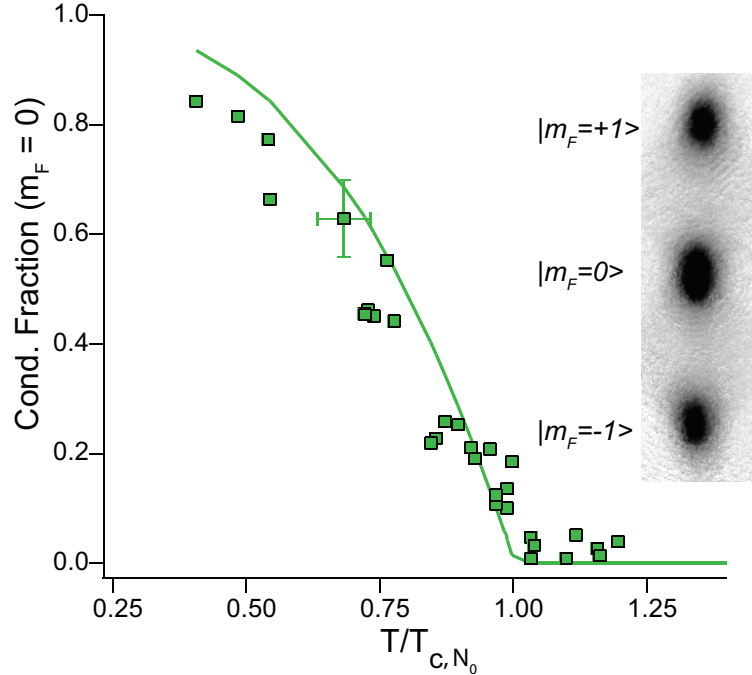


Figure 5.3: Condensate fraction as a function of the final temperature for an $\eta = 1/4$ spin mixture. Similar results were also observed for an $\eta = 0$ spin mixture.

collision rate in a thermal gas, where these collisions are necessary to establish the long-range ferromagnetic order. However, upon cooling the spin mixtures below T_{c,N_0} , the spin mixture spontaneously magnetized. The strength of the magnetization, as indicated by the brightness in each image of Figure 5.4, was equally distributed between the transverse and longitudinal components. Surprisingly, the magnetization profile was not homogenous, but showed a myriad of short-ranged modulations, appearing in both the transverse and longitudinal magnetization profiles. Qualitatively, the spin modulations appeared to occur in a somewhat regularly occurring “crystalline” pattern, with a characteristic spatial length scale of $\simeq 10 \mu\text{m}$.

5.4.2 $\eta = 1/4$ spin mixture results

For $\eta = 1/4$, we observed qualitatively different features. From TOF analysis, the distribution of atoms within the Zeeman sublevels remained roughly close to the initial composition for temperatures above T_{c,N_0} . This was quite surprising since we naively expected the population within the Zeeman sublevels to quickly redistribute to an equilibrium configuration, with equal thermal populations within each level. This unexpected result is attributed to the reduced cross-section for the spin-mixing collision rate in the thermal gas, preventing the populations within the Zeeman sublevels from becoming equally distributed within the accessible experimental timescales explored here. This was observed for temperatures above T_{c,N_0} . However, upon lowering the temperature below T_{c,N_0} , we observed

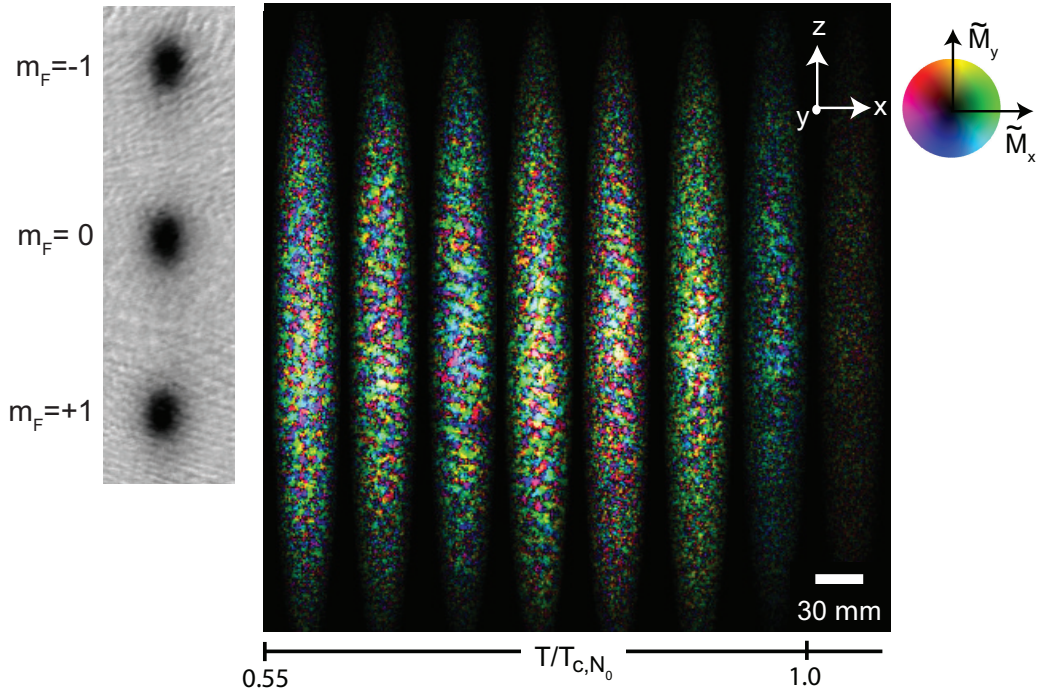


Figure 5.4: TOF density profile and *in-situ* transverse magnetization profile of spin textures at various temperatures for an initial thermal spin mixture with $\eta = 0$

the onset of condensation in the $|m_F = 0\rangle$ state, evident in the bimodal distributions in the TOF images. Accompanying this onset, we observed the thermal component of the gas rapidly equilibrate to equal populations within the three Zeeman sublevels, likely due to the strong enhancement of spin mixing collisions driven by the large density of the condensate in the $|m_F = 0\rangle$ state. The condensed portion of the gas, however, remained fairly close to the initial composition, evident in images of the TOF momentum distributions.

Imaging the gas using magnetization imaging, we observed two magnetic phases in the magnetization profiles, in contrast to the single magnetic phase observed in the $\eta = 0$ spin mixture. Upon lowering the temperature just below T_{c,N_0} , we observed the abrupt onset of magnetization, characterized by a fairly uniform spin texture and with a length scale of roughly 50-100 μm . This phase persisted as the temperature was decreased and it is only when we decreased the temperature of the gas below $0.75T_{c,N_0}$ that we observed a periodic modulation in the magnetization. The magnetization at this point was characterized by a short wavelength modulation superimposed with the long wavelength modulation, predominantly oriented predominantly in the $\hat{x} - \hat{y}$ plane (see Figure 5.5). We attribute the spin-space asymmetry of the magnetization from the asymmetry of the population of condensed atoms within the Zeeman sublevels. We can understand this if we think of atoms in $|m_F = 0\rangle$ state as superposition of atoms with spins oriented along $\pm\hat{x}$. From this perspective, the $|m_F = 0\rangle$ condensate atoms act like a transverse magnetization reservoir, where for low values of the quadratic shift, q , the condensate is dynamically unstable to the formation of transverse magnetization [52, 83, 136]. Thus, the initial composition of the

$\eta = 1/4$ spin mixture has a natural inclination towards magnetization oriented in the transverse plane.

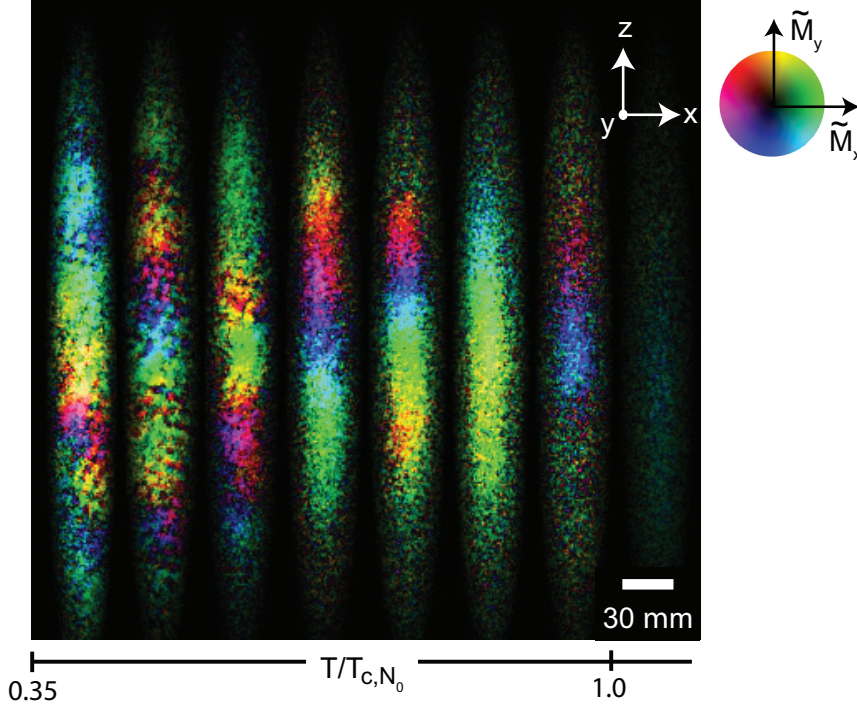


Figure 5.5: *In-situ* transverse magnetization profile of spin textures at various temperatures for an initial thermal spin mixture with $\eta = 1/4$.

5.4.3 Characterizing the magnetic order

To quantitatively describe these magnetic phases, we make use of the spatial Fourier transform of the vector magnetization, $\tilde{M}(k_x, k_y)$. In particular, we extract the spectral power of the condensate magnetization, $|\tilde{M}(k_x, k_y)|^2$, for each transverse magnetization component. We take the average of the two spectral powers and use this to characterize the short- and long-range magnetic order. For the $\eta = 0$ initial spin mixture, spectral peaks become visible immediately below T_{c,N_0} and are primarily concentrated at an inverse length scale of $\lambda^{-1} \simeq 10 \mu\text{m}^{-1}$. The orientation of the modulations is characterized by two wave vectors which are pinned to the optical trap axis. This was verified by observing a rotation of the modulation orientation when rotating the optical trap about the \hat{y} axis. The absence of a spectral peak at zero wave vector is an indication of the lack of long-range ferromagnetic order in the $\eta = 0$ mixture.

The $\eta = 1/4$ mixture, however, shows no short-range order immediately below T_{c,N_0} . In fact, we find that the all of the spectral power is concentrated at zero wave vector, where the anisotropic profile of this component reflects the aspect ratio of the trap. As observed in the magnetization profile, at $T \leq 0.75 \times T_{c,N_0}$, the spin modulation pattern reveals itself in the form of short-range magnetic order in the spectral power. These

modulation components are characterized by two wave vectors, as seen in the $\eta = 0$ images, showing a similar orientation. Decreasing the temperature further, we observe that the spectral weight at the two wave vectors increases until approximately 50% of the total power is concentrated in the short-range modulation, occurring at the lowest attained temperatures and confirming our qualitative analysis of the *in-situ* magnetization images.

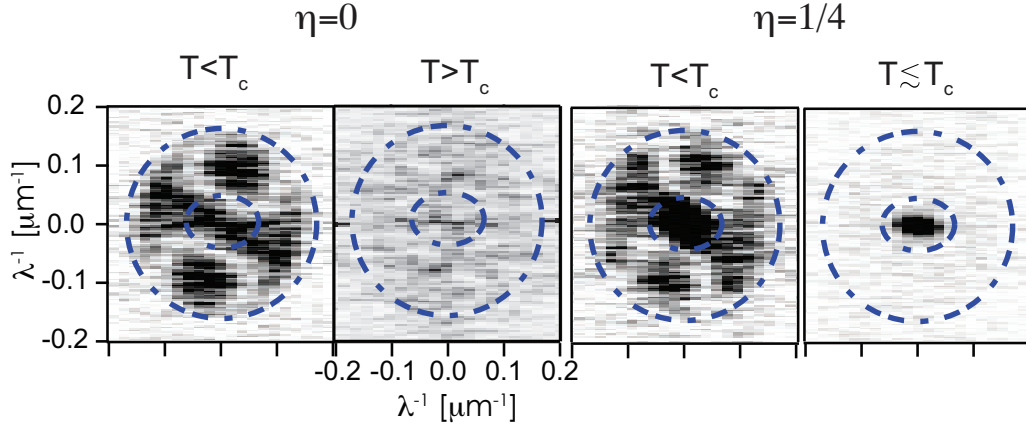


Figure 5.6: Power spectra for $\eta = 0$ and $\eta = 1/4$ spin mixtures. Shown are two sets of images for each spin mixture for two different temperatures. For $T > T_{c,N_0}$, the spin mixtures show no magnetic order, but for lower temperatures, magnetic order in the form of short- and long-range modulations appear, occurring at two distinct wave vectors. The orientation of the modulations coincides with an angle of $\approx 20^\circ$ with respect to the trap axis.

Dipole-Dipole interactions

The “crystalline” magnetic phase observed for the $\eta = 1/4$ mixture appears in the magnetization profile at a temperature that is roughly $0.75T_{c,N_0}$. The fact that this phase occurs at a temperature different from the theoretical prediction for Bose condensation suggests that it is perhaps mediated by some interaction other than the coherent spin mixing which establishes the long-range magnetic order observed at temperatures immediately below T_{c,N_0} . Fine measurement and control of the temperature have allowed us to pinpoint the exact location of this magnetic phase, occurring at $T \simeq 130$ nK. Using this temperature as an estimate for the strength of the mediating interaction, we find close agreement to the dipolar interaction energy between two spins. To understand this, we compute the potential energy between one spin and the magnetic field generated by an adjacent spin as

$$|U_{dd}| = \mu \cdot B \quad (5.15)$$

$$\sim \frac{\mu_0}{4\pi} \frac{1}{l^3} \mu^2, \quad (5.16)$$

where $\mu = \mu_B g_F$ is the magnetic moment, μ_B is the Bohr magneton, μ_0 is the magnetic permeability, and l is the separation between the spin domains. Taking the magnetic moment

of the spins to be

$$\mu \simeq N g_F \mu_B, \quad (5.17)$$

where the total number is $N = \tilde{n}l^2$, \tilde{n} is the integrated column density, and l is the distance between spin domains ($\sim 10 \mu\text{m}$), we arrive at an estimate for the dipolar energy,

$$|U_{dd}| \sim \mu_0 (g_F \mu_B \tilde{n} l^2)^2 / l^3. \quad (5.18)$$

Using typical experimental parameters, we estimate the dipolar energy to be ~ 100 nK, where we have assumed a condensate density $n = 2 \times 10^{14} \text{ cm}^{-3}$ and $N \simeq 10^6$. From this simple calculation, we find very good agreement between this estimate of the dipolar energy and the energy equivalent occurrence of the “crystalline” phase.

5.4.4 Equilibrium Properties?

The differences in the magnetic phases for each spin mixture is attributed to the dynamics that give rise to the ferromagnetic order below T_c . For $\eta = 0$, Bose condensation occurs simultaneously in all three Zeeman sublevels, from which each level is able to spontaneously magnetize. In contrast, for the $\eta = 1/4$ spin mixture, Bose condensation occurs first in the predominately occupied $|m_F = 0\rangle$ state, with a condensate forming on the time scale determined by the collision rate, $1/\tau_{BEC} \sim \text{kHz}$. Following this, coherent spin mixing then mediates the formation of transverse magnetization, taking the form of the long-range ferromagnetic order, occurring on a time scale $\tau_{SM} \sim \hbar/c_2 \langle n \rangle \gg \tau_{BEC}$. To verify this understanding, using the same experimental sequence described above, we prepared an $\eta = 1/4$ spin mixture at large quadratic shifts where a polar state is dynamically stable. Indeed the absence of spin mixing collisions was apparent in both the magnetization profiles and the TOF momentum distributions, where no transverse magnetization or bimodal distributions in the $|m_F = \pm 1\rangle$ states were observed.

The consistency of the “crystalline” phase raises the question as to whether this is an equilibrium phenomenon or a long-lived metastable phase. To address this question, we temporally resolved the evolution of these mixtures for different evolution times. First, we measured the equilibration timescale for the thermal components within each Zeeman sublevel to equalize for $\eta \neq 0$ spin mixtures. This was done for $\eta = 1/4$ and $\eta = 1$ spin mixtures, which present an out-of-equilibrium composition for the thermal atoms. Immediately below T_{c,N_0} , the thermal population becomes equally distributed among the sublevels within 100-150 ms of reaching the final trap depth. This timescale was observed for both the $\eta = 1/4$ and $\eta = 1$ spin mixtures. Additionally, we also observed similar magnetic phases beginning with an $\eta = 1$ spin mixture. Below T_{c,N_0} long-range ferromagnetic order appears, followed by a modulated magnetic phase for lower temperatures, as seen in the $\eta = 1/4$ spin mixture (Figure 5.7). Furthermore, altering the evaporation trajectory by decreasing cooling rate or doubling the evolution times showed no quantitative difference in the TOF distributions or the observed magnetic phases. The consistent observation of the short-range ferromagnetic order, which seems to be independent of the initial conditions, equilibration time, and evaporation trajectory suggests that this is potentially an equilibrium property of an $F = 1$ spinor gas [135].

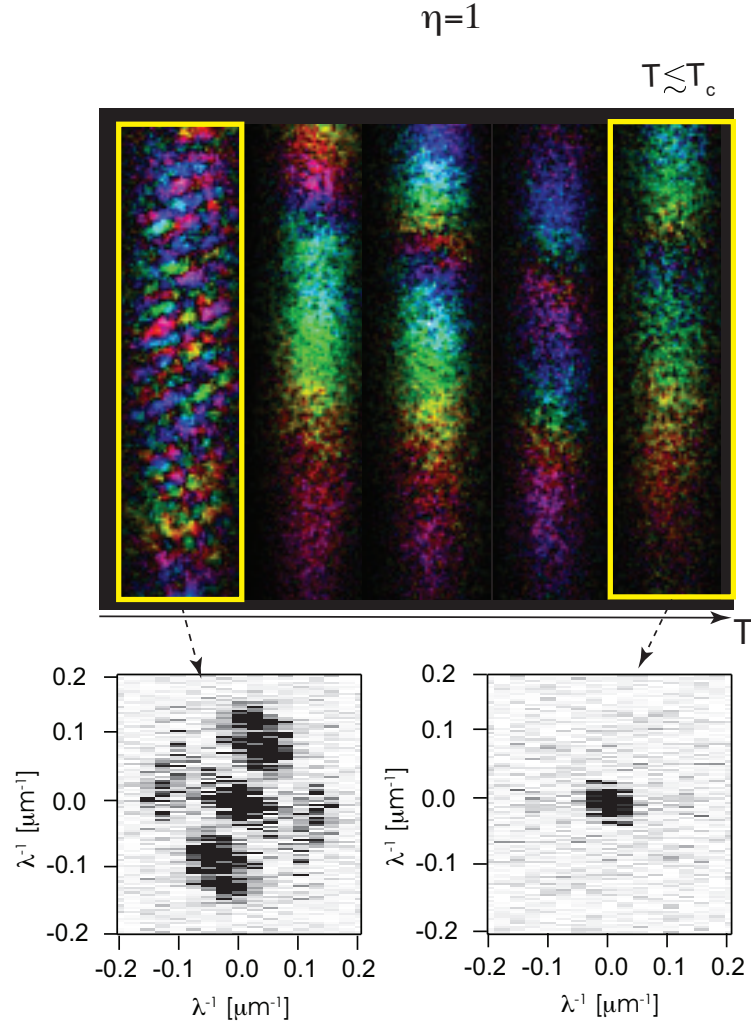


Figure 5.7: Images of the transverse magnetization profile for an initial $\eta = 1$ spin mixture, probed 150 ms after reaching the final optical trap depth. Similar to the $\eta = 1/4$ spin mixture, below T_{c,N_0} , the gas shows fairly uniform regions of transverse magnetization. Cooling the sample further, we observe the emergence of short wavelength modulation, characterized by a length scale of $\approx 10 \mu\text{m}$. This is easily seen in the spatial Fourier transform, composed from a single image of the magnetization profile (not averaged). Evident in these images is the long-range ferromagnetic order near T_{c,N_0} and the appearance of short-range magnetic order at lower temperatures. In addition, there is an asymmetry in the distribution spectral power, with the modulation primarily along one axis.

5.5 Equilibrium Properties: Attempt 2

The results reported in [135] provide a very convincing argument that dipolar interactions may be important in determining the ground state structure for spinor Bose gases. However, such studies were limited to short evolution times (< 300 ms), due to condensate

lifetimes of ~ 1 s. Thus, we repeated the studies discussed above with a new experimental chamber to verify, or at least to provide some clarity for the surprising results on a new modulated magnetic phase [135, 113]. In particular, we probed the phase diagram for the $F = 1$ spinor gas by performing measurements on the temporal evolution of unmagnetized spin mixtures at a variable quadratic Zeeman shift.

5.5.1 Apparatus Improvements

Before performing these studies, we had a major overhaul of the experiment. The apparatus used in [135, 83, 113, 52, 51] was replaced in the spring of 2009. The experimental apparatus is thoroughly reviewed in Chapter 2, but will be briefly reviewed here.

- The atoms are magnetically transported 200 mm to a glass cell yielding improved optical access.
- Increased magnetic bias and gradient control along with improved vacuum has allowed for evolution times as long as several seconds.
- The vector magnetization profile is measured using spin-echo imaging.

5.5.2 Experimental Sequence

For these studies, we collect spin-polarized atomic samples of ^{87}Rb atoms in the $|F = 1, m_F = -1\rangle$ state at a temperature of $30 \mu\text{K}$ in an optical dipole trap (ODT) derived from a free-running linearly polarized Ytterbium fiber laser, characterized by trap frequencies of $(\omega_x, \omega_y, \omega_z) = 2\pi(220, 4150, 63)$ Hz. The spin mixtures are created by the application of resonant $\pi/2$ rf pulses in the presence of a magnetic field gradient. The spin mixtures are then cooled by lowering the power of the optical trap over 2.4 s to final trap frequencies of $(\omega_x, \omega_y, \omega_z) = 2\pi(25, 380, 7.3)$ Hz. At the final trap depth, the mixtures, typically containing 3×10^6 atoms with a peak density $n_p = 1.3 \times 10^{14} \text{ cm}^{-3}$, are allowed to equilibrate for timescales up to 4 s.

Throughout the evaporation process, both static and modulated magnetic fields were applied. A uniform magnetic field of $B=267$ mG, oriented along the \hat{x} axis is applied, where the spatial coordinates are referenced with respect to the optical trap axes. Using this convention, \hat{y} is parallel to gravity and \hat{z} is along the more weakly confined direction of the optical trap. The magnetic field gradients were reduced to 0.1 mG/cm, resulting in a spatial inhomogeneity of less than $1 \mu\text{G}$ across the extent of the gas. The magnetic field gives rise to a quadratic Zeeman energy shift of $q_B = h(70.6 \text{ Hz/G}^2)B^2 \approx h \times 5$ Hz. In addition, a linearly polarized microwave field, with Rabi frequency Ω and a detuning of $\delta/2\pi = \pm 40$ kHz from the $|F = 1, m_F = 0\rangle$ to $|F = 2, m_F = 0\rangle$ hyperfine transition was applied. By tuning the Rabi frequency and the sign of the detuning, we were able to tune the total quadratic shift, $q = q_B + q_\mu$ [83, 137]. For this study, the polar to ferromagnetic phase transition is $q_0 = 2|c_2|n_p = h \times 10$ Hz.

5.5.3 Temporal Evolution

To first verify that we are observing the equilibrium tendencies within the accessible experimental time scales of the experiment, we made time resolved measurements of the fractional populations within the Zeeman sublevels imaged in TOF.

TOF Results

Beginning with an $\eta = 0$ thermal spin mixture, we perform time-resolve measurements of the gas and repeated this for different quadratic shifts. We characterize these measurements by fitting the data to a bimodal distribution and extract the condensate fraction within each Zeeman sublevel. Shown in Figure 5.9 is the fractional population of atoms within the $|m_F = \pm 1\rangle$ states, defined as

$$\zeta_{\pm 1} = \frac{1}{2} \times \frac{\zeta_{+1} + \zeta_{-1}}{N_{total}}, \quad (5.19)$$

where N_{total} is the total atom number. At short equilibration times, we observe the emergence of a bimodal distribution, within each Zeeman sublevel, appearing as early as $t \simeq -50$ ms, where t denotes the evolution time after reaching the final optical trap depth. Following this and for the next ~ 300 ms, the distribution of atoms within the Zeeman sublevels remains close to its initial spin composition. For $t > 300$ ms, however, we observe three clear trends in the data. First, the fractional population shows a dependence on the quadratic Zeeman shift. For negative values of q , the populations tends toward $\zeta_{\pm 1} = 0.5$, for positive values it tends toward zero, and for $q \approx 0$, $\zeta_{\pm 1} = 1/3$. Second, the populations appear to reach steady-state values within 1-2 seconds, thus ensuring that the measurements made are representative of the equilibrium properties of the system. Third, the observed tendencies are independent of the initial spin composition, as similar results were observed starting with an $\eta = 1/4$ thermal spin mixture (Figure 5.9 (bottom)). Thus it appears that the within a 1 – 2 s evolution window, we are able to achieve equilibrium.

At large quadratic Zeeman shifts, however, we do not observe steady-state behavior. This is seen by comparing the population distribution among the Zeeman sublevels for large and small quadratic Zeeman shifts. Plotted in Figure 5.10 is a time-resolved scan for an $\eta = 1/4$ spin mixture for quadratic shifts that range from -66 Hz to 4 Hz. From this scan we note a few interesting features. First, within the range $-6 < q/h < 0$ Hz, the fractional populations tend towards $\zeta_{\pm 1} = 0.5$, with the fractional populations in $\zeta_{\pm 1}$ increasing with decreasing values of the quadratic shift. Decreasing the quadratic shift further, we do not observe a corresponding increase in the fractional population, $\zeta_{\pm 1}$, as the fractional population remains close to the values measured at $q/h = -6$. Beyond $q/h \approx -15$ Hz, however, $\zeta_{\pm 1}$ decreases with increasing quadratic shifts, evident in the data taken at $q/h = -26$ Hz and $q/h = -66$ Hz. While these spin mixtures do show evolution towards the presumed equilibrium distribution, the timescales appear to be far slower than those observed for $|q/h| \leq 10$ Hz. Thus, it appears that within these experimental accessible timescales, equilibrium can only be achieved for a narrow range of quadratic Zeeman shifts, $|q/h| \leq 10$ Hz.

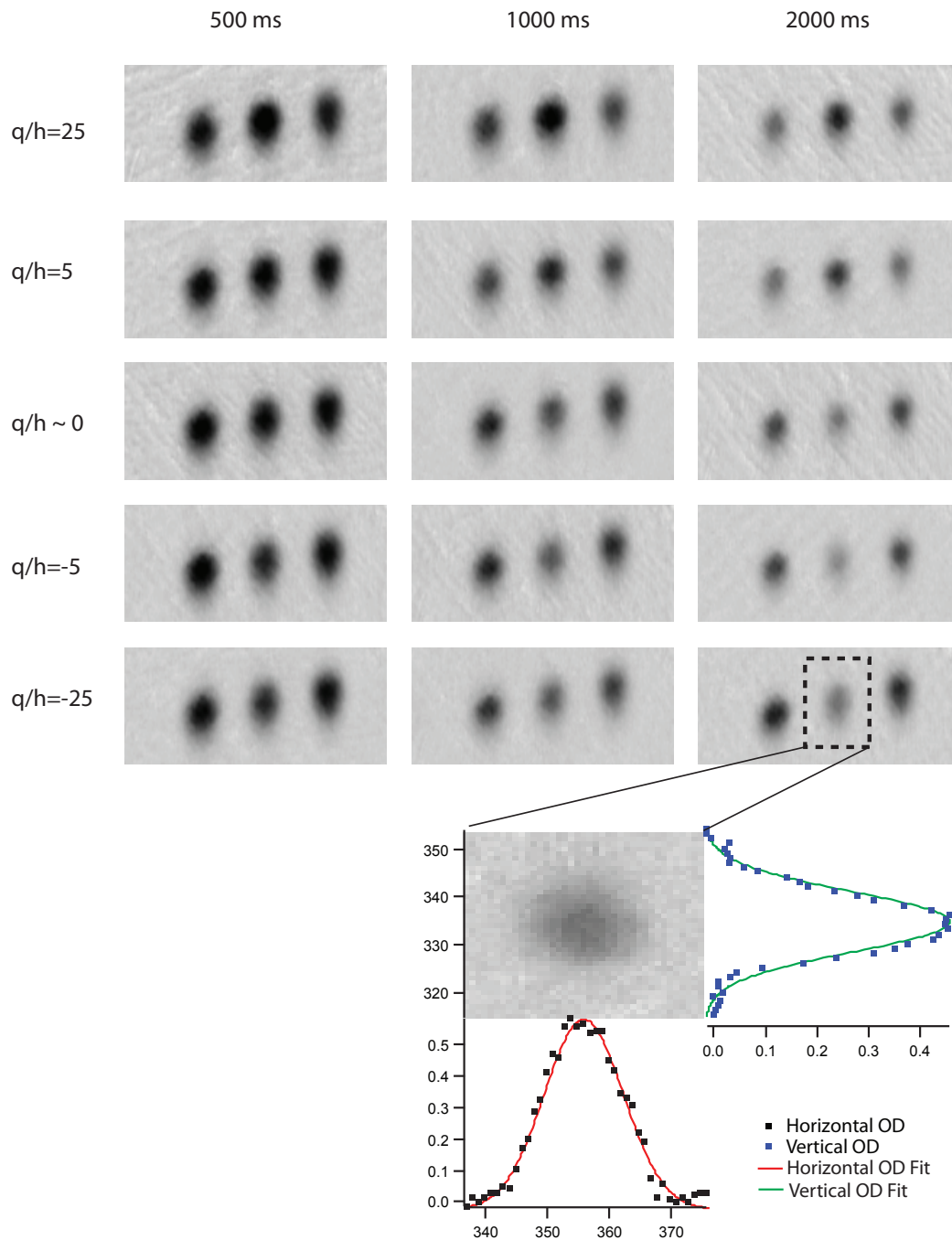
$\eta=0$ 

Figure 5.8: Sample TOF images for an $\eta = 0$ spin mixture for different applied quadratic Zeeman shifts and different evolution times. Samples are heated by being over-repumped for 6-10 ms and the number of atoms is estimated using a fit to a Gaussian profile.

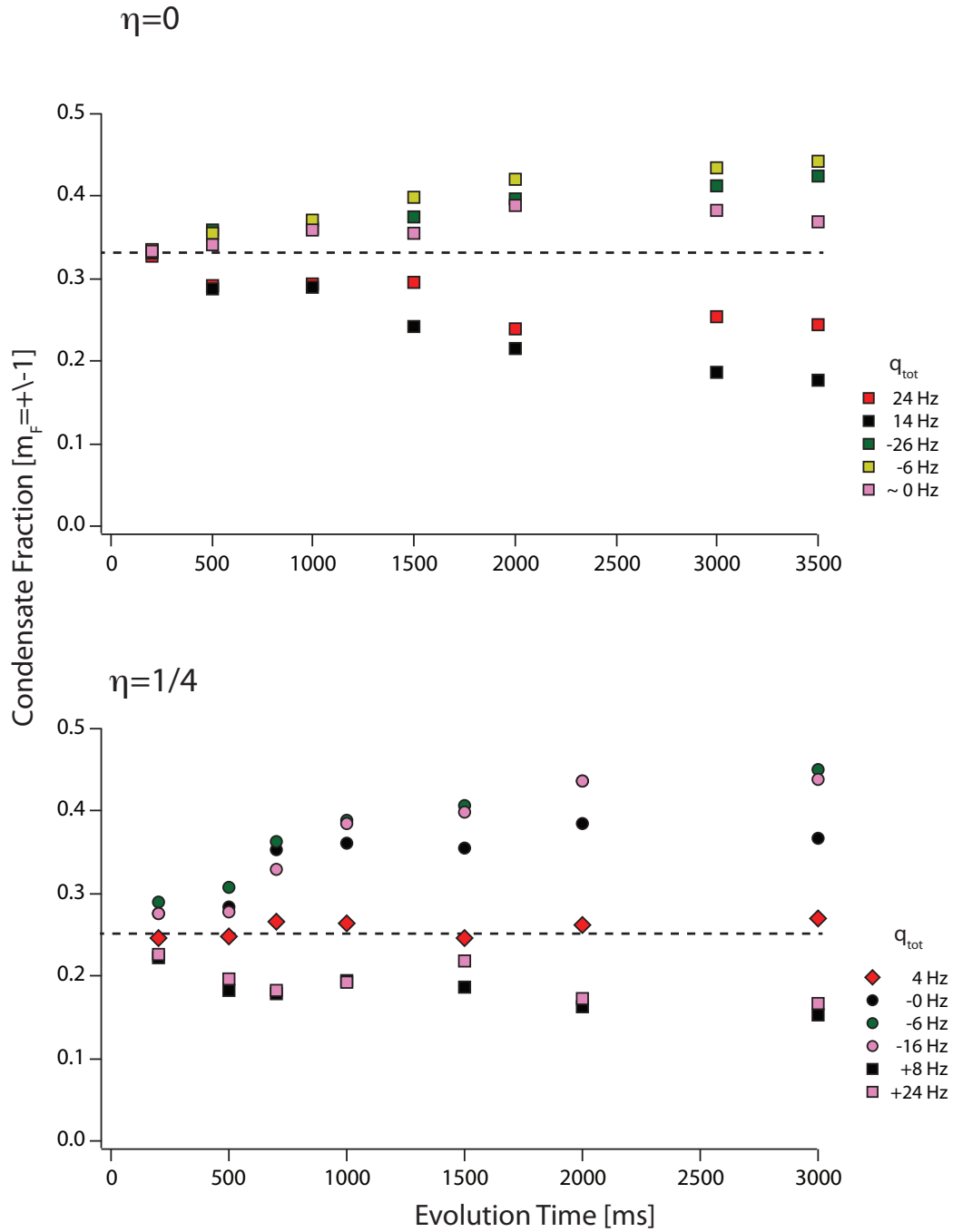


Figure 5.9: Temporal evolution of condensate fractions within the $|m_F = \pm 1\rangle$ states for different applied quadratic Zeeman shifts for $\eta = 0$ (top) and $\eta = 1/4$ spin mixtures. (top) The condensate fraction evolves from the initial spin composition, and evolves toward a distribution that depends on q . This fraction evolves toward $1/2$ for $q/h < 0$, $1/3$ for $q/h = 0$, and 0 for $q/h > 0$ within $1.5 - 2$ s evolution time, after which it ceases to change. These same tendencies and equilibration timescales are also observed starting with $\eta = 1/4$ spin mixture shown in the bottom plot.

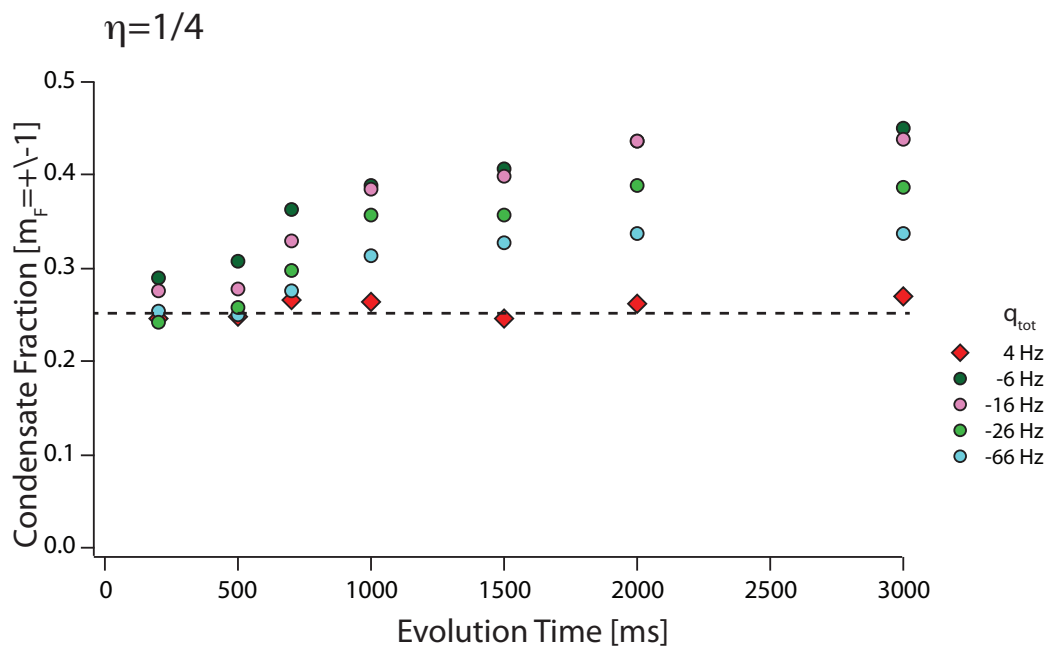


Figure 5.10: Temporal evolution of condensate fraction for and $\eta = 1/4$ thermal spin mixture for quadratic shifts ranging from -66 Hz to $+4$ Hz. The condensate fraction continues to evolve towards $\zeta_{\pm 1} = 0.5$ for quadratic Zeeman shifts near $|q/h| < 10$ Hz, after which the evolution is stalled. The condensate fraction for $|q/h| \geq 10$ Hz remains close to its initial spin composition, despite seconds long evolution time, easily seen in the fractional population taken at $q/h = -66$ Hz.

In-situ Results

While the TOF populations measurements are useful in determining the timescales for equilibration, they do not contain information regarding the magnetization of the gas or the spatial composition of spin domains.

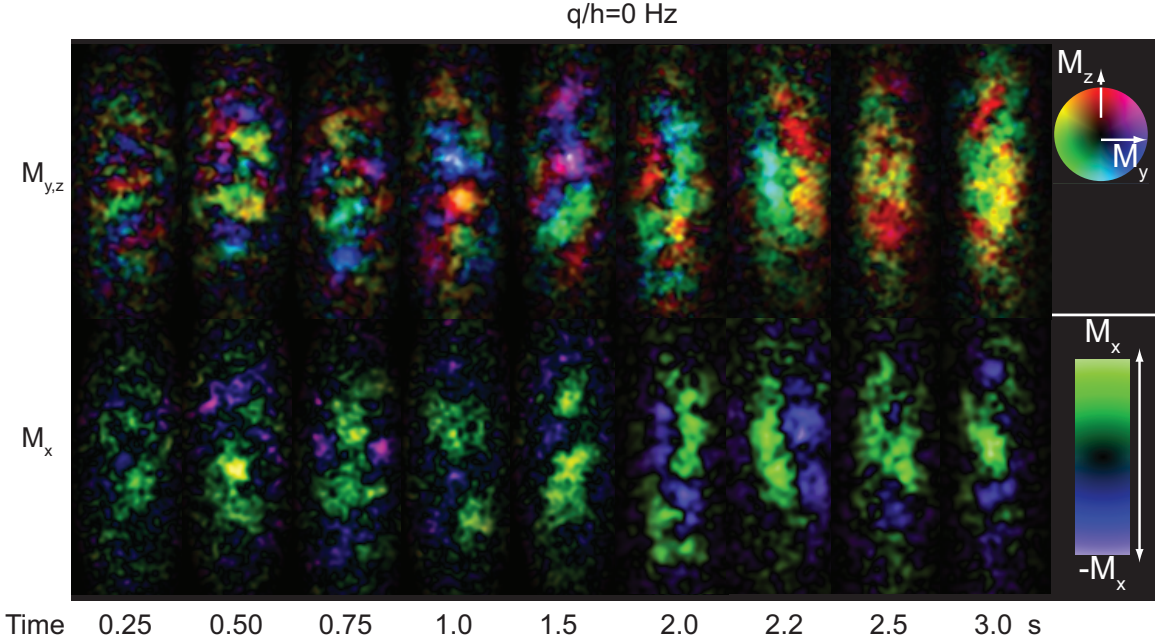


Figure 5.11: Transverse (top) and longitudinal magnetization (bottom) for an initial $\eta = 0$ thermal spin mixture after a variable evolution time at $q/h = 0$ Hz. Here the magnetization strength and orientation are indicated by the brightness and color. At short evolution times, the spatial magnetization profile is dominated by small domains, randomly oriented. At late times, the small domains are replaced by larger domains, with length scales that are comparable to the long axis of the condensate. The data included here have been blurred using a 3×3 Gaussian filter and have been cropped to include only the condensate.

To measure the vector magnetization of the condensate, we made use of a sequence of non-destructive phase contrast images as described in Chapter 3. After a specified evolution time, a sequence of phase-contrast images was taken using ~ 200 ns-long imaging probe pulses using linearly polarized light propagating along the thin axis of the condensate (\hat{y} axis). The vector magnetization of the condensate was then acquired by employing spin-echo-imaging, where accurately timed probe pulses were used to obtain a direct snapshot of the magnetization density, $\tilde{M}_{x,y} = \tilde{n}F_{x,y}$, where \tilde{n} is the column number density [51, 3, 104].

Focusing our studies to small quadratic Zeeman shifts ($|q/h| \lesssim 10$), we conducted a time-resolved scan of the vector magnetization starting with an $\eta = 0$ spin mixture. Representative images are shown in Figure 5.11 for evolution times ranging from 250 ms to 3 s, at $q/h = 0$. For short evolution times, $t < 200$ ms, the observed condensate magnetization profile was fairly homogeneous, lacking any pronounced spatial features. We attribute this to

two possibilities. One possibility is that the measured magnetization variance is equivalent or smaller than the noise floor of our imaging system. Another possibility is the size of the domains present are smaller than the resolution of our imaging objective, $< 2 \mu\text{m}$.

For longer evolution times, the magnetization profile is comprised of a spatially inhomogeneous pattern of spin domains. Within a few hundred milliseconds, the longitudinal and transverse magnetization profiles are comprised of a mix of domains and domain walls, oriented isotropically in space. The domains are characterized by $\sim 8 - 10 \mu\text{m}$ length scales, in agreement with previous results discussed above, but show no obvious preferred modulation axis (see power spectrum below).

However, probing the spin mixture for longer evolution times ($t > 500 \text{ ms}$), we observed distinct change in both the composition and the spatial arrangement of the spin domains. The magnetization which previously had no preferential orientation, has now developed a quadratic shift-dependent spin-space anisotropy, evident in the magnetization amplitudes for different quadratic shifts (Figure 2 of [104]). For $q < 0$ the magnetization is predominantly concentrated in the longitudinal component, while for $q > 0$ the magnetization is mostly transverse, and for $q \simeq 0$, the magnetization is evenly distributed among the transverse and longitudinal components. Additionally, we also observed the development of larger domains of common magnetization. At the shortest evolution times, the magnetization texture is comprised of small randomly oriented domains, but within $t \simeq 2\text{-}3 \text{ s}$, the magnetization profile is characterized by a more homogenous spin texture, composed of just a few domains that span the entire length of the condensate, each separated by domain walls.

Magnetization correlation function

A good probe to characterize the observed changes in the magnetization profile is the dimensionless correlation function of the i component of the magnetization vector,

$$G_i(\delta\mathbf{r}) = \frac{\sum_{\mathbf{r}} \tilde{M}_i(\mathbf{r} + \delta\mathbf{r}) \tilde{M}_i(\mathbf{r})}{\mu^2 \sum_{\mathbf{r}} \tilde{n}(\mathbf{r} + \delta\mathbf{r}) \cdot \tilde{n}(\mathbf{r})}, \quad (5.20)$$

where $\mu = g_F \mu_B$ is the atomic magnetic moment, and \tilde{n} is the \hat{y} -integrated column density. This correlation function is evaluated over the central $50 \times 160 \mu\text{m}^2$ area of the condensate. Using the correlation function, we are able to obtain a quantifiable measure of the spin-space anisotropy and the characteristic domain size.

Magnetization Variance To quantify the observed spin-space anisotropy, we make use of the magnetization variance, $G(0)$, which measures the ferromagnetic tendency of a condensate, yielding a value of one, when fully magnetized, and zero when unmagnetized. This is accomplished by setting $\delta\mathbf{r} = 0$ in Equation 5.20. We characterize any trends in the longitudinal and transverse magnetization by computing the magnetization variance for each magnetization component, $\tilde{M}_{x,y,z}$ and evaluate this over the central region of the condensate. We denote the longitudinal variance as $G_L(0) = G_x(0)$, and the transverse variance as $G_T(0)$, where $G_T(0)$ is the arithmetic mean of $G_y(0)$ and $G_z(0)$.

To resolve any trends, we extract the magnetization variance from the time-resolved studies of the magnetization profile at quadratic shifts of $0, -5, 5 \text{ Hz}$. For short

equilibration times, $t < 500$ ms, the magnetization variance grows monotonically, with equal amplitude in the longitudinal and transverse components. However, at intermediate evolution times, $500 < t < 1000$ ms, we observe a distinct difference in the variances between $G_T(0)$ and $G_L(0)$ which has a clear dependence on the quadratic Zeeman shift. For $q/h < 0$, a preference for longitudinal magnetization is observed. This is indicated by the brightness in the longitudinal magnetization images (see Figure 2 of [104]) and in the magnetization variance, where $G_L(0) > G_T(0)$. For $q/h > 0$, the opposite is true, as a preference for magnetization oriented in the transverse plane is observed, $G_L(0) < G_T(0)$. Lastly, for $q/h = 0$, we see an isotropic distribution of domains, with $G_L(0) = G_T(0)$. These trends are also observed when starting with an $\eta = 1/4$ spin mixture and persist for the 2-3-second long evolution times accessible in the experiment.

Using the magnetization variance, $G(0)$, we also observe that the vector magnetization of our sample saturates within ~ 2 s evolution time. The total variance is computed from the sum of $G_x(0)$, $G_y(0)$, and $G_z(0)$ for an $\eta = 0$ spin mixture at $q/h = 0$ (Figure 5.12). At short evolution times, the variance is approximately zero. We can understand this as being an indication of zero total magnetization or a magnetization signal which is below or equivalent to our noise floor. However, for intermediate evolution times, $t \lesssim 1500$ ms, the magnetization variance increases monotonically with time, after which it saturates at a total variance of approximately one, where a variance of one is expected for a fully polarized gas. However, for much larger quadratic Zeeman shifts, $q/h = 70$ Hz, we find that the variance increases more slowly, never appearing to approach a steady-state value, in agreement with our preliminary findings from the bulk measurements in TOF.

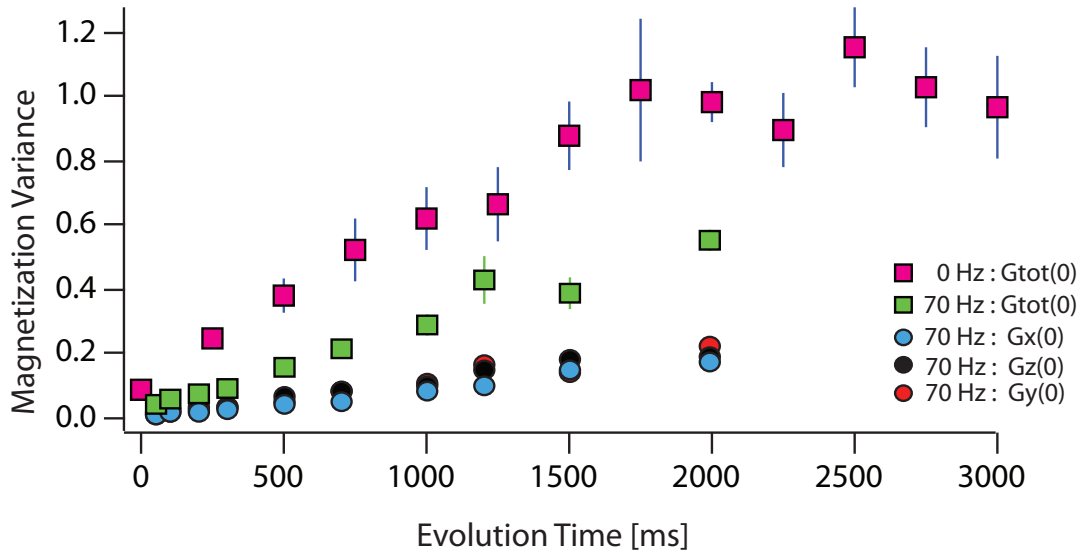


Figure 5.12: Temporal evolution of magnetization variance starting with an $\eta = 0$ spin mixture at $q/h = 0$ Hz and $q/h = 70$ Hz. For $q/h = 0$, the magnetization variance approaches the expected value for a fully polarized gas near $t \simeq 2000$ ms. At larger values of the quadratic shift, $q/h = 70$ Hz, the variance does not appear to reach any steady-state value within the experimentally accessible timescales.

Computing the normalization for $G(0)$ In practice, our variance measurements are subject to noise and to reduce such effects, $\delta\mathbf{r}$ is evaluated over a $3.5 \times 3.5 \mu\text{m}^2$ region centered at $\delta\mathbf{r} = 0$. Additionally, each measure of the variance at a specific evolution time is the average over many repetitions of the experiment, typically 7-8.

In addition, appropriate steps must be taken to ensure proper normalization of the variance. The normalization factor for $G(0)$, corresponding to the amplitude of the variance for a fully magnetized cloud, is typically determined from the magnetization amplitude in the data. That is, assuming we have a fully magnetized sample, we normalize the correlation map of each magnetization component to the amplitude of the correlation map derived from the full vector magnetization near $\delta\mathbf{r} = 0$. However, for shortest evolution times ($t \lesssim 700$ ms), the vector magnetization amplitude of the spin texture is only a fraction of the amplitude for a fully polarized sample, and thus provides the wrong normalization.

We determine the appropriate normalization both empirically and theoretically. For the same initial conditions as the $\eta = 0$ spin mixture, we prepared a transversely magnetized condensate and measured magnetization amplitude after a given evolution time. As expected, over the course of a few seconds, the amplitude of precession diminished due to atom loss. We also compute the magnetization signal and compare this to our measurements. To compute the theoretical normalization, we use condensate number measured in TOF absorption imaging and the functional form of the polarization contrast signal presented in Chapter 3. The two normalizations are shown below (see Figure 5.13) and are in fairly good agreement. Thus, to obtain the correct normalization for the variance measurements presented here, we typically rely on measurements of the atom number measured in TOF and compute the corresponding normalization factor.

Lastly, necessary in the normalization is an accurate determination of the depletion of the magnetization signal during the imaging process. When taking the sequence of images to obtain a measure of the vector magnetization, there is undoubtedly losses due to scattering with the probe beam, resulting in atom loss, scaling as $1/\Delta^2$, where Δ is the detuning of the probe beam from atomic resonance. To account for these losses and to obtain an accurate measure of the magnetization and variance, we model the depletion of the condensate as an exponential decay of the phase contrast signal, $e^{-f_n/\tau}$, where f_n is the camera frame number, and τ is the decay constant of the probe-induced depletion. A fortunate consequence of spin-echo imaging is the sampling redundancy. In particular, multiple snapshots of \tilde{M}_x are imaged within the last few camera frames. Using these repeated images, we can obtain a measure of τ . To do this, we extract the magnetization signal from the central region of the condensate, roughly a 50×100 pixel² region. Next we bin over a 3×3 pixel² region in an effort to reduce noise and fit this data to an exponential. For our typical light intensity and detuning, we find that roughly 50% of the signal has decayed by the time we image the longitudinal magnetization. This decay may seem quite large, especially in comparison to phase contrast imaging when using a phase dot. But recall that the imaging of choice here is polarization contrast imaging, and that when detecting the phase shift, we are only measuring half of the photons. Improvements could definitely be made by devising an imaging setup to measure all of the probe light (see Chapter 3).

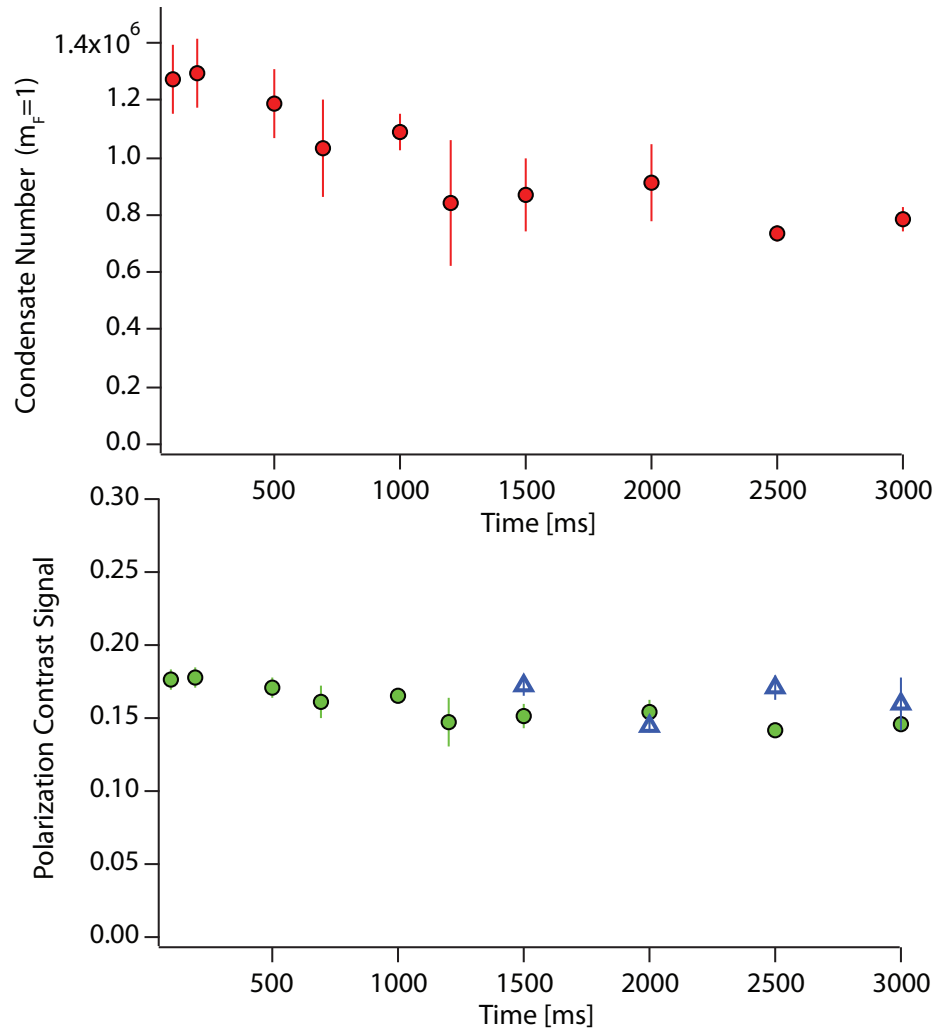


Figure 5.13: Phase contrast amplitudes for a fully polarized gas. The green circles are computed from atom number measured in TOF with absorption imaging and the blue triangles are measured quantities.

Domain size The correlation function can also be used to quantify the typical domain size in the spatial profile of our spin mixtures. The characteristic domain area is taken as the central area, A , of positive correlation. We define the area, A , to be the region of correlation located at the origin (defined to be positive) extending to where the correlation acquires its first zero.

To measure the domain size, we implemented a routine which counts the number of pixels within the central area A for each correlation map. Essentially, the routine counts the number of pixels within each domain in an image. Next, the routine determines if any of these domains are connected and thus part of the same domain, the latter being the more challenging aspect of the code. For this particular analysis, we take the central

area of positive correlation to define the typical domain area, but in generalizing this code, we can potentially use the amplitude and phase of the magnetization profile to determine the number of domains and their corresponding size, rather than restricting ourselves to correlation maps. Upon successfully counting the number of domains, we now have a measure of the domain size corresponding to regions of common orientation. This process does not yet discriminate between different types of domains, such as those where the orientation of the spin slowly meanders across the gas, also referred to as a spin wave. To characterize these types of domains, the magnetization amplitude, $\sqrt{\tilde{M}_y^2 + \tilde{M}_z^2}$, and the magnetization phase, $\arctan(\tilde{M}_y/\tilde{M}_x)$ would be more appropriate.

Using this analysis, the characteristic domain was found to grow in size with increasing evolution time. At the shortest evolution times, $t \sim 200$ ms, the typical domain size started around $8 \mu\text{m}$. Increasing the evolution time, we observed the domain size to grow monotonically, saturating at $\sim 40 \mu\text{m}$ by 2 s evolution time (see Figure 5.14)

Coarsening The observed coarsening dynamics is an indication that our spin mixture is far from equilibrium. The evolution towards an equilibrium phase occurs by increasing the characteristic domain size, where the system can thus lower its free energy by decreasing the interfacial area between different domain walls. Such systems are statistically similar to themselves at a later time except for an overall rescaling of the domain length scale, $l(t)$ [138]. The temporal evolution of these length scales follow a power law, $l(t) \propto t^b$, where the exponent, b , depends on the order parameter of the system. The two most commonly studied systems involving coarsening are those with a scalar order parameter that is either conserved or not conserved. If the order parameter is conserved, the exponent is known to be $1/3$, and if it is not conserved, the exponent is $1/2$ [139, 138]. The existence of the conservation law severely limits the way an interface between two domains can move. While the mechanism of domain coarsening involves the reduction of the local curvature, such evolution has to be accompanied by a global rearrangement of domain interfaces in order to ensure that the order parameter is conserved, resulting in a slower rate of domain growth.

Extending such theories to the coarsening of spin textures in our spinor condensates, we expect the dynamics to be governed by a conserved order parameter, where the order parameter is synonymous with the magnetization [140, 141, 139, 134]. The order parameter (i.e. magnetization) of the spinor condensate is determined by the mean-field phase diagram and depends on the sign and magnitude of the quadratic Zeeman shift. For $q/h < 0$, the equilibrium phase is one where the magnetization is oriented parallel to the magnetic field. In this case, the magnetization is well described by an Ising model and the order parameter is a scalar. However, for $q/h = 0$, the magnetization is well described by a Heisenberg ferromagnetic, with magnetization that is isotropically oriented, and for $0 < q/h < q_0$, we have a planar ferromagnet (easy-plane), with magnetization confined to the plane transverse to the magnetic field. Thus for $0 \leq q/h < q_0$, the order parameter is a vector, confined to a sphere or plane. The exponent for these systems is $1/3$ for the scalar order parameter and $1/4$ for the vector order parameter [142, 143, 141]. Thus for $q/h > 0$ we expect similar domain coarsening dynamics to the behavior observed for $q/h = 0$, whereas for $q/h < 0$, the rate of domain growth is expected to be slightly faster.

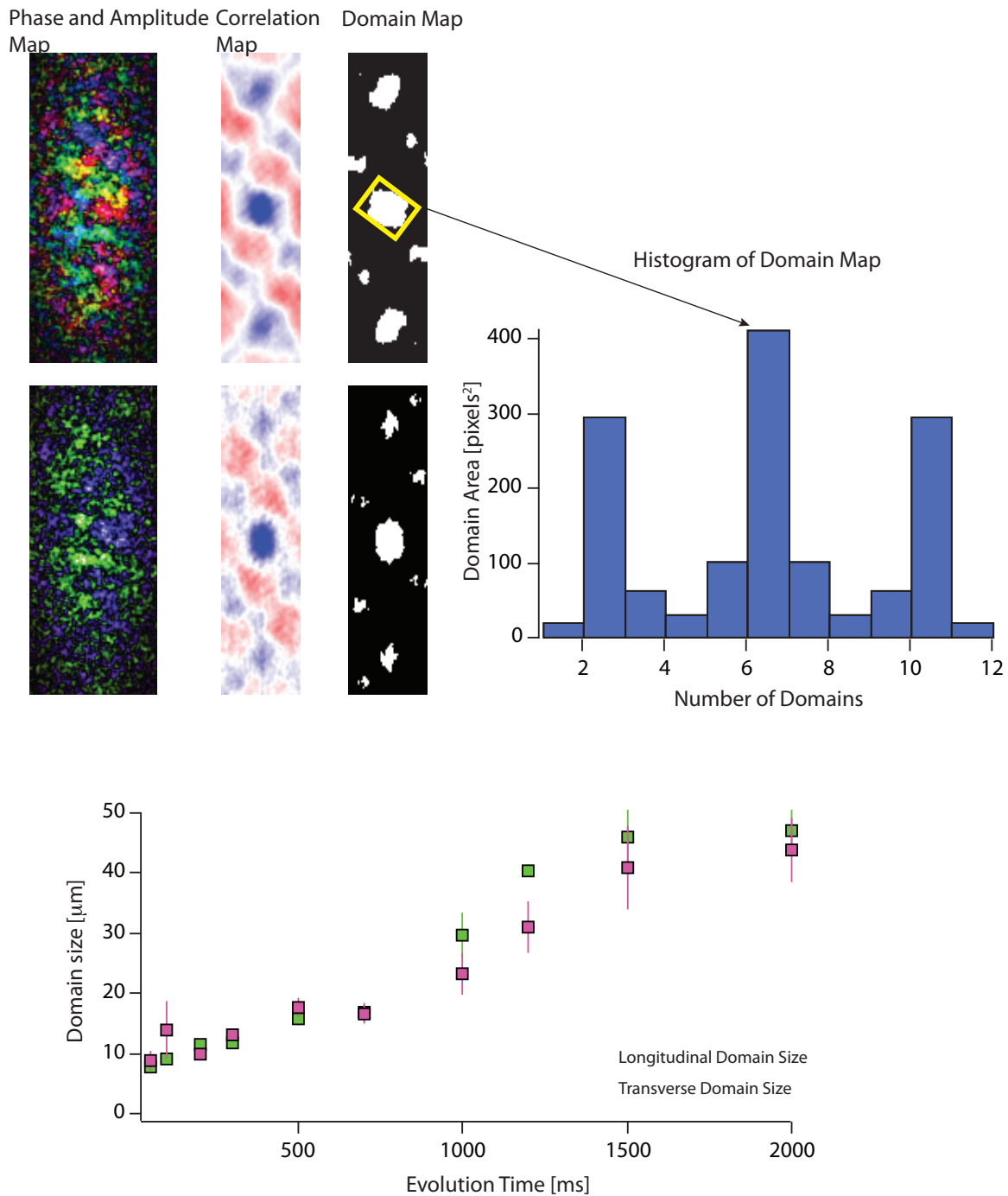


Figure 5.14: Temporal evolution of the domain size. Also shown is a magnetization profile, the corresponding correlation map and the domain map for the longitudinal and transverse magnetization at $t = 300$ ms and at quadratic shift of $q/h = 0$ Hz.

In order to make a comparison with domain coarsening theory, we compare the temporal evolution of spin domains for two values of the quadratic shift: -5 Hz and 0 Hz. For each value of the quadratic shift, we extract the characteristic domain size from time-resolved measurements of the vector magnetization. From these measurements, we observe the domain size to increase monotonically in time, where at the longest evolution times the size is comparable the condensate size along the \hat{x} -dimension, $\sim 40 \mu\text{m}$. In order to compare with the theory of phase-ordering kinetics, we fit the data to a power law growth, shown in Figure 5.15. For $t < 1000$ ms, the data follows a power law growth, while for $t > 1000$ ms the growth follows a more complicated trajectory, which we attribute to the finite size of the condensate. At $t = 1000$ ms, the domain size is comparable to the Thomas-Fermi radius R_{TF} , which may be the reason for the modified growth rate. To reduce potential effects from the finite size of the condensate, we limit the fit to times where the corresponding domain size is $\ll R_{TF}$, thus limiting the fit to times $t < 1000$ ms. We fit the data to the following model,

$$l(t) = A \times t^b, \quad (5.21)$$

where A is the amplitude and b is the exponent which depends on the order parameter. The fits to the data result in the following values for b : 0.36 for $q = -5$ Hz, and 0.27 for $q = 0$. The values for b that we extract from the fits are in good agreement with the theory for the scalar and vector order parameters.

The observed agreement with theory is somewhat surprising. Most theories of phase ordering kinetics assume an infinite system, anticipating that the predicted growth laws will only be realized for $l(t \rightarrow \infty) \rightarrow \infty$. In our particular experiment, however, we use data that is much smaller than the size of the condensate. This means that we are not fitting to the late-stage, late-time coarsening dynamics, where the growth laws are expected to have the best agreement with theory.

Despite the good agreement with theory, limitations to our specific experiment limit the reliability of an accurate comparison with theory. In particular, the finite size of the condensate inhibits a valid comparison with phase-ordering kinetics. A better comparison could be made with a physically larger condensate, where the domain size at the longest evolution times is at least an order of magnitude larger than the initial domain size. An alternative technique could be to seed the system with domains roughly $1 - 2 \mu\text{m}$ in size in a condensate with Thomas-Fermi radii similar to those in this experiment. Nonetheless, domain coarsening in spinor condensates is a lucrative avenue for experimental pursuits, which has yet to be fully appreciated.

Power Spectrum

In addition to the magnetization correlation function, we also characterize the spatial modulation of the magnetization profile using the spatial two-dimensional Fourier transform, where we compute the power spectra, similar to the previously discussed experiment. We do this for the longitudinal and transverse magnetization, where the transverse power spectra is the arithmetic mean of the two transverse components.

For an $\eta = 0$ spin mixture, we extract the spatial modulation of the magnetization from time-resolved measurements of the vector magnetization at $q/h = 0$ Hz. At short

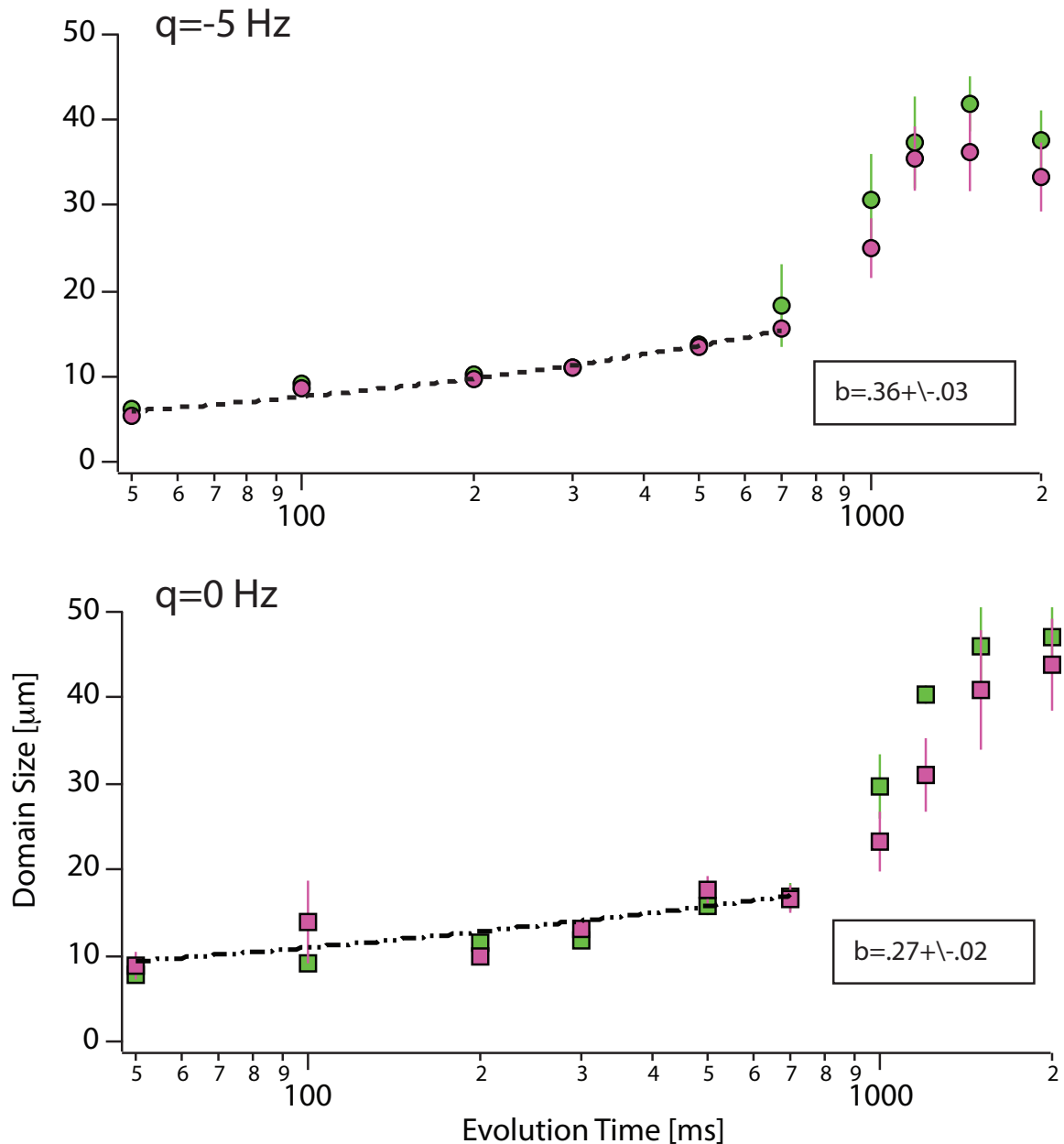


Figure 5.15: Temporal evolution of domain sizes at $q = -5$ Hz and $q = 0$ Hz. We fit the data to a power law function with two free parameters: amplitude and exponent. Using only data for $t < 1000$ ms, we extract the value of the exponent. We find good agreement with the expected values predicted from phase-ordering kinetics: $1/3$ for a scalar order parameter and $1/4$ for a vector order parameter.

evolution times, $t < 50$ ms, the power spectra is fairly isotropic, with a uniform distribution of power at all wave vectors. However, at slightly longer evolution times, $t \simeq 200$

ms, modulations at short wavelengths appear, characterized by a radially symmetric distribution of spectral weight, with inverse length scales ranging from $\lambda^{-1} \simeq 6 - 10 \mu\text{m}^{-1}$. This modulation persists for several hundred milliseconds. Near $t \simeq 700$ ms evolution time, a more pronounced modulation appears, indicated by a concentration of spectral weight at an inverse wavelength $\lambda^{-1} \simeq 25 \mu\text{m}^{-1}$. The axis of this modulation is not as precisely pinned as was observed in the previous experiment [135], evident in the un-averaged power spectra, and appears to have slightly larger concentration of spectral power along the \hat{z} -axis (top-down on the page). This is presumably due to the aspect ratio of the condensate, which permits the formation of more domains along the \hat{z} -axis. At the longest evolution times, $t > 1200$ ms, the power spectra is well described by an ellipse located near zero wave vector, where this asymmetry is due to the aspect ratio of the condensate, with the major axis of the ellipse coinciding with the narrow axis of the condensate, \hat{x} -axis. We observe no distinguishing features between the power spectral for the longitudinal and transverse magnetization components. This is shown in Figure 5.16.

For $q \neq 0$, however, we observe a q -dependent imbalance of total spectral power between the longitudinal and transverse power spectra. At short evolution times the power spectrum has a fairly uniform distribution of spectral power, which is evenly distributed between the transverse and longitudinal components, similar to the $q/h = 0$ data. At intermediate evolution times, however, near $t \simeq 700$ ms, we not only observe a pronounced concentration of power at specific wave vectors, but also an imbalance of spectral weight between the transverse and longitudinal components. The imbalance between the magnetization components is dependent on the quadratic shift; for $q/h < 0$ more power is found in the longitudinal power spectra, and for $q/h > 0$, the opposite is true. This asymmetry is clearly visible in the Fourier spectra in Figure 5.17 and Figure 5.18. In addition, the axis of the modulation is strongest along the \hat{z} axis. This is understandable since the \hat{z} -axis coincides with the long axis of the condensate, allowing for potentially more domains to form along the \hat{z} -axis than the \hat{x} -axis. These observations are in agreement with our *in-situ* spatial magnetization measurements [104].

5.5.4 Comparing to the $F = 1$ Phase diagram as predicted by Mean-Field Theory

From the data taken in TOF and *in-situ*, we find that the steady-state properties of our spin mixtures occur within two seconds evolution time. To confirm that the equilibrium properties we observe are consistent with those predicted in the mean-field phase diagram, we scan the quadratic Zeeman shift, q . Similar to the time-resolved scan, we take a series of data scans at two seconds evolution time, where for each iteration of the experiment we vary the quadratic shift from -40 to 40 Hz. We do this for data taken in TOF where we measure the populations within the Zeeman sublevels, and data taken *in-situ*, where we measure the magnetic properties of our spin mixture.

TOF Results

As a function of the quadratic shift, we observe a q -dependent effect on the population within the Zeeman sublevels for three different initial spin mixtures: $\eta = 0$, $\eta = 1/4$,

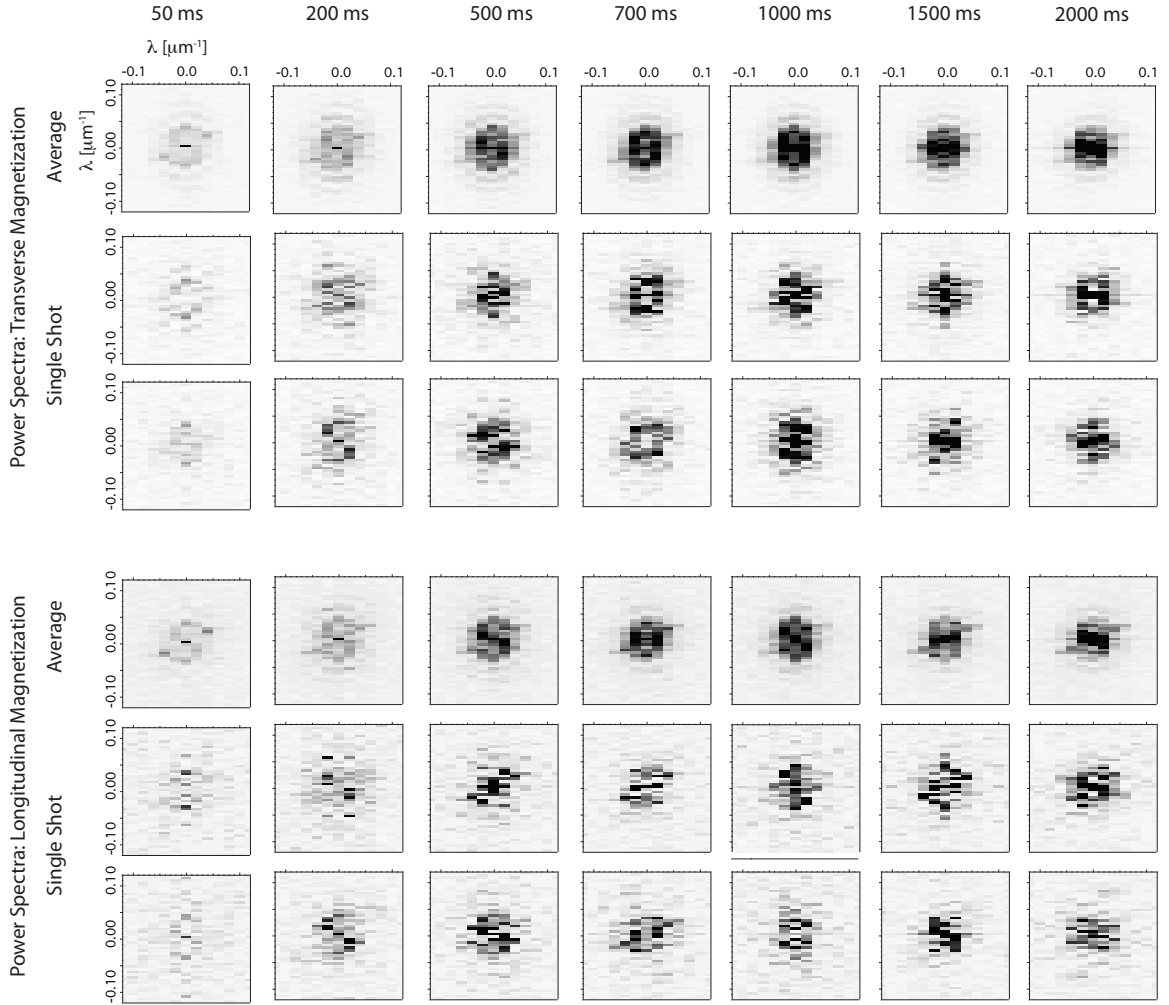


Figure 5.16: Temporal evolution of the power spectrum at $q/h = 0$ Hz. The spectra are derived from the transverse and longitudinal magnetization for an $\eta = 0$ spin mixture. Averaged and un-averaged spectra are shown to give the reader an idea of the type of fluctuations observed in the experiment. Unlike the previous experiment [135], there is no dominant two-wave vector modulation. Here, the axis of the modulation is random, easily seen in the single-shot power spectra.

and $\eta = 1$. This data is shown in Figure 2 of [104]. Restricting ourselves to small quadratic shifts, where we are more likely to observe the equilibrium properties of the system, we find consistent results between the various mixtures. For $q/h \lesssim 0$, there is an imbalance of the atom population within the Zeeman sublevels, with the majority of the atoms in the $|m_F = \pm 1\rangle$ states. However, for $0 \leq q/h < q_0$, the majority of the population is in the $|m_F = 0\rangle$ state, and for $q/h = 0$ the atoms are equally distributed amongst the Zeeman sublevels.

Comparing the measured Zeeman populations to mean-field predictions, we find

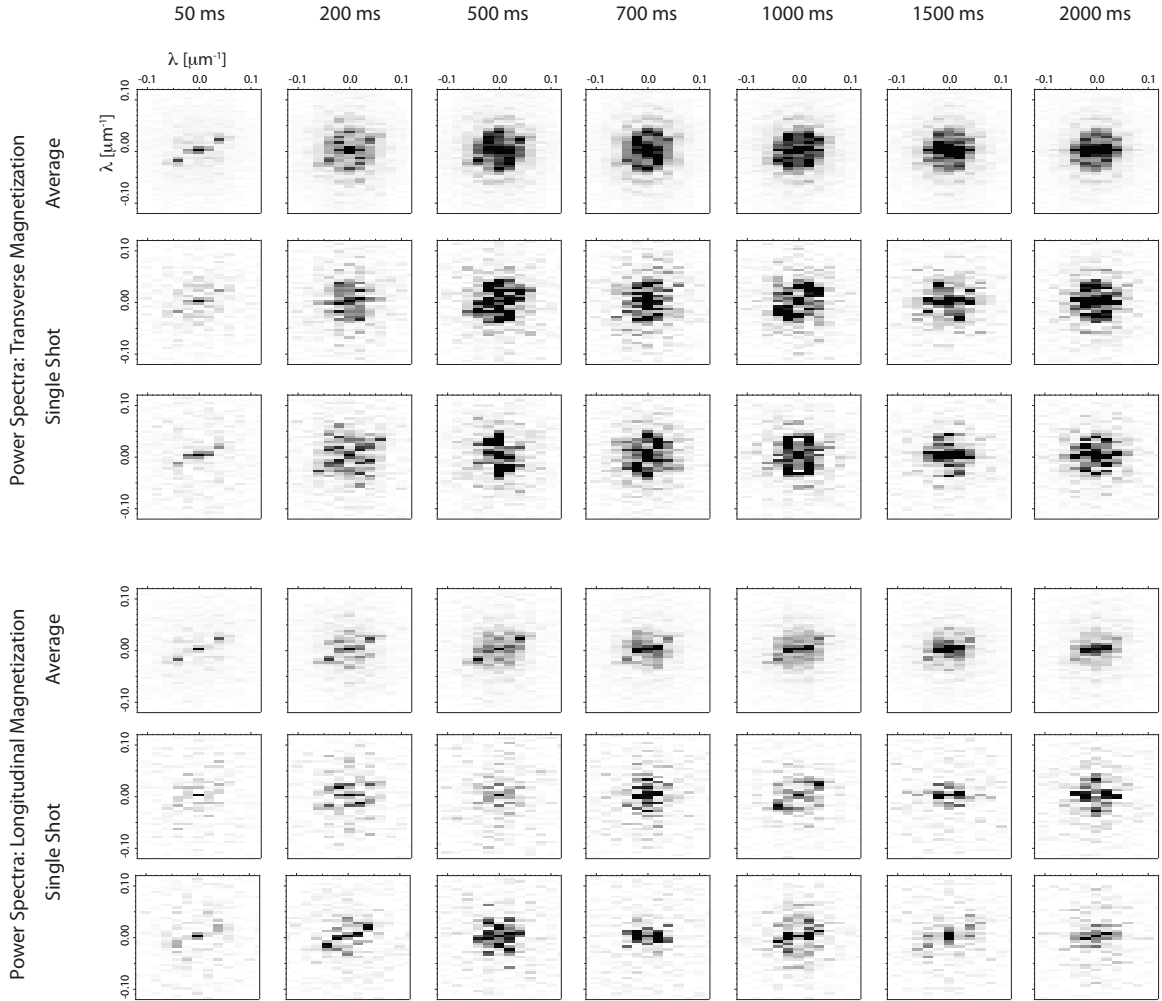


Figure 5.17: Temporal evolution of the power spectrum at $q/h = +5$ Hz. The spectra are derived from the transverse and longitudinal magnetization for an $\eta = 0$ spin mixture. The un-averaged power spectra are meant to illustrate the type of fluctuations we observed from different experimental iterations. The main contrasting feature here is that the power spectra is not characterized by two wave vectors. The axis of the modulation is random.

good agreement with our measurements. For $q < 0$, the spin-dependent contact interaction is minimized by a longitudinally magnetized condensate, resulting in $\zeta_{1(-1)} = 1$. This is in contrast to our observations, where $\zeta_{1(-1)} \approx 0.5$. However, in these experiments, the initial magnetization is zero and given this constraint, we expect the fractional populations within the Zeeman sublevels to be evenly distributed among the $|m_F = \pm 1\rangle$ states, resulting in $\zeta_{\pm 1} = 0.5$. For $0 < q < 2c_2n$, the spin-dependent contact interaction is minimized for a condensate with domains transversely magnetized, for which $\zeta_{\pm 1}$ linearly diminishes from 0.25 to zero. To see this, we minimized the spin-dependent energy functional assuming

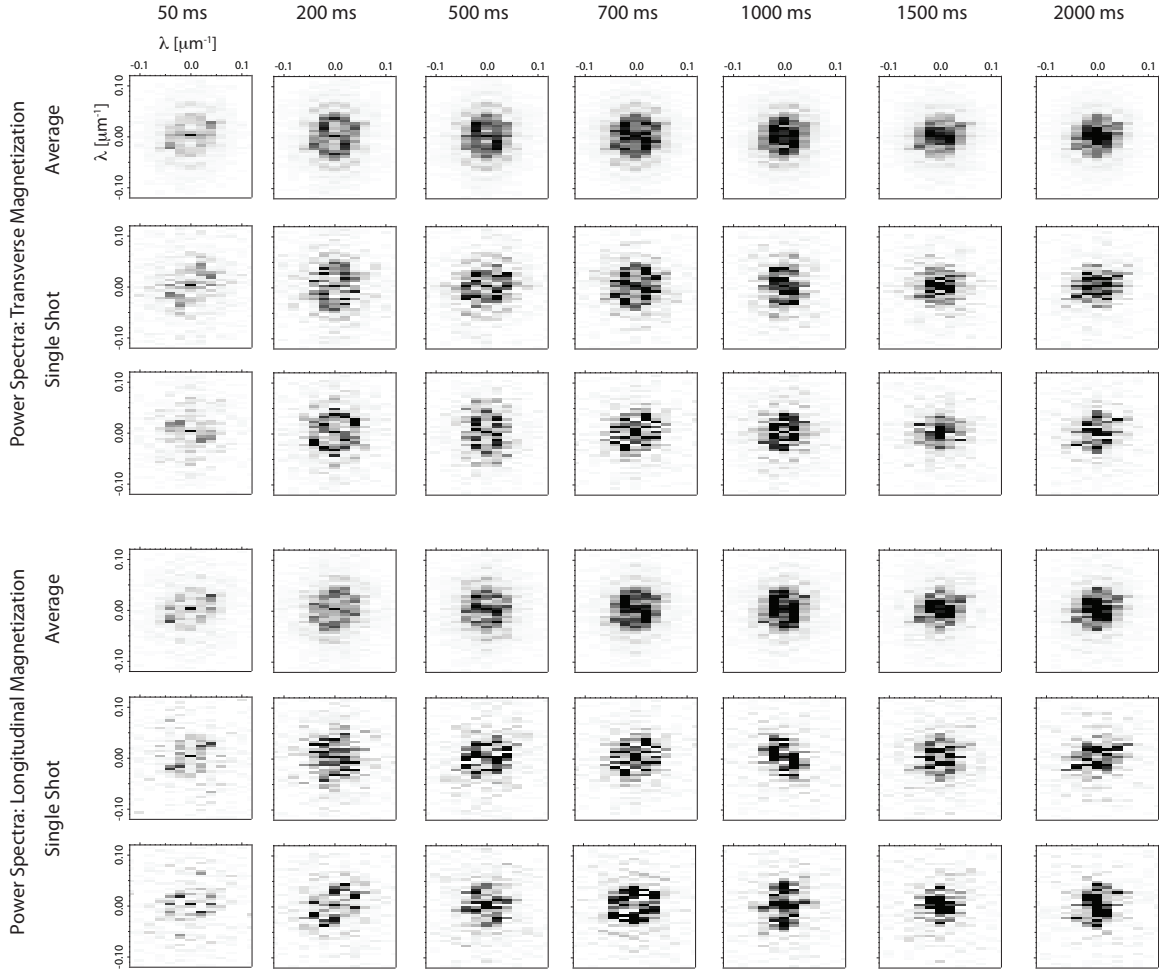


Figure 5.18: Temporal evolution of the power spectrum at $q/h = -5$ Hz. The spectra are derived from the transverse and longitudinal magnetization for an $\eta = 0$ spin mixture.

constant magnetization. We modeled the spinor order parameter as

$$\zeta = \begin{pmatrix} \sqrt{a} \\ \sqrt{1-2a} \\ \sqrt{a} \end{pmatrix} \quad (5.22)$$

where ζ is normalized as $\zeta^\dagger \zeta = 1$, while the elements of ζ are given the constraint of no net magnetization ($\zeta_{+1} = \zeta_{-1}$), and a is the variational parameter. We next computed the spin-dependent interaction energy,

$$E_{SM} = \frac{1}{2} \langle F \rangle^2 - \epsilon \langle F_z^2 \rangle, \quad (5.23)$$

where $\epsilon = -q/c_2 n$, which ranges from $\epsilon = 0$ at $q = 0$ to $\epsilon = 2$ at $q = c_2 n$, $\langle F \rangle = \zeta^\dagger \mathbf{F} \zeta$, and $\langle F_z^2 \rangle = \zeta^\dagger F_z^2 \zeta$, and $\mathbf{F} = (F_x, F_y, F_z)$ are spin-1 rotation matrices. Minimizing this energy,

we find that the population in the $|m_F = \pm 1\rangle$ states are

$$a = \frac{2 - \epsilon}{8}. \quad (5.24)$$

Finally, for $q = 0$, there is no preferred orientation of the condensate magnetization, resulting in an equal distribution of atoms within the Zeeman sublevels, $\zeta_{m_F} = 1/3$.

For larger quadratic shifts $|q/h| > 10$ Hz, however, we observe very different results for each of the different spin mixtures. Specifically, for an $\eta = 1$ initial spin mixture at $q/h < -10$ Hz, the distribution remains remarkably close to its initial composition. Similarly, for an $\eta = 0$ and $\eta = 1/4$ spin mixture, we observe the populations to remain unchanged for $|q/h| > 10$ Hz. These results are consistent with the data from our time-resolved scans, indicating that equilibrium is possible in these spinor condensate systems, but for a narrow range of parameters.

***In-situ* Results**

Although the TOF results are consistent with the phases predicted by the mean-field phase diagram, we do not know the nature of the magnetization at each value of the quadratic shift. To determine if these observations are consistent with theory, we extract the magnetization vector profile at two seconds evolution time while varying the quadratic shift. To determine the degree to which the spin mixture has evolved to a ferromagnetic state, we use extract the magnetization variance, $G_L(0)$ and $G_T(0)$ for each value of the quadratic shift. The results are summarized in Figure 3 of [104]. For $q/h \lesssim 0$, the amplitude of the longitudinal variance is larger, nearly approaching a value of one within the two-second long evolution. At $q/h = 0$, the transverse and longitudinal variances are equal, and for $0 < q/h < q_0$, the transverse variance approaches its maximum, nearly reaching half the value expected for a fully magnetized condensate. These results are in excellent agreement with the ground state magnetic phases for an $F = 1$ spinor gas.

5.5.5 Remaining Questions

The results from both experiments have answered a few questions and have unearthed a few more. From the two experiments we can confirm that the short wavelength spin modulation observed is a transitory phase and not due to dipolar interactions. Numerous theoretical discussions have shown that such low energy interactions would result in a magnetization modulation with a $\sim 30 - 40 \mu\text{m}$ wavelength [144, 145, 146, 147, 148]. In fact, the presence of dipolar interactions would alter the mean-field phase diagram, causing a preference for longitudinal magnetization for small positive values of the quadratic Zeeman shift [125]. The observed ferromagnetic phases in this experiment show a dependence on the quadratic shift in a manner that is consistent with mean field theoretical predictions.

However, the observed “crystalline” magnetic phase, characterized by a two wave vector modulation that is pinned to the optical trap axis, is likely due to an imaging artifact. This was confirmed from experiments investigating the influence of an out-of-focus imaging system on the observed spatial structure in the magnetization profile (see Chapter 4). To do this, a helical spin texture after 100 ms evolution time was imaged using phase contrast

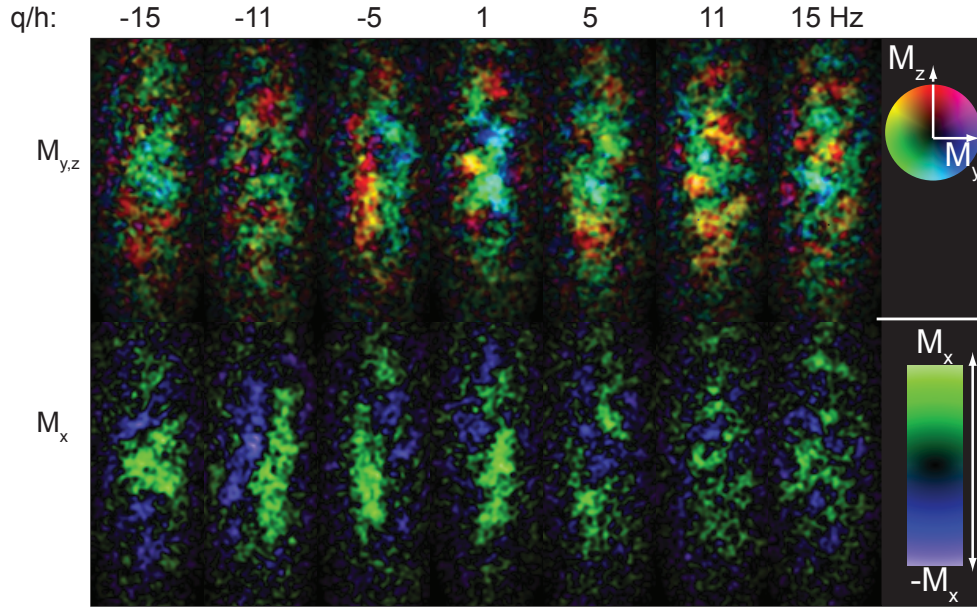


Figure 5.19: Instantaneous snapshot of the vector magnetization profile at 2 s evolution time for an $\eta = 0$ spin thermal spin mixture at different quadratic Zeeman shifts. The brightness, indicative of the strength of the magnetization, has a strong dependence with quadratic shift. For $q < 0$, \tilde{M}_x stronger, while for $q > 0$, $\tilde{M}_{y,z}$ is stronger.

imaging. The helix was observed to breakup in a similar manner as observed in [113], with the exception that the spatial structure depended on the position of the objective focus. Tuning the focus, the observed modulation was characterized by either a two wave vector modulation, single wave vector, or an annulus. Based on these observations, we have concluded that the “crystalline” magnetic phase is due to an imaging aberration.

The TOF analysis from the two experiments confirm the seconds-long timescales for the populations to redistribute to an equilibrium composition. Recent experiments probing the equilibrium phase diagram in sodium spinor condensates have also observed seconds-long equilibration times [149]. However, what determines these seconds-long dynamical timescales is still unknown. Additionally, why is equilibrium isolated to a narrow range of quadratic Zeeman shifts? Furthermore, why does the fractional population within the $|m_F = \pm 1\rangle$ state remain close to its initial spin composition for an $\eta = 1$ spin mixture at negative quadratic shifts, when clearly this a composition far from equilibrium?

Chapter 6

Exploration of long-range order in $F = 1$ ^{87}Rb spin textures

This chapter describes measurements of the coherence length of spin texture. In particular, we discuss the use of spatial heterodyne atom interferometry to probe the long range order of the system via the first-order correlation function.

6.1 Why explore long-range order in a magnetic spin texture?

During our exploratory measurements of the equilibrium magnetic phases in $F = 1$ spinor condensates, we observed the formation of a “crystalline” pattern in the magnetization profile [135, 113]. In these experiments we cooled unmagnetized thermal spin mixtures in an attempt to observe and verify the equilibrium properties of $F = 1$ spinor gases as predicted by mean-field theory [27, 125]. Upon cooling the samples, the time-of-flight (TOF) momentum distributions displayed several of the classic hallmarks of three-dimensional Bose condensation: bimodal distribution, a value of T_c consistent with the theoretical prediction for a scalar Bose gas, and a condensate fraction which scales as $1 - (T/T_c)^3$, which is the expected scaling for scalar condensates. However, *in-situ* imaging of the magnetization revealed a slew of unexpected magnetic phases. In particular, a modulated spin pattern was evident in the images, characterized by $\sim 10 \mu\text{m}$ domains of alternating magnetization orientation. This result was quite surprising given the similarities between the bulk features measured in TOF of the scalar and spinor condensates. This led us to investigate the origin of the “crystalline” magnetic phase. In particular, given that we have a magnetic phase which resembles a crystal, with domains spatially arranged in an orderly fashion, one natural question to ask is whether the system is also coherent across the extent of the gas. A simultaneous confirmation of coherence and “solidity” would hint at a potentially new and exotic phase of matter: a supersolid [150, 151, 152, 153, 154].

The experiment discussed below describes the experimental pursuit to measure the coherence length in unmagnetized spin mixtures. This is done by measuring the first order correlation function of the condensate. The topic of coherence in Bose-Einstein condensates

has received a tremendous amount of interest. For a thorough review of the topic and salient features, I refer to the reader to the following theoretical [155, 156, 15] and experimental publications [157, 158, 88, 159, 160, 161, 162].

6.2 Experimental Sequence

We measure the spatial coherence of our spinor condensates by creating two coherent and spatially displaced copies of the original condensate in the same momentum state and letting them interfere using two Ramsey-like pulses [103]. An optical standing wave is used to diffract a small fraction of atoms, transferring $2b\hbar k_1$ units of photon momentum to the atoms, where \mathbf{k}_1 is the wave vector of the standing wave [163, 164, 165]. A second light pulse, with wave vector \mathbf{k}_2 , creates a second copy of the atoms, displaced from the first by $\Delta\mathbf{r} = 2\hbar\mathbf{k}\tau/m$, where τ is the time between pulses, m is the mass of rubidium, b is the order of Bragg scattering, and $|\mathbf{k}| = |\mathbf{k}_{1(2)}| = 2\pi/\lambda$, where $\lambda = 780$ nm and \mathbf{k}_1 and \mathbf{k}_2 are equal in magnitude but differ by a small angle, $\theta \simeq 0.016$ radians. The net effect of the two pulses is create a phase gradient across the gas. The two copies of the gas then interfere where their wave functions spatially overlap. By imaging the contrast of the spatial interference, we can extract the coherence length.

In order to describe the interference, we examine the condensate wave function after each standing wave pulse. The two applied pulses were $\sim 6 \mu\text{s}$ in length, sufficiently short to assume that the atoms do not move during the pulse, and can therefore be described as Kapitza-Dirac scattering [164, 166]. The first pulse out-couples a fraction of atoms into the momentum states $|\pm 2b\hbar k_1\rangle$, where the population in the b^{th} momentum state is given by $P_b = J_b^2(\theta)$, where $\theta = (\Omega_R t_p)/(2\delta)$, Ω_R is the Rabi frequency, and t_p is the length of the light pulse. For the current experiment, we tuned the amplitude and the duration of the light pulse in order to transfer a non-negligible population into only the $b = 2$ momentum state. Thus we will restrict our discussion to the $|\pm 4\hbar k_1\rangle$ momentum states. Immediately after the first light pulse, the wavefunction of the $|\pm 4\hbar k_1\rangle$ momentum states are described by

$$\Psi_{4\hbar k_1} \sim a_1 \Psi_0(r) e^{i2\mathbf{k}_1 \cdot \mathbf{r}} \quad (6.1)$$

where $|a_1|^2$ is the fraction of atoms in momentum state $|\pm 4\hbar k_1\rangle$, and Ψ_0 is the wave function of the $|0\hbar k_1\rangle$ momentum state. After a delay of τ , a second pulse is applied to the atoms, which predominately out-couples atoms to the $|\pm 4\hbar k_2\rangle$ momentum states. The wavefunction of this momentum state is given by

$$\Psi_{4\hbar k_2} \sim a_2 \Psi_0(r + \Delta\mathbf{r}) e^{i2\mathbf{k}_2 \cdot \mathbf{r}}, \quad (6.2)$$

where $|a_2|^2$ is the fraction of atoms in momentum state $|\pm 4\hbar k_2\rangle$. The combined effect of these two pulses is to create two copies of the condensate which can then interfere. The interference pattern is captured in the density pattern for the $b = 2$ momentum states, $n_{b=2}$,

given by:

$$n_{b=2} \sim |\Psi_{4\hbar k_1} + \Psi_{4\hbar k_2}|^2 \quad (6.3)$$

$$\begin{aligned} &= |a_1 \Psi_0(r) e^{i2\mathbf{k}_1 \cdot \mathbf{r}} + a_2 \Psi_0(r + \Delta r) e^{i2\mathbf{k}_2 \cdot \mathbf{r}}|^2 \\ &= a_1^2 \Psi_0^*(r) \Psi_0(r) + a_2^2 \Psi_0^*(r + \Delta r) \Psi_0(r + \Delta r) \\ &\quad + \left(a_1 a_2 \Psi_0^*(r) \Psi_0(r + \Delta r) e^{i\Delta \mathbf{k} \cdot \mathbf{r}} + c.c. \right). \end{aligned} \quad (6.4)$$

The first two terms in Equation 6.4 describe the atomic density distributions in the $b = 2$ momentum states. The quantity of interest is contained in the third term, which describes the interference [158, 161]. This is essentially the first-order correlation function, which describes the degree of spatial coherence. Neglecting the offset terms from the density contributions in Equation 6.4, the normalized correlation function is:

$$g^{(1)}(\Delta r) = \frac{\langle \Psi_0^*(r) \Psi_0(r + \Delta r) \rangle}{n_0} \quad (6.5)$$

where n_0 is the initial density distribution in the $F = 1$ state. By measuring the average spatial contrast of the interference fringes in an image, while varying the spatial overlap, $\Delta \mathbf{r}$, we can then extract the normalized first order correlation function [88, 161, 158].

6.2.1 Measurement of the coherence length

Using the first order correlation function, we extract the coherence length of gases produced by gradually cooling unmagnetized thermal spin mixtures into the regime of quantum degeneracy. The coherence length is measured using three different initial spin compositions: $\eta = 0$, $\eta = 1/4$, $\eta = 1$, where η is defined as $\eta = \zeta_0 - \zeta_1$ and $(\zeta_1, \zeta_0, \zeta_{-1})$ denote the fractional populations within the three Zeeman sublevels (eigenstates of F_z). These initial spin compositions are identical to those discussed in Chapter 5.

To create these spin mixtures, we use an experimental sequence similar to the experiment discussed in reference [135] and Chapter 5. Briefly, we prepared a thermal sample of atoms in the $|F = 1, m_F = -1\rangle$ state in an optical dipole trap, characterized by initial trapping frequencies $(\omega_x, \omega_y, \omega_z) = 2\pi \times (80, 800, 9)$ Hz, using linearly polarized light at 825 nm. Next, we create unmagnetized thermal spin mixtures by applying a series of rf pulses in an inhomogeneous magnetic field (see Chapter 5). These mixtures are characterized by zero longitudinal and transverse magnetization. Following this, the spin mixtures were evaporatively cooled by gradually decreasing the optical trap power over a time scale of 200 ms. Upon reaching the final trap depth, the samples were then allowed to equilibrate for an additional 200-500 ms.

To image the spatial coherence length, we employed a two-pulse Ramsey-like sequence. After allowing the sample to equilibrate in the optical trap, the trapping potential was suddenly switched off and following this the two-pulse Ramsey sequence was initiated. The purpose of this turnoff was to reduce the effect of interactions between atoms by reducing the condensate density. In order to image the different spin components, we use Stern-Gerlach analysis [52, 79], where a magnetic field gradient is applied to the atoms and is used to spatially separate atoms with differing magnetic moments. After 12 ms of free expansion, the atoms were imaged using resonant light.

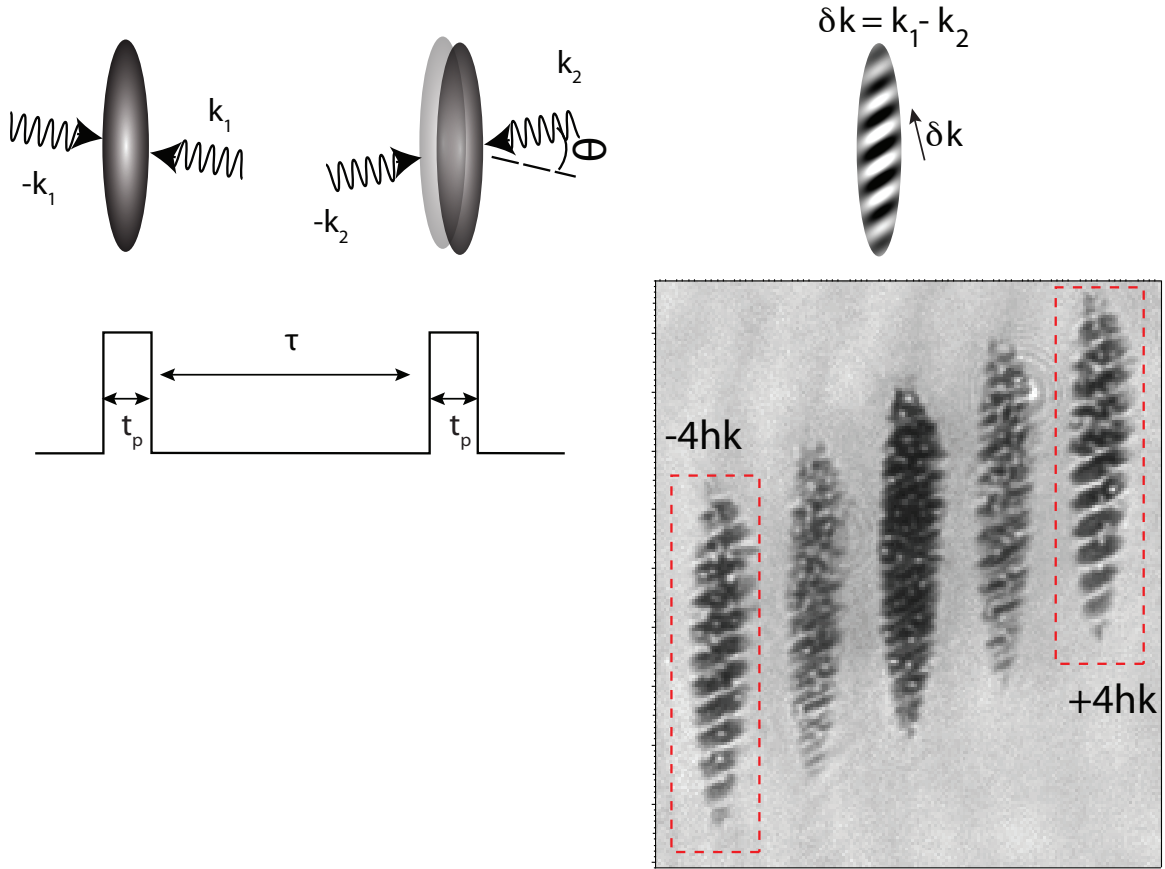


Figure 6.1: Experimental setup of two pulse Ramsey-like method. The effect of the first pulse is to out-couple a small fraction of atoms into the $|\pm 4\hbar k_1\rangle$ momentum state. After a variable delay, a second pulse is applied which out-couples atoms into the $|\pm 4\hbar k_2\rangle$ momentum state. The net effect is to create two copies of the condensate which interfere. By repeating this for different delay times between the two pulses, τ , we can obtain a measurement of the coherence length.

The resulting TOF momentum distribution consists of an interference between two copies of the condensate in the same momentum state. The two pulses of light out-couple atoms into momentum states $|2b\hbar k_{1,2}\rangle$, with $b = 0, \pm 1, \pm 2, \pm 3$. After sufficient TOF, the only condensate copies with sufficient spatial overlap are those with identical b , resulting in an interference between condensate copies in the same momentum state and a spatial modulation along $\delta \mathbf{k} = \mathbf{k}_1 - \mathbf{k}_2$, which is mostly parallel to the \hat{z} -axis.

6.3 Analysis and Results

6.3.1 Scalar BEC

As an initial verification of the technique, we use this spatial heterodyne method to extract the coherence length for a scalar condensate. The preparation procedure is identical to the scheme described above but forgoes the application of rf pulses and the magnetic field gradient to decohere the sample.

The correlation function is acquired by taking a sequence of interference images with different separations, varied by changing the time between pulses, τ , between $200 \mu\text{s}$ and $1200 \mu\text{s}$. Figure 6.2 shows the interference pattern for a scalar condensate for a few values of τ . The contrast is determined by measuring the amplitude of the Fourier component of the image at the spatial frequency of the fringes relative to the peak density of the fringes. This is repeated for different spatial separations. For small separations, we observe a maximum contrast of ~ 0.8 . The less than unity contrast is attributed to residual phase defects in the condensate during formation. These are seen as density holes in the time-of-flight images in Figure 6.2. For the maximum values of $\tau = 1200 \mu\text{s}$, the contrast is reduced such that the fringes are no longer discernible above the background noise. The signal decay is mainly due to the reduced geometrical overlap of the condensate copies with increasing $\Delta\mathbf{r}$ [158]. The interference contrast as a function of the pulse separation, τ , is shown in Figure 6.3.

In addition to the reduced contrast as a function of the spatial overlap, we also observe a rotation in the fringe pattern. For short value of $\tau \simeq 200 \mu\text{s}$, the interference pattern is mostly oriented along the long axis of the condensate. However, for larger pulse separations, we observe a rotation in the fringe pattern where at the largest value of τ , the fringe pattern is oriented at 45° in the $\hat{x} - \hat{z}$ plane. This rotation is easily seen in the Fourier spectra of the TOF images in Figure 6.2. This rotation is attributed to a velocity chirp during the TOF expansion of the condensate. After the atoms are released in TOF, the condensate expands as the atoms are no longer confined. The differing velocities in the atomic sample result in a velocity chirp across the gas relative to the pulsed standing wave, resulting in a fringe pattern which rotates as a function of the time between the pulse separation.

6.3.2 Spinor BEC

For the $\eta = 0$ and $\eta = 1/4$ spin mixtures, the coherence length is acquired by measuring the spatial contrast of interference fringes for different spatial separations, $\Delta\mathbf{r}$, and for each Zeeman sublevel, m_F . Similar to the contrast measurement for the scalar condensate, we make use of the two-dimensional Fourier transform to extract the contrast of the interference fringes. For each magnetic sublevel, m_F , we compute the Fourier transform. The contrast is determined from the amplitude of the Fourier component at the spatial frequency of the fringes relative to the peak density of the fringes for each magnetic sublevel and summed. The total contrast for each spin mixture is shown in Figure 6.4.

In general, the coherence measurements for each spin mixture closely resemble those of the scalar condensate. The maximum contrast at the smallest time τ is consistent

with a value of 0.8, as seen for the scalar condensate. Increasing τ (and hence increasing the separation between the clouds) causes the contrast to smoothly decrease to zero at $\tau \sim 1000 \mu\text{s}$. However, unlike the scalar case, the coherence for these spin mixtures is distributed between the different $F = 1$ components. For instance, the coherence is shared equally between the three magnetic sublevels for the $\eta = 0$ spin mixture. This is seen in the equal amplitudes of the contrast measurements for each sublevel. In contrast, for the $\eta = 1/4$ spin mixture, the $m_F = 0$ component has the largest interference contrast and coincidentally the largest number of atoms. Furthermore, we do not observe evidence of the “crystalline” magnetic phase. Such a phase would appear as an increase in the amplitude of the contrast measurement at a cloud separation of $10 \mu\text{m}$ (see Figure 6.4). However, the data only show a monotonic decrease in the contrast, with no experimental indication of a magnetization modulation at $10 \mu\text{m}$ or any other length scale.

Notable features in the data are the differences with and without Stern-Gerlach analysis. Without Stern-Gerlach analysis, where the individual spin components are spatially overlapped, the TOF pattern is otherwise uniform, except for the interference pattern. This is true for both the $\eta = 0$ and $\eta = 1/4$ spin mixtures. However, imaging the clouds after spatially separating the spin components reveals a slew of density fluctuations in all three spin components. The density fluctuations are most noticeable in the $m_F = 0$ component for the $\eta = 1/4$ spin mixture, which has the majority of the atoms and equally apparent in all three components for the $\eta = 0$ spin mixture. The most striking observation is how density fluctuations in one spin component are compensated by those in another, yielding a fairly smooth profile when spatially overlapped. Interestingly, the spin degree of freedom appears to reduce the entropy associated with thermal fluctuations; when the TOF profiles of the spin components are spatially overlapped, the profile is more spatially uniform than the single component case.

6.3.3 Coherence Length

We approximate the overlap of the two interfering clouds, and hence the correlation function, as a Gaussian, characterized by,

$$Ae^{\frac{\tau^2}{\tau_w^2}} + \text{constant} \quad (6.6)$$

where the width, τ_w , is defined as the time where the amplitude of the fringe contrast falls to $1/e$ of its initial value. This is related to the size of the condensate, $\tau_w \approx 0.75 r_{TF}/v_r$, where r_{TF} is the Thomas-Fermi radius along the \hat{x} -axis and $v_r = \hbar k/m_{RB} \approx 5 \mu\text{m}/\text{ms}$ is the recoil velocity [167, 168]. For our experimental parameters, $r_{TF} \approx 20 \mu\text{m}$, giving a “coherence time” of $1000 \mu\text{s}$ assuming $4 \times v_r$ or $4k$.

In practice, we determine the coherence length by fitting the data to a Gaussian function. We convert the measured width to a measure of the coherence length by using the recoil velocity of the atoms. As a first test of this technique, we extract the coherence length for the scalar condensate. From a fit, the “coherence time” is $\sim 800 \mu\text{s}$, resulting in a coherence length of $16 \mu\text{m}$. This is close agreement with the size of the condensate. The slightly faster decay is attributed to the finite resolution of the imaging system, which reduces the signal contrast at the largest values of $\Delta\mathbf{r}$.

Unfortunately, impeding the interpretation of these measurements is an incomplete understanding of the spatial frequency of the fringe pattern. For each experimental iteration, the TOF distribution has momentum components at $\pm 2b\hbar\mathbf{k}$, for $b = 0, \pm 1, \pm 2$ and ± 3 , where the signal is comprised of an interference between condensate copies in the same diffracted order, b . This results in an interference pattern with a spatial periodicity that scales as $2b\mathbf{k}$. However, close inspection of the components at $\pm 2\hbar\mathbf{k}$ and $\pm 4\hbar\mathbf{k}$ reveals interference patterns with the same modulation frequency. Assuming that the interference pattern at $b = \pm 2$ is predominantly due to interference of $2\hbar\mathbf{k}_1$ and $2\hbar\mathbf{k}_2$, we would expect the spatial frequency of the interference pattern to be proportional to $2\delta\mathbf{k}$, while those at $b = \pm 4$, to be at twice this spatial frequency. Thus, if we instead assume that the modulation periodicity is at $2\mathbf{k}$, then the coherence length is $8\mu\text{m}$, much smaller than the condensate size. The confusion associated with the spatial frequency of the fringe pattern is attributed to a problem with the intensity of the pulsed standing waves.

Furthermore, the imaging resolution of the objective prevents a measurement of long-range phase coherence. At the largest values of $\Delta\mathbf{r}$, we observe a reduction in the contrast of the interference fringes that is not completely explained by the reduced geometrical overlap of the condensates. This is primarily attributed to our finite imaging resolution of $\simeq 2.5\mu\text{m}$, which reduces our sensitivity to coherence length measurements beyond $\tau = 1000\mu\text{s}$. The resulting TOF measurement is a convolution of the first order correlation function with the modulation transfer function of the imaging system. It is possible to extract the first order correlation function from these measurements by deconvolving the data with the modulation transfer function. This would accentuate the coherence length measurements at the highest spatial frequencies but with the added expense of increased noise, making this not the best viable option for extracting long-range phase coherence.

Lastly, further analysis of the data in presented in [113, 135] led us to question the existence of the “crystalline” magnetic phase. In those studies, the position of the objective focus was finely tuned using the “crystalline” magnetic phase. The optimal position of the objective was determined by our ability to resolve the modulated magnetic phase. At the time it was assumed that these features were a reliable test pattern to finely adjust the focal position of the objective. Unfortunately, as discussed in Chapter 4, misalignments associated with the position of the objective focus can artificially enhance certain spatial features, leading us to question if the original observation of a “crystalline” magnetic phase was due to an imaging aberration.

Unfortunately, we were not able to duplicate the data under the exact same experimental parameters. Soon after these data were taken, the experimental apparatus was disassembled and replaced with the chamber discussed in Chapter 2. Thus, without the ability to revisit the conditions under which these data were taken, we were unable to definitively extract the coherence length of these spin mixtures. Further experimental pursuits of the correlation function in the new chamber were not pursued due to our assumption that the “crystalline” phase was due to an imaging aberration.

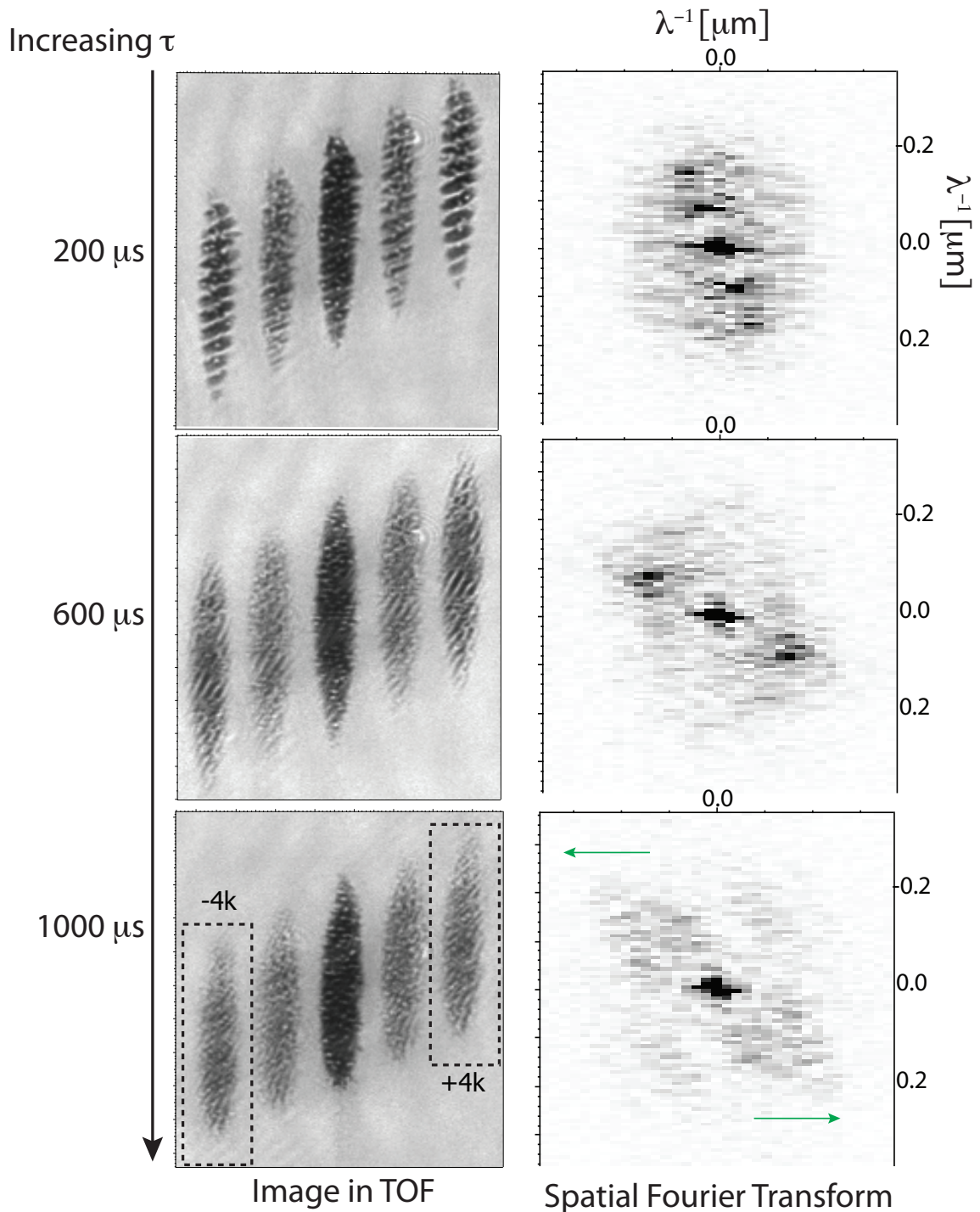


Figure 6.2: Interference of scalar condensate. On the left are TOF images of a scalar condensate after 13 ms of free expansion. The corresponding two-dimensional spatial Fourier transform are shown on the right. As a function of the pulse duration, the relative overlap is smaller, leading to a decrease in the contrast of the interference fringes, evident in the TOF pattern and the spatial Fourier transform.

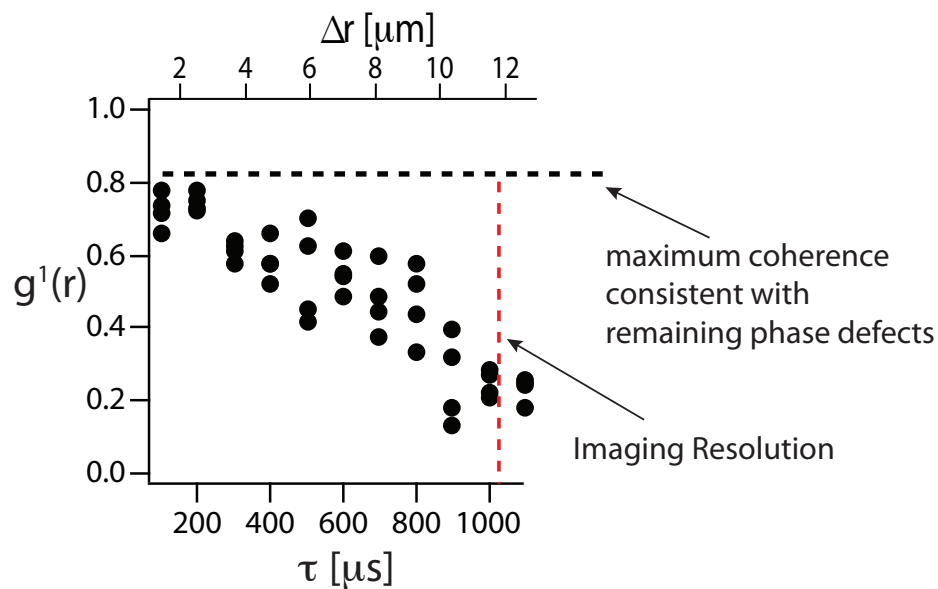


Figure 6.3: Measured contrast of the interference fringes as a function of the separation of the two clouds in the heterodyne interferometer. The contrast is measured by making use of the spatial Fourier transform. The amplitude of the Fourier component at the spatial frequency of the fringes is measured and plotted versus the delay time between pulses, τ , where the delay time determines the spatial separation between the two cloud copies. The spatial separation, $\Delta \mathbf{r}$ is computed assuming $\Delta \mathbf{r} = 2v_r \tau$

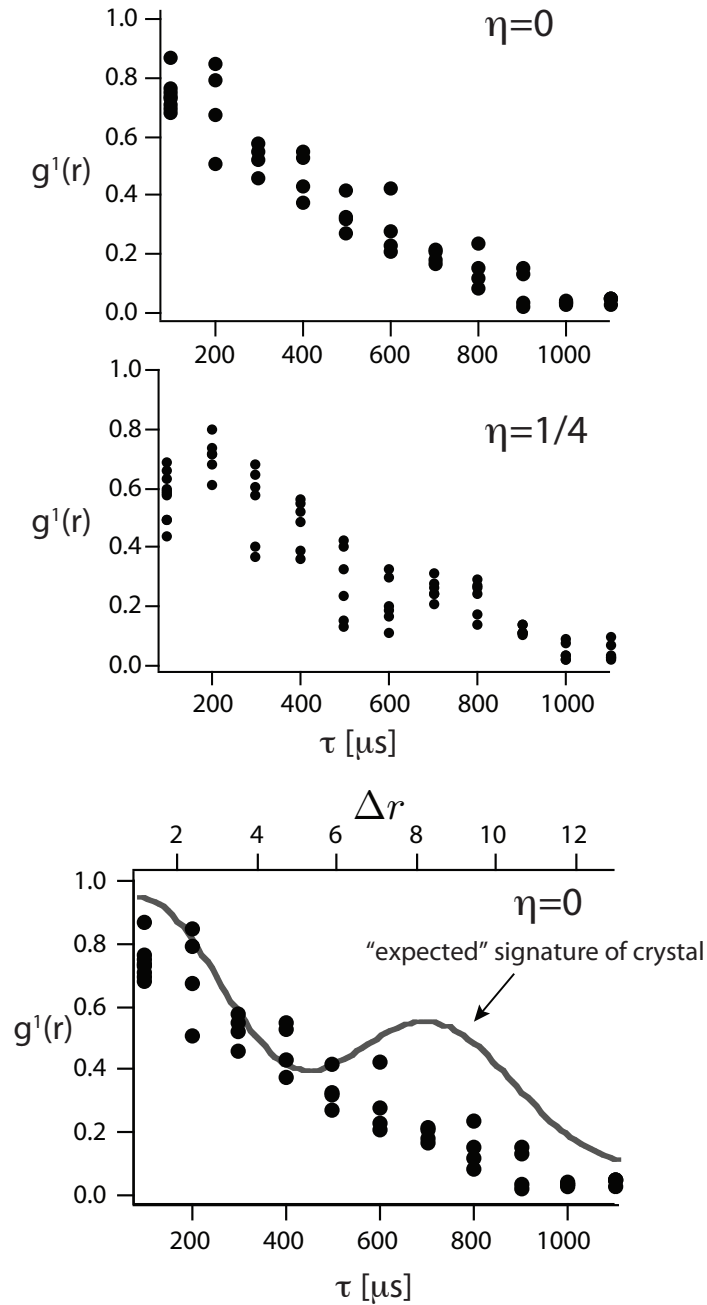


Figure 6.4: First order correlation function for $\eta = 0$ and $\eta = 1/4$ spin mixtures. The contrast is measured using the spatial Fourier transform for each magnetic sublevel. The contrast shown in the combined sum of the contributions from each sublevel. For each mixture, the contrast decreases smoothly to zero, with no striking differences between the two. Also shown is the experimental signature of a “crystalline” phase with a $\simeq 10 \mu\text{m}$ spatial modulation. This would result in an increase in the amplitude of the first order correlation function at a separation consistent with the spatial modulation of the phase. The spatial separation, $\Delta \mathbf{r}$ is computed assuming $l = 2v_r\tau$.

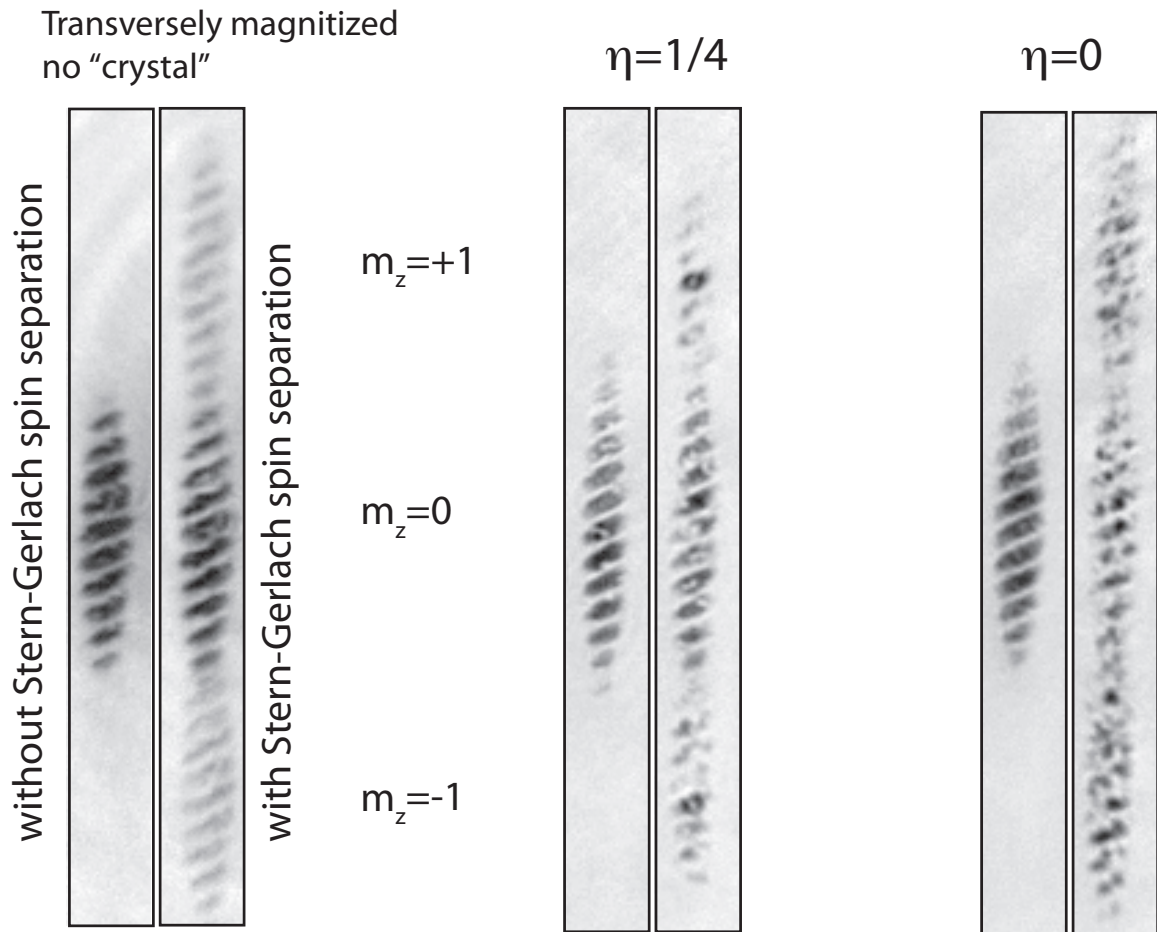


Figure 6.5: Interference of spinor condensates for $\eta = 0$ and $\eta = 1/4$ initial spin mixtures. To resolve the individual spin components, a magnetic field gradient is used to spatially separate each spin component.

Chapter 7

Realization of an optical kagome lattice

Presented in this section is an overview of the changes in the apparatus for the implementation of the kagome optical lattice experiment, followed by a discussion of the kagome potential and how we are able to engineer different lattice geometries using the bi-chromatic lattice. Also included is work related to the following publication:

- *Gyu-Boong Jo, Jennie Guzman, Claire Thomas, Pavan Hosur, Ashvin Vishwanath, and D. M. Stamper-Kurn. "Ultracold Atoms in a Tunable Optical Kagome Lattice" *Physical Review Letters* **108**, 045305 (2012).*

The kagome pattern borrows its name from the Japanese bamboo-woven baskets such as the one in Figure 7.1, consisting of a planar lattice with corner sharing triangles. Recently, however, physicists have found a way to promote this pattern into interesting and challenging condensed-matter problems, making this lattice geometry one of the most highly studied strongly correlated system. In particular, the kagome geometry has a large degree of geometric frustration. Competing exchange interactions between spin $1/2$ particles at each vertex of this kagome pattern can not be simultaneously satisfied, leading to a macroscopic ground-state degeneracy. It is this intrinsic ground-state degeneracy in the $S = 1/2$ kagome lattice geometry that makes it a promising candidate for realizing unconventional quantum phases such as the elusive quantum spin liquid at low temperatures [44, 45, 46]. However, despite decades of theoretical work, the ground state of the kagome quantum anti-ferromagnet remains uncertain [169, 170, 44].

Attempts to resolve this uncertainty using solid-state kagome magnets, such as herbertsmithite ($\text{ZnCu}_3(\text{OH})_6\text{Cl}_2$) or volvorthite, have been hampered by significant anisotropies and disorder [171]. An elaborate and sensitive process is needed to synthesize these magnetic materials making it difficult to achieve very high purities. For example, during the Zn-doping process in herbertsmithite, non-magnetic impurities may appear in the kagome planes, which may result in the material not reflecting the intrinsic physics of the kagome anti-ferromagnet. For these reasons, more faithful realizations of the kagome lattice are needed. The technology of cold-atom systems has provided a means for studying the physics of condensed-matter systems in a well controlled environment [8, 169, 9]. Using a tunable

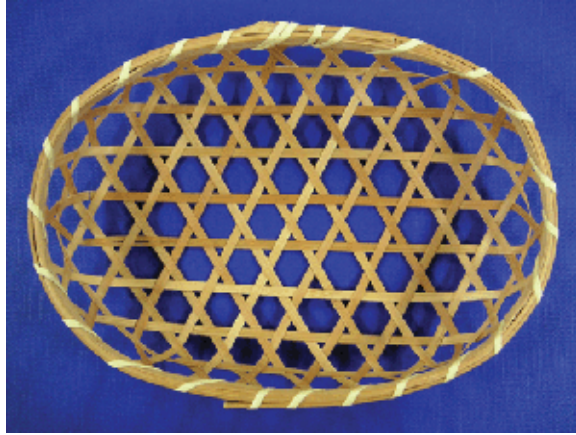


Figure 7.1: Picture of a kagome basket.

bi-chromatic optical lattice, we are able to realize an ideal kagome lattice with ultracold samples of ^{87}Rb [38], free of defects and anisotropies.

In the following sections, a description of the bi-chromatic lattice is presented along with the realization of the kagome optical lattice and the possible lattice geometries, which include the 1D stripe and the decorated triangular lattice.

7.1 Changes to the experimental apparatus

In order to accommodate the many optics necessary to make an optical lattice potential, a few changes to the experimental apparatus were needed.

- **Optical Access** To increase the amount of optical access available for the kagome experiment, the optics around the glass cell were redistributed and the separation between the Feshbach coils was increased from 30 mm to 50 mm. Additionally, the magnetic field coils surrounding the glass cell were removed.
- **Common breadboard** One large aluminum breadboard, 5' x 1.5', was used for the lattice optics. The breadboard consists of two aluminum 1/2" breadboards, glued together. The hope was that this thicker breadboard would be more rigid than the use of a single 1/2" breadboard. The goal of using a common breadboard for all of the lattice optics was to prevent instabilities in the lattice potential caused by differential movements of the lattice optics from being on multiple breadboards.
- **New optics table** In order to accommodate the extra lasers, a new optics table was needed.

7.1.1 Coordinate system

In comparison to the spinor experiments, the coordinate system has been slightly altered. For the lattice experiment, the \hat{z} axis is along gravity and the \hat{x} and \hat{y} axes are oriented in the horizontal plane, with \hat{y} oriented along the long-axis of the condensate.

7.2 Kagome Lattice Geometry

The two-dimensional kagome optical lattice employed in our experiment is created by overlaying two commensurate triangular lattices. The light used to generate the optical lattice consists of two wavelengths of light; light at 532 nm, blue-detuned of atomic resonance and light at 1064 nm, red-detuned from atomic resonance. The short wavelength (SW) lattice derived from the 532 nm light creates a triangular lattice of intensity nodes, which acts to attract the atoms. The long wavelength lattice (LW) derived from the 1064 nm light, also creates a triangular lattice of intensity nodes, but in this example, acts to repel atoms from these sites. By carefully overlapping these two potentials, where the intensity nodes of the SW lattice overlap with the intensity nodes of the LW lattice, we are able to engineer a lattice which selectively removes atoms from specific sites of the SW triangular lattice (see Figure 7.2).

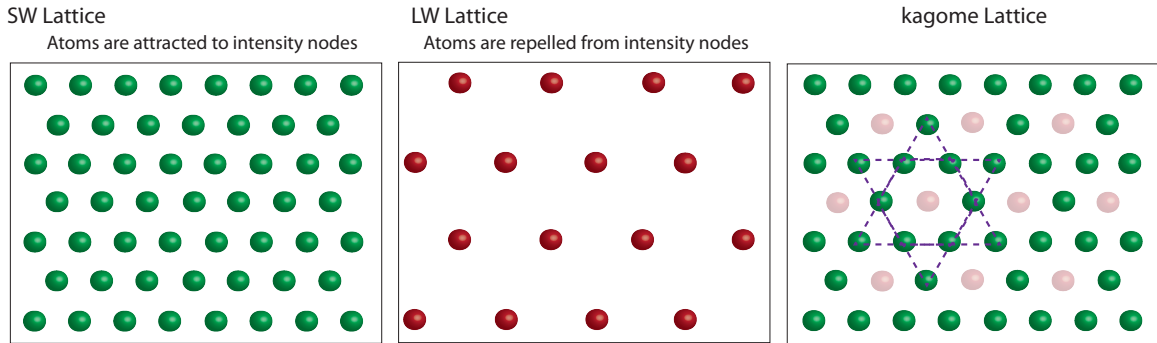


Figure 7.2: Illustration of intensity nodes for the SW and LW triangular lattice. For light blue-detuned of atomic resonance, the atoms are attracted to the intensity nodes, where the potential energy is minimized. In contrast, for light red-detuned of atomic resonance the intensity nodes corresponds to an potential maximum. By overlaying the SW and LW lattice where the intensity nodes coincide, the minimum of the lattice potential takes the form of a kagome geometry.

Typically, the explanation of this lattice setup generates an atmosphere of confusion. The fact that the blue detuned lattice is the attractive potential and the red-detuned lattice is the repulsive potential is somewhat counterintuitive. Most optical lattice experiments trap atoms at the intensity maxima, where the potential energy is minimized [41, 30, 37, 32, 172]. However, here we trap the atoms at the intensity minima, which makes the blue detuned lattice the attractive potential and the red detuned lattice the repulsive potential. In the following sections, an explanation of the lattice is broken down into the two triangular lattices. From there we show how the kagome lattice geometry engineered.

7.2.1 Triangular lattice

Each triangular lattice is created by three linearly polarized laser beams of equal intensity, intersecting at 120° in the horizontal ($\hat{x} - \hat{y}$) plane, with the polarization of the

light in the horizontal plane. The corresponding lattice wave vectors are defined as

$$\mathbf{k}(\theta) = k(-\sin(\theta), \cos(\theta)) \quad (7.1)$$

$$\mathbf{k}_1 = k(0) = k(0, 1), \quad (7.2)$$

$$\mathbf{k}_2 = k(2\pi/3) = k(-\sqrt{3}/2, -1/2), \quad (7.3)$$

$$\mathbf{k}_3 = k(4\pi/3) = k(\sqrt{3}/2, -1/2), \quad (7.4)$$

where θ defines the mutually enclosed angle for each pair of laser beams, and \mathbf{k} is the wave vector of the light used to generate the lattice. For this particular coordinate system, \mathbf{k}_1 refers to a laser beam propagating South, along the glass cell axis, \mathbf{k}_2 refers to one that is propagating along the North-East, and \mathbf{k}_3 refers to the laser beam propagating along the North-West direction.

The general form of the lattice potential is computed from summing the electric field for each lattice beam. For one lattice beam, the electric field takes the form of $\mathbf{E}(x, y) = E_0 e^{i\mathbf{k}\cdot(\mathbf{x}, \mathbf{y})} \hat{\epsilon}$, where $\hat{\epsilon}$ defines the polarization of the electric field. If we add up the electric field of the individual beams of a triangular lattice, using one wavelength of light, we arrive at

$$\mathbf{E}(x, y) = \sum_{i=1}^3 E_{0,i} e^{i\mathbf{k}_i \cdot (x,y)} \hat{\epsilon}_i. \quad (7.5)$$

For the case where the polarizations are perpendicular to the plane spanned by the laser beams, $\hat{\epsilon}_i$ s are the same. However, for the triangular lattices employed here, the polarizations are in the plane spanned by the laser beams. The corresponding polarization for each lattice beam is

$$\hat{\epsilon}_1 = (1, 0) \quad (7.6)$$

$$\hat{\epsilon}_2 = (-1/2, \sqrt{3}/2) \quad (7.7)$$

$$\hat{\epsilon}_3 = (-1/2, \sqrt{3}/2), \quad (7.8)$$

where the polarization $\hat{\epsilon}_1$ corresponds to the \mathbf{k}_1 lattice wave vector. In order to get to the lattice potential, we need to compute the intensity, $I = |\mathbf{E} \cdot \mathbf{E}^*|$. The resulting intensity profile is

$$I(x, y) = E_0^2 \left(e^{i\mathbf{k}_1 \cdot (x,y)} \hat{\epsilon}_1 + e^{i\mathbf{k}_2 \cdot (x,y)} \hat{\epsilon}_2 + e^{i\mathbf{k}_3 \cdot (x,y)} \hat{\epsilon}_3 \right). \quad (7.9)$$

$$\left(e^{i\mathbf{k}_1 \cdot (x,y)} \hat{\epsilon}_1 + e^{i\mathbf{k}_2 \cdot (x,y)} \hat{\epsilon}_2 + e^{i\mathbf{k}_3 \cdot (x,y)} \hat{\epsilon}_3 \right)^* \quad (7.10)$$

$$(7.11)$$

After simplifying the above expression, the lattice potential for a triangular lattice consisting of a single wavelength of light simplifies to the following form,

$$V(x, y) = V_0 [3 - \cos(b_1 \cdot (x, y)) - \cos((b_1 - b_2) \cdot (x, y)) - \cos(b_2 \cdot (x, y))], \quad (7.12)$$

where V_0 is proportional to the potential depth of two counter-propagating lattice beams and b_i are the reciprocal lattice vectors, related to the lattice wave vectors by $b_i = \epsilon_{ijk}(k_j - k_k)$.

A contour plot of a triangular lattice potential is shown in Figure 7.3. Here, the locations of zero intensity form a triangular lattice. In addition to the triangular lattice of intensity minima, there also arises a honeycomb lattice of maximum intensity. The intensity at these locations is $4.5I_0$, where I_0 is the intensity of a single plane wave. Surrounding each of these intensity maxima are saddle points with intensity $4I_0$. These subtleties in the triangular lattice potential landscape are illustrated in Figure 7.3.

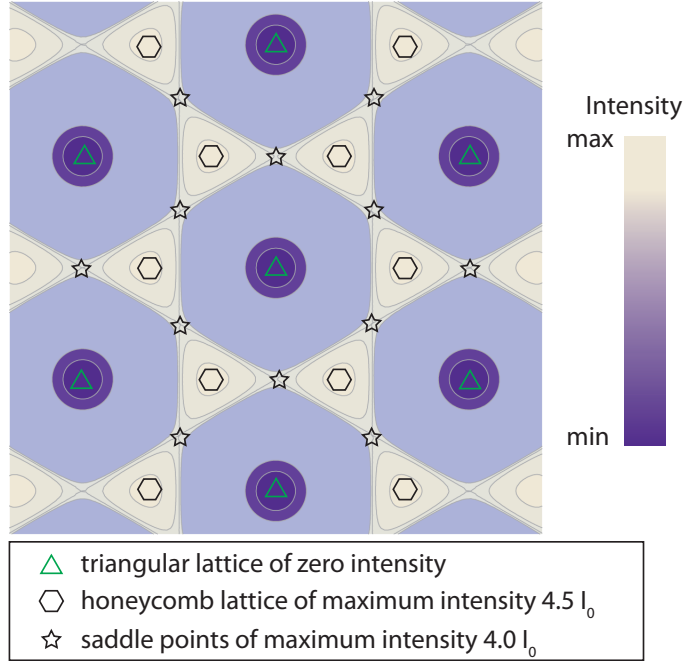


Figure 7.3: Contour map of triangular lattice intensity profile. The darker colors represent lower intensities. Also illustrated is the intensity maxima in a honeycomb configuration and saddle points surrounding each point of zero intensity.

7.2.2 Bi-chromatic optical lattice

To create the kagome potential, we overlay the optical lattice potentials from the SW and LW triangular lattices, such that their intensity minima overlap. The time-averaged optical potential for the 2D superlattice is

$$I(x, y) = \left| \sum_i E_{0,i}^{LW} e^{i\mathbf{k}_i \cdot (\mathbf{x}, \mathbf{y})} \hat{\mathbf{e}}_i + \sum_i E_{0,i}^{SW} e^{i(2\mathbf{k}_i \cdot (\mathbf{x}, \mathbf{y}) + \phi_i)} \hat{\mathbf{e}}_i \right|^2 \quad (7.13)$$

where ϕ_i is the phase for each lattice beam which will be used to tune the lattice geometry (see below). The resulting lattice potential when $\phi = 0$ is shown in Figure 7.4. Here, the SW lattice forms a triangular lattice of intensity minima while the LW lattice creates a similar lattice, but with twice the lattice spacing. Realizing that the attractive lattice in this case is the SW lattice, generated from 532 nm light, may seem counterintuitive. We can

better understand the lattice potential by determining the location of the potential minima, which coincides with the location of the atoms. We can determine this by considering the shift of the ground state energy, U_{dip} , arising from the ac Stark effect,

$$U_{dip}(x, y) = -\frac{3\pi c^2 \gamma}{2\omega_0^3} \sum_j c_{i,j}^2 \left(\frac{1}{\omega_j - \omega_L} + \frac{1}{\omega_j + \omega_L} \right) \times I(x, y), \quad (7.14)$$

where ω_L is the frequency of the light field, ω_0 is the electronic transition frequency, and $c_{i,j}$ is the Clebsch-Gordan coefficient between the ground state $|i\rangle$ and the excited state, $|j\rangle$. Thus for blue detuned light, $\omega_j < \omega_L$, the shift of the ground state is positive, $U_{dip} > 0$ for any nonzero intensity, while for red detuned light, $\omega_j > \omega_L$, the ground state is shifted towards negative energies, $U_{dip} < 0$. Applying this logic to our bi-chromatic superlattice, we see that the SW triangular lattice of intensity minima is a potential energy minimum, and is thus attractive, while the LW lattice of intensity minima is a potential energy maximum, and is thus repulsive.

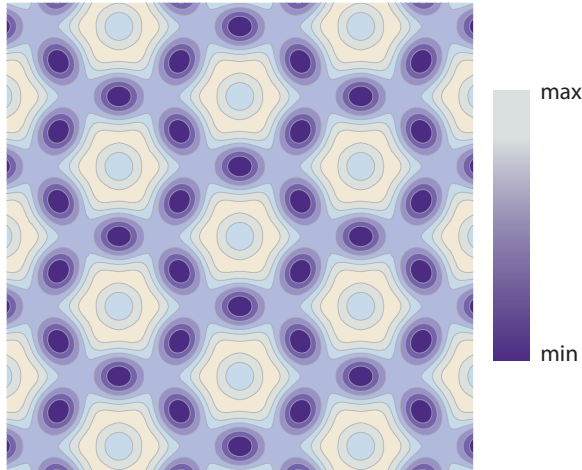


Figure 7.4: Contour map of the kagome lattice potential. The potential is made by overlaying the SW and LW triangular lattice potentials.

7.2.3 Unit Cell

The unit cell of the LW lattice is a rhombus, containing one site of the LW lattice or four sites of the SW lattice, which we refer to as sites A, B, C and D for simplicity. When the intensity node of the LW lattice overlaps with the intensity node of the SW lattice, for instance site D , the potential energies at this sites A, B, C are reduced equally. This reduction is defined as $\Delta V = V_D - V_{ABC} = \frac{8}{9}V_{LW}$, where V_{LW} is the energy shift of the ground state due to the LW lattice. Then as ΔV is increased, the atoms are ultimately expelled from site D . The three occupied sites within the unit cell represent the unit cell of the kagome lattice. An illustration of the kagome unit cell is shown in Figure 7.5.

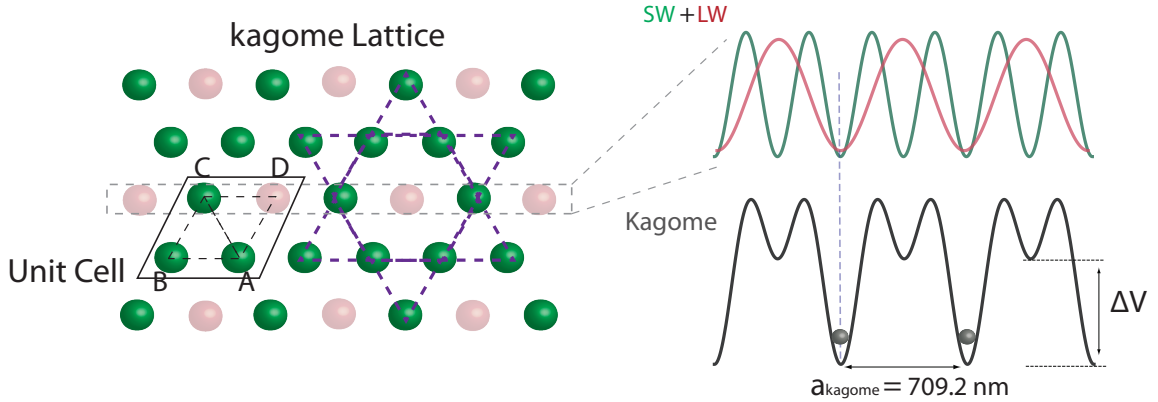


Figure 7.5: The unit cell of the kagome lattice. For simplicity, we label each site within the unit cell alphabetically, where sites A, B, C are identical for the kagome potential, and site D is the site that is removed using the repulsive LW lattice. A 1D profile of the combined potential of the LW and SW is also shown. When the depth of the LW is large enough, atoms from site D are excluded.

7.3 Tuning the lattice geometry

One important aspect of the experiment is to stabilize the relative position of the intensity nodes with respect to each other. This is accomplished by means of a two-color Mach-Zehnder interferometer, where the optical phase of the lattice beams are controlled and stabilized.

Two independent Mach-Zehnder interferometers are used to stabilize the phases of the light beams of the SW lattice to the those of the LW lattice. This is accomplished by first monitoring the phase difference between the lattice beams for the SW and LW lattice and then stabilizing the phase difference using piezo-electric transducers on a path common to both lattices, which then synchronizes their phases (see Figure 7.6). Specifically, after propagating through the atoms and glass cell, a small fraction of light from Beam 1 and 2 is picked off (see Section 7.7.1 for lattice beam orientations). The light from Beams 1 and 2, consisting of light at 1064 and 532 nm, is then combined using a broadband polarization beam-splitter. Beam 2, however, passes through a dispersive element, in this case a glass wedge, before combining with Beam 1. The combined light passes through a dichroic mirror, which separates the two colors of light, before being sent to a photodiode. The resulting signal is fed back to two sets of piezo-electric transducers, where each piezo-electric transducer is used to stabilize Beam 2 to Beam 1 of the SW and LW lattice, and the piezo-electric transducer common to both beams synchronizes the relative phases of the LW to the SW lattice. In the experiment, the outputs of the photodetectors are demodulated, having been modulated using EOM's located before the glass cell. This error signal is then fed back to the two sets of piezo-electric transducers. A similar setup exists to stabilize Beam 3 to Beam 1 and to synchronize the SW to the LW lattice.

The glass wedge in the Mach-Zehnder interferometer is used to tune the lattice geometry. The dispersive nature of the glass wedge introduces a relative phase shift between

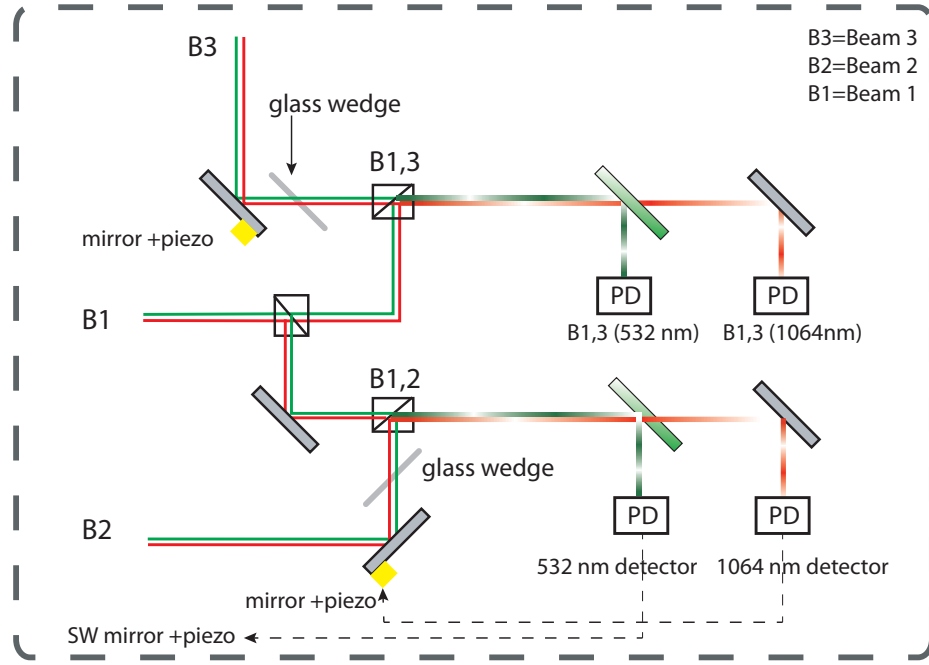


Figure 7.6: Illustration of two-color Mach-Zehnder interferometer. A small fraction of light is picked off from each lattice beam. The beams are combined using polarizing beam splitters, where “B1,3” refers to the beam splitter which combines Beam 1 and 3. Before being combined one beam from each interferometer arm is sent through a glass wedge which adds a tunable phase shift to that lattice beam. The beams are interfered at a photodiode. The beat-note is used fed back to the PZT’s in the SW and LW lattice path for Beams 2 and 3 which is used to stabilize the relative path lengths.

the SW and LW lattices which scales linearly with the total length traveled d as $\phi \sim \Delta nkt$, where d is the thickness of the dispersive medium, $\Delta n = n_{532} - n_{1064}$ is the difference in the refractive indices for the two wavelengths of light (532 nm and 1064 nm), and k is the wave vector of the light. We can vary the phase difference by tuning the angle of the wedge with respect to the light beam, thus changing the total length traveled. The thickness of the glass that each beam traverses is determined by the refraction angle,

$$d_{532} = d_0 \sec[\theta - \arcsin(\sin(\theta/n_{532}))] \quad (7.15)$$

$$d_{1064} = d_0 \sec[\theta - \arcsin(\sin(\theta/n_{1064}))], \quad (7.16)$$

where $d_0 = 60$ mm is the glass thickness, the refractive index n_{532} and n_{1064} is 1.521947 and 1.50663, and θ is the tilt angle. The total phase difference for each is $\phi_\lambda = n_\lambda k_\lambda t$, where k is the wave vector of the lattice. To determine the relative displacement between the SW and LW lattices, we compute the relative phase shift for each color of light and take the sine of the difference,

$$\sin \left[\left(\frac{\phi_{532}}{k_{532}} - \frac{\phi_{1064}}{k_{1064}} \right) \times k_{532} \right], \quad (7.17)$$

where the displacement is represented in units of k_{532} , the wave vector for the 532 nm lattice. A plot of the relative displacement is shown in Figure 7.7

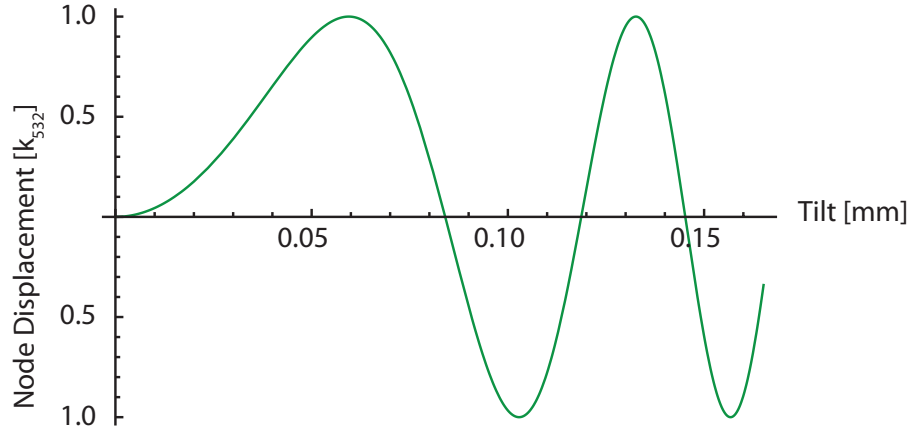


Figure 7.7: Displacement of 532 nm intensity nodes with respect to the 1064 nm intensity nodes. By tilting the wedge we are able to tune the relative displacement between the SW and LW lattice, thus tuning the lattice geometry.

7.4 Other lattice geometries

Since we have the ability to move and stabilize the relative locations of the intensity nodes, we can also access different lattice geometries. The bi-chromatic optical lattice can be tuned to create the following lattice geometries: kagome, 1D stripe, or the decorated triangular lattice.

Tuning the lattice geometry is accomplished by adjusting the relative overlap of the intensity nodes of the SW and LW optical lattice via the dispersive wedge in the interferometer setup. An illustration of the possible lattice geometries is shown in Figure 7.8. For instance, placing the intensity node of the LW triangular lattice such that it is located halfway between two nodes of the SW triangular lattice, we are able to create a set of 1D coupled chains. This can be understood through use of the unit cell (see Figure 7.8). By placing the repulsive LW intensity node between sites A and D of the unit cell, we increase the potential energy at these sites relative to the other two sites, and at sufficiently high power atoms are expelled from these two sites. The unit cell in this case contains two occupied and unoccupied sites, leading to the observed stripe pattern. However, if the LW intensity node is placed at an equal distance from all three nodes of the SW lattice, for instance sites A , B , and D , then the potential energies of these three sites is raised relative to site C . Thus, the atoms are expelled from these sites, leaving one site per unit cell which is allowed to be occupied. The resulting potential is a triangular lattice with twice the lattice spacing.

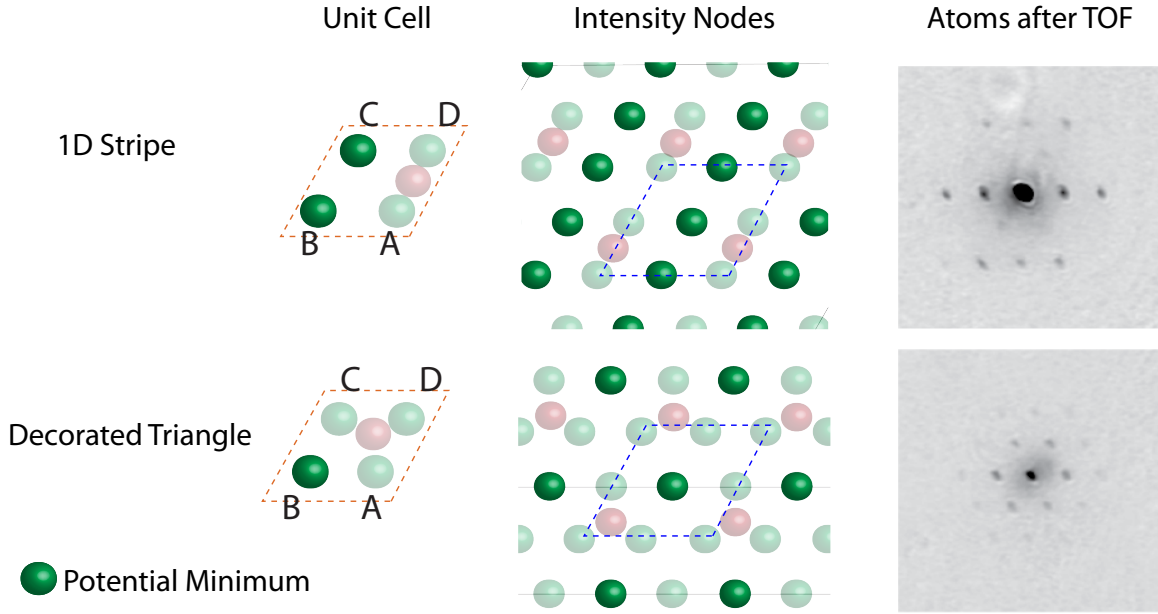


Figure 7.8: Illustration of other accessible lattice geometries in this bi-chromatic lattice. These include the 1D stripe (top row) and decorated triangular lattice (bottom row). As a visual guide, the unit cell, spatial distribution of intensity nodes, and the momentum distribution in TOF are shown. The green circles indicate a minimum in the potential energy.

7.5 Calibrating the lattice potential

The depth of the lattice potential is measured using Kapitza-dirac scattering [166]. Kapitza-Dirac scattering is the diffraction of a particle beam by a standing wave light field when the particle motion can be neglected (Raman-Nath approximation). This effect is fairly well known and there are many review articles on the topic [173, 174, 166, 175], so it won't be covered in much detail here. The result of Kapitza-Dirac scattering is a coherent transfer of momentum to the atoms in units of $2N\hbar k$, where k is wave vector of the standing wave. The probability of populating these momentum states is linearly related to the integral of the pulse duration. Thus, by determining this exact relation, we can obtain a measure of the lattice depth at the location of the atoms.

The application of a pulsed standing wave field acts to imprint a phase on the condensate wave function, $|\Psi_0\rangle$. Immediately after the application of the pulse, the wave function can be described as:

$$|\Psi\rangle = |\Psi_0\rangle e^{-i \int dt U(z,t)} \quad (7.18)$$

$$= |\Psi_0\rangle e^{-i \frac{\Omega_R^2}{2\delta} \tau} e^{-i \frac{\Omega_R^2}{2\delta} \tau f^2(t) \cos(2kz)}, \quad (7.19)$$

where $\tau = \int dt f^2(t)$ is the integral over the pulse duration, $f(t)$ is the temporal envelope

function, and the potential of the standing wave is

$$U(z, t) = \hbar\Omega_R^2 f^2(t) \sin^2(kz) \quad (7.20)$$

$$= \hbar\Omega_R^2 f^2(t) \frac{1 - \cos(2kz)}{2}. \quad (7.21)$$

We can simplify this expression through use of the relation for Bessel functions of the first kind,

$$e^{i\alpha \cos(\beta)} = \sum_{n=-\infty}^{\infty} i^n J_n(\alpha) e^{in\beta}. \quad (7.22)$$

The wave function can thus be rewritten in the following form

$$|\Psi\rangle = |\Psi_0\rangle \sum_{n=-\infty}^{\infty} i^n J_n\left(\frac{\Omega_R^2}{2\delta}\tau\right) e^{i2nkz}, \quad (7.23)$$

where we have absorbed the overall phase into the initial wave function. Thus, a state with momentum $2N\hbar k$ has a probability

$$P_N = J_N^2\left(\frac{\Omega_R^2}{2\delta}\tau\right) \quad (7.24)$$

for $N = 0, \pm 1, \pm 2, \dots$. To obtain a measure of the lattice depth, which is proportional to the Rabi frequency, we can rewrite the probability as

$$P_N = J_N^2(\eta P \Delta\tau) \quad (7.25)$$

where $\Delta\tau$ is the pulse duration, η is the calibration factor which relates the lattice depth to the lattice beam power (i.e. Rabi frequency) in units of Hz/mW, and P is the lattice power.

In practice, we obtain a measure of the lattice potential by measuring the number of atoms in the 0th order and the 1st order. As the power in the pulse is increased, the number of atoms scattered into higher momentum states increases. We fit the fraction of atoms in a given momentum state to a Bessel function as $P_N = J_N^2(\eta P \Delta\tau)$. From the fit we obtain a measure of the lattice calibration. An example of calibration curve is shown in Figure 7.9. This procedure is repeated for each pair of lattice beams.

7.6 Measurement Techniques

In order to demonstrate the tunability of the bi-chromatic lattice, we used two different techniques: Kapitza-dirac diffraction and momentum-space analysis. For these measurements, we begin with a BEC of $\sim 3 \times 10^5$ atoms in the $|F = 1, m_F = -1\rangle$ state at a temperature of 80 nK. The condensate is held in a crossed optical dipole trap using linearly polarized light at 1064 nm, characterized by trap frequencies $(\omega_x, \omega_y, \omega_z) = 2\pi \times (60, 50, 350)$ Hz. The relative position of the LW and SW lattices was measured using the two-color Mach-Zehnder interferometer discussed above and actively stabilized by using actuator on mirrors in the relevant optical paths. The lattice geometry was then varied by tuning the phase shift between the two lattices in the interferometer [38].

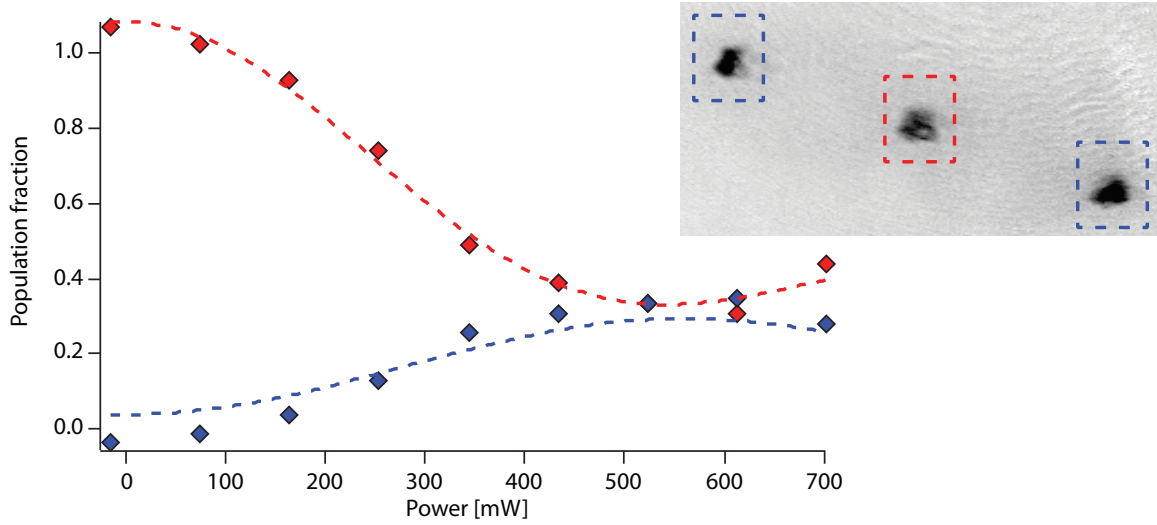


Figure 7.9: Calibration curve for SW lattice depth for Beam 1 and Beam 2. The SW lattice light is controlled using an SRS pulse generator. A short pulse duration of $8\ \mu\text{s}$ is used which is about an order of magnitude shorter than one over the recoil frequency, ensuring that the Raman-Nath approximation is still valid.

7.6.1 Kaptiza-Dirac

One method used to demonstrate the how the bi-chromatic lattice is tuned between different lattice geometries is Kaptiza-dirac diffraction [164, 166, 163, 174] (see Section 7.5). In this technique, the condensate is released from the optical trap and immediately following this release, the lattice potential is pulsed on then off. The pulse duration, τ , is sufficiently short to ensure that the atoms were not moving during the pulse, and can therefore be described as Kaptiza-Dirac scattering. The effect of this sudden turn on then off is to imprint a phase shift, $V(\mathbf{r})\tau/\hbar$, onto the condensate wavefunction which is proportional to the lattice potential, $V(\mathbf{r})$.

The momentum-space distribution after the pulse of the lattice potential is sensitive to the relative displacement of the LW and SW lattices. For simplicity, we consider a one dimensional superlattice formed by two bi-chromatic lattice beams intersecting at 120° . The potential energy of this lattice configuration is

$$V(x) = V_{LW} \sin^2(q(x + \delta x)/2) - V_{SW} \sin^2(qx), \quad (7.26)$$

where $2\pi/q = 614\ \text{nm}$ is the one-dimensional lattice spacing and δx is the distance between the intensity nodes of the LW and SW lattices. We can determine the effect of the pulse by

considering the phase imprinted onto the condensate wavefunction, $|\Psi_0\rangle$, described as,

$$|\Psi_0\rangle = |\Psi_0\rangle e^{-i \int dt V(x)} \quad (7.27)$$

$$|\Psi_0\rangle = e^{i(V_{LW} \sin^2(q(x+\delta x)/2) - V_{SW} \sin^2(qx))} \quad (7.28)$$

$$|\Psi_0\rangle = \left[\sum_m (i)^m J_m^{LW}(V_{LW}) e^{2mq(x+\delta x)} \sum_m (i)^m J_m^{SW}(V_{SW}) e^{4mqx} \right], \quad (7.29)$$

where J_m is the m^{th} order Bessel function. Considering diffraction up to second order in the phase modulation depth, the populations at wave vectors $\pm q$ are given as $P_{\pm q}$,

$$P_{\pm q} \propto \left| \pm i J_{\pm 1} J_0^{SW} + J_{\mp 1}^{LW} J_{\pm 1}^{SW} e^{\mp i 2q \delta x} \right|^2, \quad (7.30)$$

where the Bessel function is evaluated at $V_{LW,SW}\tau/2\hbar$, according to the superscript. Thus, from Equation 7.30 the exponential phase factor shows up in the diffraction pattern as a left-right asymmetry in the TOF momentum distribution. An example of the left-right asymmetry is seen in Figure 7.10. Thus, varying the displacement between the intensity nodes of the LW and SW lattices will result in a corresponding change in the left/right asymmetry in the momentum distribution imaged in TOF. A scan of the displacement, δx and the corresponding Kapitza-Dirac diffraction is shown in Figure 2 of [38]

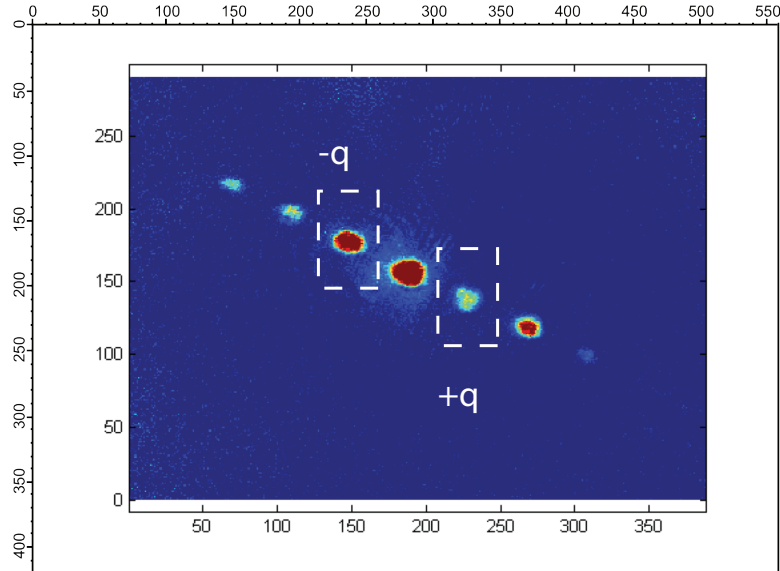


Figure 7.10: Kapitza-Dirac scattering from a one-dimensional bi-chromatic lattice. The peaks at $\pm q$ show a left/right asymmetry. This asymmetry varies as the displacement δx between the LW and SW lattice intensity nodes is varied.

7.6.2 Momentum-space analysis

In order to demonstrate the tunability of this optical superlattice, we also monitored the characteristic momentum distribution of the atoms for different relative displacements of the SW and LW triangular lattices. For this analysis, the optical lattice potential depth was ramped up exponentially over 90 ms. The atoms were held in the lattice for an additional 100 ms, after which the optical traps were switched off. Imaging after 15 ms of free expansion revealed coherent momentum peaks at the reciprocal lattice vectors of the LW lattice.

TOF Momentum Distribution for a multi-atom basis

The TOF momentum distribution can be computed from the atom field operator, $\phi_{\mathbf{k}}$ [48, 49]. To do this we must obtain the functional form for the atom field operator in a four-atom basis. Extending the case of the single atom basis to a four-atom basis is done by summing over the basis sites within the unit cell, b_i . The atom field operator takes the following form,

$$\phi_{\mathbf{k}} = w(\mathbf{k}) \sum_{p=1}^4 \sum_{R_i} \hat{a}_{\mathbf{R}_i + \mathbf{b}_p} e^{-i\mathbf{k} \cdot (R_i + b_p)}. \quad (7.31)$$

Here $\tilde{w}(\mathbf{k})$ is the Fourier transform of the Wannier wavefunction, where the Wannier wavefunction, $w(\mathbf{k})$ is a localized wavefunction at individual lattice sites, R_i denotes the primitive lattice vectors of the LW lattice, $\hat{a}_{\mathbf{R}_i + \mathbf{b}_p}$ is the annihilation operator at position $\mathbf{R}_i + \mathbf{b}_p$, and the atom field operator, $\phi_{\mathbf{k}}(r)$, destroys a particle at position r [176, 14]. The TOF momentum distribution is obtained from the expectation value of $\phi_{\mathbf{k}}^\dagger \phi_{\mathbf{k}}$,

$$\begin{aligned} \langle \Psi | \phi_{\mathbf{k}}^\dagger \phi_{\mathbf{k}} | \Psi \rangle &= n_k \quad (7.32) \\ &= |\tilde{w}(\mathbf{k})|^2 \sum_{p=1}^4 \sum_{R_i, R_j} e^{-i\mathbf{k} \cdot (R_i - R_j)} \langle a_{R_i + b_p}^\dagger a_{R_j + b_p} \rangle \\ &+ |\tilde{w}(\mathbf{k})|^2 \sum_{p, q=1}^4 \sum_{R_i, R_j} e^{-i\mathbf{k} \cdot [(R_i - R_j) + (b_p - b_q)]} \langle a_{R_i + b_p}^\dagger a_{R_j + b_q} \rangle. \quad (7.33) \end{aligned}$$

Momentum Ratio

From the momentum distribution we can compute the momentum peak ratio between $\mathbf{k} = 0$ and $\mathbf{k} = \mathbf{2G}$, $n_{\mathbf{2G}}/n_0$ and obtain a characteristic signal for each lattice geometry. For the kagome geometry, a symmetric TOF interference pattern results in a symmetric momentum peak ratio, $n_{\mathbf{G}/\mathbf{n}_0} = 1/9$. In contrast, a LW triangular lattice, with one atom per unit cell, has a value of $n_{\mathbf{2G}/\mathbf{n}_0} = 1$ and $n_{\mathbf{2G}/\mathbf{n}_0} = 0$ for the SW triangular lattice. For a 1D stripe lattice geometry, two sites are occupied and two sites are unoccupied, resulting in an asymmetric momentum distribution, with one axis at $k = 2G_1$ enhanced and the remaining two axes, $k = 2G_{2,3}$, suppressed.

To demonstrate our control of the lattice geometry, we extract the momentum population ratio as we scan the lattice geometry from the one-dimensional stripe to the

kagome geometry. We start in the kagome configuration and then vary the angle of the dispersive window which serves to displace the LW lattice with respect to the SW lattice. The change in the lattice geometry is seen by monitoring the expansion out of the lattice. We quantify these changes using the momentum population ratio for each position of the LW lattice. An example of this is shown in Figure 3 of [38] and a calculation is shown in Figure 7.11.

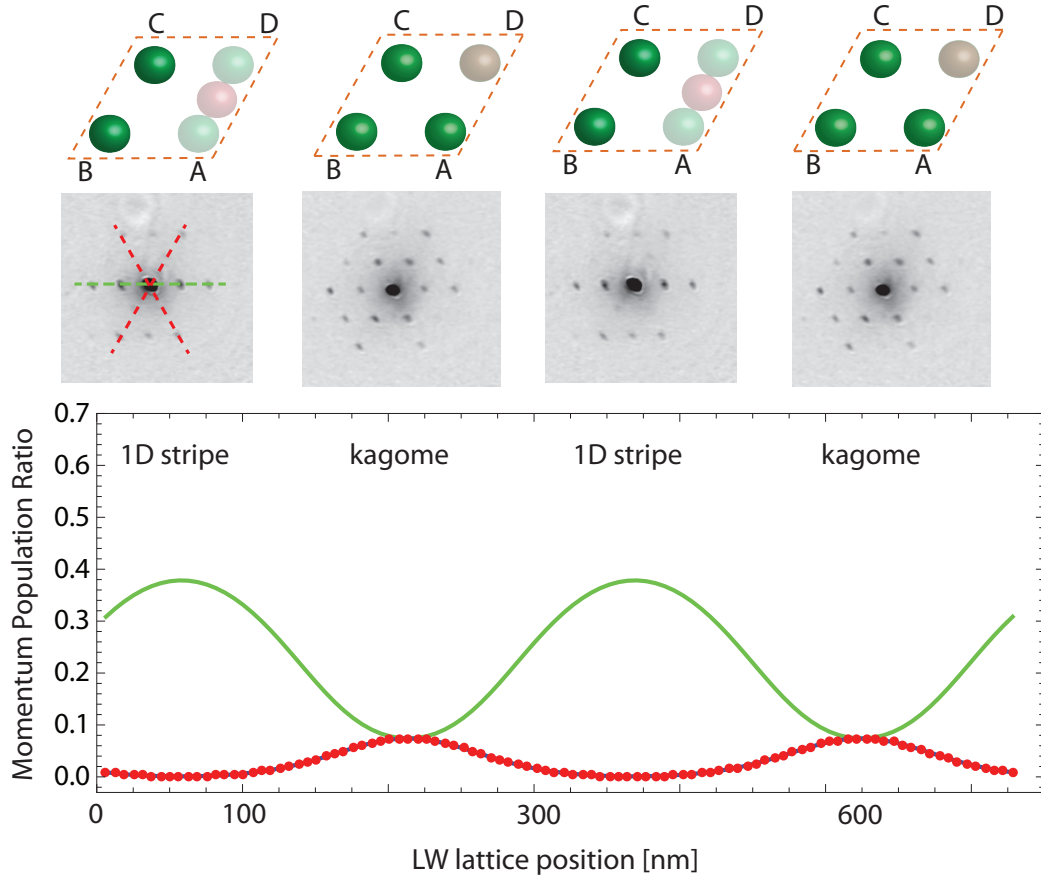


Figure 7.11: TOF calculations of the momentum population ratio as a function of the LW lattice position. By tuning the angle of the dispersive glass in the interferometer setup, we can accurately tune the geometry of the superlattice. In this particular instance, the intensity node of the LW lattice is scanned from midway between sites D and A to D , thus varying the lattice geometry from 1D stripe to kagome. The green line is the momentum ratio corresponding to the horizontal axis in the TOF images, while the red lines are the other two axes, which have equal ratios.

Unit Cell populations

We can also extract the fractional populations within the unit cell using the form of the momentum distribution discussed above. We can express these fractional populations,

P_A, \dots, P_D , in terms of the momentum peaks at $0, 2G$ and $4G$, where G is the reciprocal lattice vector of the LW lattice. Considering a uniform superfluid in the lattice, the fractional population within the unit cell is given by $a_{R_i+b_u}|\Psi\rangle = e^{i\phi_{SF}}\sqrt{P_u}|\Psi\rangle$, where we define $\phi_{SF} = 0$. For $\mathbf{k} = 0$, the momentum distribution is

$$n_{k=0} = M^2|\tilde{w}(0)|^2 \left[\sum_{p=1}^4 P_p + \sum_{p,q} \sqrt{P_p P_q} \right] \quad (7.34)$$

$$(7.35)$$

where M denotes the number of plaquettes, with $4 \times M$ being the total number of lattice sites. For $k = \pm 4\hbar G_i$, where \mathbf{G}_i is the reciprocal lattice vector of the LW lattice, $n_{k=\pm 4\hbar G_1}$ is

$$n_{k=\pm 4\hbar G_1} = M^2|\tilde{w}(4\hbar G_1)|^2 \left[\sum_{p=1}^4 P_p + \sum_{p,q} \sqrt{P_p P_q} \right]. \quad (7.36)$$

$$(7.37)$$

A similar result is achieved for $k = \pm 4\hbar G_2$ and $k = \pm 4\hbar G_3$. Finally for $k = \pm 2\hbar G_i$, the peak density is:

$$n_{k=\pm 2\hbar G_1} = M^2|\tilde{w}(2\hbar G_1)|^2 \left[\sum_{p=1}^4 P_p - \sum_{p,q} \sqrt{P_p P_q} + 4 \left(\sqrt{P_1 P_3} + \sqrt{P_2 P_4} \right) \right] \quad (7.38)$$

$$n_{k=\pm 2\hbar G_2} = M^2|\tilde{w}(2\hbar G_2)|^2 \left[\sum_{p=1}^4 P_p - \sum_{p,q} \sqrt{P_p P_q} + 4 \left(\sqrt{P_1 P_2} + \sqrt{P_3 P_4} \right) \right] \quad (7.39)$$

$$n_{k=\pm 2\hbar G_3} = M^2|\tilde{w}(2\hbar G_2)|^2 \left[\sum_{p=1}^4 P_p - \sum_{p,q} \sqrt{P_p P_q} + 4 \left(\sqrt{P_1 P_4} + \sqrt{P_3 P_2} \right) \right]. \quad (7.40)$$

In order to determine the fractional populations within the unit cell, we combine the results from Equations (6.21-6.27). This leads to a system of four equations that are needed to solve for P_p :

$$\tilde{n}_{\mathbf{k}=0,\pm 4\mathbf{G}} = \left(\sqrt{P_A} + \sqrt{P_B} + \sqrt{P_C} + \sqrt{P_D} \right)^2 \quad (7.41)$$

$$\tilde{n}_{\mathbf{k}=\pm 2\mathbf{G}_1} = \left(\sqrt{P_A} - \sqrt{P_B} - \sqrt{P_C} + \sqrt{P_D} \right)^2 \quad (7.42)$$

$$\tilde{n}_{\mathbf{k}=\pm 2\mathbf{G}_2} = \left(\sqrt{P_A} - \sqrt{P_B} + \sqrt{P_C} - \sqrt{P_D} \right)^2 \quad (7.43)$$

$$\tilde{n}_{\mathbf{k}=\pm 2\mathbf{G}_3} = \left(-\sqrt{P_A} - \sqrt{P_B} + \sqrt{P_C} + \sqrt{P_D} \right)^2, \quad (7.44)$$

where $\tilde{n}_{\mathbf{k}} = n_{\mathbf{k}}/|\tilde{w}(k)|^2$ is defined as the normalized density distribution and we have switched to the convention defined earlier with letters defining the different sites within the

unit cell. Assuming a normalization of the fractional populations equal to unity, $\sum P_p = 1$ and that the approximation of the Wannier function as a Gaussian function is valid, we can invert these nonlinear equations to determine the atomic distribution within the unit cell.

In practice, we use the measured fractional populations within the unit cell as a tool for lattice alignment. Since each of the lattice geometries described above have either 1, 2, 3, or 4 occupied sites within the unit cell, we can use the fractional populations to more precisely align the lattice in a specific geometric configuration. For instance, when the intensity node of the LW lattice is located midway between sites C and D (3 and 4), the fractional populations within the unit cell are $(P_1, P_2, P_3, P_4) = 0.5, 0.5, 0, 0$, where the population difference is determined by both the position and intensity of the LW intensity node. An example of different alignments between the LW and SW lattices and the corresponding fractional populations is shown in Figure 7.12.

In the experiment discussed in [38], we use the set of coupled equations to extract the unit cell population for the kagome geometry as we convert the lattice geometry from a SW triangular to kagome lattice [38]. To do this, we begin with the lattice geometry in the kagome configuration, where the intensity nodes of the SW and LW overlap. Then as a function of the LW lattice depth, we take images of the corresponding momentum distribution (see Figure 4 of [38]). At zero LW lattice depth, the geometry of the lattice is represented by the SW triangular lattice, with the population of atoms equally distributed amount the sites within the unit cell. As the LW lattice depth is increased, the potential depth at sites A, B, C is reduced, causing atoms to be expelled form site D . This results in a decrease in the the fractional population with the unit cell at site D . The population smoothly decreases from its initial value of $1/4$ to zero, while the population fraction in the remaining sites increases form $1/4$ to $1/3$.

Table 7.1: Summary of momentum distribution and corresponding unit cell populations for the different lattice geometries.

Lattice Geometry	Momentum Population ratio	Unit Cell Population
Triangular (SW)	0	$1/4, 1/4, 1/4, 1/4$
kagome	$1/9$	$1/3, 1/3, 1/3, 0$
1D Stripe	1	$0, 0, 1/2, 1/2$
Decorated Triangular	1	$1, 0, 0, 0$
Honeycomb	$1/4$	

7.7 Lattice Optics

7.7.1 Lattice optics layout

To construct the bi-chromatic optical lattice, we use light at 1064 nm and light at 532 nm. An illustration of the lattice optics is shown in Figure 7.13. The 532 nm light is derived from an 18 W Verdi laser from Coherent Inc. located on the science table, since we were unable to find high-power fibers for 532 nm light. The 18 W of power is divided

into two paths, one which directs approximately 5-6 W for construction of the lattice while the remaining unused laser light power is sent to a beam dump. The light used for the lattice is sent through a high-power AOM from IntraAction (Part Number AFM802A1 - rated to a maximum power of 6-7 W) used for intensity stabilization of the beam, after which a small fraction of the diffracted light is picked off to monitor and stabilize the beam intensity. Approximately 70% of the light is diffracted into the first-order beam which is then split into three separate paths with equal power, which we refer to as Beam 1, Beam 2, and Beam 3 (see Figure 7.13). Next, Beams 2 and 3 are sent through EOMs from Linos (Part Number 8450-204-900-0) oriented to produce mostly phase modulation of the beam and little polarization modulation. These EOMs are specifically designed to compensate phase drifts due to temperature fluctuations. After traversing through the EOMs, Beams 2 and 3 along with Beam 1 are then sent to the atoms using long-wave pass dichroics and come to a focus at the approximate location of the atoms using achromat lenses with a focal length of 250 mm from Melles Griot.

The 1064 nm light is directed towards the atoms in a similar manner as the 532 nm light. Here the approximately 2.0 W of laser light is delivered to the science table using one single-mode fiber. A small fraction of light is picked off and used for intensity stabilization of an AOM, located on the 1064 laser table. The remaining light is split into three paths with the power distributed equally among them. The light is then combined with the 532 nm light using the long-wave pass dichroics and sent to the glass cell.

The use of a single AOM for intensity stabilizing the 532 nm light is limits the amount of power we can have in the lattice beams. Currently, the AOM from IntraAction specifies the maximum laser power to be ~ 6 W, which equates to 1 W per beam at the atoms, after taking into account the loss of power on all of the optics. Exceeding 6 W into the AOM will lead to thermal lensing effects in the crystal, which can have a detrimental effect on the lattice potential. In practice, we see some thermal lensing at powers as low as 5 W. A few possible alternatives would be to use multiple AOMs or an EOM. These options, however, are also accompanied with problems of their own, where frequency noise arises from the use of multiple AOMs and EOMs are often not rated to extremely high powers.

7.7.2 Lattice Alignment

For the more roughest alignment of the optical lattice, the BEC was first imaged along the lattice direction by transmitting imaging light through the lattice beam path. The image of the BEC was focused onto the imaging CCD (Guppy Firewire camera) using a lens located just before the camera. The pixel position of the focused condensate was then marked and the lattice beam was aligned and focused to the same spot. Next, to fine tune the alignment, we monitor the effect of the lattice beams on the atoms themselves, so as to be sure that all the beams are overlapped at the condensate. For example, the lattice beams of the SW lattice create a repulsive barrier in the condensate, creating a double well potential. An example of this is shown in Figure 7.14. The final mirror or dichroic is used to center the lattice beam on the condensate. This process is roughly repeated for all lattice beams. The last stage of alignment is done by using Kaptiza-Dirac diffraction (see below). Each pair of lattice beams is pulsed on for $8 \mu\text{s}$ ($13 \mu\text{s}$) for the SW (LW) lattice. The final mirrors are used to maximize the diffraction pattern.

7.7.3 Laser table optics

The 1064 nm light is generated on a separate optics table. The 1064 nm light is derived from a grating-stabilized laser (ECDL) and amplified using a 15 W fiber amplifier from Nufern. The fiber amplifier is equipped with an optical isolator. However, a series of unfortunate events involving bad optical isolators and three damaged Nufern amplifiers has led us to install an additional high-power optical isolator. We measure approximately 80% transmission through the isolator, leaving us with about 12 W of laser light at our disposal. The output of the optical isolator is split into four paths: one for the optical dipole trap, one for the triangular lattice, one for the dimple beam, and one for the vertical lattice. Each path is directed towards an AOM used to intensity stabilize the beam and to ensure that the frequency of each beam is distinct enough to prevent interference between them. Following this, the beams are delivered to the science table using hollow core single-mode fibers.

7.7.4 New optical trap

In addition to the structural changes around the experimental apparatus, a new optical trap beam was added to the myriad of optical beams used in the experiment. The new optical trap, referred to as the dimple beam, is used to compensate the repulsive envelope of the SW triangular lattice. Without the dimple beam, the weak axial confinement of the surfboard ODT, with a trapping frequency of $\omega_y = 2\pi \times 8$ Hz, was insufficient to compensate the repulsion due to the SW lattice potential, characterized by trapping frequencies $\omega_{x,y} = 2\pi \times 30$ Hz.

The dimple beam consists of a cylindrically symmetric beam using light at 1064 nm, propagating along the \hat{z} direction. The beam is characterized by trapping frequencies $\omega_{x,y} = 2\pi \times 50$ Hz, which are large enough to compensate the repulsive 532 nm light. The light for the beam is delivered to the science table via a single mode polarization maintaining optical fiber. After exiting the fiber, a small fraction of light is picked off and used for intensity stabilization, while the remaining light is sent through a 500 mm lens before traversing to the glass cell. Because this lens is not on a translation stage, adjusting the location of the focus is nearly impossible without completely misaligning the beam. Instead, the position of the focus is adjusted using the output collimator of the optical fiber. The collimator used is from Schäfter-Kirchhoff and allows for easy adjustment of the beam collimation. In practice, the beam is slightly diverging after exiting the collimator.

One complication associated with the dimple beam is the dichroic used to combine it with resonant imaging light. At the time of construction, we did not anticipate the number of specialty optics needed and some compromises had to be made. The use of a dichroic meant for light at 780 and 850 nm is one example. At this interface, only 70 % of the 1064 nm light is transmitted. A potential improvement would be to switch this dichroic with one specified for the appropriate wavelengths of light in order to transmit a larger fraction of power.

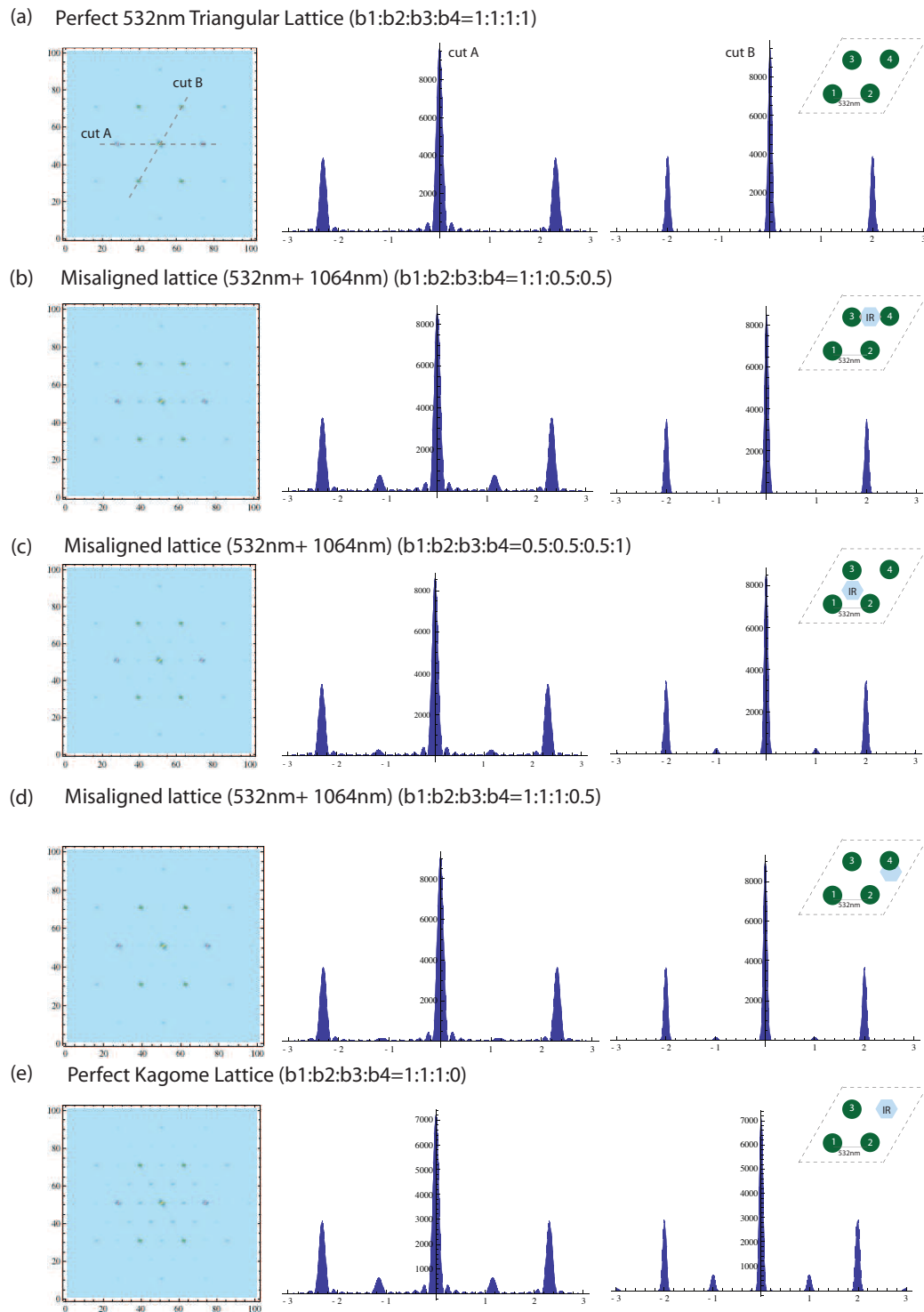


Figure 7.12: TOF calculations for misaligned lattices. The density profiles along the cuts A and B are shown in the second and third column. (a) and (e) show expected TOF images for an ideal triangular and kagome lattice. (b)-(d) show TOF patterns for misaligned lattices. b_i here represents the relative population at site i in the unit cell, as shown in the inset. The blue hexagon denotes the intensity node of the LW lattice and the orange green circles denote the SW intensity node.

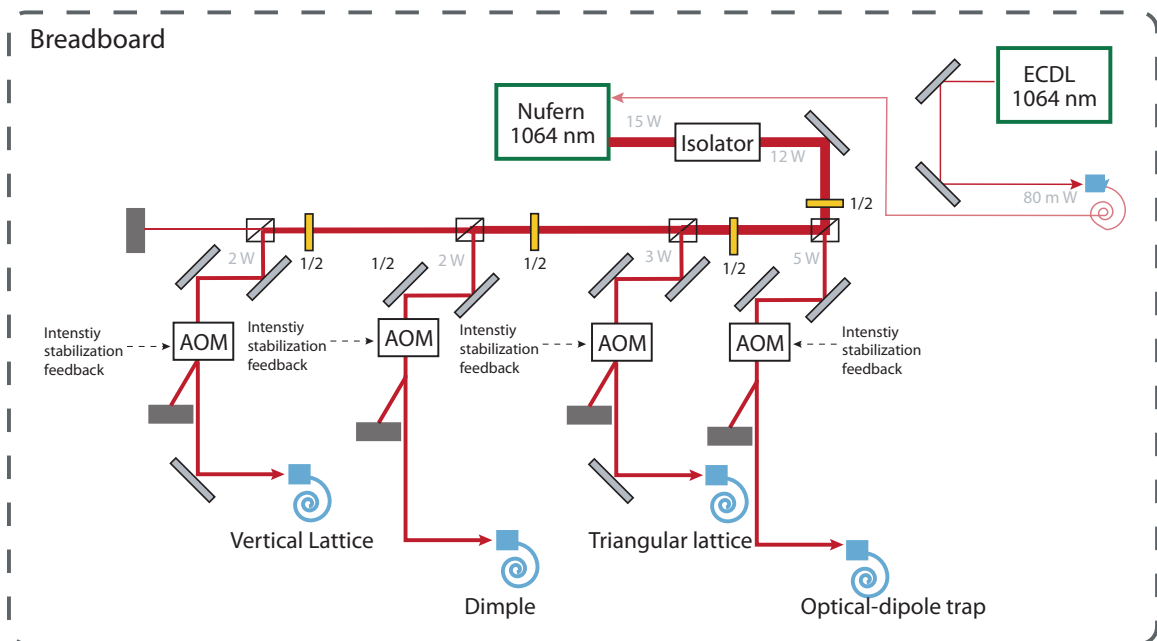


Figure 7.15: Layout of 1064 nm optics on laser table.

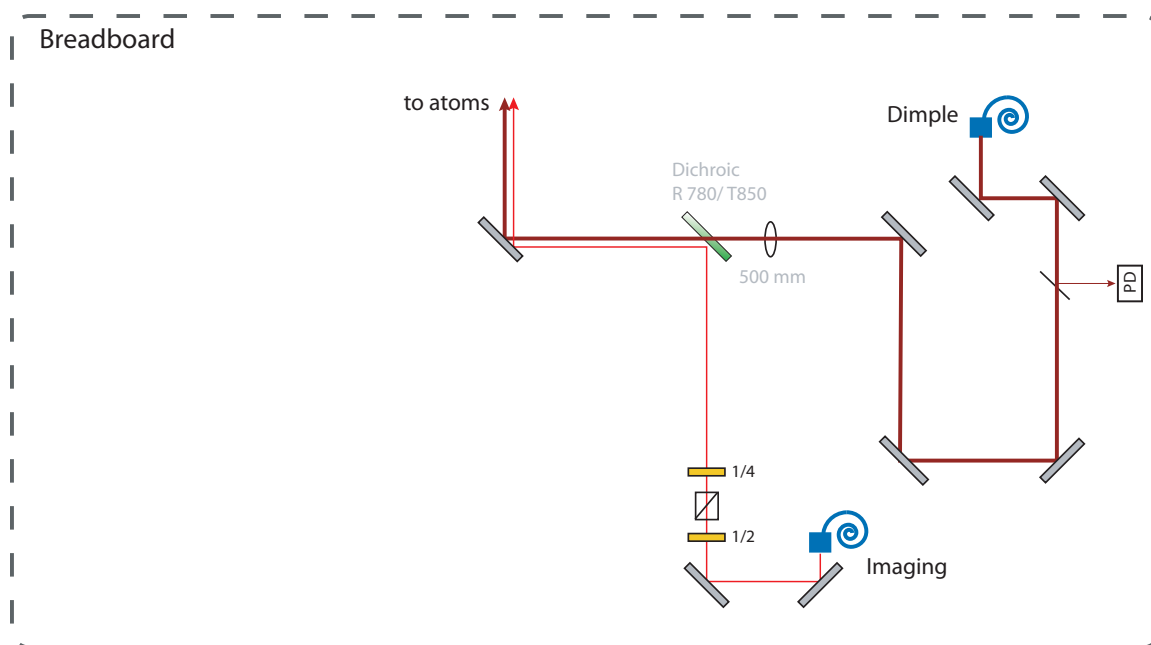


Figure 7.16: Schematic of dimple optics used to steer the beam to the glass cell. Because the optics for the dimple beam are located on the optics table below the lattice breadboard, the optics are purposefully positioned near the table edge so that they are not too inaccessible. The dimple beam is combined with the top/down imaging beam using a long-wave pass dichroic. The dichroic is meant for light at 850 nm and light at 780 nm, thus there is some power lost on this element. After being combined on the dichroic the atoms are directed to the glass cell using a 2 inch gold mirror, located directly below the glass cell.

Bibliography

- [1] M. R. Andrews, M.-O. Mewes, N. J. van Druten, D. S. Durfee, D. M. Kurn, and W. Ketterle. Direct, Nondestructive Observation of a Bose Condensate. *Science*, 273(5271):84–87, 1996.
- [2] J. R. Ensher, D. S. Jin, M. R. Matthews, C. E. Wieman, and E. A. Cornell. Bose-Einstein Condensation in a Dilute Gas: Measurement of Energy and Ground-State Occupation. *Phys. Rev. Lett.*, 77(25):4984–4987, Dec 1996.
- [3] M. Vengalattore, J. M. Higbie, S. R. Leslie, J. Guzman, L. E. Sadler, and D. M. Stamper-Kurn. High-Resolution Magnetometry with a Spinor Bose-Einstein Condensate. *Phys. Rev. Lett.*, 98(20):200801, May 2007.
- [4] G. Edward Marti, Ryan Olf, Enrico Vogt, Anton Öttl, and Dan M. Stamper-Kurn. Two-element Zeeman slower for rubidium and lithium. *Phys. Rev. A*, 81:043424, Apr 2010.
- [5] T. L. Gustavson, P. Bouyer, and M. A. Kasevich. Precision Rotation Measurements with an Atom Interferometer Gyroscope. *Phys. Rev. Lett.*, 78:2046–2049, Mar 1997.
- [6] D. S. Durfee, Y. K. Shaham, and M. A. Kasevich. Long-Term Stability of an Area-Reversible Atom-Interferometer Sagnac Gyroscope. *Phys. Rev. Lett.*, 97:240801, Dec 2006.
- [7] Holger Müller, Sheng-wei Chiow, Sven Herrmann, Steven Chu, and Keng-Yeow Chung. Atom-Interferometry Tests of the Isotropy of Post-Newtonian Gravity. *Phys. Rev. Lett.*, 100:031101, Jan 2008.
- [8] Immanuel Bloch, Jean Dalibard, and Wilhelm Zwerger. Many-body physics with ultracold gases. *Rev. Mod. Phys.*, 80:885–964, Jul 2008.
- [9] Oliver Morsch and Markus Oberthaler. Dynamics of Bose-Einstein condensates in optical lattices. *Reviews of Modern Physics*, 78(1):179, 2006.
- [10] Dan M. Stamper-Kurn. *Peeking and poking at a new quantum fluid: Studies of gaseous Bose-Einstein condensates in a magnetic and optical traps*. PhD thesis, MIT, 2000.
- [11] Heather Jean Lewandowski. *Coherences and correlations in an ultracold Bose gas*. PhD thesis, University of Colorado, 2002.

- [12] M.-O Mewes. *Bose-Einstein Condensation of Sodium Atoms*. PhD thesis, MIT, 1997.
- [13] Dieter Jaksch. *Bose Einstein Condensation and Applications*. PhD thesis, University of Innsbruck, 1999.
- [14] Markus Greiner. *Ultracold quantum gases in three-dimensional optical lattice potentials*. PhD thesis, Ludwig-Maximilians-Universitt Mnchen, 2003.
- [15] Jens O. Andersen. Theory of the weakly interacting Bose gas. *Reviews of Modern Physics*, 76(2):599, 2004.
- [16] E. A. Cornell and C. E. Wieman. Nobel Lecture: Bose-Einstein condensation in a dilute gas, the first 70 years and some recent experiments. *Reviews of Modern Physics*, 74(3):875–893, Aug 2002.
- [17] Franco Dalfovo, Stefano Giorgini, and Lev P. Pitaevskii. Theory of Bose-Einstein Condensation in trapped gases. *Reviews of Modern Physics*, 1999.
- [18] W. Ketterle, M. Andrews, K.B. Davis, D. Durfee, D. Kurn, M.-O Mewes, and N. J. van Druten. Bose-Einstein Condensation of Ultracold Atomic Gases. *Physica Scripta*, 1996.
- [19] Anthony J. Leggett. Bose-Einstein condensation in the alkali gases: Some fundamental concepts. *Reviews of Modern Physics*, 73(2):307–356, Apr 2001.
- [20] F. London. On the Bose-Einstein Condensation. *Physical Review*, 54, 1938.
- [21] W. Phillips, J. Prodan, and H. Metcalf. Laser cooling and electromagnetic trapping of neutral atoms. *Opt. Soc. Am. B*, 2, 1985.
- [22] William D. Phillips. Laser cooling and trapping of neutral atoms. *Reviews of Modern Physics*, 70, 1998.
- [23] Carl E. Wieman and Leo Hollberg. Using diode lasers for atomic physics. *Rev. Sci Instrum*, 62, 1991.
- [24] C. J. Pethick and H. Smith. *Bose-Einstein Condensation in Dilute Gases*. Camb, 2002.
- [25] Lev Pitaevskii and Sandro Stringari. *Bose-Einstein Condensation*. Oxford Science Publications, 2003.
- [26] Harold Metcalf and Peter Van der straten. *Laser Cooling and Trapping*. Springer, 1999.
- [27] Tin-Lun Ho. Spinor Bose Condensates in Optical Traps. *Phys. Rev. Lett.*, 81(4):742–745, Jul 1998.
- [28] V. S. Letokhov. Narrowing of the Doppler Width in a Standing Wave. *Journal of Experimental and Theoretical Physics Letters*, 7:272, 1968.

- [29] C. Salomon, J. Dalibard, A. Aspect, H. Metcalf, and C. Cohen-Tannoudji. Channeling atoms in a laser standing wave. *Phys. Rev. Lett.*, 59:1659–1662, Oct 1987.
- [30] Markus Greiner, Olaf Mandel, Tilman Esslinger, Theodor W. Hansch, and Immanuel Bloch. Quantum phase transition from a superfluid to a Mott insulator in a gas of ultracold atoms. *Nature*, 415(6867):39–44, January 2002.
- [31] Waseem S. Bakr, A. Peng, M. E. Tai, J. Simon, J. I. Gillen, S. Folling, L. Pollet, and Markus Greiner. Probing the Superfluid -to-Mott Insulator Transition at the Single-Atom Level. *Science*, 329:547–550, 2010.
- [32] I. B. Spielman, W. D. Phillips, and J. V. Porto. Mott-Insulator Transition in a Two-Dimensional Atomic Bose Gas. *Phys. Rev. Lett.*, 98:080404, Feb 2007.
- [33] K. Jimenez-Garcia, R. L. Compton, Y.-J. Lin, W. D. Phillips, J. V. Porto, and I. B. Spielman. Phases of a Two-Dimensional Bose Gas in an Optical Lattice. *Phys. Rev. Lett.*, 105:110401, Sep 2010.
- [34] Kenneth Günter, Thilo Stöferle, Henning Moritz, Michael Köhl, and Tilman Esslinger. Bose-Fermi Mixtures in a Three-Dimensional Optical Lattice. *Physical Review Letters*, 96(18):180402, 2006.
- [35] Robert Jordens, Niels Strohmaier, Kenneth Gunter, Henning Moritz, and Tilman Esslinger. A Mott insulator of fermionic atoms in an optical lattices. *Nature*, 455:204–207, 2008.
- [36] Michael Köhl, Henning Moritz, Thilo Stöferle, Kenneth Günter, and Tilman Esslinger. Fermionic Atoms in a Three Dimensional Optical Lattice: Observing Fermi Surfaces, Dynamics, and Interactions. *Phys. Rev. Lett.*, 94:080403, Mar 2005.
- [37] C. Becker, P. Soltan-Panahi, J. Kronjger, S. Drscher, K. Bongs, and K. Sengstock. Ultracold quantum gases in triangular optical lattices. *New Journal of Physics*, 12(6):065025, 2010.
- [38] Gyu-Boong Jo, Jennie Guzman, Claire K. Thomas, Pavan Hosur, Ashvin Vishwanath, and Dan M. Stamper-Kurn. Ultracold Atoms in a Tunable Optical Kagome Lattice. *Phys. Rev. Lett.*, 108:045305, Jan 2012.
- [39] P. Soltan-Panahi, J. Struck, P. Hauke, A. Bick, W. Plenkers, G. Meineke, C. Becker, P. Windpassinger, M. Lewenstein, and K. Sengstock. Multi-component quantum gases in spin-dependent hexagonal lattices. *Nat Phys*, 7:434–440, 2011.
- [40] Leticia Tarruell, Daniel Greif, Thomas Uehlinger, Gregor Jotzu, and Tilman Esslinger. Creating, moving and merging Dirac points with a Fermi gas in a tunable honeycomb lattice. *Nature*, 483:302–305, 2012.
- [41] Waseem S. Bakr, I. Gillen, Jonathon, Amy Peng, Simon Folling, and Markus Greiner. A quantum gas microscope for detecting single atoms in a Hubbard-regime optical lattice. *Nature*, 462:74–77, 2009.

- [42] Jonathon Simon, W. S. Bakr, Ruichao Ma, M. Eric Tai, M. Preiss, Phillip, and Markus Greiner. Quantum simulation of antiferromagnetic spin chains in an optical lattice. *Nature*, 472:307–312, 2011.
- [43] Jacob F. Sherson, Christof Weitenberg, Manuel Endres, Marc Cheneau, Immanuel Bloch, and Stefan Kuhr. Single-atom-resolved fluorescence imaging of an atomic Mott insulator. *Nature*, 467:68–72, 2010.
- [44] S.-H. Lee, H. Kukuchi, Y. Qiu, B. Lake, Q. Huang, K. Habicht, and K. Kiefer. Quantum-spin liquid states in the two dimensional kagome antiferromagnets $\text{ZnxCu}_{4-x}(\text{OD})_6\text{Cl}_2$. *Nature Materials*, 2007.
- [45] S. Dommange, M. Mambrini, B. Normand, and F. Mila. Static impurities in the $S = 1/2$ kagome lattice: Dimer freezing and mutual repulsion. *Phys. Rev. B*, 68:224416, Dec 2003.
- [46] Leon Balents. Spin Liquids in Frustrated Magnets. *Nature*, 464, 2010.
- [47] Grechen Campbell, Jongchul Mun, Micah Boyd, Patrick Medley, Aaron E. Leanhardt, Luis g. Marcassa, David E. Pritchard, and Wolfgang Ketterle. Imaging the Mott Insulator Shells by Using Atomic Clock Shifts. *Science*, 313, 2006.
- [48] P. Pedri, L. Pitaevskii, S. Stringari, C. Fort, S. Burger, F. S. Cataliotti, P. Maddaloni, F. Minardi, and M. Inguscio. Expansion of a Coherent Array of Bose-Einstein Condensates. *Phys. Rev. Lett.*, 87:220401, Nov 2001.
- [49] F. Gerbier, S. Trotzky, S. Fölling, U. Schnorrberger, J. D. Thompson, A. Widera, I. Bloch, L. Pollet, M. Troyer, B. Capogrosso-Sansone, N. V. Prokof'ev, and B. V. Svistunov. Expansion of a Quantum Gas Released from an Optical Lattice. *Phys. Rev. Lett.*, 101:155303, Oct 2008.
- [50] Gregory H. Wannier. The Structure of Electronic Excitation Levels in Insulating Crystals. *Phys. Rev.*, 52:191–197, Aug 1937.
- [51] J. M. Higbie, L. E. Sadler, S. Inouye, A. P. Chikkatur, S. R. Leslie, K. L. Moore, V. Savalli, and D. M. Stamper-Kurn. Direct Nondestructive Imaging of Magnetization in a Spin-1 Bose-Einstein Gas. *Physical Review Letters*, 95(5):050401, 2005.
- [52] Lorraine Elizabeth Sadler. *Dynamics of a Spin 1 Ferromagnetic Condensate*. PhD thesis, University of California, Berkeley, 2006.
- [53] H. C. W. Beijerinck and N. F. Verster. Velocity distribution and angular distribution of molecular beams from multichannel arrays. *Journal of Applied Physics*, 46(5):2083–2091, 1975.
- [54] G C Angel and R A Giles. The velocity distribution of atoms issuing from a multi-channel glass capillary array and its implication on the measurement of atomic beam scattering cross sections. *Journal of Physics B: Atomic and Molecular Physics*, 5(1):80, 1972.

- [55] J.B. Anderson, R.P. Andres, and J.B. Fenn. High Intensity and High Energy Molecular Beams. volume 1 of *Advances in Atomic and Molecular Physics*, pages 345 – 389. Academic Press, 1965.
- [56] Rudolf Grimm, Matthias Weidemler, and Yurii B. Ovchinnikov. Optical Dipole Traps for Neutral Atoms. volume 42 of *Advances In Atomic, Molecular, and Optical Physics*, pages 95 – 170. Academic Press, 2000.
- [57] Claude N. Cohen-Tannoudji. Manipulating atoms with photons. *Reviews of Modern Physics*, 70, 1998.
- [58] Steven Chu, J. E. Bjorkholm, A. Ashkin, and A. Cable. Experimental Observation of Optically Trapped Atoms. *Phys. Rev. Lett.*, 57:314–317, Jul 1986.
- [59] A. Ashkin. Trapping of Atoms by Resonance Radiation Pressure. *Phys. Rev. Lett.*, 40:729–732, Mar 1978.
- [60] A. Ashkin. Acceleration and Trapping of Particles by Radiation Pressure. *Phys. Rev. Lett.*, 24:156–159, Jan 1970.
- [61] A. Ashkin. Applications of Laser Radiation Pressure. *Science*, 210(4474):1081–1088, 1980.
- [62] William D. Phillips and Harold Metcalf. Laser Deceleration of an Atomic Beam. *Phys. Rev. Lett.*, 48:596–599, Mar 1982.
- [63] Thomas E. Barrett, Samuel W. Dapore-Schwartz, Mark D. Ray, and Gregory P. Lafyatis. Slowing atoms with sigma-polarized light. *Phys. Rev. Lett.*, 67:3483–3486, Dec 1991.
- [64] Michael A. Joffe, Wolfgang Ketterle, Alex Martin, and David E. Pritchard. Transverse cooling and deflection of an atomic beam inside a Zeeman slower. *J. Opt. Soc. Am. B*, 10(12):2257–2262, Dec 1993.
- [65] E. L. Raab, M. Prentiss, Alex Cable, Steven Chu, and D. E. Pritchard. Trapping of Neutral Sodium Atoms with Radiation Pressure. *Phys. Rev. Lett.*, 59:2631–2634, Dec 1987.
- [66] C. G. Townsend, N. H. Edwards, C. J. Cooper, K. P. Zetie, C. J. Foot, A. M. Steane, P. Szriftgiser, H. Perrin, and J. Dalibard. Phase-space density in the magneto-optical trap. *Phys. Rev. A*, 52:1423–1440, Aug 1995.
- [67] T. W. Hodapp, C. Gerz, C. Furtlehner, C. I. Westbrook, W. D. Phillips, and J. Dalibard. Three-dimensional spatial diffusion in optical molasses. *Applied Physics B: Lasers and Optics*, 60:135–143, 1995. 10.1007/BF01135855.
- [68] Thad Walker, David Sesko, and Carl Wieman. Collective behavior of optically trapped neutral atoms. *Phys. Rev. Lett.*, 64:408–411, Jan 1990.

- [69] Erling Riis, David S. Weiss, Kathryn A. Moler, and Steven Chu. Atom funnel for the production of a slow, high-density atomic beam. *Phys. Rev. Lett.*, 64:1658–1661, Apr 1990.
- [70] C. I. Westbrook, R. N. Watts, C. E. Tanner, S. L. Rolston, W. D. Phillips, P. D. Lett, and P. L. Gould. Localization of atoms in a three-dimensional standing wave. *Phys. Rev. Lett.*, 65:33–36, Jul 1990.
- [71] Wolfgang Petrich, Michael H. Anderson, Jason R. Ensher, and Eric A. Cornell. Behavior of atoms in a compressed magneto-optical trap. *J. Opt. Soc. Am. B*, 11(8):1332–1335, Aug 1994.
- [72] Markus Greiner, Immanuel Bloch, Theodor W. Hänsch, and Tilman Esslinger. Magnetic transport of trapped cold atoms over a large distance. *Phys. Rev. A*, 63:031401, Feb 2001.
- [73] H. J. Lewandowski, D. M. Harber, D. L. Whitaker, and E. A. Cornell. Simplified System for Creating a Bose-Einstein Condensate. *Journal of Low Temperature Physics*, 132:309–367, 2003. 10.1023/A:1024800600621.
- [74] A. Marte, T. Volz, J. Schuster, S. Dürr, G. Rempe, E. G. M. van Kempen, and B. J. Verhaar. Feshbach Resonances in Rubidium 87: Precision Measurement and Analysis. *Phys. Rev. Lett.*, 89:283202, Dec 2002.
- [75] Erik W. Streed, Ananth P. Chikkatur, Todd L. Gustavson, Micah Boyd, Yoshio Torii, Dominik Schneble, Gretchen K. Campbell, David E. Pritchard, and Wolfgang Ketterle. Large atom number Bose-Einstein condensate machines. *Review of Scientific Instruments*, 77(2):023106, 2006.
- [76] K.B. Davis. *Evaporative Cooling of Sodium Atoms*. PhD thesis, MIT, 1995.
- [77] K.B. Davis, M.-O Mewes, M. Joffe, M. Andrews, and W. Ketterle. Evaporative Cooling of Sodium Atoms. *Phys. Rev. Lett.*, 1995.
- [78] Wolfgang Ketterle and N. J. van Druten. Evaporative cooling of trapped atoms. 1996.
- [79] James Higbie. *First Steps toward Precision Measurements using Multicomponent Bose-Einstein Condensates of ^{87}Rb* . PhD thesis, University of California, Berkeley, 2005.
- [80] S. R. Leslie. *Spinor Condensates as Amplifiers, Sensors and Tunable Quantum Playgrounds for Studies of Spin*. PhD thesis, University of California, Berkeley, 2009.
- [81] Higbie J. M. Leslie S. R. Vengalattore M. Stamper-Kurn D. M. Sadler, L. E. Spontaneous symmetry breaking in a quenched ferromagnetic spinor Bose-Einstein condensate. *Nature*, 2006.
- [82] Dan M. Stamper-Kurn and Masahito Ueda. Spinor Bose gases: Explorations of symmetries, magnetism and quantum dynamics. May 2012.

- [83] S. R. Leslie, J. Guzman, M. Vengalattore, Jay D. Sau, Marvin L. Cohen, and D. M. Stamper-Kurn. Amplification of fluctuations in a spinor Bose-Einstein condensate. *Phys. Rev. A*, 79(4):043631, Apr 2009.
- [84] Aviv Keshet and Wolfgang Ketterle. A Distributed GUI-based Computer Control System for Atomic Physics Experiments. August 2012.
- [85] Y.-J. Lin, A. Perrin, R. L. Compton, I. B. Spielman, and Porto. Rapid production of Rb Bose-Einstein condens in a combined magnetic and optical potential. *Phys. Rev. A*, 79, 2009.
- [86] F. Zernike. Phase contrast, a new method for the microscopic observation of transparent objects. *Physica*, 9(7):686 – 698, 1942.
- [87] F. Zernike. Phase contrast, a new method for the microscopic observation of transparent objects part II. *Physica*, 9(10):974 – 986, 1942.
- [88] M. Andrews, C. Townsend, H. Miesner, D. Durfee, D. Kurn, and W. Ketterle. Observation of Interference Between Two Bose Condensates. *Science*, 275, January 1997.
- [89] C. C. Bradley, C. A. Sackett, and R. G. Hulet. Bose-Einstein Condensation of Lithium: Observation of Limited Condensate Number. *Phys. Rev. Lett.*, 78:985–989, Feb 1997.
- [90] R.G. Fassett, BernadetteA. Horgan, and T.H. Mathew. Detection of Glomerular Bleeding by Phase-Contrast Microscopy. *The Lancet*, 319(8287):1432 – 1434, 1982.
jce:title;Originally published as Volume 1, Issue 8287i/ce:titlej.
- [91] Paul C. Haljan. *Vortices in a Bose-Einstein Condensate*. PhD thesis, University of Colorado, 2003.
- [92] Iacopo Carusotto and Erich J Mueller. Imaging of spinor gases. *Journal of Physics B: Atomic, Molecular and Optical Physics*, 37(7):S115, 2004.
- [93] Max Born and Emil Wolf. *Principles of Optics*. Cambri, 1999.
- [94] F. L. Pedrotti and L. S. Pedrotti. *Introduction to Optics*. Prentice Hall, 1993.
- [95] R. Meppelink, R. A. Rozendaal, S. B. Koller, J. M. Vogels, and P. van der Straten. Phase contrast imaging of Bose condensed clouds. September 2009.
- [96] F Arfelli, M Assante, V Bonvicini, A Bravin, G Cantatore, E Castelli, L Dalla Palma, M Di Michiel, R Longo, A Olivo, S Pani, D Pontoni, P Poropat, M Prest, A Rashevsky, G Tromba, A Vacchi, E Vallazza, and F Zanconati. Low-dose phase contrast x-ray medical imaging. *Physics in Medicine and Biology*, 43(10):2845, 1998.
- [97] Laura M. Roth. Theory of the Faraday Effect in Solids. *Phys. Rev.*, 133:A542–A553, Jan 1964.
- [98] M Suffczynski. Faraday Effect for Direct Magneto-optical Transitions in Germanium. *Proceedings of the Physical Society*, 77(5):1042, 1961.

- [99] Horia D. Cornean, Gheorghe Nenciu, and Thomas G. Pedersen. The Faraday effect revisited: General theory. *Journal of Mathematical Physics*, 47(1):013511, 2006.
- [100] E. L. Hahn. Spin Echoes. *Phys. Rev.*, 80:580–594, Nov 1950.
- [101] J. M. McGuirk, H. J. Lewandowski, D. M. Harber, T. Nikuni, J. E. Williams, and E. A. Cornell. Spatial Resolution of Spin Waves in an Ultracold Gas. *Phys. Rev. Lett.*, 89(9):090402, Aug 2002.
- [102] J. Kronjager, C. Becker, M. Brinkmann, R. Walser, P. Navez, K. Bongs, and K. Sengstock. Evolution of a spinor condensate: Coherent dynamics, dephasing, and revivals. *Physical Review A*, 72(6):063619, 2005.
- [103] N. F. Ramsey. *Molecular Beams*. Oxford University Press, 1956.
- [104] J. Guzman, G.-B. Jo, A. N. Wenz, K. W. Murch, C. K. Thomas, and D. M. Stamper-Kurn. Long-time-scale dynamics of spin textures in a degenerate $F = 1$ ^{87}Rb spinor Bose gas. *Phys. Rev. A*, 84:063625, Dec 2011.
- [105] Anand Ramanathan, Sergio R. Muniz, Kevin C. Wright, Russell P. Anderson, William D. Phillips, Kristian Helmerson, and Gretchen K. Campbell. Partial-Transfer Absorption Imaging: A versatile technique for optimal imaging of ultracold gases. June 2012.
- [106] *Fundamental Optics*.
- [107] Joseph Goodman. *Introduction to Fourier Optics*. Roberts and Company Publishers, 2005.
- [108] Glenn D. Boreman and Sidney Yang. Modulation Transfer Function Measurement Using Three- and Four-bar Targets. *Appl. Opt.*, 34(34):8050–8052, Dec 1995.
- [109] Harel Haim, Naim Konforti, and Emanuel Marom. Performance of imaging systems analyzed with two-dimensional target. *Appl. Opt.*, 51(25):5966–5972, Sep 2012.
- [110] Harel Haim, Naim Konforti, and Emanuel Marom. Optical imaging systems analyzed with a 2D template. *Appl. Opt.*, 51(14):2739–2746, May 2012.
- [111] Chen-Lung Hung, Xibo Zhang, Li-Chung Ha, Shih-Kuang Tung, Nathan Gemelke, and Cheng Chin. Extracting density-density correlations from in situ images of atomic quantum gases. *New Journal of Physics*, 13(7):075019, 2011.
- [112] R Bucker, A Perrin, S Manz, T Betz, Ch Koller, T Plisson, J Rottmann, T Schumm, and J Schmiedmayer. Single-particle-sensitive imaging of freely propagating ultracold atoms. *New Journal of Physics*, 11(10):103039, 2009.
- [113] M. Vengalattore, S. R. Leslie, J. Guzman, and D. M. Stamper-Kurn. Spontaneously Modulated Spin Textures in a Dipolar Spinor Bose-Einstein Condensate. *Phys. Rev. Lett.*, 100(17):170403, May 2008.

- [114] M.-S. Chang, C. D. Hamley, M. D. Barrett, J. A. Sauer, K. M. Fortier, W. Zhang, L. You, and M. S. Chapman. Observation of Spinor Dynamics in Optically Trapped *Rb87* Bose-Einstein Condensates. *Phys. Rev. Lett.*, 92(14):140403, Apr 2004.
- [115] Ming-Shien Chang, Qishu Qin, Wenxian Zhang, Li You, and Michael S. Chapman. Coherent spinor dynamics in a spin-1 Bose condensate. *Nat Phys*, 1(2):111–116, November 2005.
- [116] Eva M. Bookjans, Christopher D. Hamley, and Michael S. Chapman. Strong Quantum Spin Correlations Observed in Atomic Spin Mixing. *Phys. Rev. Lett.*, 107:210406, Nov 2011.
- [117] C. D. Hamley, C. S. Gerving, T. M. Hoang, E. M. Bookjans, and M. S. Chapman. Spin-nematic squeezed vacuum in a quantum gas. *Nat Phys*, 2012.
- [118] C. Klempt, O. Topic, G. Gebreyesus, M. Scherer, T. Henninger, P. Hyllus, W. Ertmer, L. Santos, and J. J. Arlt. Parametric Amplification of Vacuum Fluctuations in a Spinor Condensate. *Phys. Rev. Lett.*, 104:195303, May 2010.
- [119] Jochen Kronjäger, Christoph Becker, Parvis Soltan-Panahi, Kai Bongs, and Klaus Sengstock. Spontaneous Pattern Formation in an Antiferromagnetic Quantum Gas. *Phys. Rev. Lett.*, 105:090402, Aug 2010.
- [120] D. M. Stamper-Kurn, M. R. Andrews, A. P. Chikkatur, S. Inouye, H.-J. Miesner, J. Stenger, and W. Ketterle. Optical Confinement of a Bose-Einstein Condensate. *Physical Review Letters*, 80(10):2027–2030, Mar 1998.
- [121] A. Lamacraft. Quantum quenches in a spinor condensate. 2006.
- [122] Yuki Kawaguchi Hiroki Saito and Masahito Ueda. Kibble-Zurek mechanism in a quenched ferromagnetic Bose-Einstein condensate. *cond-mat*, 2007.
- [123] Bogdan Damski and Wojciech H. Zurek. Dynamics of a Quantum Phase Transition in a Ferromagnetic Bose-Einstein Condensate. *Phys. Rev. Lett.*, 99:130402, Sep 2007.
- [124] Tomoya Isoshima and Sungkit Yip. Effect of Quadratic Zeeman Energy on the Vortex of Spinor Bose-Einstein Condensates. *Journal of the Physical Society of Japan*, 75:074605, 2006.
- [125] Jonas A. Kjall, Andrew M. Essin, and Joel E. Moore. Magnetic phase diagram of a spin-1 condensate in two dimensions with dipole interaction. *Phys. Rev. B*, 80(22):224502, Dec 2009.
- [126] H. Pu, C. K. Law, S. Raghavan, J. H. Eberly, and N. P. Bigelow. Spin-mixing dynamics of a spinor Bose-Einstein condensate. *Phys. Rev. A*, 60(2):1463–1470, Aug 1999.
- [127] C. K. Law, H. Pu, and N. P. Bigelow. Quantum Spins Mixing in Spinor Bose-Einstein Condensates. *Phys. Rev. Lett.*, 81(24):5257–5261, Dec 1998.

- [128] Jordi Mur-Petit. Spin dynamics and structure formation in a spin-1 condensate in a magnetic field. *Physical Review A (Atomic, Molecular, and Optical Physics)*, 79(6):063603, 2009.
- [129] Wenxian Zhang, D. L. Zhou, M.-S. Chang, M. S. Chapman, and L. You. Coherent spin mixing dynamics in a spin-1 atomic condensate. *Phys. Rev. A*, 72(1):013602, Jul 2005.
- [130] E. G. M. van Kempen, S. J. J. M. F. Kokkelmans, D. J. Heinzen, and B. J. Verhaar. Interisotope Determination of Ultracold Rubidium Interactions from Three High-Precision Experiments. *Phys. Rev. Lett.*, 88:093201, Feb 2002.
- [131] H.-J. Miesner, D. M. Stamper-Kurn, J. Stenger, S. Inouye, A. P. Chikkatur, and W. Ketterle. Observation of Metastable States in Spinor Bose-Einstein Condensates. *Phys. Rev. Lett.*, 82(11):2228–2231, Mar 1999.
- [132] Ming-Shien Chang. *Coherent Spin Dynamics of a Spin-1 Bose-Einstein Condensate*. PhD thesis, Georgia Institute of Technology, 2006.
- [133] J. Mur-Petit, M. Guilleumas, A. Polls, A. Sanpera, M. Lewenstein, K. Bongs, and K. Sengstock. Dynamics of $F = 1$ [sup 87]Rb condensates at finite temperatures. *Physical Review A (Atomic, Molecular, and Optical Physics)*, 73(1):013629, 2006.
- [134] Subroto Mukerjee, Cenke Xu, and J. E. Moore. Dynamical models and the phase ordering kinetics of the $s = 1$ spinor condensate. *Phys. Rev. B*, 76:104519, Sep 2007.
- [135] M. Vengalattore, J. Guzman, S. R. Leslie, F. Serwane, and D. M. Stamper-Kurn. Periodic spin textures in a degenerate $F = 1$ ⁸⁷Rb spinor Bose gas. *Phys. Rev. A*, 81(5):053612, May 2010.
- [136] Subroto Mukerjee, Cenke Xu, and J. E. Moore. Topological Defects and the Superfluid Transition of the $s = 1$ Spinor Condensate in Two Dimensions. *Phys. Rev. Lett.*, 97(12):120406, Sep 2006.
- [137] Fabrice Gerbier, Artur Widera, Simon Fölling, Olaf Mandel, and Immanuel Bloch. Resonant control of spin dynamics in ultracold quantum gases by microwave dressing. *Phys. Rev. A*, 73(4):041602, Apr 2006.
- [138] A. J. Bray. Theory of phase-ordering kinetics. *Advances in Physics*, 51(2):481–587, 2002.
- [139] J. F. Marko and G. T. Barkema. Phase ordering in the Ising model with conserved spin. *Phys. Rev. E*, 52:2522–2534, Sep 1995.
- [140] Keekwon Nam, Bongsoo Kim, and Sung Jong Lee. Coarsening kinetics of a two-dimensional O(2) GinzburgLandau model: the effect of reversible mode coupling. *Journal of Statistical Mechanics: Theory and Experiment*, 2011(03):P03013, 2011.
- [141] Martin Siegert and Madan Rao. Ordering dynamics of a conserved vector order parameter. *Phys. Rev. Lett.*, 70:1956–1959, Mar 1993.

- [142] A J Bray and K Humayun. Growth of order in vector spin systems; scaling and universality. *Journal of Physics A: Mathematical and General*, 23(24):5897, 1990.
- [143] A. J. Bray. Exact renormalization-group results for domain-growth scaling in spinodal decomposition. *Phys. Rev. Lett.*, 62:2841–2844, Jun 1989.
- [144] R. W. Cherng and E. Demler. Magnetoroton Softening in Rb Spinor Condensates with Dipolar Interactions. *Phys. Rev. Lett.*, 103(18):185301, Oct 2009.
- [145] Yuki Kawaguchi, Hiroki Saito, Kazue Kudo, and Masahito Ueda. Spontaneous magnetic ordering in a ferromagnetic spinor dipolar Bose-Einstein condensate. *Phys. Rev. A*, 82:043627, Oct 2010.
- [146] Yuki Kawaguchi, Hiroki Saito, and Masahito Ueda. Can Spinor Dipolar Effects Be Observed in Bose-Einstein Condensates? *Physical Review Letters*, 98(11):110406, 2007.
- [147] R. W. Cherng and E. Demler. Symmetry analysis of crystalline spin textures in dipolar spinor condensates. *Phys. Rev. A*, 83:053613, May 2011.
- [148] Krzysztof Gawryluk, Kai Bongs, and Mirosław Brewczyk. How to Observe Dipolar Effects in Spinor Bose-Einstein Condensates. *Phys. Rev. Lett.*, 106:140403, Apr 2011.
- [149] David Jacob, Lingxuan Shao, Vincent Corre, Tilman Zibold, Luigi De Sarlo, Emmanuel Mimoun, Jean Dalibard, and Fabrice Gerbier. Phase diagram of spin 1 anti-ferromagnetic Bose-Einstein condensates. September 2012.
- [150] E. Kim and M. H. W. Chan. Observation of Superflow in Solid Helium. *Science*, 305(5692):1941–1944, 2004.
- [151] John D. Reppy. Nonsuperfluid Origin of the Nonclassical Rotational Inertia in a Bulk Sample of Solid ^4He . *Phys. Rev. Lett.*, 104:255301, Jun 2010.
- [152] M. W. Ray and R. B. Hallock. Observation of Unusual Mass Transport in Solid hcp ^4He . *Phys. Rev. Lett.*, 100:235301, Jun 2008.
- [153] John Beamish. Supersolidity or quantum plasticity? *Physics*, 3:51, Jun 2010.
- [154] Massimo Boninsegni and Nikolay V. Prokof'ev. *Colloquium* : Supersolids: What and where are they? *Rev. Mod. Phys.*, 84:759–776, May 2012.
- [155] Yu. Kagan, G. V. Shlyapnikov, and J. T. M. Walraven. Bose-Einstein Condensation in Trapped Atomic Gases. *Phys. Rev. Lett.*, 76:2670–2673, Apr 1996.
- [156] M. Naraschewski and R. J. Glauber. Spatial coherence and density correlations of trapped Bose gases. *Phys. Rev. A*, 59:4595–4607, Jun 1999.
- [157] S. Dettmer, D. Hellweg, P. Ryytty, J. J. Arlt, W. Ertmer, K. Sengstock, D. S. Petrov, G. V. Shlyapnikov, H. Kreutzmann, L. Santos, and M. Lewenstein. Observation of Phase Fluctuations in Elongated Bose-Einstein Condensates. *Phys. Rev. Lett.*, 87:160406, Oct 2001.

- [158] E. W. Hagley, L. Deng, M. Kozuma, M. Trippenbach, Y. B. Band, M. Edwards, M Doery, P. S. Julienne, K. Helmerson, S. L. Rolston, and W. D. Phillips. Measurement of the Coherence of a Bose-Einstein Condensate. *Phys. Rev. Lett.*, 83:3112–3115, Oct 1999.
- [159] J. Stenger, S. Inouye, A. P. Chikkatur, D. M. Stamper-Kurn, D. E. Pritchard, and W. Ketterle. Bragg Spectroscopy of a Bose-Einstein Condensate. *Phys. Rev. Lett.*, 82:4569–4573, Jun 1999.
- [160] I. Bloch, T. W. Hansch, and T. Esslinger. Measurement of the spatial coherence of a trapped Bose gas at the phase transition. *Nature*, 403(6766):166–170, January 2000.
- [161] P. Cladé, C. Ryu, A. Ramanathan, K. Helmerson, and W. D. Phillips. Observation of a 2D Bose Gas: From Thermal to Quasicondensate to Superfluid. *Phys. Rev. Lett.*, 102:170401, Apr 2009.
- [162] Gretchen K. Campbell. *87Rubidium Bose-Einstein Condensates in Optical Lattices*. PhD thesis, MASSACHUSETTS INSTITUTE OF TECHNOLOGY, 2006.
- [163] A. F. Bernhardt and B. W. Shore. Coherent atomic deflection by resonant standing waves. *Phys. Rev. A*, 23:1290–1301, Mar 1981.
- [164] Phillip L. Gould, George A. Ruff, and David E. Pritchard. Diffraction of atoms by light: The near-resonant Kapitza-Dirac effect. *Phys. Rev. Lett.*, 56:827–830, Feb 1986.
- [165] Yu. B. Ovchinnikov, J. H. Müller, M. R. Doery, E. J. D. Vredenbregt, K. Helmerson, S. L. Rolston, and W. D. Phillips. Diffraction of a Released Bose-Einstein Condensate by a Pulsed Standing Light Wave. *Phys. Rev. Lett.*, 83:284–287, Jul 1999.
- [166] P. L. Kapitza and P. A. M. Dirac. The reflection of electrons from standing light waves. *Mathematical Proceedings of the Cambridge Philosophical Society*, 29(02):297–300, 1933.
- [167] Gretchen K. Campbell, Aaron E. Leanhardt, Jongchul Mun, Micah Boyd, Erik W. Streed, Wolfgang Ketterle, and David E. Pritchard. Photon Recoil Momentum in Dispersive Media. *Phys. Rev. Lett.*, 94:170403, May 2005.
- [168] Marek Trippenbach, Y B Band, Mark Edwards, Marya Doery, P S Julienne, E W Hagley, L Deng, M Kozuma, K Helmerson, S L Rolston, and W D Phillips. Coherence properties of an atom laser. *Journal of Physics B: Atomic, Molecular and Optical Physics*, 33(1):47, 2000.
- [169] L. Santos, M. A. Baranov, J. I. Cirac, H.-U. Everts, H. Fehrmann, and M. Lewenstein. Atomic Quantum Gases in Kagome Lattices. *Physics Review Letters*, 93, 2004.
- [170] B. Normand. Frontiers in frustrated magnetism. *Contemporary Physics*, 50(4):533–552, 2009.

- [171] Matthew P. Shores, Emily A. Nytko, Bart M. Bartlett, and Daniel G. Nocera. A Structurally Perfect $S = 1/2$ Kagom Antiferromagnet. *Journal of the American Chemical Society*, 127(39):13462–13463, 2005. PMID: 16190686.
- [172] S. Peil, J. V. Porto, B. Laburthe Tolra, J. M. Obrecht, B. E. King, M. Subbotin, S. L. Rolston, and W. D. Phillips. Patterned loading of a Bose-Einstein condensate into an optical lattice. *Phys. Rev. A*, 67:051603, May 2003.
- [173] Subhadeep Gupta. *Experiments with Degenerate Bose and Fermi Gases*. PhD thesis, MIT, 2003.
- [174] Subhadeep Gupta, Aaron E. Leanhardt, Alexander D. Cronin, and David E. Pritchard. Coherent manipulation of atoms with standing light waves. *Comptes Rendus de l'Academie des Sciences - Series IV - Physics*, 2(3):479 – 495, 2001.
- [175] Peter J. Martin, Bruce G. Oldaker, Andrew H. Miklich, and David E. Pritchard. Bragg scattering of atoms from a standing light wave. *Phys. Rev. Lett.*, 60:515–518, Feb 1988.
- [176] I. Bloch and M. Greiner. Exploring Quantum Matter with Ultracold Atoms in Optical Lattices. *Advances in Atomic, Molecular and Optical Physics*, 52, 2005.

Appendix A

Operation of the Ti-sub pump

A.1 Operating Procedure

To run the Ti-sub, the filaments must be lowered into the chamber using the translation stage, an water must flow through the 4-way cross before running current through the filaments. The filaments are in close proximity to the vacuum flanges and to prevent significant temperature gradients which may cause a small vacuum leak, tap water is used to cool the chamber. Typically, currents of 25-30 A were applied to the filaments for 2-3 minutes. The cooling water was left to run for 20 additional minutes. While hot, the filaments have expanded from their original size, and to prevent coming in contact with the vacuum chamber, the filaments were left in their lowered position overnight.

In order to prevent the deposition of titanium onto the slower viewport, we inserted a Viton O-ring sealed gate valve. When running the Ti-sub, the gave valve is closed, thus preventing any titanium from reaching the viewport.

A.2 Pumping Area

In order to determine the optimal location of the Ti-sub, we considered its proximity to viewports as well as the potential vacuum surface area that would be covered with titanium. In its current location, there is no direct line-of-sight for the titanium and the MOT chamber viewports or glass cells. Furthermore, a conservative estimate of the surface area to be covered is fairly substantial, $\approx 844 \text{ cm}^2$. This number takes into account only the five- and four-way cross, and the conical reducer, without including the surface area of the Zeeman slower tube. Based on this very conservative area estimate, pumping due to the Ti-sub is:

$$A_{CR} = 90 \text{ cm}^2 \tag{A.1}$$

$$A_{4WC} = 340 \text{ cm}^2 \tag{A.2}$$

$$A_{5WC} = 415 \text{ cm}^2 \tag{A.3}$$

$$Pumping \approx 2500 \text{ L/s} \tag{A.4}$$

where A_{CR} , A_{4WC} , A_{5WC} refers to the interior surface areas of the conical reducer, the four-way cross and the 5-way cross, and the pumping speed for molecular hydrogen at room temperature is 3 L/s/cm².

Running the Ti-sub in the spring of 2009 enabled us to reach pressures in the main chamber near 2×10^{-11} Torr. Since then, the Ti-sub has not been used.

Appendix B

Initial installment of an ODT

Aligning an optical trap with no reference point is nearly impossible unless you have a few helpful suggestions when starting such a process.

1. Image a thermal gas along the ODT direction by transmitting light through the ODT beam path. Focus the BEC onto the camera using a lens added right before the camera. This is typically easier if imaging light is sent along the ODT optical fiber.
2. Mark the atom location onto the camera.
3. Repeat this procedure with a physically smaller thermal sample to ensure that the position and focus are correct.
4. Now send repump light along this path and without adjusting any optics and image the atoms along an orthogonal direction. For our particular experiment, we this imaging axis is oriented along gravity.
5. If there is no image of atoms on the camera, repeat the previous steps.
6. Adjust the focus of the final ODT lens.
7. In order to determine the correct location of the final lens, the interaction of the repump and the atoms has a distinct signature. When correctly aligned, the strength of the atom-signal will appear weakest at the cloud center and strongest at the edge. This is because the spatial profile of the repump beam is largest at the cloud edge and smallest at the cloud center, if properly aligned. Note that adjusting the focus may steer the beam slightly.

Appendix C

Generating the rf-pulse sequence

Many of the details pertaining to the generation of the rf pulse sequence are described below. To generate the series of π/n pulses and have them be synchronized with the probe pulses as well as the shifting frames of the camera, we have developed an elaborate scheme, which most likely could have been accomplished and simplified greatly with a few micro-controllers. It is here for the sake of documentation, nonetheless.

We use a single TTL (camera trig.) from the word generator (WG) to trigger the imaging sequence. The TTL is divided into two paths; one path goes to the camera and probe, while the other path goes to generate the series of π/n rf pulses (see Fig. C.1).

Focusing on the first path, the TTL from the computer triggers a Stanford Research System function generator (SRS DS345). The SRS is configured in “Burst Mode” to generate a series of square pulses at its output. The output is directed into the trigger port of an SRS 4 Channel digital delay generator (DG535), the output of which goes to the camera and the image probe. Specifically, output AB is sent to the imaging probe rf switch. By controlling the delay timing between A and B, we are able to accurately control the probe pulse duration. In the experiments pertaining to spin-echo imaging, $B=A+200$ ns. Output CD is sent to the trigger input of the Princeton Instruments camera which is configured in kinetics mode. Thus, for every trigger the 4 Channel SRS receives (from the initial SRS), imaging light is directed onto the camera followed by the camera shifting frames, where one cycle time (probe light plus camera shifting frames) is determined by the frequency of the function generator, which we operated at 14.4 kHz (2.5 Vpp and 2.5 V offset).

Essentially, for path one of the setup, all that is required is that; (i) there is imaging light when the camera is not shifting frames, (ii) the camera has enough time to shift the required number of frames (maximum shift rate is 1 row/ μ s), and (iii) that the probe light only illuminate the atoms for less than $\leq \tau_{LP}/4$ [79].

For path two, the TTL from the WG is directed to a second 4 Channel digital delay generator. Output AB triggers the series of π rf pulses and output CD triggers the $\pi/2$ rf pulse for imaging the longitudinal magnetization. Focusing on output AB; the output triggers an SRS function generator (SRS Trig1), configured in “Burst Mode” and this output triggers the second SRS function generator (SRS π). The output of SRS π is directed to the DC+RF port of a Bias-T (part number) to eliminate any DC offset, most likely due to

ground loops. Finally, the RF port of the Bias T is sent to an rf switch, followed by an rf amplifier and then to the atoms via a coil. For this aspect of path two, SRS Trig1 sends a train of square pulses which then create a series of π rf pulses occurring at a rate of 14.4 kHz, identical to the imaging SRS generator frequency, ensuring that the π rf pulses, probe, and camera shifting occur with the proper timing. The typical delay values used are:

$$T = A + 40 \mu s \quad (\text{C.1})$$

$$B = C + 260 \mu s, \quad (\text{C.2})$$

where the delay time between A and B as well as C and D are not important as they are only serving as a trigger for devices (configured for rising edge TTL).

Output CD is identical to output AB except that only one $\pi/2$ rf pulse is generated. The elaborate setup for this one rf pulse is to ensure its proper timing with respect to the π rf pulse and imaging pulse. Additionally, for $\pi/2$ rf pulse, we use identical parameters as the π rf pulse, but control the amplitude externally.

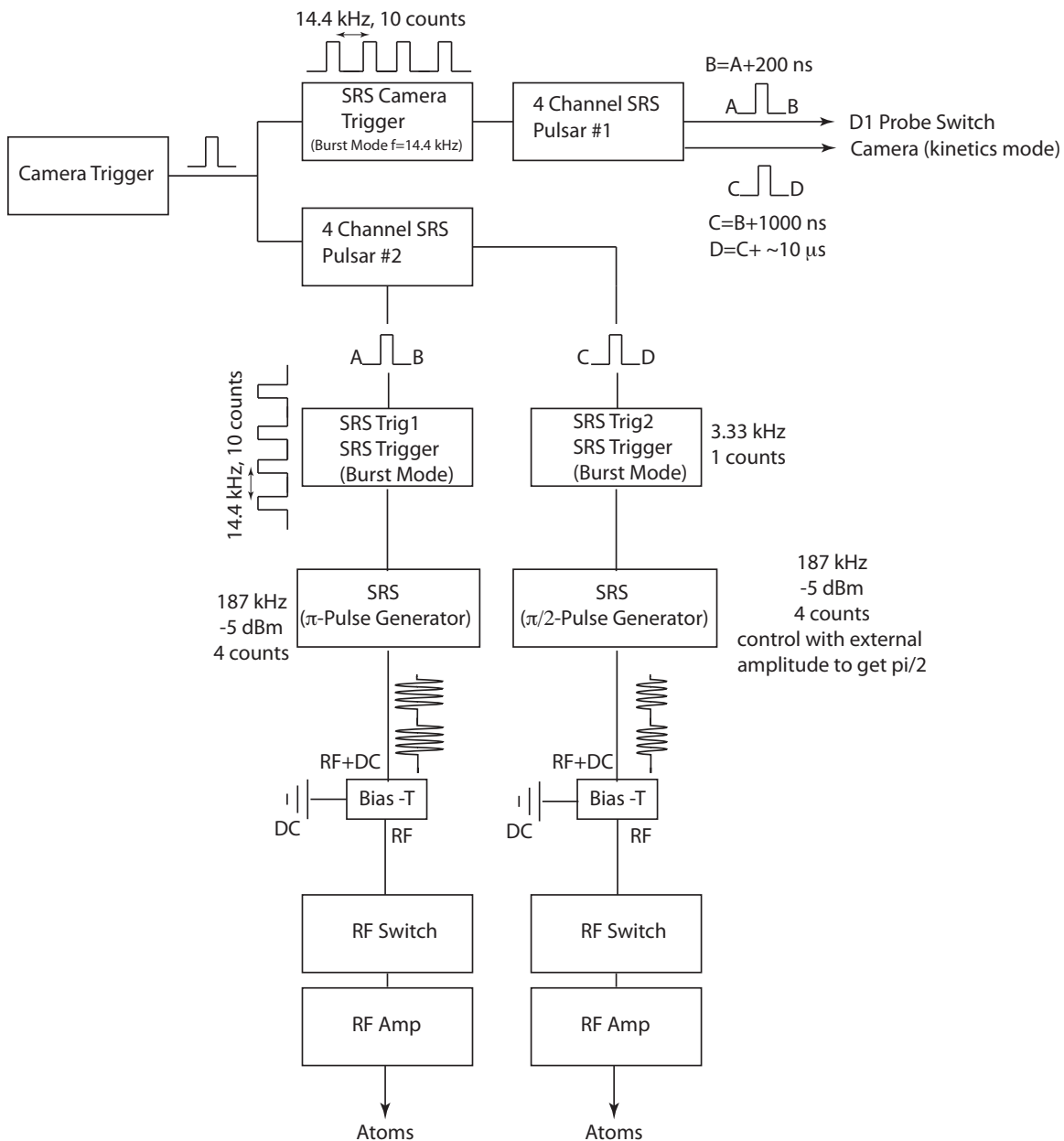


Figure C.1: Schematic of pulse generators used to create rf-pulse sequence for spin-echo imaging.

Appendix D

Alignment of an imaging system

Proper alignment is critical in high NA imaging systems. The order in which optics are aligned is determined by their relative position to the camera, beginning with the lens nearest to the camera and ending with the objective. The main alignment tool will be to use the back reflection of each lens.

Below is a general procedure for the alignment used to test the objective, consisting of the objective, a glass cell, and a 750 mm lens.

1. Determine the desired imaging path using HeNe light. This path will be the imaging axis and the axis with which you will align each lens within the imaging system. It is usually easiest if the path is level with the optics table or breadboard. The use of HeNe is optional since it is easy to see and will produce a fairly substantial back reflection by each optical element (assuming their antireflection (AR) coating does not cover HeNe). However, with the high power Verdi in the room, that would probably also suffice.
2. Position the camera such that it is centered about the imaging axis, located along the imaging axis where you anticipate the final image location. It is usually best to use a translation stage as you will undoubtedly need to adjust this position with respect to the final lens.
3. Position the $f = 750$ mm lens (final lens) approximately f away from the camera. This can be done rather coarsely. Next, place an iris between the light source and the 750 mm lens, concentric with the light source. Aperture down the iris until the clearance hole is the size of the imaging light. This will be used as a target to see the back reflections from the lens.
4. Identify the back reflections from each surface of the 750 mm lens (there should be two) which should appear near the face of the iris if the lens is not too far misaligned. By translating and rotating the lens the two back reflections should overlap with each other and coincide with the imaging axis. Translating the lens in the plane transverse to the imaging axis, the two back reflections should overlap, but this is not necessarily concentric with the imaging axis. Then by rotating the lens, it should be possible to move the two back reflections such that they overlap with the imaging axis.

5. Once the back reflections and imaging beam overlap, check if the distance between the camera and the lens is correct. This can be done by trying to image an object (or a face shown here in Fig. D.1) far from the lens; essentially something that is at “infinity.” Using the translation stage, move the camera until the image is in focus. This will almost certainly guarantee that the distance between the lens and camera is correct.
6. Position the glass cell. To do this, using a similar procedure as above, we centered the glass cell on the imaging beam and adjusted the tilt of the cell to overlap the back reflections.
7. Position the objective. This was a more difficult given the high NA. To translate the objective, we used short range nonmagnetic translation stages and adjusted the tilt using a mirror mount, resulting a finer control of the angle and position. There are approximately 3 back reflections to overlap; two from each surface of the meniscus and one from the flat side of the aspheric lens. The reflection from the curved surface of the aspheric lens has a significant divergence making it difficult to see and align to.
8. Next, position a test pattern inside the glass cell and while adjusting the focus of the objective, the test pattern should come into focus.

Typically, to check the overlap of the back reflections and to ensure a well aligned imaging system, a path length of at least 1 m is useful.



Figure D.1: Image of Andre Wenz while trying to align final lens with respect to the imaging camera. For this image, a 300 mm lens was being aligned. In order to place the lens a position f away from the camera, the objects needs to be located distance away that is $\gg f$. Here that distance was between 3-4 m.

Appendix E

Phase contrast imaging 101

This appendix includes a general outline for obtaining a phase contrast signal.

E.1 Phase contrast signal with no phase dot

In the early developmental stages of E5 (the next generation of E1), a reasonable phase-contrast signal was not easy to come by. There could be many reasons for this, some of which include:

- misaligned phase dot
- wrong probe detuning
- low density
- imaging $\langle F_y \rangle$, where the Clebsch-Gordan coefficients are smaller

The list can go on and on and during those first few months, any one of those reasons could be the culprit. Thus, we came up with a full proof plan to obtain a signal, which could later be optimized. The plan is as follows:

- Remove the phase dot - half the time your aligning to dust or to a scratch which is located near (within 1 mm) the ever tiny $250 \mu\text{m}$ dot. Just to be clear, only one of the two phase dots in the lab have a scratch, so you have a 50/50 chance at picking the better one.
- Park your probe detuning close to resonance, $\approx 80 \text{ MHz}$, blue/red detuned, it doesn't matter. Yes you will lose lots of atoms due to absorption, but this can be changed once a reasonable signal has been achieved
- Use linearly polarized light (reason to follow)
- Find a linear polarizer (half wave plate and a PBS works too) and place it anywhere after the atoms. Near the camera works fairly well since this is where you likely have the most room on the optics table.

- Rotate the polarizer such that it is at 45° with respect to the probe polarization; this occurs when roughly half the light is transmitted.
- Orient the spins of the condensate to be parallel to the imaging axis. This is typically done by rotating the magnetic field to be parallel to the imaging axis.

Appendix F

Lattice Alignment

F.1 Alignment Procedure

A total of eight optical beams need to overlap at the location of the atoms to make this lattice successful. To make the alignment process efficient and relatively quick, we have developed a systematic procedure for the aligning each beam.

1. **Dimple Beam** This should be centered on the in-trap surfboard ODT location. Being slightly off center axially would suffice as well. As stated above, the alignment of the dimple can be quite challenging and very sensitive to slight adjustments to the mirrors.
2. **Misaligned Dimple Beam** If the dimple beam is very misaligned, the top/down imaging camera can be used to image the dimple beam. After recording the in-trap surfboard position, run the camera in video mode and turn on the dimple beam. The beam should appear on the camera, despite the filters used to block out the 1064 nm light. Now the dimple beam can be coarsely tuned to the in-trap position of the ODT.
3. **SW: Beam 1 and Beam 2** After aligning the dimple beam and recording the position of the combined dimple/ODT potential, block all of the SW lattice beams except for Beam 1 or Beam 2. Then when running the sequence with the dimple beam OFF, align the 532 nm beam until it is splitting the condensate into two parts at the recorded location of the dimple/ODT. Continue to adjust the position with less power to ensure proper alignment and repeat this for the other beam.
4. **LW: Beam 1 and Beam 2** Follow a similar procedure for the 1064 nm beams. The exception here is that proper alignment is seen when the axial extent of the condensate profile is minimized, since the 1064 nm light is attractive.
5. **Kapitza-Dirac** The alignment of each lattice can be independently optimized using Kapitza-Dirac. This is typically done for each pair of beams for each wavelength of light, though optimizing all three beams for each lattice can also be done.